

Sheffield Hallam University

Computer simulation of self-assembling amphiphilic systems.

MICHEL, David.

Available from the Sheffield Hallam University Research Archive (SHURA) at:

<http://shura.shu.ac.uk/20062/>

A Sheffield Hallam University thesis

This thesis is protected by copyright which belongs to the author.

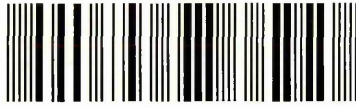
The content must not be changed in any way or sold commercially in any format or medium without the formal permission of the author.

When referring to this work, full bibliographic details including the author, title, awarding institution and date of the thesis must be given.

Please visit <http://shura.shu.ac.uk/20062/> and <http://shura.shu.ac.uk/information.html> for further details about copyright and re-use permissions.

Adsett's Centre City Campus
Sheffield S1 1WB

101 835 379 8



Adsett's Learning Centre
Fines are charged at 50p per hour

- 4 OCT 2007
4-20

REFERENCE

ProQuest Number: 10697369

All rights reserved

INFORMATION TO ALL USERS

The quality of this reproduction is dependent upon the quality of the copy submitted.

In the unlikely event that the author did not send a complete manuscript and there are missing pages, these will be noted. Also, if material had to be removed, a note will indicate the deletion.



ProQuest 10697369

Published by ProQuest LLC (2017). Copyright of the Dissertation is held by the Author.

All rights reserved.

This work is protected against unauthorized copying under Title 17, United States Code
Microform Edition © ProQuest LLC.

ProQuest LLC.
789 East Eisenhower Parkway
P.O. Box 1346
Ann Arbor, MI 48106 – 1346

COMPUTER SIMULATION OF SELF-ASSEMBLING AMPHIPHILIC SYSTEMS

David Michel

A Thesis submitted as partial fulfillment of the
requirements of Sheffield Hallam University for the degree
of Doctor of Philosophy

June 2006

Materials & Engineering Research Institute, Sheffield
Hallam University

Abstract

In this thesis, the results of a series of molecular computer simulation studies undertaken to investigate amphiphilic self-assembly are presented. Here, the aim has been to develop a coarse-grained model for amphiphilic behaviour, and examine its ability to exhibit free self-assembly of complex structures at moderate computational cost.

Firstly, the development of a novel single-site model for an amphiphilic molecule is addressed. The model is based on mixtures of (rod-like) Gay-Berne and (spherical) Lennard-Jones particles, the rods being taken to be single-site models of amphiphilic molecules immersed in a solvent of spheres. The hydrophobic effect, believed to be the main driver of amphiphilic self-assembly, is incorporated by giving the rod-sphere interaction a dipolar symmetry. Results obtained indicate that free self-assembly of micellar, lamellar and inverse micellar arrangements can be readily achieved.

Following on from these preliminary simulations, a refined rod-sphere potential has been used to study the micellar region in greater detail. The effects of both the amphiphilic strength and hydrophilic-lipophilic balance on micellar properties are examined. We find that these key molecular interaction parameters can be used to control the size, shape and internal structure of micelles. Interesting intermicellar phenomena can also be accessed within these simulations such as micelle fusion and exchange of long-lived monomers between micelles. Furthermore, a ‘rattling’ motion of short-lived monomers, leaving and re-entering micelles, can be observed.

Finally, binary mixtures of amphiphiles have been studied as a function of their mutual degree of attraction and the mixture composition ratio. The amphiphile with longest ‘hydrophobic’ tail is found to dominate the monomer phase whereas the micelles showed very different structures. A two-layer radial shell structure in the well-mixed micelles is found for mutually attractive amphiphile types. As the mutual attraction is reduced, structurally segregated spherocylindrical micelles dominate. In these, amphiphiles with large head groups tend to form the end caps of a cylinder made of amphiphiles with short head groups. When the mutual interaction is reduced even further, two distinct coexistent micellar phases are then observed with most micelles containing only one type of amphiphile.

Acknowledgments

I would like to thank my supervisors, Dr. Doug Cleaver and Prof. Chris Care, for their constant support and guidance during this thesis. I also wish to thank Dr. Ian Halliday and all the staff of the Materials & Engineering Institute for their help during my time in the Modelling Lab. I would like to acknowledge the great technical help of Terry Hudson, system administrator of the computer cluster and network.

It also gives me pleasure to thank all my colleagues from the Modelling Lab with whom I have worked and share the lab over the past three years. So thanks to Mike (aka *Miguelito*), Fred, Dmytro, Tim, Rachael, Fatima, Richard, Sergey, Laurence, Candy, Adam and Mikhail (aka *Mi-miche*) who have made it such an enjoyable place to study. Needless to say that I particularly thank Laurence Ellison who found a bug in my code when I thought everything was fine and bug-free!

I am very grateful to all my friends and housemates, most notably, Lee, Fatiha, Edouard, Boomi, Mike, spanish David 1, spanish David 2, Aysen, Katie, Marie, Matthieu, Prasanth, Uday, Louise and Antoine who made me feel so welcome in England. I also would like to thank Christina who knew how to support me, especially towards the last months of writing up, and made me feel very happy to live in Sheffield.

Finally, I'd like to say a big *Merci* to my family, especially my parents, who pushed me making the decision to move to Britain from France and for their constant encouragement and understanding, without which I would not have achieved all that I have today. Thanks also to my former G.P. in France who somehow found the right words to convince my mum that a thesis cannot be written in 2 weeks.

"A hypothesis or theory is clear, decisive, and positive, but it is believed by no one but the man who created it. Experimental findings, on the other hand, are messy, inexact things, which are believed by everyone except the man who did that work."

- Harlow Shapley (1885-1972) -

Advanced Studies

The following is a chronological list of related work undertaken and meetings attended during the course of study:

- MGMS Young Modellers' Forum in conjunction with the RSC Materials Modelling Group, Royal Institute of Physics, December 2002
- MERI seminars at Sheffield Hallam University (UK). "Molecular modelling of freely self-assembling amphiphilic structures" (talk), June 2003
- CCP5 Summer School for Methods in Molecular Simulation, King's College, London (UK). "Molecular modelling of self-assembling amphiphilic structures" (poster), July 2003
- CECAM workshop "Self organization in (bio)molecular systems", Lyon (France). "Molecular modelling of freely self-assembling amphiphilic structures" (contributed talk), October 2003
- NATO ASI "Soft condensed matter physics in molecular and cell biology", Edinburgh (UK). "Molecular modelling of bio-inspired self-assembling systems" (poster), April 2004
- BLCS Annual meeting, University of Manchester, Manchester (UK). "Molecular modelling of bio-inspired self-assembling systems" (poster), April 2004

- ILCC conference, Ljubljana (Slovenia). "Molecular modelling of bio-inspired self-assembling systems" (poster), July 2004
- CECAM workshop "Biomembrane organization and protein function", Lyon (France). "Bio-inspired computer simulation of self-assembling amphiphilic systems" (contributed talk), April 2005
- Mainz Materials Simulation Days 2005, Max-Planck Institute for Polymer research, Mainz (Germany). "Molecular modelling and simulation of micellar systems" (poster), June 2005
- CCP5 annual meeting, Keele University, Keele (UK). "Bio-inspired computer simulation of self-assembling amphiphilic systems" (contributed talk), August 2005
- Northern Atomistic Simulation Group (NASG) meeting, University of Sheffield, Sheffield (UK). "Molecular modelling of micelles and mixed micelles: structure and dynamics" (contributed talk), December 2005
- Royal University of Groningen (RUG), Groningen (Netherlands). "Molecular modelling of micelles and mixed micelles: structure and dynamics" (invited talk to the Molecular Dynamics group of Prof. Marrink), March 2006
- Max-Planck-Institut für biophysische Chemie, Göttingen (Germany), "Coarse-grained model of micelles and mixed micelles" (invited talk to the theoretical and computational biophysics group of Prof. Grubmüller), May 2006

This work has also been presented by my supervisor Dr. Doug Cleaver in Seminars at Avecia (Blackley), the University of Manchester (Physics Dept), as an

invited talk at the European Molecular Liquids Group Meeting (Sheffield, UK, Sept 2004), as an contributed talk at a CECAM meeting "Multiscale modelling of macromolecule/membranes interactions" (Lyon, France, August 2005) and as an invited talk at the Max-Planck Institute for Colloids and Interfaces (Golm, Germany, November 2005).

Table of Contents

1	Introduction	1
1.1	Aims & objectives	2
1.2	Outline of the thesis	3
2	Behaviours of amphiphilic systems	5
2.1	From soap to cell membrane	6
2.2	Phase behaviour of amphiphilic systems	8
2.2.1	Amphiphilic phases	8
2.2.2	Geometric considerations to phase behaviour	15
2.2.3	Experimental characterization of amphiphilic phases	18
2.3	Self-assembly of amphiphilic systems	19
2.3.1	The hydrophobic effect	19
2.3.2	Theoretical considerations of self-assembly	26
2.3.3	Surfactant mixtures	30
3	Computer simulations of amphiphilic systems	36

3.1	Computer simulation techniques	37
3.1.1	Molecular Dynamics	37
3.1.2	Other molecular simulations techniques	51
3.2	Simulations of amphiphilic systems: History and methods	53
3.2.1	Monte Carlo simulation of lattice models	53
3.2.2	Molecular Dynamics of all-atom models	57
3.2.3	Coarse-grained models	62
3.2.4	Mesoscopic models	69
3.3	Conclusion	73
4	Design of a novel single site amphiphilic model	76
4.1	Introduction	77
4.2	Computer model of rod-sphere mixture	78
4.2.1	The Gay-Berne Model	78
4.2.2	The rod-sphere potential	82
4.2.3	Preliminary simulations results	84
4.3	Modelling amphiphilic behaviour	86
4.3.1	The cubic model	87
4.3.2	The exponential model	91

4.4	Results	94
4.4.1	Effect of concentration on phase behaviour	95
4.4.2	Effect of molecular parameters	114
4.5	Conclusion	118
5	Effect of amphiphilic properties on micellar behaviour	120
5.1	Refinement of the rod-sphere potential	121
5.1.1	Definition of the model	121
5.1.2	Phase behaviour as a function of H and κ' with increasing concentration	124
5.2	Preliminary simulations at 5% rod concentration	128
5.3	Observed structures and processes of the micellar phase	130
5.3.1	Self-assembly properties	131
5.3.2	Micelle structure	133
5.3.3	Micelle dynamics	137
5.3.4	Monomer exchange and dynamics	147
5.4	Effect of model parameterisation on system properties	152
5.4.1	Micelle structures	156
5.4.2	Structure and dynamic aspects of the micellar behaviour	164

5.4.3	Monomer Dynamics	168
5.5	Conclusion	170
6	Behaviour of mixed micelles	172
6.1	Simulation methods	172
6.2	Results	174
6.2.1	Effect of mutual attraction between unlike amphiphiles . .	175
6.2.2	Effect of changing mixing ratios	190
6.2.3	Summary	200
7	Conclusion	203
7.1	Conclusions	203
7.2	Discussion and critique	205
7.3	Suggestions for future work and improvements	206
	Appendices	207
A	Derivation of Forces and Torques	208
A.1	Calculation of forces for Lennard-Jones particles	208
A.2	Calculation of forces and torques for Gay-Berne particles	209
A.2.1	Derivation of the forces and torques	209

A.2.2	Explicit analytical forms of all necessary derivatives	212
A.3	Calculation of forces and torques for the rod-sphere interaction . .	213
A.3.1	Original model	214
A.3.2	Cubic model	215
A.3.3	Exponential potential	216
A.3.4	Tanh potential	216
	Bibliography	217

CHAPTER 1

Introduction

An amphiphatic or amphiphilic molecule (from the greek *amphis*: both and *philia*: love) is a chemical compound possessing both an hydrophobic region and an hydrophilic region. The term *hydro* is often coined due to the omnipresence of water as a solvent, however, the term solvophilic/solvophobic is probably more appropriate for generic systems. As a result of this chemical frustration, these molecules are able to dissolve, to some extent, to both water and non-polar solvent such as oil. The duality induced by the combination of two antagonistic properties give rise to remarkable self-assembling lyotropic liquid crystalline phases over a wide range of composition and temperature.

The role of this class of molecules is immense in both nature and industrial applications. Indeed, phospholipids, a class of amphiphilic molecules, are the main components of biological membranes and the amphiphilic nature of this molecules defines the way in which they form these membranes. They are also dominant in the detergent industry through the use of surfactants (surface active agents). However, despite their wide technological applications and many years of investigations, little is known about the underlying physics of their self-assembly.

For the last few decades, many theoretical and experimental studies have been

performed on this matter in order to improve detergent efficiency but also for pure academic reasons. Indeed, the hydrophobic effect, key phenomena at the origin of their behaviour, is still poorly understood and, therefore, represents a fundamental question for many scientific communities, from biological to physical chemistry. New perspectives are also rising from so-called bio-inspired material science which aim at developing complex molecular systems which mimic nature. By adopting the principles of self-assembly found in biological systems to our own purposes, one could, for example, design novel materials with self-healing properties or novel drug delivery vehicles.

However, full theoretical treatment are usually extremely difficult to achieve due to the complex nature of these systems and most experimental techniques cannot achieve the molecular resolution required to make a link between molecular properties and the observed macroscopic phenomena. This is where computer simulation, as tool in between experimentation and theories, can be well-suited for investigating these systems and gain in-depth insights of the molecular behaviour.

1.1 Aims & objectives

The work presented in this thesis addresses the study of amphiphilic self-assembly processes by means of molecular simulations. The aims of this study were initially defined as follows:

- to understand the self-assembly processes involved in amphiphilic systems, in terms of generic molecular models, *i.e.* not bound to any chemical specificity. The main goal was to identify the underlying physics in order to simulate phenomena common to all amphiphilic molecules from phospholipids of the cell membrane to the surfactants used in detergents.
- to develop a model able to retrieve entire phase diagrams, *i.e.* not biased towards the formation of a given phase.

- to study in greater details one of this phase, *e.g.* the micellar phase, to identify and characterise generic processes of micellar formation, structures and dynamics. In particular, the effect of molecular interactions on the curvature of amphiphilic aggregates was of interests.

1.2 Outline of the thesis

Aside from this introduction, this thesis is organised as follows.

In chapter 2, some background information about amphiphilic systems is given. Specifically, the description of the types of molecules which exhibit such amphiphilic phases and details of the structures involved as well as experimental characterisation techniques, are discussed. This chapter also provides a description of the main theoretical models of amphiphilic self-assembly and a review of the hydrophobic effect, main driver of this amphiphilic self-assembly. Finally, details on the theoretical characterisation of mixed micellar phases is given.

Chapter 3 considers the description of the relevant Molecular Dynamics (MD) simulation technique used in this thesis and a comprehensive literature review of the different simulations performed on amphiphilic systems, from models with atomistic resolution to mesoscopic simulations.

Chapter 4 combines a detailed description of the proposed molecular model for generic amphiphilic behaviour and the preliminary results associated with this initial model. Specifically, the phase behaviour with amphiphile concentration is investigated and some discussion on the viability of this model is provided.

Chapter 5 presents an alternative parameterisation of this molecular model. This model is then used to study the micellar phase in greater details. Firstly, a description of the observed processes involved in a particular micellar system is given. Then, the effects of molecular interaction parameters on this processes are analysed.

In chapter 6, binary mixtures of amphiphiles are considered. Here, comparisons with single component system is provided in order to assess the effect of the mixing behaviour on micellar structures and self-assembly properties.

Finally, chapter 7 brings together the main results and conclusions of this thesis and suggestions for future areas of work are listed.

CHAPTER 2

Behaviours of amphiphilic systems

Amphiphilic molecules are used in a wide range of applications [1] in industry as well as in everyday life. Amphiphiles are found in soaps and detergents, paints, ink, paper coatings, food and pharmaceutical applications, etc... Amphiphilic molecules are also found in nature, being fundamental to a feature found in every single living organism on the planet: the cell membrane. Biological amphiphiles, such as phospholipids, serve as the building blocks of cell membranes. Thus their behaviour has attracted interest from several communities. Not only biology, biochemistry and biophysics, where the interest is obvious, but also physical chemistry and chemical engineering, due to the fascinating variety of self-assembling supermolecular structures available. Theoretical physics and mathematics have also contributed to this field, novel theoretical models having been developed to aid understanding of the conformational behaviour of these structures.

In this chapter, the phase behaviour of amphiphilic systems is reviewed as well as the properties of amphiphilic self-assembly in dilute solutions. First, an introduction to surfactant systems and their applications in real life is presented.

The second part of this chapter deals with a more detailed study of the phase behaviour of systems involving amphiphiles. Finally, The factors affecting the self-assembly properties of these molecules are reviewed.

2.1 From soap to cell membrane

The word surfactant is an abbreviation of surface active agent and means, by definition, active at surfaces and interfaces. Surfactant or amphiphiles usually are linear molecules with a hydrophilic ('attracted' to water) head and a hydrophobic ('repelled' by water) tail. This 'dual personality' is characteristic of surfactant systems which have the tendency to be absorbed at interfaces between two immiscible phases such the air/water or oil/water interface. In doing so, they enable the system to reduce its free energy by removing hydrophobic groups from the aqueous environment. Thus surfactant molecules are well known as being able to reduce the surface tension of an interface. On the same basis, these molecules tend to aggregate in aqueous solution in order to shield their hydrophobic tail(s) from the solvent. This phenomenon occurs due to a combination of several factors but the so-called 'hydrophobic effect' is believed to be the main driver of this self-assembly (see next section).

Due to their molecular anisotropy, amphiphiles are capable of forming numerous supramolecular structures, some of which are of biological interest. The simplest of these is the spherical micelle in which the molecules tend to cluster with their hydrophilic groups pointed outward and their hydrophobic groups pointed inward, so forming a spherical aggregate. A more detailed description of this phase behaviour can be found in the next part of this chapter.

In a typical amphiphilic system, the head groups carry a small electrical charge, which makes them soluble in water but not very soluble in oil. In contrast, the long, uncharged hydrophobic tails are much less soluble in water but are more

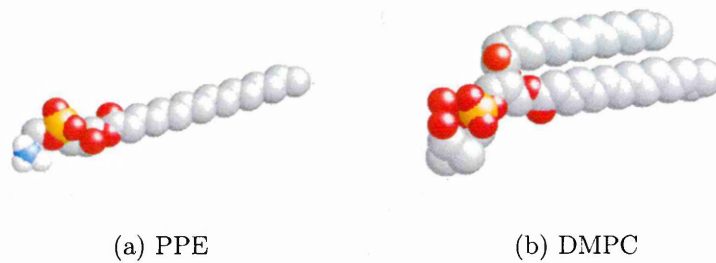


Fig. 2.1: Polypropylene (PPE) and Disphosphatidyl-choline (DMPC)

soluble in oil, which is also non-polar. The tail usually consists of a hydrocarbon or fluorocarbon chain while the polar or ionic head can be a variety of chemical structures. These different chemical structures can give the head an overall charge which will alter the properties of the amphiphile. This charge is, therefore, often used to categorise the amphiphile into one of this groups:

- Non-ionic (neutral)
- Anionic
- Cationic
- Zwitterionic (contains both anionic and cationic charge)
- Amphoteric (can be either cationic, anionic or zwitterionic depending on solution pH)
- Gemini (surfactant possessing more than one hydrophobic tail and hydrophilic head group)

Surfactant systems are also related to other soft condensed matter systems such as colloidal suspensions and liquid crystals: they can all spontaneously self-assemble into correlated structures with very useful materials properties. For instance, lyotropic liquid crystals exhibit a key characteristic of biomolecular self-assembly

in that the amphiphilic nature of a lipid (on the nanometre scale) generates self-organized structures on the mesoscopic scale. Lamellar lyotropic phases are composed of stacks of lipid bilayer separated by a solvent. Here, the spacing between the bilayers is well defined and can be hundreds of nanometres even though the structure remains liquid-like at the molecular scale.

In fact, amphiphilic systems have been shown to encompass a much wider range of phase behaviour than biological systems and it is clear that numerous materials with novel properties could be elaborated through an improved knowledge of the self-assembling process (*e.g.* creating template for organic mesoporous materials [2] or creating artificial liposomes). Many amphiphilic systems exhibit a very rich phase diagrams even in simple binary surfactant-water combinations. These systems are also very dependent on concentration, temperature and other characteristics of the solvent such as the pH. Many other structures can be found in the nature on a larger scale. The shapes of these assemblies are as varied as the capacity of the molecules to move though space will allow: from spheres and planes to highly interconnected bi-continuous structures.

2.2 Phase behaviour of amphiphilic systems

2.2.1 Amphiphilic phases

At very low concentration, amphiphiles are scattered throughout an aqueous environment and form a disordered isotropic solution (phase L). At a certain concentration, the surfactants spontaneously aggregate into globular constructions known as micelles (phase L_1). A micelle can be simply described as a spherical surface of polar heads dissolved in water, while the inner portion consists of a pure hydrocarbon liquid core. However, this description is rather simplistic and much work has been done experimentally, theoretically and by simulation, to clarify micellar structure. Contrary to the illustration shown in Fig. 2.2(a), a micelle

is characterised by a liquid-like core with disordered hydrocarbon chains and a rough surface.

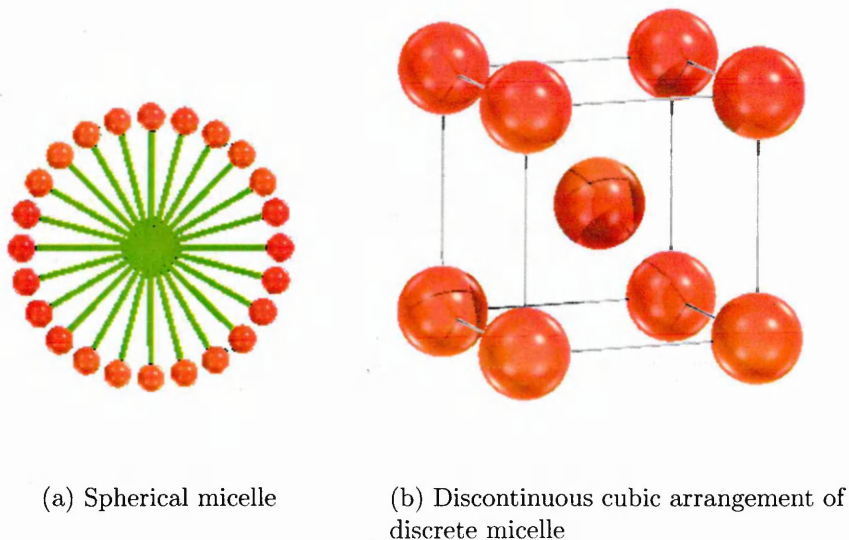


Fig. 2.2:

The micellar phase is mainly characterised by its dynamic properties: micelles are in dynamic equilibrium with each other and with their monomers (un-aggregated amphiphiles) in solution. In other words, micelles exchange monomers between one another and also form and break-up at certain rates. Intermicellar exchange rate occurs on the nanosecond scale while micelle formation/break-up occurs on a time scale of the order of a second.

Throughout the micellar concentration region, one can find micelles of various shapes and sizes. As concentration increases, for example, it is not uncommon to find cylindrical micelles of bigger size.

This basic structure can itself then be arranged into a further supramolecular structure with a higher degree of order. As the concentration increases, for example, micelles can organize themselves into a body-centered cubic liquid crystal structure (phase I_1) as shown on Fig. 2.2(b).

Rod-shaped or tubular micelles of indefinite length forming hexagonal structures

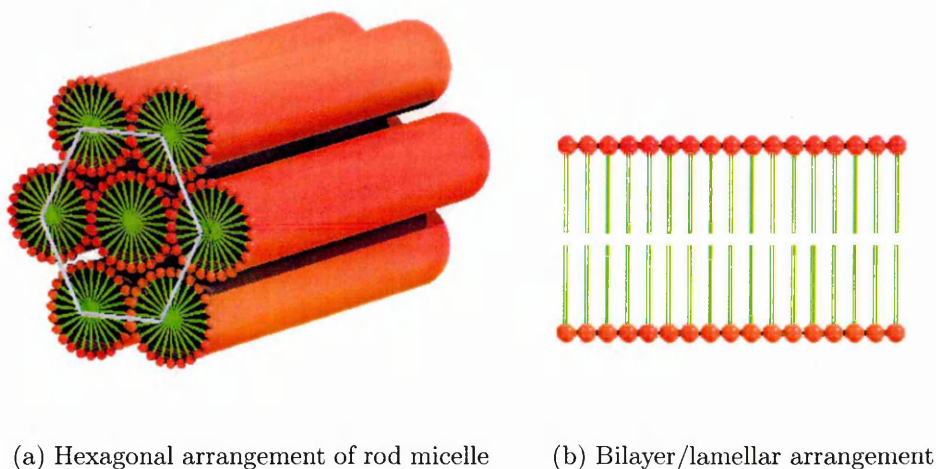


Fig. 2.3:

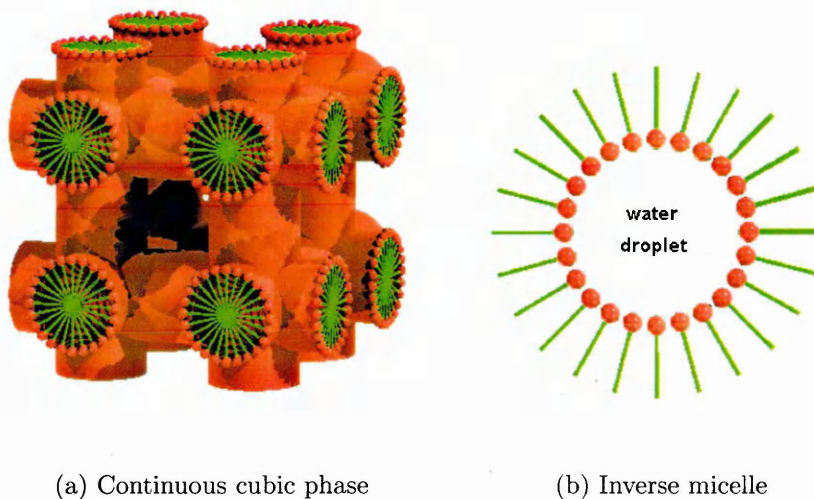
can be observed as well (phase H_I). Here, the distance between adjacent cylinders depends on the water content, but can vary over the range 8-40 Å (Fig. 2.3(a)). At higher concentrations, another liquid crystalline form can be produced : the lamellar phase (L_α) which is characterised by a stack of double layered sheets of amphiphiles (Fig. 2.3(b)). These bilayers generally extend over length scales of the order of microns or even more. The interbilayer distance typically ranges between 2-220 Å whereas the bilayer thickness can vary from $\sim 8\text{Å}$ to $> 100\text{Å}$. These phases are not as dynamic as the micellar phase and the molecules remain in the bilayer for a relatively long time, rather than continually diffusing in and out the aggregate.

As for the micelle, the schematic representation of a bilayer shown in (Fig. 2.3(b)) is misleading. The L_α phase is characterized by a liquid-like structure of the chains. By decreasing the temperature, in fact, a gel phase (denoted L_β) can be found in which the hydrocarbon chains are well ordered. This gel phase can also adopt a tilt compared to the bilayer normal (L_c) due to an asymmetry in the amphiphile molecular shape; alternatively, the 2 layers can significantly overlap each other, leading to a thinner bilayer membrane ($L_{\beta 1}$). An intermediate between the L_c phase and the L_α is the L'_β where the bilayer is tilted but the chains are still in a fluid state. Also, a so-called 'ripple phase' has been found in phospholipid

bilayers which exhibit a co-existence between liquid phase L_α domains and gel phase L_β or L_c domains.

For some systems, an isotropic phase constituted of multiple interconnected bilayers, or sponge phase (L_{III}), can be found at high temperature (50-80C).

Between the lamellar phase and the hexagonal phase, one can usually find another cubic phase called V_I (see Fig. 2.4(a)) or V_{II} for the reverse form.



(a) Continuous cubic phase

(b) Inverse micelle

Fig. 2.4:

As the amphiphile concentration is increased even further, inverse phase start to be formed, in which the water forms droplets surrounded by amphiphiles (see Fig. 2.4(b)). Like normal micelles, inverses micelles (L_2) come with different size and shape depending on the concentration and the type of amphiphiles. Inverse hexagonal phase (H_{II}) also exists between the inverse micellar phase and the lamellar phase, where water cylinders are packed into hexagonal arrays.

Phospholipids, which are found in cell membrane, spontaneously form vesicles in water, encapsulating a small water droplet in a spherical shell of phospholipid bilayer. Both the inner and outer wall of the shell are composed of hydrophilic heads, whereas the alkane tails occupy the inside of the vesicle shell. Fig. 2.2.1 below show a slice through a spherical vesicle.

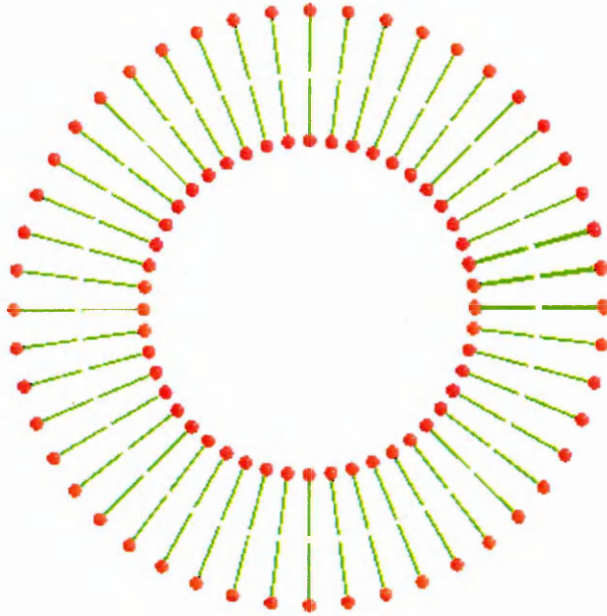


Fig. 2.5: Vesicle

Vesicles can be described as ideal membrane systems since the vesicle's underlying membrane molecular arrangement is the lipid bilayer. The elasticity of membrane bilayers was studied independently in the 1970's by Canham [3], Evans [4] and Helfrich [5], the aim being to understand the formation of vesicles from planar lipid bilayers. Shear and stretch are in fact very negligible forces acting on a vesicle floating in water. Therefore, the main force to play a role in vesicle formation is flexion. On applying a flexion force, the membrane is deformed and a curvature is induced. The flexion that determines the elastic energy of the membrane in its final state is proportional to the mean curvature of the membrane. The elastic energy of curvature or bending energy is, therefore, directly related to the geometrical shape of the vesicle. Thus, if the vesicle is at thermal equilibrium, it attains a shape corresponding to the minimum bending energy, assuming a fixed volume and surface area. This has led to the definition of the 'curvature model' from the Canham-Helfrich hamiltonian which describes how a surface will coalesce with itself to form a vesicle. This model can predict the shape of a vesicle for a fixed volume and surface area (assuming that the exchange of molecules with the

surrounding solution is very slow and so the area is essentially constant on experimentally relevant timescales). It involves parameters like the bending rigidity, the spontaneous curvature and gaussian curvature modulus as well as the pressure difference between the inside and the outside of the vesicle and the lateral tension.

Vesicles, and especially liposomes (vesicles made up of phospholipids) are extensively used in research and industry (see [6] for review). They can be a very useful tool for the reconstitution of artificial biological membrane and be, therefore, used for elucidating the mechanisms of membrane fusion. (e.g. virus-cell interactions can be studied experimentally for immunological research). Liposomes also have an important technological impact as transport vehicle for new drug delivery systems and DNA transport. Liposomes can also provide a model system relevant for the emergence of life and the study of their self-assembly could, help understanding its origin [7].

Phase behaviour of a binary water/amphiphile

The stability of all the phases described above depends largely on the type of surfactant used. Thus, the sequence of structures observed with increasing concentration is always the same but their windows occurrence may be different. Also, it is seen experimentally that the phase behaviour of amphiphilic systems is a function of concentration and temperature. Therefore, from this point of view, amphiphiles can be considered as lyotropic liquid crystals (the so-called thermotropic liquid crystals exhibit ordering transition as temperature only is changed).

Some work has been done experimentally to construct phase diagrams for different amphiphiles with different molecular geometries. For example, phase behaviour of series of pure polyoxyethylene surfactants (C_nEO_m) with water has been studied using optical microscopy techniques, adiabatic calorimetry [8] or small-angle neutron scattering and electrical conductivity measurements [9]. From these studies,

complete phase diagrams of these linear surfactants for different chain and head group lengths have been constructed over a temperature range of 0 – 100°C.

As can be seen from Fig. 2.6, the phase diagram changes dramatically with increasing the head group size. On the phase diagram of $C_{12}EO_8$, all of the phases described earlier are present, with the micellar and hexagonal phase being predominant, but the lamellar phase existing in a very small region of temperature and concentration. In contrary, $C_{12}EO_3$ displays only a lamellar phase, this being available over a large range of concentration.

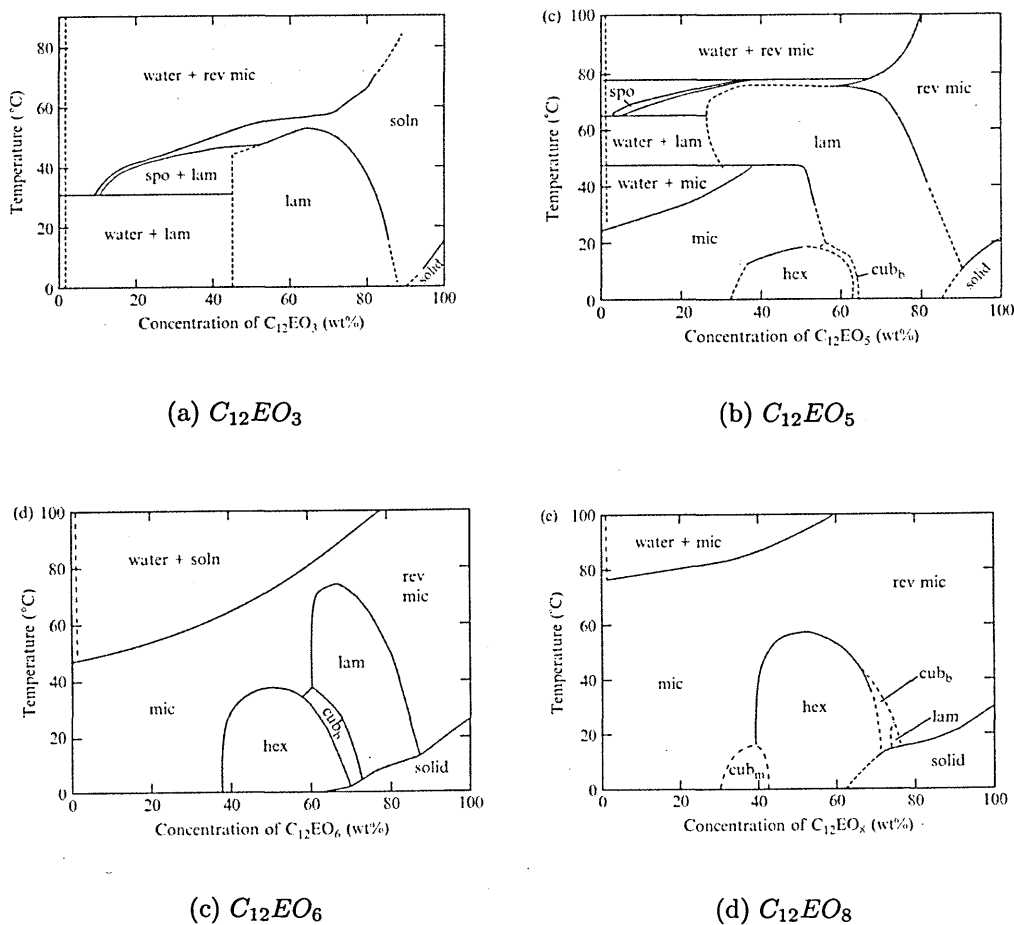


Fig. 2.6: Phase diagrams of non-ionic surfactant-water systems for C_{12} chain surfactant with different head group size (3,5,6 and 8 oxyethylenes). mic: micellar phase L_1 , rev mic: inverse micellar phase L_2 , lam: lamellar phase L_α , spo: sponge phase L_3 , hex: hexagonal phase H_1 , cub_m : micellar cubic phase I_1 , cub_b : bicontinuous cubic phase V_1 - From [10]

By observing the phase diagrams of other C_nEO_m systems, one can also see the effect of increasing the head group size: certain phases like the hexagonal phase and micellar phase are favoured by large head groups while other phases, such as the lamellar phase, become less and less prevalent.

Also, throughout the micellar phase L_1 , by increasing concentration and/or temperature, micelle morphology can change, leading to rod-like and/or disk-like aggregates. Thus, the nature of the low temperature LC mesophase can be related to the shape of the micelle formed at high temperature. For instance, cooling down a rod-like micelle, can lead to formation of a H1 phase.

More recently, the structure-properties relationship of surfactant/water systems have been investigated by looking at different surfactant shapes while keeping the hydrophilic-lipophilic-balance, or HLB, constant (the HLB represents the ratio between the net hydrophobic volume and the net hydrophilic volume in a given system). Such studies have clearly indicated the relationship between molecular geometry and the LC phase behaviour and micellar aggregate shapes.

2.2.2 Geometric considerations to phase behaviour

The complex behaviour of amphiphiles in an aqueous medium is governed by complex thermodynamics forces, particularly the hydrophobic effect (see section 2.3.1 for a more detailed review). While the concentration is a crucial parameter in controlling the final structure, however the geometry of the molecule plays a significant role in determining, e.g., the natural curvature of the interface between water-rich and amphiphile-rich regions.

In the 1930's, Hartley *et al.* [11] suggested that surfactants can self-assemble to form globular aggregates (micelles) in which the hydrophobic chain is molten. This hypothesis leads to the idea that in order for them to pack, their molecular dimensions must be compatible. For instance, in a micelle, the length of the molecule is equal to the radius of the spherical micelle. Thus, some aspect of the

mesoscopic geometry can be interpreted in terms of the molecular geometry of the amphiphile: the phase favoured by a particular amphiphile partly reflect its molecular shape [12]. This phenomenon is quantified by the surfactant shape factor or critical packing parameter CPP, $S_p = v_{hc}/a_0l_{hc}$. This parameter describes the geometry of the molecule in terms of the volume of the hydrophobic chain region v_{hc} , the length of the chain l_{hc} and the polar head group cross-section a_0 .

- Spherical micelle

A micelle of radius R has a surface area of $4\pi R^2$ and a volume of $4\pi R^3/3$. Thus the number of particles in a micelle can be written as $4\pi R^2/a_0$ or $4\pi R^3/3v_{hc}$. Equating these expressions gives: $R = 3v_{hc}/a_0$. Then, since there is no void inside a micelle, R must be less than or equal to the length of the hydrocarbon chain l_{hc} and the last equation becomes $v_{hc}/a_0l_{hc} \leq 1/3$. In other words, spherical micelles are favored by a shape factor $S_p \leq 1/3$. This corresponds to a conical shape, *i.e.* single-chained lipids with large head-group areas.

- Cylindrical micelle

Following the same algebra leads to $1/3 < S_p < 1/2$ for the range of shape factor favoring cylindrical micelles. These are single-chained lipids with small head-groups.

- Curved bilayer

With a shape factor in the range $1/2 < S < 1$, curved bilayers can be observed as well as vesicles. These are double-chained lipids with large head-group area, like phosphatidylcholine.

- Planar bilayer

if interdigitation is neglected, the packing geometry of a bilayer is best satisfied by cylindrical molecules and hence the shape factor favored for bilayers is $S \approx 1$. These are double-chained lipids with small head-group areas like phosphatidyl ethanolamine.

- Inverted micelle

For $S > 1$, the head group is relatively small and the favored aggregate is an inverse micelle.

This geometric argument can be quite useful in linking the shape of an aggregate with the molecular packing properties of the amphiphiles. However, from a geometric point of view, different structures could fit the same molecular geometry. This critical packing parameter is, therefore, not the only parameter to consider. From a thermodynamic perspective, too large a structure can create too much order (low entropy) whereas too small a structure can cause the surface area of the hydrophobic part in contact with water to be undesirably large.

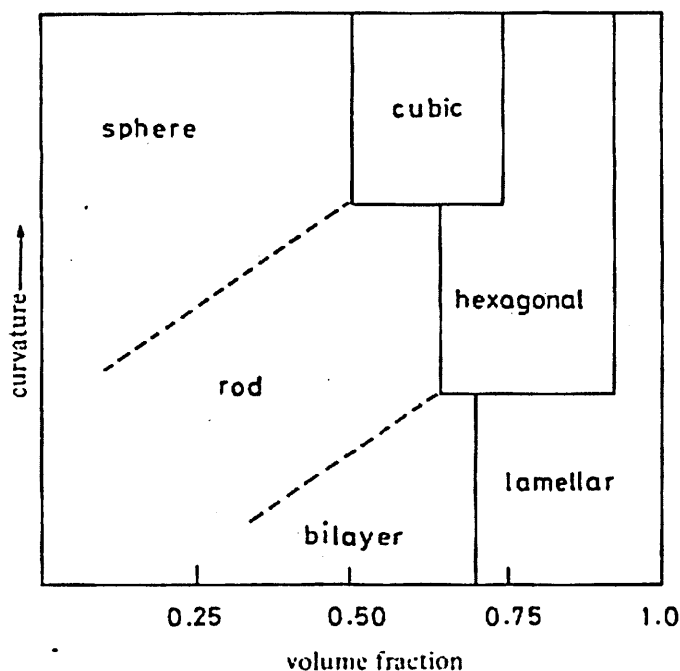


Fig. 2.7: Schematic diagram representing shape of the aggregate as a function of the intrinsic curvature and concentration of the amphiphilic molecules in the family C_nEO_m [10]

Following these considerations, however, the model phase diagram presented on Fig. 2.7 has been developed for the family of linear surfactants C_nEO_m . It shows

how the overall shape of the structure formed varies with concentration and curvature. The curvature here is a rather abstract variable, representing the intrinsic curvature associated with a particular molecular geometry.

This concept of packing constraint has been very useful for understanding the geometrical structure of surfactant aggregates. However, this concept only works with non-ionic surfactants. For systems containing ionic surfactants, the complex electrostatic interaction between the head groups also has to be considered in order to explain the observed phase behaviour.

2.2.3 Experimental characterization of amphiphilic phases

Micellization properties

As stated above, at low concentration amphiphilic molecules are dispersed through the solvent. The physicochemical properties of the solution are then the same as those of a simple electrolyte. When reaching a critical concentration, known as the "Critical Micelle Concentration" or CMC, the amphiphiles start to aggregate. This change can be experimentally determined by measuring many different physicochemical properties.

Properties of other phases

The other amphiphilic phases are usually determined by polarized optical microscopy. Each phase has a specific texture which allows them to be identified: A lamellar phase has a mosaic or streaked texture while a hexagonal phase displays fan-like features. However the cubic phases (I_1 , I_2 , V_1 , V_2) do not have any axes of symmetry and, therefore, are not optically bi-refringent. However, these isotropic phases can be identified by their viscosity and the phases surrounding them. Other techniques such as nuclear magnetic resonance (NMR), electron-spin resonance (ESR) and X-ray diffraction methods are often useful complementary

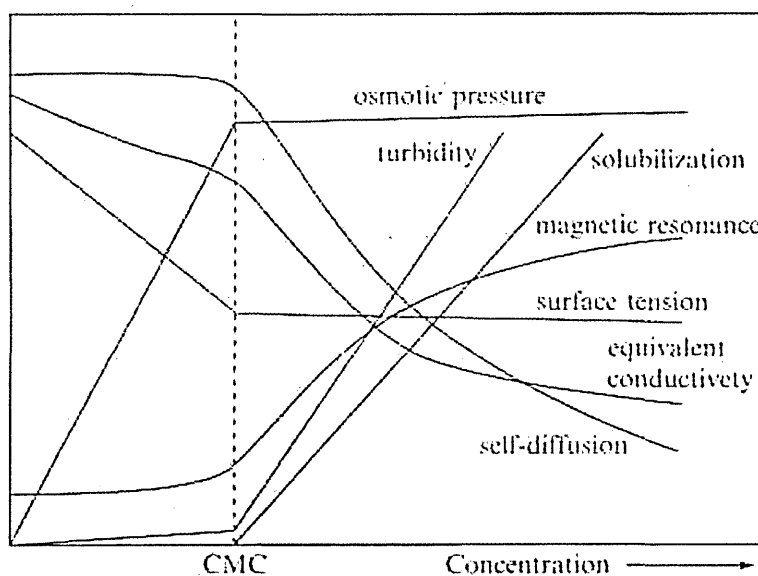


Fig. 2.8: schematic representation of the concentration dependence of some physicochemical properties around the CMC

techniques used to clarify ambiguous information.

2.3 Self-assembly of amphiphilic systems

In the previous section, the phase behaviour of amphiphilic systems was reviewed and some geometric argument were given relating molecular packing to the shapes of the various aggregates formed. The aim of this section is to identify the driving forces that promote this self-assembly. Some theories accounting for micellar self-assembly are briefly presented and, finally, the interesting case of mixed micelles is presented.

2.3.1 The hydrophobic effect

The self-aggregation of amphiphilic molecules does not occur due to a strong attraction between the amphiphiles and it is not appropriate to consider only the

amphiphile-amphiphile interaction when considering these systems. As a matter of fact, micelles do not form in the gas phase, or in non-polar solvent. The self-aggregation of amphiphiles can be, rather, explained through the action of an effective interaction: the hydrophobic effect.

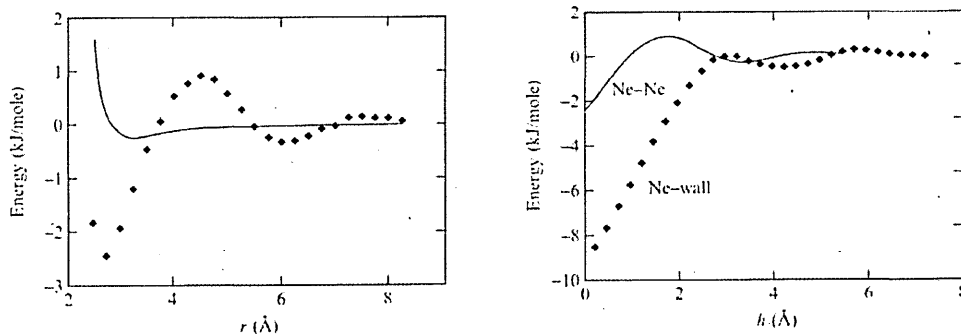
In spite of being treated quite extensively in the literature, it seems that some aspects of hydrophobic interactions (HI) are still to be addressed. In fact, it seems that HI are used by different authors to describe different phenomena. The term hydrophobic effect usually encompasses several phenomena under a single appellation. Hydrophobic hydration is usually used to describe the solvation of a hydrophobic particle in water. On the other hand, hydrophobic interactions usually refers to the interactions between two hydrophobic solutes in water. For any solvent, the words solvophobic and solvophilic are commonly applied.

Furthermore, it seems that the concept of hydrophobicity is not fully understood and there are still some fundamental questions to answer. Is there a relation between HI and the peculiar properties of water ? Is this hydrophobic effect limited to aqueous solvents ? Are HI important for biological processes (protein folding, amphiphilic bilayer self-assembly) ?

Hydrophobic hydration and hydrophobic interactions

Many experiments, theoretical arguments and simulation studies have been performed to examine the low solubility of non-polar solutes such as noble gases in aqueous solvents.

Forsman and Jönsson performed a Monte Carlo simulation (see next chapter for a brief description of this simulation technique) of the transfer of a non-polar molecule (Neon) into water at room temperature [13, 14]. Fig. 2.9 shows the calculated free energy of interaction between two neon atoms in the gas phase and in liquid water (Fig. 2.9(a)) and that of a neon atom with an hydrophobic wall in water (Fig. 2.9(b)). It can be clearly seen that the interaction between 2 neon



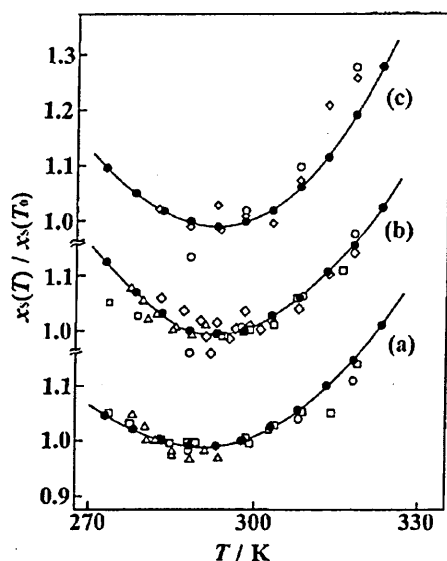
(a) Free energy of interaction between 2 neon atoms in liquid water (dotted line) and in the gas phase (continuous line)

(b) Free energy of interaction of a neon atom with a hydrophobic wall in liquid water (dotted line). The continuous line represent interaction between 2 neon atoms in water

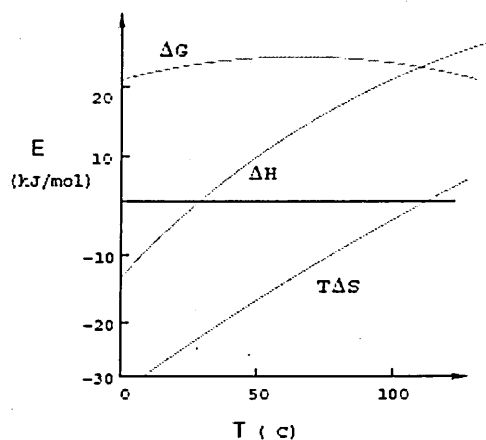
Fig. 2.9: Monte Carlo simulation of the hydrophobic effect from [13]

atoms in water has a much stronger attractive minimum than that found in the gas phase. Also, as an hydrophobic wall is introduced, the neon-wall interaction increases even further.

'Oil and water don't mix'. This fact is so ingrained into our every-day life that we never ask why it is so. The hydrophobic effect could be described as the tendency of non-polar solutes to cluster so as to shield themselves from contact with an aqueous environment. To account for this, Langmuir proposed the existence of a strong mutual interaction between non-polar solutes together with a repulsive potential between them and water. However, hydrophobic de-mixing processes actually appear to be related to entropy driven ordering and are, therefore, quite different from the enthalpy driven mixing/demixing processes exhibited by other liquids. In most liquids, phase separation depends on the enthalpies of mixing, *i.e.* how favorable the interactions are between similar compounds compared to their interactions with one another. One could model this by considering two types of particles A and B and setting the interaction energies between them such that: $AA = BB \gg AB$.



(a) Temperature dependence of solubility of alkylbenzenes in water at 0.10 MPa: (a) toluene, (b) ethylbenzene (c) propylbenzene from different authors: \bullet [15], \circ [16], \triangle [?], \square [17], \diamond [18]. Taken from [15]



(b) Gibbs free energy ΔG , enthalpy ΔH and entropy ΔS of solvation measured experimentally by calorimetry, reproduced from [19]

Fig. 2.10: Signature of the hydrophobic effect - at room temperature: solubility is lowest, entropy is negative and enthalpy is zero.

The hydrophobic effect is, however, distinct from generic de-mixing. First, the solubility curve of a typical hydrocarbon in water shows a different behaviour from that seen for most liquids (Fig. 2.10(a)). Instead of increasing monotonically with temperature, the solubility curve display a minimum at around room temperature. This is consistent with the free energy of solvation ΔG displaying a maximum around room temperature. This is explained by the entropic contribution being negative (favoring de-mixing) and the enthalpic contribution being around zero (even negative for some compounds like pentane and cyclohexane) at room temperature (Fig. 2.10(b)). The early data of Eley from 1937 [20] showed that (i) gas solubility in water is much lower than it is in organic liquids and that (ii) it decreases with increasing temperature, the opposite trend to that seen for other solvents. While these results contradicted Langmuir's model, they were in

agreement with an alternative hypothesis introduced by Harkins. A contemporary of Langmuir, Harkins put forward the idea that the low solubility of apolar solutes in water was due to the strong association of water rather than any direct interactions involving hydrocarbons. Indeed, Oss *et al.* in 1980 [21] showed that the hydrocarbon-hydrocarbon interaction energy is in fact about the same as the water-hydrocarbon interaction energy. This picture is fundamentally very different from Langmuir's theory: there is no 'phobia' between hydrocarbons and water but a relative 'philia' between them [22].

In 1945, Frank and Evans [23] invoked an 'ordering' of the water molecules around a non-polar solute to account for the entropic loss. By adopting certain configurations, the water molecules surrounding a solute were considered able to maintain their hydrogen bonds without losing enthalpy. This ordering of the water molecules induced a rotational restriction which may be related to the observed increased strength of the hydrogen bonds [24]. Self-assembly could, though, still occur if the entropic cost of demixing water and hydrophobic solutes proved smaller than the entropic cost of ordering water molecules at the hydrophobic surface of the molecule. From this, one can see that the effective attraction of two hydrophobic molecules is not a result of a direct pairwise potential between them. Rather, it results from a solvent-induced interaction which tends to minimize the surface area of the solute exposed to water (see Fig. 2.11). As pointed by Hildebrand in 1968 [25], the term 'hydrophobic' is misleading and it would probably be more accurate to refer to water being 'lipophobic'.

From this perspective, one can also consider the effect of the solute on hydrophobic interactions. When solutes are small, water can form a cavity without losing hydrogen bonds, so it is more likely that water will separate such species rather than drive them together. In contrast, water is not able to accommodate large hydrophobic objects as a complete hydrogen bond network then becomes unachievable for geometric reasons. This situation leads, therefore, to a strong effective attraction between large hydrophobic objects [26-28]. This size dependence is

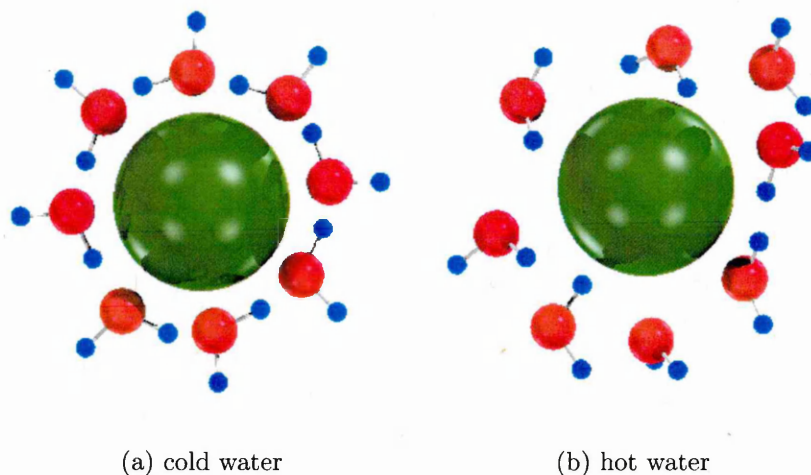
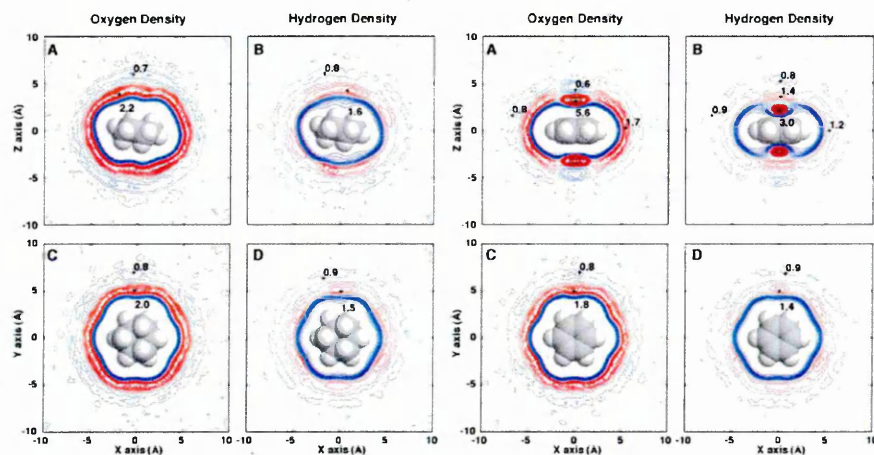


Fig. 2.11: ‘iceberg model’ for the large negative entropy of transfer of nonpolar solutes into water. (a): at room temperature the water molecules adopt a cage-like structure (large negative entropy) to avoid wasting hydrogen bonds (low enthalpy). (b) in hot water, more configurations become accessible (higher entropy) but at the cost of breaking hydrogen bonds (high energy)

in agreement with experimental results and simulations. It also explains why the neon-wall free energy interaction is more attractive than the neon-neon interaction in liquid water (recall Fig. 2.9(b)). Also recent studies of hydration map calculations and RDF calculation for several hydrocarbon molecules [29] show that this effect seems to be largely independent of the molecular details of the solute-solvent interaction within broad families (see Fig. 2.12).

According to this explanation, the hydrophobic effect is due exclusively to hydrogen bonding. This means that other hydrogen bonding liquids could potentially display equivalent behaviour. This suggestion has now been verified experimentally several times as amphiphilic aggregation has been established in hydrazine [30, 31], ethylammonium nitrate [32], formamide [33] and glycols [34]. All of these solvents share the properties of having hydrogen bonding capability and a high dielectric constant. It has also been shown [35] that amphiphilic aggregation does not occur in 3-methylsnydnone, a solvent with high dielectric constant and a cohesive energy comparable with that of an hydrazine and ethylammonium nitrate, but no O-H bonds (aprotic solvent).



(a) Water Density Surrounding Cyclohexane

(b) Water Density Surrounding Benzene

Fig. 2.12: Detailed 3D hydration maps of Cyclohexane (a) and Benzene (b) from [29]

However, other studies suggest that the property of water responsible for hydrophobicity is its small size. Madan and Lee [36] showed that the free energy of cavity formation in water is very similar to that of non-polar liquids of the same size. Lee has also proposed that while the hydrogen bonding properties of water play a role in determining the enthalpy and entropy of solvation, these contributions act to cancel each other out [37]. This enthalpy-entropy compensation makes the small size of water a dominating factor in hydrophobic interactions. This view has been confirmed by Pohorille and Pratt [38] who used a simulation study to show that the work required for cavity formation in water is only about 20% higher than in hard-sphere fluid of equivalently sized particles.

As pointed by Lazaridis [39], the relative importance of cohesive energy and the small size of water has not been yet resolved. However, whatever the molecular mechanism, the net free energy change is unfavorable for dissolution, resulting in the aggregation of solutes. As pointed out by Chandler, though, a fundamental difference between water-oil phase separation and amphiphilic self-assembly is stoichiometry [40]. Each amphiphile contains an oily species that is constrained to remain within a molecular length of the hydrophilic species. This constraint frus-

trates macroscopic phase separation and, so, limits these systems to mesoscopic assemblies such as micelles.

2.3.2 Theoretical considerations of self-assembly

The self-assembly of amphiphiles into aggregates can be described energetically by considering the cluster formation processes to be ‘entropy driven’ in an aqueous medium. Cluster formation lowers the number of independent objects in the system and thus reduces the entropy. At the same time, by clustering into aggregates, the amphiphiles’ hydrophobic segments are shielded from the aqueous solvent, leading to a reduction in the system’s potential energy. Therefore, the self-assembly processes of amphiphiles in water can be described in terms of a competition between the potential energy, which favours clustering, and the entropy, which favors a homogeneous distribution of the molecules in the solution.

Considering the micelle state as a reference with zero free energy, one can define an energy penalty E_{bind} for an amphiphile to escape from the micelle. On leaving a micelle, the molecule increases its energy by E_{bind} but also increases the entropy of the system: to assess the resultant behaviour of the system, it is useful to draw an analogy between the dilute solution and an ideal gas.

The entropy per molecule of an ideal gas at number density ρ is :

$$S_{gas} = k_b \left[\frac{5}{2} - \ln \left(\rho \left[\frac{h^2}{2\pi m k_b T} \right]^{\frac{3}{2}} \right) \right] \quad (2.1)$$

Thus, we write the free energy per molecule in the solution phase as:

$$F_{sol} = E_{bind} - TS_{gas} = E_{bind} - T k_b \left[\frac{5}{2} - \ln \left(\rho \left[\frac{h^2}{2\pi m k_b T} \right]^{\frac{3}{2}} \right) \right] \quad (2.2)$$

- at low density (small ρ) S_{gas} dominates and the dispersed phase is favored.

- at higher density (large ρ) E_{bind} dominates and the condensed phase is favoured.

This simple analysis leads to the idea of a threshold for the micelle formation at $E_{bind} = TS_{gas}$, corresponding to an aggregation density of

$$\rho_{agg} = \frac{\exp(5/2 - E_{bind}/k_bT) h^3}{(2\pi m k_b T)^{3/2}} \quad (2.3)$$

This leads to the concept of a critical micelle concentration (CMC) described earlier in this chapter.

The micellization process has been extensively studied experimentally but also theoretically with four main models being developed to observe micelle formation. These are the phase separation model, the mass action model, the multiple equilibrium model and the small system model.

Phase separation model

In this model, the monomers and the micelles are considered as two different phases. The system is treated as if it undergoes a phase transition as the concentration reaches the CMC. The micellar pseudo phase is then considered as a separated phase from the free monomers. This model is easy to understand and easy to use but experimental values show discrepancies with predicted values. In contradiction with this model, it is observed, experimentally that the monomer number does not remain constant above the CMC, leading to some important changes in micelle size and shape, which are not taken into account in this simple model [41, 42]

The mass action model

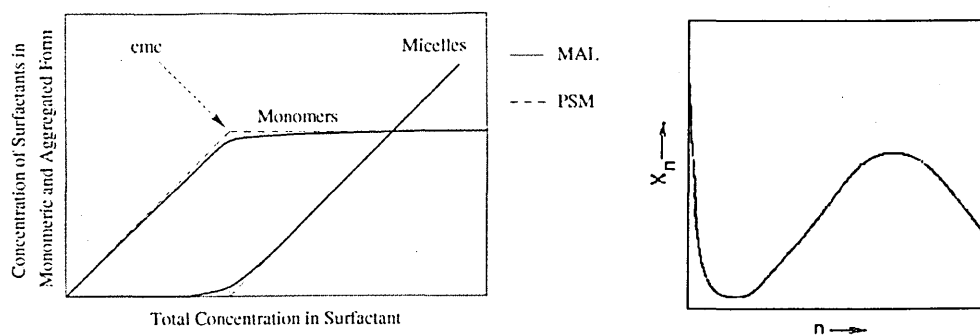
In the mass action model, each micelle is described by an aggregate A_n of a unique size n in equilibrium with monomers A_1 :



with the equilibrium constant $K = \frac{f_n X_n / n}{(f_1 X_1)^n}$

where X_n and X_1 are the molar concentrations of micelles and monomers, respectively, and f_n is the activity coefficient of a molecule in a cluster of size n .

This model has proved to be a better approximation to micellar formation than the phase separation model. It shows a smoother transition in the micelle/monomer concentration at the CMC (Fig. 2.13(a)). However, as with the phase separation model, the monomer concentration remains constant above the CMC and, therefore, this approach fails to explain non-ideality phenomena seen with, *e.g.* ionic surfactants [43, 44]



(a) Schematic distribution of amphiphiles between monomers and micelles: typical predictions from mass action model (plain lines) and the phase separation model (dashed lines) [45]

(b) Schematic size distribution plot for a typical micelle-forming amphiphile [46]

Fig. 2.13:

The multiple equilibrium model

Both the phase separation model and the mass action model fail to describe the inherent polydispersity of the micellar phase. The assumption that the micelles are monodisperse constitutes an over simplification that prevents micelle size and shape from being studied adequately. Thus, the multiple equilibrium model represents a refinement of the mass action model, since it considers micelles of different sizes in equilibrium with each other. To do this, the original single-step reaction is replaced by a series of association/dissociation reactions of monomers with aggregates of size $n - 1/n$.



The reaction equation can be summarised by a single-step reaction:



and corresponds to the case where an aggregate is formed directly from monomers rather than through a stepwise addition of monomers. τ_1 and τ_2 represent the two characteristic relaxation times; a fast relaxation time (τ_1), microseconds, and a slow relaxation time (τ_2), milliseconds to minutes.

This model allows account to be taken on polydispersity of micellar phases. As shown on Fig. 2.13(b), the micelle size distribution function, not available experimentally, comprises two main peaks: one peak corresponding to the presence of monomers and a second broader peak indicating micelles. The maximum of this second peak typically occurs at aggregation number of the order of 50-100. Thus, a true micellar phase contains both monomers and micelles, the presence of sub-micellar aggregates and very large micelles being very unlikely. Indeed, the presence of a minimum in the size distribution plot was proposed to be a

characteristic of micellar phases [46].

Ben-Shaul *et al.* [47] have extended this model by incorporating an extra term in the expression for the chemical potential so as to account for non-ideality due to changes in aggregate shape above the CMC. This leads a better description of micellar behaviour and allows analysis of micelle shape transitions. For example, the micelle sphere-to-cylinder transition, which can occur on increasing the amphiphile concentration above the CMC, can be described by decomposing the free energy of a rod-like micelle into contributions from the cylindrical centre and the semi-spherical end caps.

The small system model

Another method uses a modified version of the theory of small systems [48] in which micelles are considered as ‘small systems’ in dynamic equilibrium with each other and surrounded by a bath defining the environment variables [49]. It allows prediction of size distributions as a function of temperature, pressure and free monomer chemical potential. However, despite a rigorous treatment, this approach has not yet been very popular and is often regarded as unnecessary complicated.

2.3.3 Surfactant mixtures

Many theoretical and experimental studies involve only one type of amphiphile for simplicity. However, most everyday life applications of amphiphilic molecules employ mixtures. Commercial detergents usually include several kinds of surfactants. Pure surfactants are expensive and have very little advantage over less expensive mixtures [50]. Indeed, in many cases, mixtures have superior properties to those of the individual surfactant components involved [51–53]. Biological membranes can also contain up to a thousand different lipids [54]. The study of amphiphilic

mixtures is, therefore, of great interest for many scientific fields. However, the complexity involved in treatment of mixtures has limited their studies and the available literature is relatively sparse.

We have seen, in the previous section, that different amphiphilic molecules can give very different phase behaviours. By changing their molecular geometry or the chemical nature of the head or tail groups, large variations can be observed in the phase properties such as the CMC. In mixed amphiphile systems, the CMC may lie somewhere between those of the pure amphiphiles, but there are many examples for which this is not the case [55].

Another issue relevant to mixture systems is that the surfactant composition of its micelles may differ greatly from that of both surfactant monomers with which they are in equilibrium. In other words, the tendency of these molecules to distribute themselves between the monomer phase and the micelle phase, may vary from component to component. Thus, it is possible to obtain a binary mixture in which the micelle composition is 50/50 whereas the monomer composition is 90/10 [50]. This is of practical importance as a certain monomer or micelle composition may be needed. For example, in the adsorption of surfactant on to solids the monomer concentration is crucial whereas the solubilisation of these solids will largely be controlled by the micelle composition. This monomer-micelle equilibrium is, therefore, an important issue to understand in order to predict micelle and monomer compositions.

When dealing with mixtures of amphiphiles, the interaction between different amphiphile types has to be considered. In a mixture comprising 2 different amphiphiles, denoted A and B with very similar hydrophilic head groups and tails containing similar hydrophobic groups, the only difference between the amphiphiles may lie in the chain lengths. In this circumstance, the A-A, B-B and A-B interactions can be considered equal, and, the net interaction between the different amphiphile species can be set to zero. In many real systems, however, the repulsion between head groups can be very different for the intra-species and inter-

species interactions. For example, in a mixture of ionic and non-ionic amphiphiles, the repulsion between the head groups of the ionic amphiphiles is shielded by the non-ionic amphiphiles, leading to a net interaction between the two species. In an anionic/cationic mixture, there is an even stronger net interaction between the two species which need to be taken into account in any theoretical treatment of this kind of mixtures.

Mixtures with no net interaction

In the case of mixtures with no net interactions, one can calculate the CMC of the mixture as the weight average of the CMCs of the two amphiphiles types, i.e.:

$$CMC = x_A CMC_A + x_B CMC_B \quad (2.7)$$

where x_i is the mole fraction and CMC_i the critical micelle concentration of amphiphile i , with $i = A, B$. However, this linear combination describing the CMC of the solution can lead to incorrect results when considering the concentration of the species in system as a whole.

A better description can be achieved by considering the fraction of the amphiphile species within the micelles, x_i^m

$$CMC = x_A^m CMC_A + x_B^m CMC_B \quad (2.8)$$

x_i^m can be written as

$$x_A^m = \frac{x_A CMC_B}{x_A CMC_B + x_B CMC_A} \quad (2.9)$$

Also, one can derive the expression for the CMC as a function of the mole fraction of the amphiphiles in the whole system, i.e. the solution composition:

$$\frac{1}{CMC} = \frac{x_A}{CMC_A} + \frac{x_B}{CMC_B} \quad (2.10)$$

Figs. 2.14(a) and 2.14(b) show the calculated values of the CMC and the micelle composition as a function of the solution composition for three cases, $CMC_B/CMC_A = 0.01, 0.1$ and 1 .

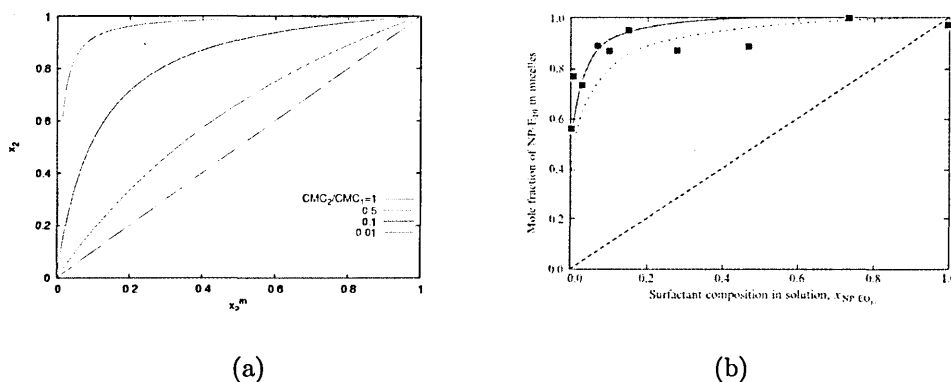


Fig. 2.14: (a): Micellar composition as a function of the solution composition in the bulk solution for $CMC_B/CMC_A = 1, 0.1$ and 0.01 calculated using Eqn. 2.9 (b): Surfactant composition in micelles, $x_{NP-E_{10}}^m$, in a $SDS + NP - E_{10}$ system, as a function of the surfactant composition. The dashed line represents the same composition in the micelles and bulk. The dotted line is the calculated composition assuming no interactions using Eqn. 2.9. Full line is calculated from Eqn. 2.14

From these, one can clearly see the effect of adding a second amphiphile with a smaller CMC to the solution. As amphiphile B is added, the mole fraction of amphiphile B in the micelles increases dramatically. For 20% amphiphile B in the solution, the micelle composition exceeds 97.5% in amphiphile B. This also leads to the monomer composition being very different from the solution composition. Fig. 2.14(b) illustrates a comparison between this predicted behaviour and experimental results obtained from sodium dodecyl sulfate (SDS) + ethoxylated monylphenol $NP - E_{10}$ mixture. In this case, the theory gives a reasonable fit. However, this is not always the case due to non-ideal effects in the mixing behaviour. This can, nevertheless, be taken into account by considering a net interaction between the two surfactant species.

Mixtures with a net interaction

In this case, Eqn. 2.8 is rewritten as:

$$CMC = x_A^m f_A^m CMC_A + x_B^m f_B^m CMC_B \quad (2.11)$$

where f_i^m is the activity coefficient of the amphiphile in the micelle and is described by the regular solution theory:

$$\ln f_i^m = (x_i^m)^i \beta \quad (2.12)$$

with β being an interaction parameter quantifying the net interaction between the amphiphile species. Positive values of β represent a net repulsion while negative β implying a net attraction. Substituting these alternative expressions into the above treatment finds that

$$\frac{1}{CMC} = \frac{x_A}{f_A^m CMC_A} + \frac{x_B}{f_B^m CMC_B} \quad (2.13)$$

From this, one can readily derive an expression describing the mole fraction of component A in micelles, x_A^m , as a function of the total mole fraction of A in the bulk, x_A . Thus:

$$x_A^m = \frac{x_A f_B^m CMC_B}{x_A f_B^m CMC_B + x_B f_A^m CMC_A} \quad (2.14)$$

Using this equation, one can study the variation of the micelle composition vs. bulk concentration curve as a function of the mutual interaction between both species set by the parameter β . This is shown for the $SDS + NP - E_{10}$ mixture in Fig. 2.14(b). Fig. 2.15 illustrates the behaviour of micelle composition for two surfactants having the same CMC ($CMC_A/CMC_B = 1$). The theoretical predictions are shown on Fig. 2.15(a) for different values of β . Experimental measurements are shown in Fig. 2.15(b) for a mixture of a sodium decylsulfate (SDeS) and de-

cyltrimethylammonium bromide (DeTAB). This is a typical system with a large net attraction between the surfactants ($\beta=-13.2$). For this mixture, the micellar composition is constant at almost all bulk compositions due to the effect of the electrostatic attraction between the two surfactant species. As the CMC ratio between the two species is changed, the behaviour of the micellar composition can also be dramatically modified, as shown on Fig. 2.16.

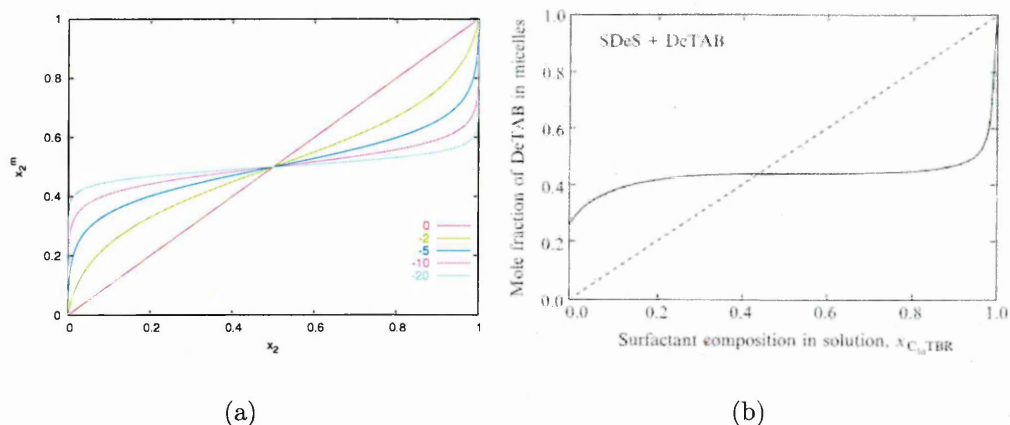


Fig. 2.15: micellar composition vs. bulk composition for different β values, calculated for $CMC_A/CMC_B = 1$. (a): predicted micellar composition using Eqn. 2.14 (b): Experimental results from [56]. The dashed line shows the predicted behaviour for $\beta = 0$. The sigmoid continuous curve corresponds to $\beta = -13.2$

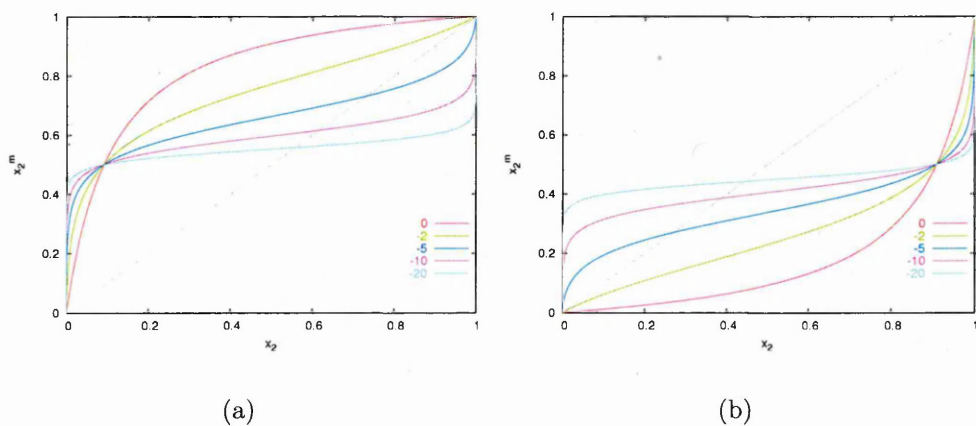


Fig. 2.16: micellar composition vs. bulk composition for (a): $CMC_A/CMC_B = 0.1$ and (b): $CMC_A/CMC_B = 10$ calculated using Eqn. 2.14

CHAPTER 3

Computer simulations of amphiphilic systems

Theories of hydrophobic molecule self-aggregation in water commonly focus on comparing the chemical potentials of free solute molecules with the associated ones. Thus, for each specific aggregate size and shape, the system free energy can be calculated and the most stable arrangement selected as the equilibrium phase. Numerical methods using this approach have been very successful at predicting size distributions and phase boundaries for amphiphilic systems but are not able to probe the dynamics and pathways by which such systems evolve. Also, the *a priori* specification of the aggregate structure needed for such treatments prevents the identification of novel and unexpected phases. These shortcomings can be overcome, however, by studying self-assembly systems using computer simulation techniques. Various simulation techniques have been used over the past 20 years to study amphiphilic systems. These have proved to be very useful in giving insights into the molecular behaviour underlying these systems that are relatively inaccessible to both experiment and theory.

The first part of this chapter contains a review of the different simulation tech-

niques used to study soft condensed matter system and a detailed description of the main method used in material simulation at atomistic and molecular scale, called Molecular Dynamics. Following this, previous work on the simulation of amphiphilic systems is reviewed.

3.1 Computer simulation techniques

This section presents an overview of the numerous simulation techniques available for studying soft condensed matter systems. These different techniques have been developed through the years in order to access different time and length scales relevant to these systems. One of the most common techniques used is the Molecular Dynamics technique (MD), described in detail in the following section.

3.1.1 Molecular Dynamics

The basic idea

Molecular dynamics is a method which solves the classical equations of motion for N atoms and/or molecules to obtain the time evolution of the system, assuming quantum mechanical effects to be negligible. Considering a system of molecules with Cartesian coordinates \mathbf{r}_i , the equations of translational motion are

$$\frac{d^2}{dt^2} (m_i \mathbf{r}_i) = \mathbf{f}_i \quad (3.1)$$

$$\mathbf{f}_i = -\nabla_{\mathbf{r}_i} U \quad (3.2)$$

where m_i is the mass of molecule i and \mathbf{f}_i the force acting on that molecule. The forces are derived from the potential U that describes the interactions between

the particles.

The simplest model of a liquid is a system of spherical particles, interacting via a pairwise potential, that depends on the distance between them, $r_{ij} = |\mathbf{r}_i - \mathbf{r}_j|$. As we know, molecules repel when they are very close to each other, but attract each other at larger separation. The most widely used model for such an interaction is the Lennard-Jones potential.

$$U_{LJ}(\mathbf{r}_{ij}) = 4\epsilon \left[\left(\frac{\sigma}{r_{ij}} \right)^{12} - \left(\frac{\sigma}{r_{ij}} \right)^6 \right] \quad (3.3)$$

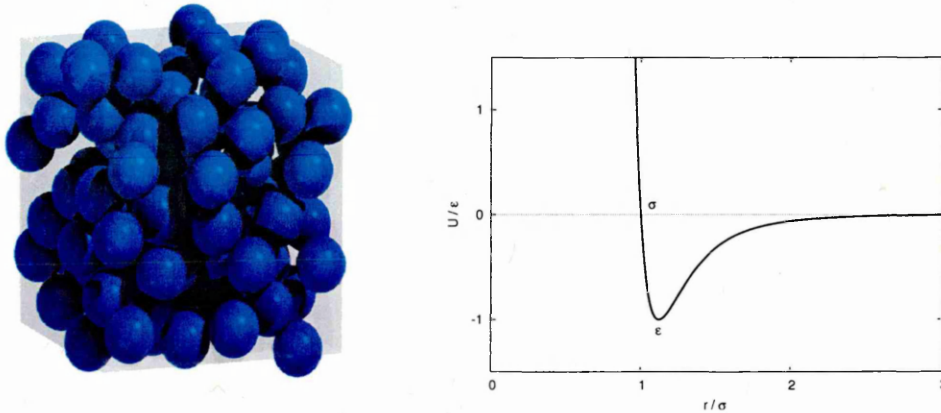


Fig. 3.1: (a): A Lennard-Jones fluid in a 3d box (b): Plot of the Lennard-Jones potential function from Eqn. 3.3

The functional form $1/r^6$ describes the attractive term and comes from the leading term in the quantum-mechanical solution for non-polar, neutral atoms with spherically symmetric electron shells, like e.g. noble gas atoms. Whilst it only has a sound foundation for this class of particle, it is, nevertheless, frequently used as an approximation for many other atom types.

Unlike attraction, the exact functional form for the repulsive interaction is not well known and is commonly approximated either by an exponential, or by the inverse power term. Use of the inverse twelfth power is a pragmatic approach in computer simulations, as it is the square of $1/r^6$ and, hence, leads to an efficient

calculation of the energy.

The constants ϵ and σ are used to parameterise the strength and shape of the interaction and, hence, define the properties of the simulated liquid. σ defines the distance at which the potential gets repulsive and ϵ sets the strength of the interaction or the depth of the potential ‘well’. In fact it can be shown that the depth of the well is just $-\epsilon$.

For the purpose of modelling complex molecules like liquid crystals, proteins or polymers, several Lennard-Jones particles can be linked together by the use of bonding potentials. Taking each atom as a Lennard-Jones site, one can model a fully-atomistic representation of a particular molecule and can expect a reasonably realistic simulation to come out of it. However, for many systems, this requires a huge amount of computing time due to the large system size and simulation time needed. Thus, for some applications, coarse-grained models are more appropriate. Hydrogen atoms are sometimes not included explicitly, but absorbed into the more ‘massive’ neighbour atoms. In this case, the coarse-graining corresponds to a united atom model.

The basic form of a MD algorithm is as follows:

- step 1: set up the initial configuration, i.e. give all atoms a position and a velocity.
- step 2: calculate of the forces on all atoms using the chosen potential.
- step 3: update positions/forces, i.e. move the atoms for a short timestep according to the calculated forces and the equations of motion.

Steps two and three are then repeated until the simulation is completed.

Initialisation

There are two concerns to address when setting up the starting structure. First the positions of the atoms need to be assigned without appreciable overlap of the atomic sites. This is often achieved by simply placing the particles on a cubic lattice. For most of cases, this is a highly unstable structure, which means it contains a lot of excess potential energy, and will melt quickly as the simulation runs and the particles spontaneously develop more stable configurations.

Secondly, velocities need to be assigned to the desired temperature. From statistical mechanics, a Gaussian-like distribution called the Maxwell-Boltzmann distribution describes the velocity distribution of particles in a canonical ensemble in thermal equilibrium with its surroundings. For particles with a mass m and a temperature T , velocities are usually assigned to the particles randomly according to the following distribution function:

$$F_v = \left(\frac{m}{2\pi k_B T} \right)^{3/2} \exp(-mv^2/2\pi k_B T) \quad (3.4)$$

The integration algorithm

When applied to many-particle systems, a general analytical solution to Eqn. 3.1 is not possible. There are, however different algorithms available for integrating the equations of motion numerically [57]. An important point to consider in this is the accuracy with which a given algorithm is able to determine a particle's path over a long timestep. Another important criterion is the conservation of energy. We usually distinguish between short term and long term conservation. Short term energy conservation is connected to the first consideration: an algorithm with a good accuracy over a long time step conserves energy well over that timestep. However, such algorithms tend to develop drifts in the energy after many time steps.

An often chosen algorithm is the velocity-Verlet algorithm [58]. It has only moderate short term energy conservation but little long term drift. It is also a symplectic algorithm which gives it a useful time reversibility property. It calculates the positions, velocities and forces at step i from the last step $i - 1$ using the expressions:

$$\mathbf{r}_i(t + \delta t) = \mathbf{r}_i(t) + \delta t \cdot \mathbf{v}_i(t) + \frac{\delta t^2}{2} \mathbf{a}_i(t) \quad (3.5)$$

$$\mathbf{v}_i(t + \delta t) = \mathbf{v}_i + \frac{\delta t}{2} [\mathbf{a}_i(t) + \mathbf{a}_i(t + \delta t)] \quad (3.6)$$

where δt is the simulation timestep.

The implementation of these 2 equations involves, however, two stages: First, the new positions of the particles at time $t + \delta t$ is calculated using Eqn. 3.5 and mid-step velocities are calculated with

$$\mathbf{v}_i\left(t + \frac{1}{2}\delta t\right) = \mathbf{v}_i + \frac{\delta t}{2} \mathbf{a}_i(t) \quad (3.7)$$

Then the forces and accelerations are computed before completing the velocity update using

$$\mathbf{v}_i(t + \delta t) = \mathbf{v}_i\left(t + \frac{1}{2}\delta t\right) + \frac{1}{2}\delta t \mathbf{a}_i(t + \delta t) \quad (3.8)$$

When considering non-spherical particles, rotational coordinates, *i.e.* orientation vectors, and angular velocities have to be considered. Special measures have to be taken to maintain the orientation vector \mathbf{u}_i at unit length and to keep its first derivatives, $\dot{\mathbf{u}}_i$, in a plane perpendicular to \mathbf{u}_i .

For this purpose, the following equations are used:

$$\dot{\mathbf{u}}_i \left(t + \frac{1}{2} \delta t \right) = \dot{\mathbf{u}}_i(t) + \frac{1}{2} \delta t \mathbf{g}_i^\perp(t) + \lambda \mathbf{u}_i(t) \quad (3.9)$$

$$\mathbf{u}_i(t + \delta t) = \mathbf{u}_i(t) + \delta t \dot{\mathbf{u}}_i \left(t + \frac{1}{2} \delta t \right) \quad (3.10)$$

where $\mathbf{g}_i^\perp(t)$ is the perpendicular component of the torque causing rotation of particle i , and λ is the Lagrange multiplier calculated as

$$\lambda_0 = -\frac{1}{2} \delta t (\dot{\mathbf{u}}_i \cdot \dot{\mathbf{u}}_i) + \frac{1}{2} \delta t \mathbf{g}_i^\perp(t) \left(2\dot{\mathbf{u}}_i + \frac{1}{2} \delta t \mathbf{g}_i^\perp(t) \right) \quad (3.11)$$

further refined by two iterations of

$$\lambda \leftarrow \lambda - \frac{(1 + \lambda \delta t)^2 (\mathbf{u}_i \cdot \mathbf{u}_i) - 1 - 2\lambda_0 \delta t}{2\delta t (1 + \lambda \delta t)} \quad (3.12)$$

Finally, after calculating the torques, the angular velocities at time $t + \delta t$ are evaluated:

$$\dot{\mathbf{u}}_i(t + \delta t) = \dot{\mathbf{u}}_i \left(t + \frac{1}{2} \delta t \right) + \frac{1}{2} \delta t \mathbf{g}_i^\perp(t + \delta t) - \left(\dot{\mathbf{u}}_i \left(t + \frac{1}{2} \delta t \right) \cdot \mathbf{u}_i(t + \delta t) \right) \mathbf{u}_i(t + \delta t) \quad (3.13)$$

The explicit expressions for the forces and torques for the systems studied in this thesis (Lennard-Jones and Gay-Berne systems) can be found in Appendix B.

As stated before, an MD procedure basically comprises two steps which are repeated throughout the simulation. First all the forces on all atoms are calculated, then the equations of motion are integrated over a certain time interval. The length of this time interval has to be carefully chosen. It is important to make it as long as possible to save computer time, as the calculation of forces is by far the

most time consuming part of an MD simulation. On the other hand it cannot be made too long, since the forces on the atoms are taken to be constant during the time step, an assumption that clearly breaks down as δt is increased.

Practical aspects

Boundary conditions and the minimum image convention Due to the limitation of computational power, all computer simulations are restricted to a limited number of molecules. For these small systems, a large proportion of the particles are close to the boundaries of the system. Usually, however, the interest of a simulation is not these surface effects. The standard way of reducing these effects involves the use of periodic boundary conditions. As shown on Fig. 4.1, this amounts to replicating the simulation box periodically through space in all directions. When a molecule reaches the edge of the simulation box, it does not bounce against a boundary; instead it passes through and instantaneously reappears on the opposite side of the box with the same velocity. These periodic boundary conditions remove unwanted surface effects at the expense of imposing an artificial periodicity in the system, a so-called finite-size effect. Furthermore, the system cannot exhibit fluctuations of wavelength greater than L , the length of the simulation box. Therefore care has to be taken in studying systems where large lengthscale phenomena take place.

In such a periodic system, the interaction between a pair of particles is computed according to the ‘minimum image convention’: here, each particle interacts with its nearest neighbours, including ‘images’ from the replicated boxes. The use of a cut-off distance r_c allows the neglect of weak interactions between particles with large separation. Introducing this cutoff into the potential energy calculation considerably improves the efficiency of the energy calculation as the size of the system increases. In a system of size L , the condition $r_c < \frac{L}{2}$ has to be satisfied in order to avoid interaction of a molecule with more than one image of a second

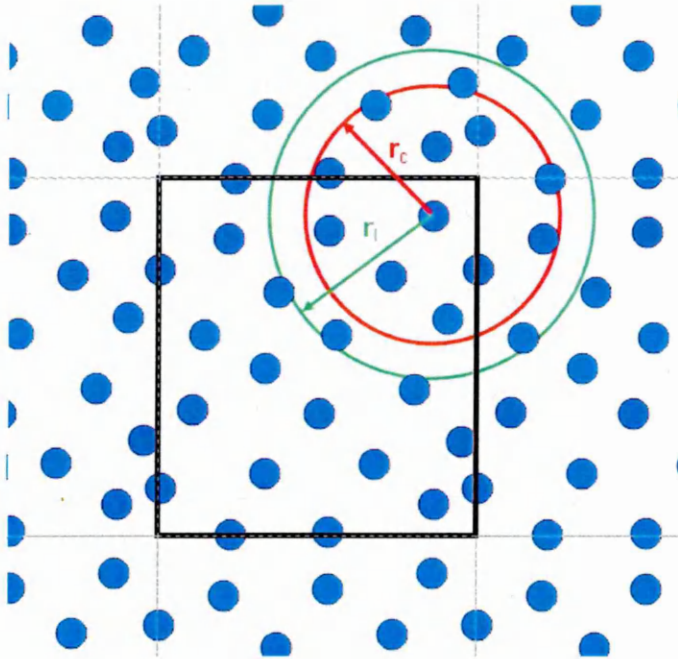


Fig. 3.2: A two-dimensional periodic system with cutoff radius r_c and neighbour list radius r_L

molecule.

Verlet Neighbour list For further efficiency in the computation of the pair-interaction within the system, a neighbour list is created for each particle. When a potential function has a spatial cutoff, particles at a large separations do not interact. The Verlet neighbour list [38] is an algorithm which exploits this property. The neighbour list contains all of the particles which are within a radius r_L of each particle (see green circle in Fig. 3.1.1). When calculating the forces and torques acting on a given particle, the program does not then loop through all the particles but only those appearing in the list.

As r_L is larger than the cutoff r_c in the potential, it is only necessary to update this array periodically. Specifically, when an atom has moved a distance of $0.5 (r_L - r_c)$ then it is necessary to update the list. If $(r_L - r_c)$ is set too small then the array update frequency is too high; if it is too large, however, then at every function evaluation an unnecessary number of calculations will be performed. Typically

an $(r_L - r_c)$ value of $0.1 r_c$ is found to be a good compromise between these two competing factors.

Weak coupling to a temperature bath The methods described above allow simulations to be performed in the constant NVE ensemble, in which the number of molecules N , volume V and total energy E are held fixed. In order to simulate other ensembles, modifications to this method need to be made. The simple constraint method is applied to simulate the system in the canonical or constant NVT ensemble (N , V and the temperature T are fixed). This system is equivalent to a coupling of the system to an external bath. The equations of motion are modified such that there is a first order relaxation of T towards the preset reference temperature T_0 . The coupling equation equivalent to a first-order system is:

$$\frac{dT(t)}{dt} = \frac{1}{\tau_T} [T_0 - T(t)] \quad (3.14)$$

where τ_T is the relaxation time and corresponds to the rate at which the method forces the system towards the desired T_0 . Discretising the last equation using the MD timestep δt gives

$$\Delta T(t) = \frac{\delta t}{\tau_T} [T_0 - T(t)] \quad (3.15)$$

The change in kinetic energy corresponding to a change in temperature is :

$$\Delta K(t) = N_{df} C_V \delta T(t) \quad (3.16)$$

where C_V and N_{df} are, respectively, the heat capacity per degree of freedom at constant volume and the number of degrees of freedom. This change in kinetic energy can alternatively be expressed in terms of the changes in the velocities:

$$\frac{dK(t)}{dt} = \frac{1}{2} \sum_{i=1}^N m_i \frac{dv_i^2(t)}{dt} \quad (3.17)$$

Considering the changes in velocities due to a rescaling from v_i to λv_i

$$\Delta K(t) = \frac{1}{2} \sum_{i=1}^N m_i \Delta v_i^2(t) = \frac{1}{2} \sum_{i=1}^N m_i [\lambda^2(t) v_i^2(t) - v_i^2(t)] \quad (3.18)$$

$$= [\lambda^2(t) - 1] \frac{1}{2} \sum_{i=1}^N m_i v_i^2(t) = [\lambda^2(t) - 1] \frac{1}{2} N_{df} k_B T(t) \quad (3.19)$$

From Eqns. (4.8) and (4.11), therefore

$$\Delta T(t) = [\lambda^2(t) - 1] \frac{1}{2} \frac{K_B}{C_V} T(t) \quad (3.20)$$

Combining (4.7) and (4.12), then gives

$$\lambda^2(t) = \frac{2C_V}{k_B} \frac{\Delta t}{\tau_T} \frac{(T_0 - T(t))}{T(t)} + 1 \quad (3.21)$$

$$\lambda(t) = \left[1 + \frac{2C_V}{k_B} \frac{\Delta t}{\tau_T} \left(\frac{T_0}{T(t)} - 1 \right) \right]^{1/2} \quad (3.22)$$

The heat capacity C_V may be approximated by $k_B/2$, which leads to:

$$\lambda(t) = \left[1 + \frac{\Delta t}{\tau_T} \left(\frac{T_0}{T(t)} - 1 \right) \right]^{1/2} \quad (3.23)$$

The strength of the coupling depends on τ_T . if τ_T is large, the system goes slowly to the preset value T_0 . This scaling conserves the Maxwellian shape of the velocity distribution but does not generate a canonical ensemble.

Measuring system properties

Reduced units It is often convenient to express quantities such temperature, density, pressure, etc.. in reduced units instead of dimensional ones. If a system has some characteristic length, *i.e* the width of the molecule, it is convenient to set it to be a unit length. Similarly, simulated systems often have natural units of energy, length and mass, from which it is possible to express all other quantities in terms of these basic units. It is natural to measure all distances in units of σ_0 and energies in units of ϵ_0 . From these, the unit of temperature becomes ϵ_0/k_B , where k_B is the Boltzmann constant. Similarly, the unit of time is equal to $\sigma_0\sqrt{m/\epsilon_0}$ and the unit of pressure is ϵ_0/σ_0^3 . The mass of the molecule can be chosen as a unit of mass which makes molecular momentum \mathbf{p}_i and velocities \mathbf{v}_i numerically identical, as well as the forces \mathbf{F}_i and accelerations \mathbf{a}_i . For example, in a Lennard-Jones model of liquid argon, $\epsilon_0/k_B = 120K$ and $\sigma_0 = 0.34nm$ which corresponds to a unit of time of $2 \times 10^{-12}s$.

Thermodynamic observables The calculation of many observables is based on the statistical mechanics assumption that an ensemble average of a given macroscopic property A_{obs} can be obtained from the time average of its instantaneous values $A(\mathbf{X})$ taken over a long time interval, where \mathbf{X} is a particular point in phase space

$$A_{obs} \approx \langle A(t) \rangle_{time} = \langle A(\mathbf{X}(t)) \rangle_{time} = \lim_{t_{obs} \rightarrow \infty} \frac{1}{t_{obs}} \int_0^{t_{obs}} A(\mathbf{X}(t)) dt \quad (3.24)$$

In other words, the so-called ergodic hypothesis states that if one allows a system to evolve in time indefinitely, that system will eventually pass through all possible states. Using this result, such thermodynamic quantities as the potential energy, temperature and pressure can be evaluated in a MD simulation every step. The potential energy is given by the sum of all pairwise potentials in the system:

$$E_{pot} = \sum_{i=1}^N \sum_{j>i}^N U_{ij} \quad (3.25)$$

The kinetic energy is defined as the sum of the translational and rotational velocity terms.

$$E_{kin} = \sum_{i=1}^N \frac{m\mathbf{v}_i^2}{2} + \sum_{i=0}^N \frac{I\omega_i^2}{2} \quad (3.26)$$

According to the equipartition theorem, an average of $\frac{1}{2}k_B T$ contributes to all independent quadratic degrees of freedom in the system, *i.e.* to each translational and rotational degree of freedom.

$$k_B T = \frac{\langle 2K \rangle}{f} \quad (3.27)$$

From this, the temperature T of a mixture of N_{rod} rods and N_{sph} spheres can be expressed as

$$\sum_{i=1}^{N_{sph}} \frac{m_{sph}\mathbf{v}_i^2}{2} + \sum_{i=1}^{N_{rod}} \frac{m_{rod}\mathbf{v}_i^2}{2} + \sum_{i=1}^{N_{sph}} \frac{I\omega_i^2}{2} = \left(\frac{5}{2}N_{rod} + \frac{3}{2}N_{sph} \right) k_B T \quad (3.28)$$

In this equation, the spheres contribute 3 degrees of freedom, through their positional coordinates x , y and z . The rods, being axially symmetric, contribute to 5 degrees of freedom: 3 positional coordinates and 2 rotational coordinates, the rotation around the molecule's long axis being ignored. Note that this also allows one to set the inertia tensor I to unity as the 2 rotational axis share the same moment of inertia.

The pressure is calculated using the virial theorem,

$$P = \rho k_B T + \frac{1}{3V} \sum_{i=1}^N \sum_{j>i}^N \mathbf{r}_{ij} \cdot \mathbf{F}_i \quad (3.29)$$

Structural observables As well as the thermodynamic observables described above, structural properties can be measured through order parameters and distribution functions.

Order parameters are used to quantify the degree of order in a given system. Ideally, an order parameter would give a value of 1 for a perfectly ordered phase and a value of zero for an isotropic distribution. Experimentally, one can measure the so-called nematic parameter P_2 defined as the average over all particles of the second order Legendre polynomial in $\cos \alpha$, where α is the angle between a particle and the director $\hat{\mathbf{n}}$.

$$P_2 = \langle P_2(\cos \alpha) \rangle_{particles} \quad (3.30)$$

$$P_2 = \left\langle \frac{3}{2} \cos^2 \alpha - \frac{1}{2} \right\rangle_{particles} \quad (3.31)$$

In a Molecular Dynamics simulation, the orientational order parameter is measured as the largest eigenvalue of the Q-tensor

$$Q_{\alpha\beta} = \frac{1}{N} \sum_{i=1}^N \left(\hat{\mathbf{u}}_{i\alpha} \cdot \hat{\mathbf{u}}_{i\beta} - \frac{1}{2} \delta_{\alpha\beta} \right) \quad (3.32)$$

Positional order can be examined by computing distribution functions of particle positions by compiling histograms. The radial pair distribution function or RDF, $g(r)$, represents the probability of finding a pair of particles i and j with intermolecular separation r_{ij} . This function is particularly useful for giving insight into the positional correlations of particles. This function can be expressed as:

$$g(r) = \frac{V}{N^2} \left\langle \sum_i \sum_{j < i} \delta(r - r_{ij}) \right\rangle \quad (3.33)$$

$g(r)$ is constructed by computing a histogram of all pair separations $r_{ij}[r : r + \delta r]$ where $0 < r < \frac{L_{min}}{2}$ and L_{min} is the shortest simulation box length. Thus, each bin represents the particle occupancies in a series of concentric spherical shells. The width of these shells represents the resolution of the method. The number of particles in each shell is then normalised by $\rho \times V_{shell}$, *i.e.* the expected occupancy of an ideal at the same density for a particular shell such that

$$V_{shell} = \frac{3}{4}\pi [(r + \delta r)^3 - r^3] = \frac{3}{4}\pi [(\delta r)^3 + 3r^2\delta r + 3r(\delta r)^2] \quad (3.34)$$

This procedure is repeated for several uncorrelated configurations in order to obtain smooth functions

It can also be useful to consider different distribution functions, for instance, resolving only the parallel or perpendicular projection of the the pair separation r_{ij} . The parallel distribution $g_{\parallel}(r_{\parallel})$ measures the degree of layering and the parallel distribution $g_{\perp}(r_{\perp})$ measures the positional order within a layer. A similar method as the one used for $g(r)$ is used to compute these two distribution functions. Here histograms of the parallel projection $r_{\parallel} = \hat{\mathbf{n}} \cdot \mathbf{r}_{ij}$ and perpendicular projection $r_{\perp} = \sqrt{r_{ij}^2 - r_{\parallel}^2}$ of the pair separation vector \mathbf{r}_{ij} are considered.

The normalisation by $\rho \times V_{shell}$ is performed in a cylindrical geometry such that:

$$V_{shell} = \begin{cases} \pi r_{cyl}^2 \delta r & \text{for } g_{\parallel}(r_{\parallel}) \\ h_{cyl} \pi [(\delta r)^2 + 2r\delta r] & \text{for } g_{\perp}(r_{\perp}) \end{cases} \quad (3.35)$$

h_{cyl} and r_{cyl} represent the dimensions of the cylinder in which the calculation is performed (see Fig. 3.3). The cylinder is set to be smaller than the simulation box but kept large enough to allow analysis of the widest possible area. For this

purpose, the cylinder dimensions are set to $h_{cyl} = 0.8L_{min}$ and $r_{cyl} = b \tan \alpha$, where $b = \frac{L_{min}(\sqrt{3}-1)}{2}$ and $\alpha = \arccos \sqrt{\frac{2}{3}}$.

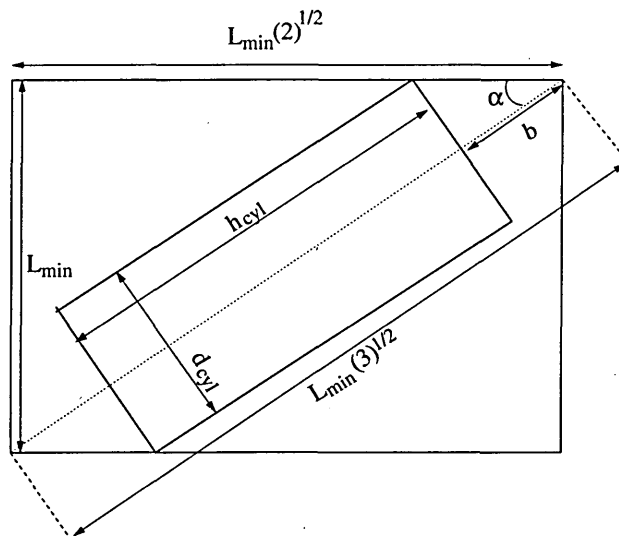


Fig. 3.3: Representation of the geometry used in the calculation of $g_{||}(r_{||})$. The diagram shows a projection of a cylinder in a 3d box in the plane parallel to the axis of the cylinder

Finally, the shape of aggregates can be described by analysis of the principal moments of inertia [59]. This three components of the inertia tensor I_L , I_M , I_S are usually normalized such that $I_L > I_M > I_S$ and $I_L + I_M + I_S = 1$.

Different shapes of aggregate correspond to different sets of principal moments of inertia:

- for a sphere, $I_L = I_M = I_S = \frac{1}{3}$
- for a cylinder, $(I_L, I_M) > I_S$ and $I_L = I_M$
- for a disk, $I_L > (I_M, I_S)$ and $I_M = I_S$

3.1.2 Other molecular simulations techniques

There are many techniques other than MD that have been used to simulate soft condensed matter [60]. Depending on the time and length scale of the problem at

hand, one can choose the appropriate simulation technique. In certain cases these different methods overlap, allowing direct comparison between them. As described earlier, the MD methodology deals with the atomic structure of molecules and assumes an homogeneous distribution of the electrons around the atomic nuclei. In other words, the electronic and nuclear structure of atoms is not modelled explicitly but is, rather, embedded in pair-potential functions such as the Lennard-Jones potential. At the sub-atomic level of detail, a quantum mechanical approach is required. Methods such as ab-initio can then be used to derive macroscopic properties that depend on the electronic distribution around atom nuclei and can also be useful for investigating chemical reactions.

While MD and ab-initio approaches can give very detailed information about the behaviour of a given system, these simulations are computationally very expensive and are currently limited to very small system size. This limitation is due to the fact that the time-step is imposed by the highest frequency mode that can occur in a system. Typically, hydrogen bond stretching is the fastest frequency present in a molecular system and imposes a timestep of 1fs . To increase the time-step, the so-called ‘united-atom’ approach can be used where the hydrogen atoms are ‘englobed’ into neighbouring large atoms. This allows bigger time/length scales to be accessed but still limits simulations to few nanoseconds/nanometres.

As opposed to these deterministic simulation methods, the Monte Carlo (MC) simulation technique is based on stochastic trial moves of particles. This non-deterministic method uses a statistical sampling of the phase space rather than working out the actual trajectory of the particles as in MD and ab-initio. This simulation is therefore useful for determining the configuration with the lowest potential energy. However, analysis of dynamic behaviours is impossible and, therefore, this technique cannot provide time-dependent quantities due to its stochastic nature.

Over the recent decades, several techniques have been developed to access processes occurring over supramolecular scales. Methods such as Lattice Boltzmann

(LB) and Dissipative Particle Dynamics (DPD) do not offer the atomic detail that atomistic models provide but represent very effective approach for modelling large system sizes over a large time. The DPD method considers ‘soft beads’ containing several molecules. In this coarse-graining, each bead represents an element of the fluid under consideration rather than an atom or small group of atoms, allowing overlaps and exchange of materials between these beads. The LB method, in contrast, is based on a discrete description of the Navier-Stokes equation for fluids dynamics and allows even bigger scales to be accessed.

3.2 Simulations of amphiphilic systems: History and methods

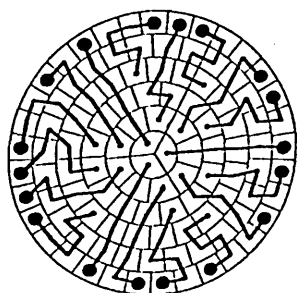
3.2.1 Monte Carlo simulation of lattice models

Early isolated micelle models

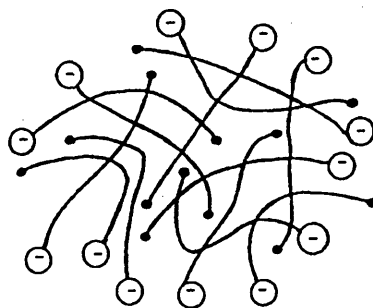
From a computer simulation point of view, micellar systems are difficult to study. The dynamics of such systems involves very short timescales of $10^{-8} - 10^{-6}s$ (exit/entry rate of monomers into micelles) as well as longer timescales $10^{-2}s$ (typical micelle life time). Furthermore, nowadays fully atomistic simulations are only reaching few nanoseconds which makes the bridging of timescales an obvious problem. Therefore, due to their computational simplicity, pre-assembled isolated micelles were the first amphiphilic systems to be studied. In these simulations, a micelle was constructed at the beginning of the simulation in order to study its evolution. This approach was pioneered by Pratt *et al.* [61,62] and co-workers with a highly idealized lattice model of a isolated micelle (no explicit solvent) studied by MC. This work used 2 different surfactant chain length ($n = 4$ and $n = 6$) with a very simple set of parameters: an attractive tail-tail interaction together with a head-head repulsion. Starting from an initial spherical arrangement, the

surfactant aggregate relaxed to an aspherical structure. While this differs from the conventional picture of a micelle from Hartley *et al.* [11], these results have been verified by more recent and more realistic atomic simulations.

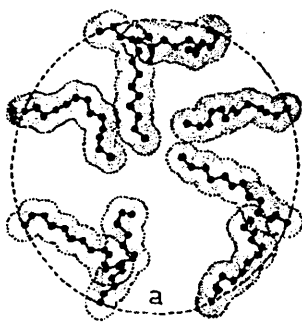
At the same period, however, another early micelle model was the spherical model developed by Dill and Flory [63], in which the micelle had an almost ‘crystalline’ interior, an absence of looping of the chains, a completely radial distributions of the chain and a smooth spherical surface. Menger *et al.* [64] argued that there was no evidence for these attributes and proposed a rather different picture. Subsequently, more realistic models were achieved by Haile and O’Connell [65,66] using a MD approach. Here, the model used was a united-atom representation of the carbon chain with a head group fixed on a spherical shell.



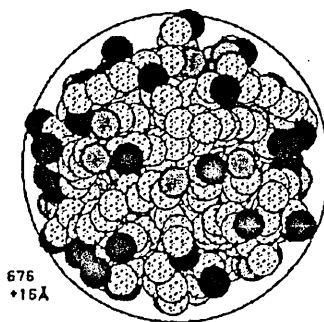
(a) Dill-Flory lattice representation of a micelle



(b) Menger micelle model



(c) fixed head group model



(d) harmonic spring model

Fig. 3.4: Primitive MD model of micelle

However, the results of Pratt *et al.* cast doubt on the assumptions made in Haile and O'Connell's original model. To resolve this, therefore, the model surfactants were allowed to move on the surface of the sphere while still being constrained, by an external potential, to lie inside the sphere. From this it was found that conformational structure was only slightly affected by the introduction of head group mobility when compared with that seen in the previous model in which the heads were rigidly fixed to the confining shell.

The spherical model was then further extended by introduction of a potential barrier which particles had to cross in order to leave/enter the micelle. In this case, small fluctuations in size and shape were observed in MD simulations, so confirming the initial results of Pratt *et al.*

Self-assembly of micellar phase

The previous simulations were limited to single micelles whereas, in order to simulate micellar solutions, 3D systems of large sizes are required. Complex 3D lattice models were developed to this end in the mid 1980's by Larson *et al.* [67–72] and then by Care *et al.* [73–79]. Here, a sufficient number of amphiphiles were present to enable formation of several micelles. In this kind of model, each amphiphile was represented as a flexible chain of connected lattice sites, with each site typically representing the hydrophilic head group and the remainder of the chain representing the hydrophobic tail of the molecule. Despite making no *a priori* assumptions on the final structures, this model was found to self-assemble into micellar, lamellar and even vesicle arrangements.

When compared with the work of Pratt *et al.*, where the molecules were constrained to form a connected micelle, this lattice model represented a major advance in that the amphiphiles were allowed to self-assemble freely into the preferred structure. Cluster size distribution functions were qualitatively captured as a function of temperature [75] and it was shown that, for any value of the head-

solvent interaction, the system exhibited a high temperature monomeric phase. On decreasing the temperature, the system showed a temperature region where micelle-like clusters formed. Then, at lower temperature, with the same head-solvent interaction, these micelles coalesced to give a spontaneous multi-bilayer structure.

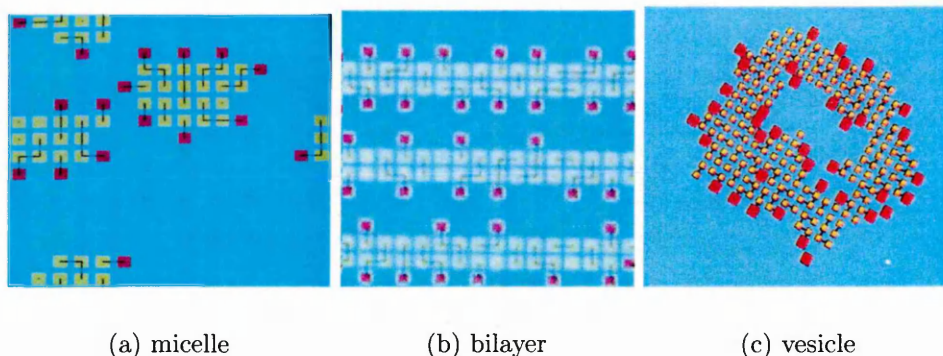


Fig. 3.5: Configuration snapshots representing the different phases observed with Care's lattice model [73, 74, 77]

It is interesting to note that even early results for a chain length of 4 showed that this model was capable of self-assembling into structures analogous to those exhibited by real amphiphilic materials. By increasing the chain length to 6 (with 2 sites being used to represent the head group), self-assembly of the amphiphiles into a vesicle was found. This work showed that single-chain surfactants can form the three main structures found in real amphiphilic systems: micelle, bilayer and vesicle. In both Care's and Larson's model, it was observed that the free monomer concentration decreases above the CMC. This was subject of debate as this decrease was seen experimentally, but simple theories predicted a constant monomer concentration above the CMC.

Subsequent to this, more complex simulations involving ternary systems were performed. Phenomena such as micellar encapsulation [80] and the asymmetric growth of micelle while adding oil were observed [81]. Similar types of model were used to study the self-assembly of block co-polymers [82].

More recently, off-lattice models have been developed by Mahanti *et al.* [83–86].

Here, the amphiphiles are not attached to a 3D lattice mesh, leading to improved reliability of the aggregate shape description. By introducing long-ranged Coulombic interactions, it has also been shown that ionic surfactants display more intermicellar ordering due to the repulsion of head groups. This type of model has proved to be very successful at calculating micellar distribution functions: the system sizes accessible to these models are large enough to show smooth distributions of micelle size and shape. Rutledge *et al.* [87] also studied the shape of the micellar distribution function and showed an asymmetric peak comprising a Gaussian distribution, characterizing spherical micelles, combined with an exponential tail corresponding to cylindrical micelles.

3.2.2 Molecular Dynamics of all-atom models

In 1986, Jönsson *et al.* performed the first MD simulation of a pre-constructed sodium octanoate micelle with full atomic detail. This was limited however to a very short run of less than 100ps [88]. Following on from this, Watanabe and Klein [89, 90] studied the same system by simulating 10-20 molecule for a few 100ps. It is only much more recently that all-atom models have been used to study the self-assembly processes of amphiphilic systems. In 1999, Maillet *et al.* performed a NPT simulation of two surfactant molecule systems, *C₉TAC* and *EMAC*, for 3ns [91]. For both systems, only 50 molecules were considered. However, these were proved sufficient to observe shape fluctuations of initially pre-constructed micelles and, more importantly, the self-assembly of a random configuration into a single micelle. Depending on the thermodynamic conditions and the type of surfactant used, spherical and cylindrical micelles were formed. From this, it was concluded that the self-aggregation process was of Smoluchowsky + Becker-Döring type, which describes the kinetics of aggregation/fragmentation of clusters (see previous chapter). In agreement with experiments and theoretical expectations, it was found that the molecules first approached one another to form aggregates without any well defined organisation. Then, these random aggregates

merged to form stable micelles.

These simulations have been performed in various ensembles for non-ionic surfactants, these simulations being less time consuming since long-range interactions can be ignored when ionic species are absent. So far, no MD simulation has been carried out on an atomistic system large enough to contain several micelles, for a time long enough to allow micelle-monomer and micelle-micelle dynamic properties to be studied.

Bilayer simulations are relatively recent compared to simulations of other biological structures like micelles. Through the progress of computer technology and the need to reconcile theory with experimental data, such work has focused on MD simulations of all-atom models and studied the dynamics of 'realistic' systems. This was pioneered by Berendsen *et al.*, particularly in 1988 through his work with Egberts [92] on a ternary alcohol-fatty acid-water system. This was the first all-atom MD simulation of a phospholipid bilayer (hydrated DPPC membrane) in the liquid crystalline phase.

Since then, such studies have been extended to bigger time/length scale MD simulations. In 1993, Heller *et al.* [94] performed a MD simulation of a bilayer of 200 lipids in the gel and liquid crystalline phases. More recently, Lindahl and Edholm [95] achieved a major advance in the scale of such simulations by performing a simulation of 1024 lipids (over 120,000 particles or interaction sites in total) reaching the $20nm$ length scale and $60ns$ time scale. It was then possible to calculate mesoscopic properties, such as the bending modulus and bilayer area compressibility, to sufficient accuracy to enable comparison with experimental values.

However, studying biological systems through MD is a considerable computational challenge and several important methodological issues have risen. The need for bigger time and length scales, together with the need to perform appropriate analysis on such systems, leads to some fundamental questions that need to be re-

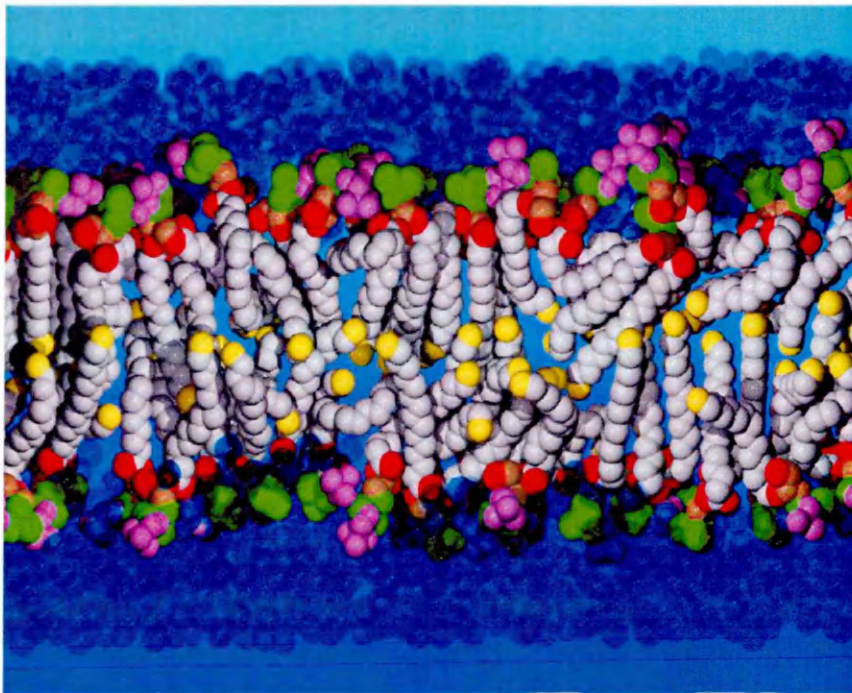


Fig. 3.6: Slab from a DPPC lipid bilayer simulation [93] - color scheme: PO_4 green, $N(CH_3)_3$ violet, H_2O blue, terminal CH_3 yellow, O red, glycerol C brown, CH chain, grey

solved. The first thermodynamic ensemble employed in the study bio-membranes was the constant NVT (constant volume and constant temperature) or canonical ensemble. However, the study of these systems under the isobaric-isothermal ensemble (i.e. constant pressure and temperature) has the great advantage of allowing the size of the system to change. Thus, in response to the chosen force field environment, a given bilayer system is able to find its equilibrium density by itself. Therefore, only a rough estimate of the initial density is required, whereas under NVT conditions an accurate value for the bilayer density is essential. Early constant pressure simulations were reported by Egberts *et al.* [96] and by Huang *et al.* [97] but used methods that did not sample the NPT ensemble correctly. Shinoda [98] and Tu [99] have, more recently, used simulations performed in conditions that do truly correspond to the NPT ensemble. However, Chiu *et al.* [100] and Feller *et al.* [93] have argued that a ‘constant’ surface tension ensemble is a more correct approach for simulating biological membranes. Thus, using the so-called

NP γ T ensemble, they defined a surface tension γ as being constant during the simulation. However, Tielemann *et al.* [101] have argued that changing from the NPT to the NP γ T ensemble has no significant effect on bilayer behaviour.

In recent years, it has been possible to simulate bilayer self-assembly of all-atom detailed amphiphilic molecules in a water-like solvent using MD in the constant NPT ensemble. The first such self-assembly process observed with an all-atom model was that simulated by Marrink *et al.* in 2001 [102]. This self-assembly process was found to take only 15ns for a system containing 64 DPPC lipids and 3000 water molecules. It was observed to occur through a rapid microphase separation of the initial random mixture (Fig. 3.7(a)) into lipid and aqueous domains (Fig. 3.7(b)). Then, a bilayer-like formation developed on the time scale of $t = 5ns$ (Fig. 3.7(c), ceq). The last step (Fig. 3.7(d)) involved surmounting the free energy barrier associated with formation of a defect-free bilayer. From this, the authors concluded that the life-time of a pore is the rate-limiting variable of bilayer self-assembly. This sequence of events is cogently summarised in the schematic Fig. 3.8.

Marrink *et al.* also studied the effect of undulations on the surface tension of lipid bilayers [103] as well as pore formation due to mechanical and electric stresses [104]. Other phases have also been modelled successfully, such as a lipid diamond cubic phase [105] and its transition to hexagonal phase [106] using non-cubic simulation boxes. Recently, the first vesicle self-assembly with an all-atom description of DPPC molecule have been performed [107]. Here to reduce the probability of forming a lamellar phase through the PBC, an extra layer of water molecules was added around an initially equilibrated configuration containing the randomly distributed lipids. These 1017 DPPC molecules then formed a small vesicle of 10 – 15nm run over 90ns.

Even though recent advances in computer hardware allow large scale MD simulations to be performed, reaching up to 100ns over a length of 20nm (corresponding to about ≈ 1000 lipids), atomistic models are still very limited. Many interesting

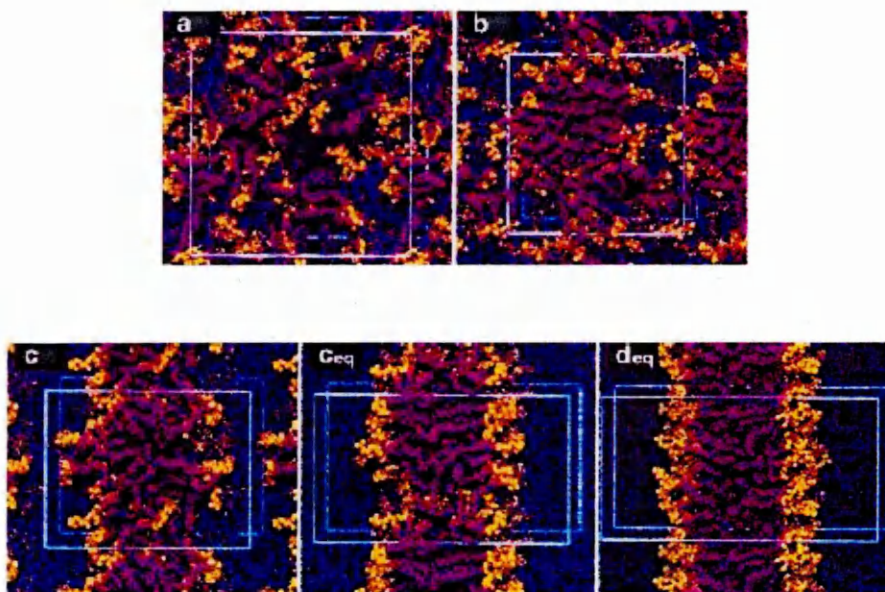


Fig. 3.7: Configuration snapshots showing the evolution of the self-assembly process of a DPPC molecule in a bilayer [102]

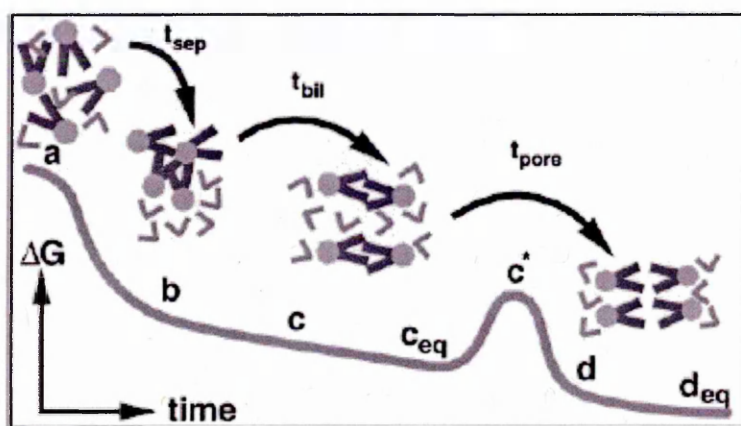


Fig. 3.8: Schematic diagram of free energy change during self-assembly [102]

phenomena, *e.g.* biological processes can span anywhere from femtoseconds to minutes/hours. The significant gap between the space/time scales that govern typical intramolecular events and those which are relevant for collective motion, therefore renders this technique inappropriate for modelling numerous biological application.

3.2.3 Coarse-grained models

Due to the severe limitations associated with all-atom models, many coarse-grained (CG) models have been developed over the years. Here, one approach is to start with an atomistic description of real molecules and reduce the degree of freedom involved by approximating several primary chemical units (*e.g.* carbon groups) by an effective monomer. The interaction between these monomers can then be set by a simple potential form such as the Lennard-Jones potential or some effective tabulated potential. By adjusting and tuning these site-site interaction potentials, one can then, in principle, achieve an improvement in the computational efficiency depending on the level of coarse-graining. As stated above, a first level of coarse-graining can be achieved by ignoring the hydrogen atoms in the united atoms approach (UA), which corresponds to a global speedup of 2 orders of magnitude. More speedup can be increased by further coarse-graining as in the CG model developed by Smit *et al.* in 1990 [108–112]. In this model, the amphiphile was represented by a chain of Lennard-Jones beads. Only 2 types of particles were considered: a hydrophilic particle, representing either the solvent particle or the head group particle, and a hydrophobic particle, representing either the oil particle or a tail particle. Self-assembly into micelle-like structures and monolayers formed between oil and the water phases were observed. However, inverse micelles did not form in the oil phase (see Fig. 3.9).

Cluster size distribution functions were reported and different head group sizes and shapes as well as different hydrophobic tail lengths were studied. However, no systematic studies were performed on the effect of molecular properties on the micellar structure and morphology. Nevertheless, these workers found that by setting the head-head interaction to a repulsive potential and by increasing the head group size, the ‘effective’ shape could be made to have a dominant role in determining the obtained aggregate size and shape.

Similar bead-spring models followed Smit *et al.*’s pioneering work. In particular,

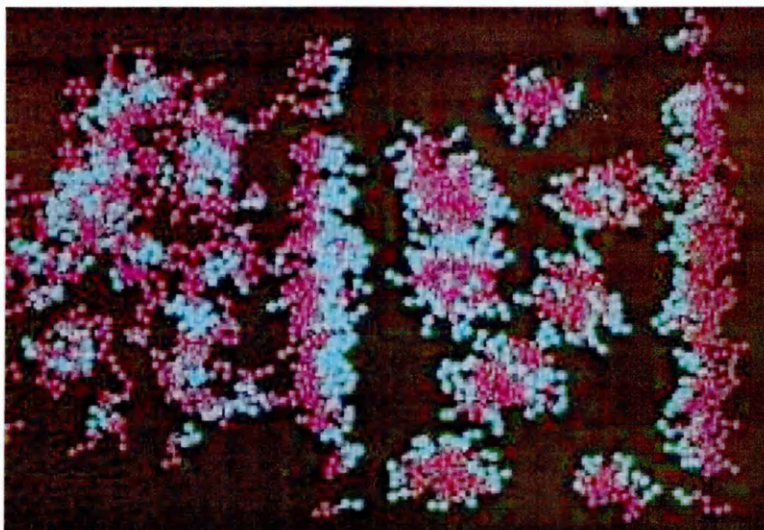


Fig. 3.9: System of oil and water phase separated by a monolayer containing micelles in the water phase. Configuration snapshot taken from a bead-spring coarse-grained model [109]

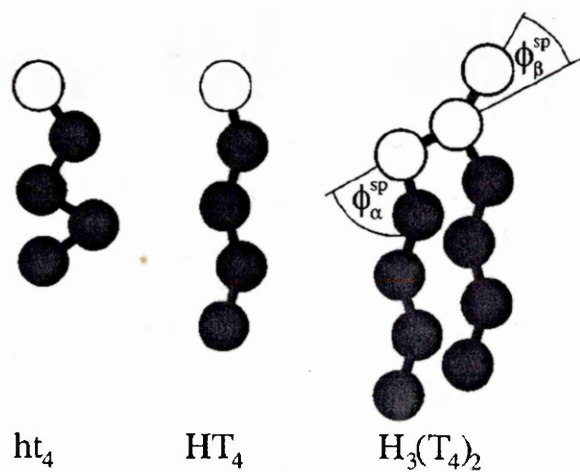


Fig. 3.10: Lipowsky's bead chain model representation of amphiphilic molecules [113]

Lipowsky *et al.* [113,114] developed a CG model (shown in Fig. 3.10) considering 3 different surfactants of differing size and tail flexibility. These studies focused on behaviour of amphiphilic systems with different concentrations.

As the concentration was increased, the micelle-like aggregate formed by 20 am-

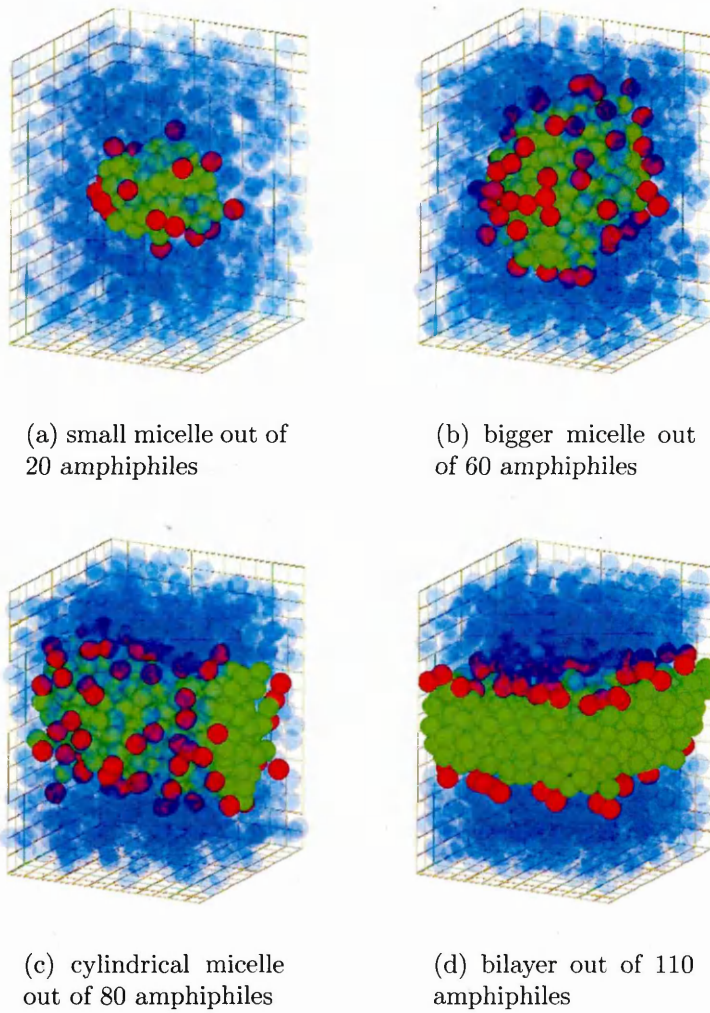


Fig. 3.11: Lipowsky's ht_4 model results for different amphiphilic concentration - from [113]

phiphiles (Fig. 3.11(a)) increased its size to 60 amphiphiles (Fig. 3.11(b)) until it stretched throughout the box forming an infinite cylindrical micelle (Fig. 3.11(c)). At even higher concentration, the aggregate fused through the PBC in 2 directions to form a bilayer (Fig. 3.11(d)). Instead of adopting a multi-micellar arrangement, the amphiphiles kept aggregating as if there were phase separating and could not be shown to be really forming a true micelle. A series of larger simulations spanning the same concentration range would be required to verify whether or not this model is able to produce a genuine micellar phase with several micelles in equilibrium.

These models have in common the symmetry of the potentials between the hydrophobic and hydrophilic particles, *i.e.* the solvent-hydrophilic particle interaction is the same as the oil-hydrophobic particle interaction. These models are, thus, very simple in their design, despite which they have proved to be successful in reproducing qualitative phase diagrams for generic amphiphilic behaviour. However, being intrinsically generic in their design, it is not appropriate to map the simulation results from these CG models into a specific experimental system.

To overcome this limitation, some CG bead-spring models have been derived from all-atom simulation models in order to combine both computational efficiency and chemical specificity of a particular molecule [115–121]. Marrink *et al.* have tuned their bead-spring model using density profiles and diffusion constant from an all-atom simulation of a DPPC or DPPE bilayer [117].

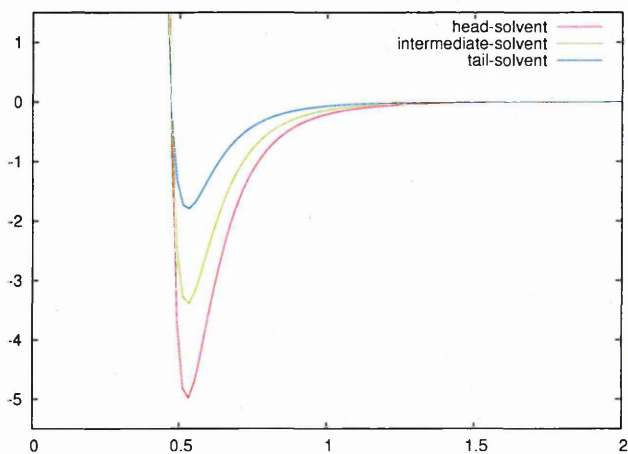


Fig. 3.12: Lennard-Jones potential used in Marrink's CG model [117].

Marrink's model defined 3 types of interactions with strengths ranging from 5kJ/mol for the head-water interaction to 1.8kJ/mol for the tail-water interaction (see Fig. 3.12). Through recent improvement in hardware technology, this CG model has been used to simulate the free-assembly of vesicles [116] and to study the mechanisms of vesicle fusion [115], suggesting two different pathways in agreement with theoretical predictions and other simulation methods. Another model developed by Stevens [121], similar to Lipowsky's model (*e.g.* not based on

all-atom simulations), has suggested yet another path-way for membrane fusion where the presence of a double hydrocarbon tail is compulsory.

Shelley *et al.* also developed an alternative CG lipid model by adjusting the potential functions in order to retrieve the correct radial distribution of the lipid head-groups in a lamellar phase of a DMPC molecule [118–120]. From this, it was shown that the lipid-solvent interaction could be modelled through LJ potentials, whereas the lipid-lipid interactions required nonphysical tabulated potentials determined using a reverse Monte Carlo scheme (Fig. 3.13).

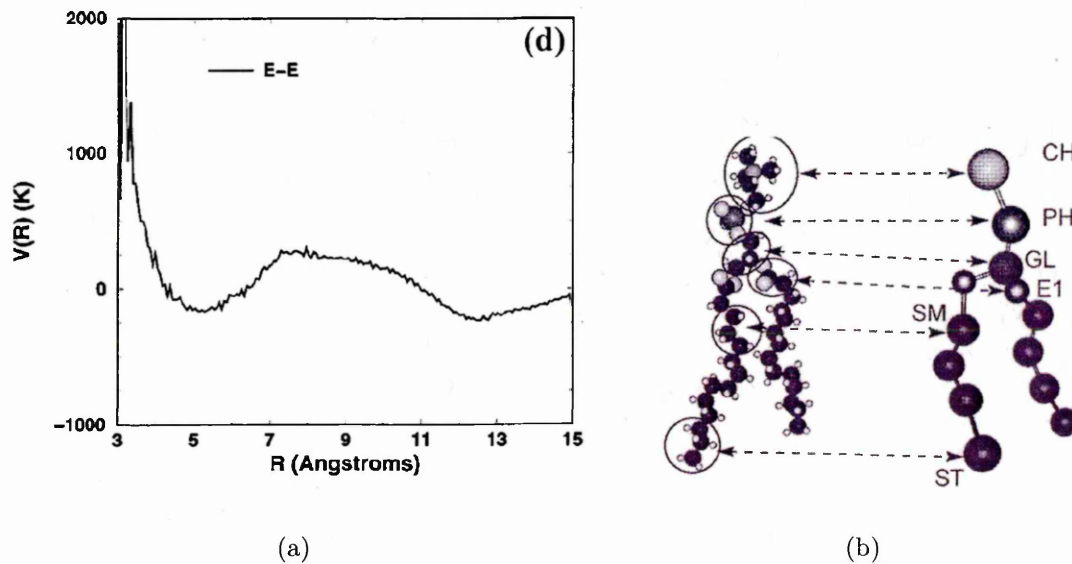


Fig. 3.13: (a): Tabulated potential for the E1-E1 interaction used in Shelley *et al.*'s model (b): Atomistic to coarse grain mapping of the DMPC molecule [118, 119]

Fig. 3.14 shows a plot obtained by summing the interactions between Shelley's CG lipid model and a single solvent bead. From this, it is clear that the hydrophilic head presents a strong attraction to the solvent spheres, while the hydrophobic tail displays a weaker (but still attractive) interaction with the solvent. Note that, in contrast, in Smit and Lipowsky's models, the tail-solvent interaction is modelled via a repulsive potential.

The CG models described above have successfully reproduced the behaviour seen

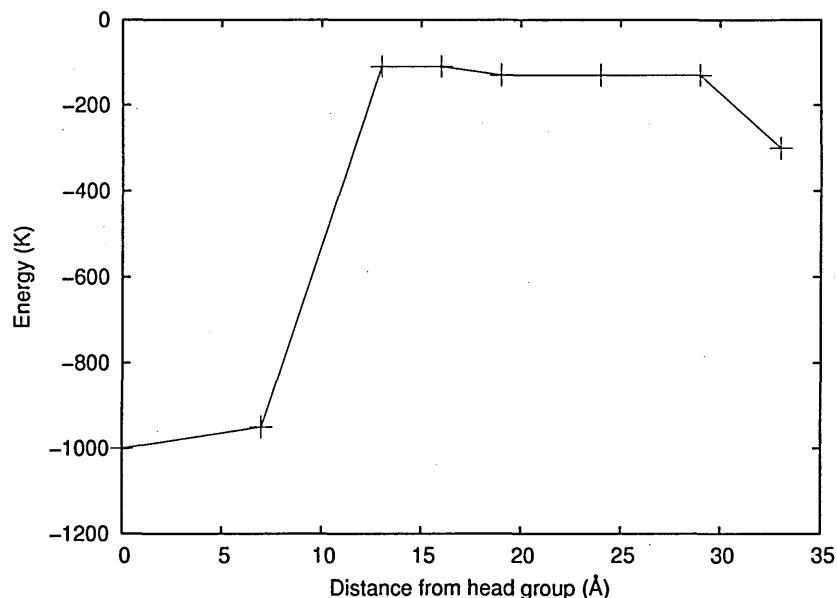


Fig. 3.14: Plot of the interaction potential between the CG lipid beads and a CG solvent bead used in Shelley *et al.*'s model on a path parallel to the DMPC molecule axis. The abscissa represents the distance along this path from the top of the molecule, *i.e.* adjacent to the head group ($r = 0 \text{ \AA}$) to the tail ($r = 3.2 \text{ \AA}$). The lipid beads- solvent bead interaction is based on Lennard-Jones 12-6 potentials stronger at short distances (around the head group) and weaker at larger distance (around the tail)

in experiential and all-atom simulation studies and have allowed extension of the scope of MD simulations to larger time and length scales. However, these models have generally been tuned to match specific characteristics such as diffusion [117] or structural conformations [118, 119] based on the lamellar phase only. Their transferability to other amphiphilic phases (e.g. more dilute structures such as the micellar phase and more concentrated phases like the inverse micellar phase) is therefore questionable.

Very recently, solvent free models of amphiphilic self-assembly have been developed [122–129]. Having an implicit solvent implies the use of additional cohesive forces between the amphiphiles. The phase diagram for implicit solvent models employing LJ interaction only contains a gas/crystal transition then and no fluid lamellar phase is achievable. Multi-body potentials were therefore developed as well

as highly tuned potentials [123, 124] and angle-dependant potentials [125–129]. Other authors proposed to widen the range of the Lennard-Jones potential in order to create a fluid lamellar phase in a system which, otherwise, has only a gas/crystal transition [123, 124]. This is a fundamentally different approach from that used in previous models based on an anisotropic amphiphile-solvent interaction, i.e. a solvent-induced interaction. This class of models has proved attractive to the modelling community due to their high computational efficiency. However, most of these models have been designed so as to study a specific phase such as the bilayer phase with a very strong cohesive energy between the amphiphiles. Therefore, the other lamellar phases such as the ripples phase, gel phases, tilted phase and the other amphiphilic phases observed experimentally with varying concentration may not be reproduced successfully.

In 1989, an alternative CG model for lyotropic systems was presented by Gunn and Dawson [130]. Attempting to bridge the gap between the more primitive lattice models described earlier and the highly complex all-atom simulations, they developed an even more coarse-grained model in which each amphiphilic molecule was modelled as a single site ellipsoidal-shaped particle. Using an anisotropic version of the Lennard-Jones potential, namely the Gay-Berne potential (see next chapter for a detailed description), to model the amphiphiles, the solvent molecules being modelled as simple Lennard-Jones spheres. The amphiphile-solvent interaction energy was then designed such that one end of the ellipsoid had an attractive potential whereas the other had a repulsive one. This model proved able to form a bilayer, however no other concentrations were studied and the use of a very strong side-side attraction for the amphiphile-amphiphile interaction ($\epsilon_{side-side}/\epsilon_{end-end} = 16$) probably strongly promoted the formation of these bilayers. Unfortunately, no further work was performed to investigate the behaviour of this model.

3.2.4 Mesoscopic models

Mesoscopic scale simulations have also been carried out using Brownian dynamics (BD), Dissipative Particle Dynamics (DPD) and Lattice Boltzmann (LB) approaches. This work is complementary to the molecular simulations and gives another insight into how these systems behave since it operates at different length and time scales. Therefore, if one is looking to develop a coarse-grained model aimed at bridging the gap between the microscopic and macroscopic world, it is interesting to compare these studies with the atomic scale simulations. These mesoscopic techniques also offer the advantage of allowing the study of hydrodynamics effects. Although MD should, in theory, recover correct hydrodynamic behaviour, no studies have lead to meaningful data for this to be observed as MD is limited to relatively small length and time scales.

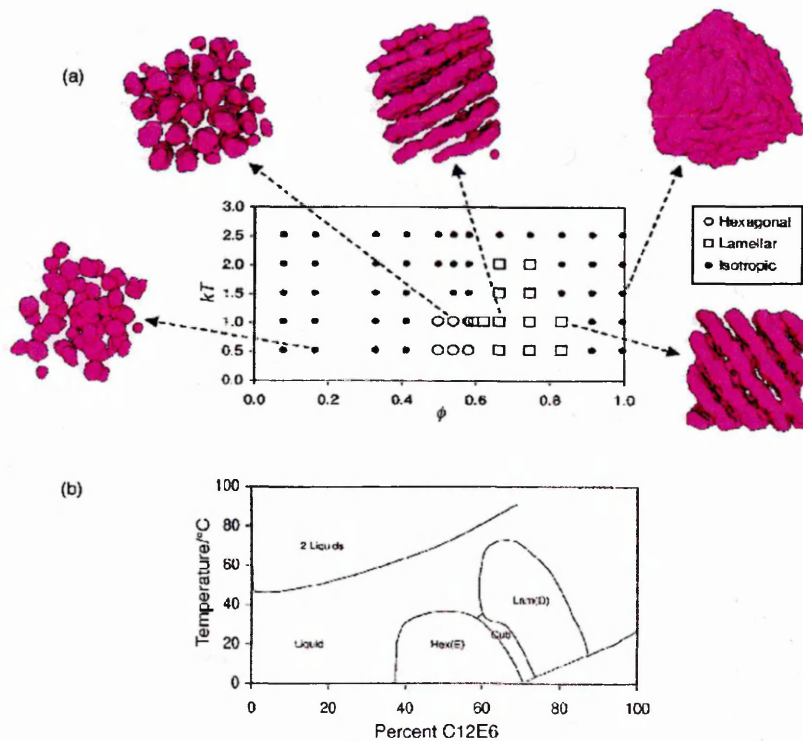


Fig. 3.15: (a) Phase diagram of amphiphilic dimer from a DPD simulation showing micellar, lamellar, hexagonal and inverse micellar phase vs. density and temperature [131] (b) Equivalent experimental phase diagram of the non-ionic surfactant $C_{12}E_6$ [10]

One of the first applications of the DPD technique to amphiphilic systems was performed by Warren *et al.* [131–133]. In these simulations, amphiphilic dimers (A-B) were immersed into a solvent fluid C. Similarly to MD, the DPD methodology considers beads, but they interact via soft repulsive potentials so allowing the use of longer timesteps. The strength of the soft repulsive potential is governed by the parameter a such that: $a_{AA} = a_{BB} = a_{CC} = 25$, $a_{AB} = 30$, $a_{AC} = 0$ and $a_{BC} = 50$. This indicates that the sites B are relatively immiscible with fluid C (large a_{BC}) whereas the sites A are miscible with C (small a_{AC}). The A-B and like-like interactions were set so that the dimer-dimer interaction for a parallel configuration is slightly more favorable than the equivalent anti-parallel configuration ($a_{AB} \Rightarrow a_{AA}$, $a_{AB} \Rightarrow a_{BB}$). The choice of a ‘minimal’ amphiphile (dimer) is *a priori* surprising as it is known from MC lattice models that relatively large chain molecules are required (*e.g.* A_2B_3) to observe self-assembly of mesophases [72]. However as noted by Groot *et al.* [134], the DPD technique allows phenomena, usually observed experimentally for long chain block copolymer molecules, to be observed using DPD ‘molecules’ with relatively small chain lengths. Fig. 3.15(a) illustrates the phase behaviour observed for this amphiphilic dimer as function of concentration and temperature. It can be seen that the phase behaviour of this dimer matches the experimental phase behaviour (Fig. 3.15(b)) of a non-ionic surfactant $C_{12}E_6$ with a similar HLB ratio of 50%. Also mesoscopic phases such as the hexagonal phases, difficult to obtain with coarse-grained MD, are easily obtained with this technique.

Following the pioneering bead-spring models used in MD, similar models have been developed by Smit *et al.* using this DPD methodology and similar interaction parameters [135–142]. The phase behaviour of lipid bilayer has then been studied thoroughly as a function of the chain stiffness, chain length and temperature. Interdigitated phases, ripple phases and gel phases have been readily found with this approach and proved to be consistent with experimental studies.

The DPD technique has also been used to study the fusion of a vesicle with a

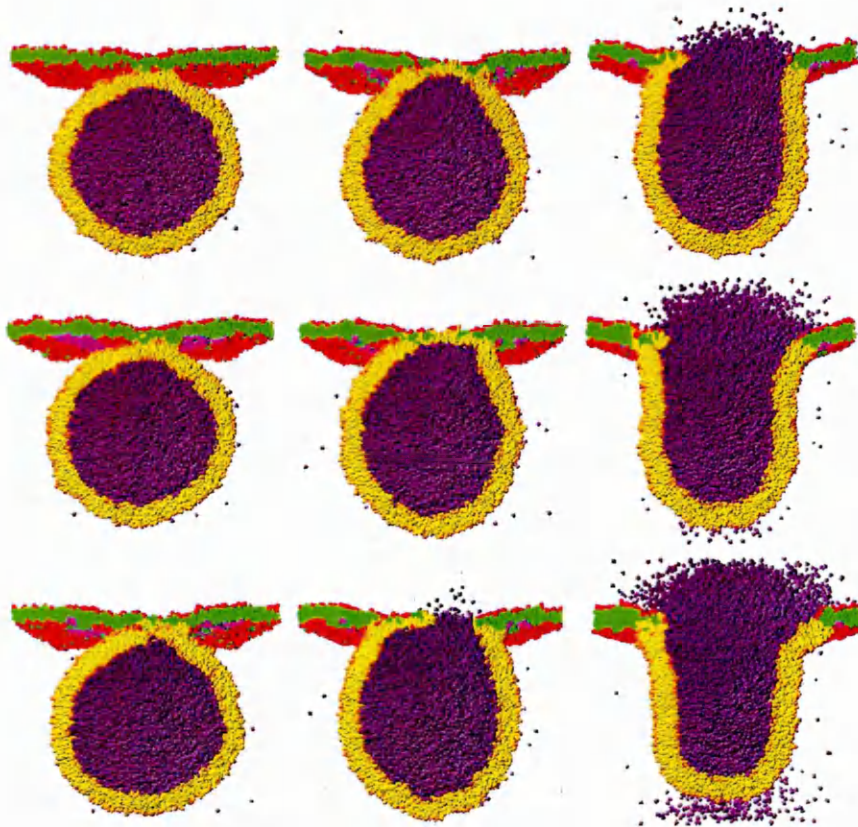


Fig. 3.16: Fusion of a vesicle with a planar membrane by DPD simulation [143]

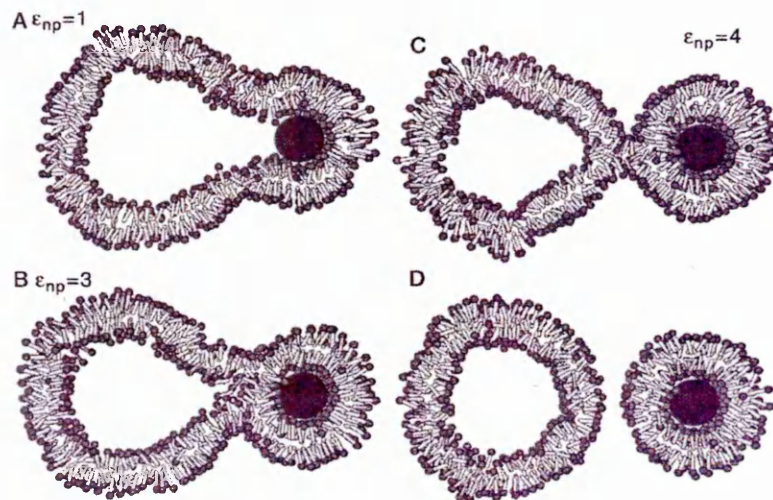


Fig. 3.17: Fission - budding of a vesicle through a colloidal particle modelled by Brownian Dynamics simulation [144]

planar membrane [143, 145–147] (see Fig. 3.16). Experimentally, such processes are believed to be mediated by proteins, although the molecular details of their action remains unclear. In this work, the action of the proteins was mimicked by applying a transient curvature change and a tension change in a circular ring around the fusion zone. In other words, an externally induced surface tension gradient was imposed on the planar membrane, inducing a flow of lipids from the vesicle into the planar membrane.

Noguchi *et al.* have studied the interaction of vesicles and adhesive nanoparticles using a Brownian dynamics simulation [144, 148–151]. Here, the nanoparticles can be seen as simple models for proteins or colloidal particles (see Fig. 3.17). This work showed that the nanoparticle induced morphological changes in the vesicle promoting budding, fission and fusion processes (see Fig. 3.17).

At a bigger length scales, amphiphilic molecules tend to form even more exotic phases than bilayers and micelles. These structures have been studied by macroscopic curvature models based on the Helfrich hamiltonian [5] that describes their equilibrium properties. However, the self-assembly of such ordered structures cannot be described by these models. To fill this gap, Coveney *et al.* [152–154] have developed LB simulations to compute the self-assembly of cubic and lamellar phases from random initial configuration (see Fig. 3.18). The lamellar phase was obtained from the same initial random configuration but with the interaction between amphiphiles switched off. However this work did not show what happens at different concentrations or different temperatures. Furthermore, the lamellar phase was only found by changing the interaction potential of the fluid system, whereas, a perfectly working model should be able to retrieve all phases available in the time/length scale of the simulation with a single model potential.

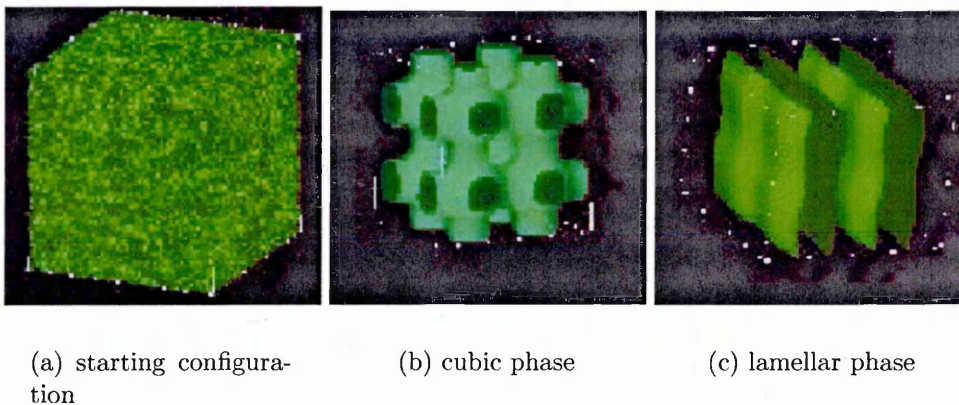


Fig. 3.18: Lattice Boltzmann simulation of an binary surfactant/water fluid mixture [153]

3.3 Conclusion

In this chapter, the main simulation techniques available for soft-condensed matter studies have been briefly reviewed. A wide range of time and length scales is accessible, from atomic detailed simulations to mesoscopic fluid flow dynamics simulations. The main method, namely MD, covers a subset of this wide range of scales through the use of all-atom (AA), united-atom (UA) and coarse-grained (CG) models.

The computer simulation literature for amphiphilic and lyotropic liquid crystal systems is extensive and contains examples incorporating a wide range of different simulation techniques. It has been seen that, the early primitive lattice models developed for single micelles have evolved, with time and increasing computer power, to 3D lattice models of large systems capable of calculating useful quantities such as micelle size distribution functions and various dynamic quantities. These models are, in general, capable of simulating several micelles for a few micelle life-times, allowing the modification of existing theories of micellar formation, leading to better fits to experiments and simulations.

However, the intrinsic simplicity of these models has brought about the use of atomistic MD simulations to gain more detail about the underlying behaviour of

these systems. The computing challenge that these systems bring has also triggered many debates and fundamental improvements in the simulation techniques themselves (*e.g.* the choice of thermodynamic ensemble).

Although, it is possible, nowadays, to simulate the self-assembly of a single micelle with an all-atom description, unfortunately, the computing cost of atomistic simulations is still very high and precludes the study of the large scale systems considered the simpler Monte Carlo lattice models. Even in the simulation of long chain surfactants (expected to have fast monomer exchange with bulk), almost no monomer exchange can be observed. As a result, most of all-atom simulations are still based on pre-assembled structures. Therefore, coarse-grained models have been developed and have proved to be very successful at reproducing generic behaviour. Many of these CG off-lattice models are based on Smit's pioneering bead chain model based on Lennard-Jones potentials. The interactions are set so that the like-like (hydrophilic-hydrophilic and hydrophobic-hydrophobic) interactions are attractive and the hydrophobic-hydrophilic interaction is purely repulsive. These models have proved to be efficient enough to study the self-assembly of various amphiphilic molecules. However, the use of completely repulsive potentials for unlike interactions can be questioned as it might promote phase separation rather than true amphiphilic self-assembly. Most successful models have overcome this by considering relatively weaker attractions. Some groups have even made a complete mapping of an all-atom model to a coarse-grained model in order to gain more chemical specificity.

Despite their success, these CG models have, however, one drawback. Intrinsically governed by interaction potentials, these models are all based on relatively weak tail-solvent interactions compared with the other interactions in the system. The self-assembly processes described by these models are, therefore, enthalpic in origin and should be essentially independent of temperature. It is, nevertheless, important to recall that the self-assembly of surfactant molecules in aqueous solutions is mainly an entropy-driven process which, therefore depends on tem-

perature. One could, therefore, argue that these models are not appropriate for studying self-assembly phenomena in aqueous solutions. As already noted by Lipowsky *et al.* [113], these enthalpic models could, indeed, correspond better to enthalpy-driven self-assembly in non-polar solvents [155–158]. However, one could argue that the entropic effect of the hydrogen bonding is somehow incorporated into those models via the required packing of the solvent around the hydrophobic tail due a strong solvent-solvent attraction. Furthermore, whatever the molecular mechanism responsible for the self-assembly (whether entropy or enthalpy dominates the hydrophobic effect - see chapter 2), the net free energy is positive and unfavorable for dissolution which is successfully reproduced with these models.

Recently, the advent of new mesoscopic simulation techniques such as DPD and LB has brought about new perspective in the field. Complex structures such as the hexagonal or cubic phases, reputed difficult to obtain via traditional MD simulation, are now readily obtained using these techniques. The explicit presence of hydrodynamic interactions also seems to be important in long-range ordering, fundamental to these complex 3D arrangements. However, these simulations lack molecular details and render the link between between molecular parameters and mesoscopic properties difficult to obtain.

CHAPTER 4

Design of a novel single site amphiphilic model

In the previous chapter, the need for a coarse-grained model to elucidate some aspects of the self-assembly process was discussed. From this it is apparent that a single site amphiphilic molecular model could be computationally very efficient and so allow one to study generic behaviour of amphiphilic systems.

In this chapter, the design of such a generic model, capable of retrieving global amphiphilic phase behaviour, is presented. The first part of this chapter contains an introduction to the type of molecular model used. Following this, the incorporation of amphiphilic behaviour into this model is described. Finally, some preliminary simulations of this model are presented for a wide range of concentrations.

4.1 Introduction

In the previous chapter, atomistic and coarse-grained models were reviewed. Most coarse-grained models use bead-chains to represent the amphiphilic molecules. For instance, in Lipowsky's model, a chain of 5 beads is used in which bond angles are able to vary. This multi-site model therefore allows intramolecular flexibility. Furthermore, one can readily design molecules with different topographies (e.g. 2-tail amphiphiles or molecules with different head group sizes). However, in a 5 bead-chain model, 25 contributions are still required per molecule-molecule interaction. Furthermore, this type of bead-based coarse grained model requires both inter and intra molecular potentials. In seeking to develop a generic simulation model for an amphiphile with greater computational efficiency, one could try to reduce this number of interaction contributions. This can be achieved by increasing the level of coarse-graining, i.e. reducing the number of beads. A more dramatic route is to consider the amphiphile as a single-site rod-shaped particle (see Fig. 4.1).

In such a model, the amphiphile-amphiphile interaction is reduced to a single contribution potentially leading to an increase in computational efficiency. However, any intramolecular flexibility, easily incorporated in a bead-chain model, is obviously lost in such a single site model.

In the following, we describe the development of such a model in which each amphiphile is represented by a single rod-shaped particle and each solvent molecule by a single spherical particle. In this mixture of two different species, one has to deal with 3 different intermolecular potentials: one for each class of like-like interaction and a further one to describe interactions between unlike species. Here, the solvent-solvent interactions are governed by the Lennard-Jones potential (described in previous chapter), the amphiphile-amphiphile interaction by the Gay-Berne potential (see below) and, finally, the amphiphile-solvent interaction by a novel modification of the Gay-Berne potential.

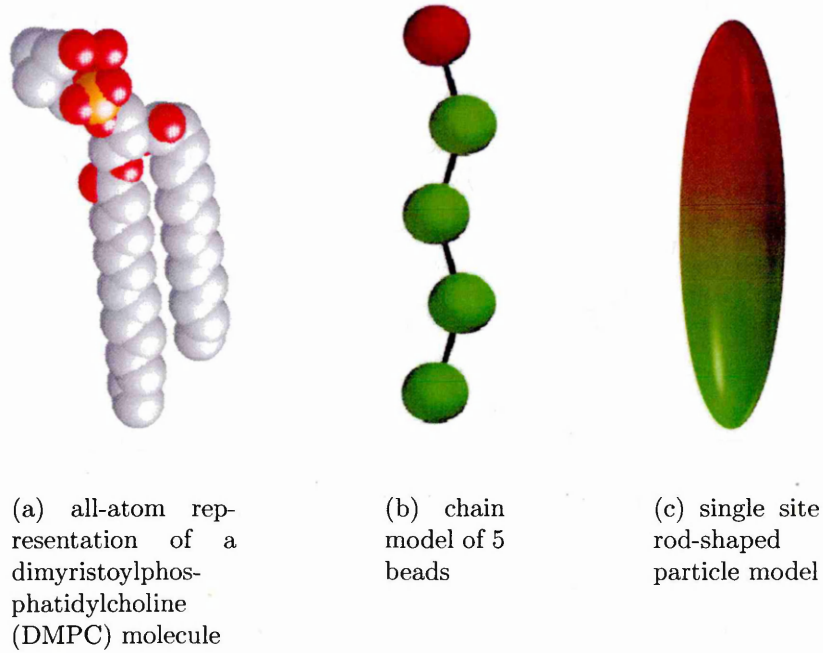


Fig. 4.1: Schematic pictures of the coarse-graining process from all-atom (a) to bead-chain (b) to single-site rod-shaped particle (c)

4.2 Computer model of rod-sphere mixture

4.2.1 The Gay-Berne Model

For the purposes of modelling anisotropic molecules as single-site objects (instead of as multi-site molecules made of Lennard-Jones particles), Berne and Pechukas [159] proposed a generalised form of the Lennard-Jones potential with an angular dependence of the shape parameter σ determined by considering the overlap of two ellipsoidal Gaussian distributions.

This model describes the interaction between soft ‘rod-shaped’ particles through a potential U_{BP} taking the following form :

$$U_{BP}(\hat{\mathbf{r}}_{ij}, \hat{\mathbf{u}}_i, \hat{\mathbf{u}}_j) = 4\epsilon(u_i, u_j) \left[\left(\frac{\sigma(\hat{\mathbf{r}}_{ij}, \hat{\mathbf{u}}_i, \hat{\mathbf{u}}_j)}{r_{ij}} \right)^{12} - \left(\frac{\sigma(\hat{\mathbf{r}}_{ij}, \hat{\mathbf{u}}_i, \hat{\mathbf{u}}_j)}{r_{ij}} \right)^6 \right] \quad (4.1)$$

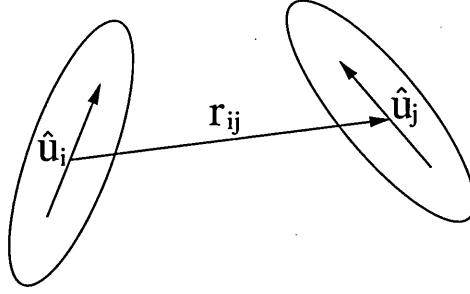


Fig. 4.2: Schematic diagram showing orientations and displacement of particle i and j

where \hat{u}_i and \hat{u}_j are unit vectors describing the orientations of the molecules and $\hat{r}_{ij} = r_{ij}/r_{ij}$ is the unit intermolecular vector (see Fig. 4.2.1). The energy parameter $\epsilon(\hat{u}_i, \hat{u}_j)$ and the shape parameter $\sigma(\hat{r}_{ij}, \hat{u}_i, \hat{u}_j)$ (which are constant for the Lennard-Jones potential) are now given by

$$\epsilon(\hat{u}_i, \hat{u}_j) = \epsilon_0 [1 - \chi^2 (\hat{u}_i \cdot \hat{u}_j)^2]^{-\frac{1}{2}} \quad (4.2)$$

and

$$\sigma(\hat{r}_{ij}, \hat{u}_i, \hat{u}_j) = \sigma_0 \left[1 - \frac{\chi}{2} \left[\frac{(\hat{r}_{ij} \cdot \hat{u}_i + \hat{r}_{ij} \cdot \hat{u}_j)^2}{1 + \chi(\hat{u}_i \cdot \hat{u}_j)} + \frac{(\hat{r}_{ij} \cdot \hat{u}_i - \hat{r}_{ij} \cdot \hat{u}_j)^2}{1 - \chi(\hat{u}_i \cdot \hat{u}_j)} \right] \right]^{-1/2} \quad (4.3)$$

where ϵ_0 and σ_0 define the units of energy and distance, respectively. The parameter χ controls the shape anisotropy of the rod such as:

$$\chi = \frac{\kappa^2 - 1}{\kappa^2 + 1} \quad (4.4)$$

where $\kappa = \sigma_e/\sigma_0$ is the length to breadth ratio with σ_e and σ_0 defined as the length and the width of the molecule, respectively.

When compared with the potential obtained for linear arrays of Lennard-Jones sites, this model was not entirely satisfactory; the energy parameter given in Eqn. 4.3 does not depend on the intermolecular vector \mathbf{r}_{ij} so that there is no difference between the side-side and the end-end interaction strengths. Also, the width of the attractive minimum scales with σ , whereas for linear Lennard-Jones arrays, it has little orientation dependence.

To address these unrealistic features of the Berne-Pechukas potential, Gay and Berne [160] proposed the alternative shifted form:

$$U_{GB}(\hat{\mathbf{r}}_{ij}, \hat{\mathbf{u}}_i, \hat{\mathbf{u}}_j) = 4\epsilon(\hat{\mathbf{r}}_{ij}, \hat{\mathbf{u}}_i, \hat{\mathbf{u}}_j) \left[\left(\frac{\sigma_0}{r_{ij} - \sigma(\hat{\mathbf{r}}_{ij}, \hat{\mathbf{u}}_i, \hat{\mathbf{u}}_j) + \sigma_0} \right)^{12} - \left(\frac{\sigma_0}{r_{ij} - \sigma(\hat{\mathbf{r}}_{ij}, \hat{\mathbf{u}}_i, \hat{\mathbf{u}}_j) + \sigma_0} \right)^6 \right] \quad (4.5)$$

Here, the shape parameter is the same as that in the Berne-Pechukas model, while the energy parameter is given by:

$$\epsilon(\hat{\mathbf{u}}_i, \hat{\mathbf{u}}_j) = \epsilon_0 [\epsilon_1(\hat{\mathbf{u}}_i, \hat{\mathbf{u}}_j)]^\nu [\epsilon_2(\hat{\mathbf{r}}_{ij}, \hat{\mathbf{u}}_i, \hat{\mathbf{u}}_j)]^\mu \quad (4.6)$$

where ϵ_0 is a constant and $\epsilon_1(\hat{\mathbf{u}}_i, \hat{\mathbf{u}}_j)$ is the energy parameter used in the Berne-Pechukas potential.

The second term of Eqn. 4.6 takes the same form as the Berne-Pechukas $\sigma(\hat{\mathbf{r}}_{ij}, \hat{\mathbf{u}}_i, \hat{\mathbf{u}}_j)$ (see Eqn. 4.3):

$$\epsilon_2(\hat{\mathbf{r}}_{ij}, \hat{\mathbf{u}}_i, \hat{\mathbf{u}}_j) = 1 - \frac{\chi'}{2} \left[\frac{(\hat{\mathbf{r}}_{ij} \cdot \hat{\mathbf{u}}_i + \hat{\mathbf{r}}_{ij} \cdot \hat{\mathbf{u}}_j)^2}{1 + \chi'(\hat{\mathbf{u}}_i \cdot \hat{\mathbf{u}}_j)} + \frac{(\hat{\mathbf{r}}_{ij} \cdot \hat{\mathbf{u}}_i - \hat{\mathbf{r}}_{ij} \cdot \hat{\mathbf{u}}_j)^2}{1 - \chi'(\hat{\mathbf{u}}_i \cdot \hat{\mathbf{u}}_j)} \right] \quad (4.7)$$

where χ' is the energy anisotropic parameter:

$$\chi' = \frac{(\kappa')^{1/\mu} - 1}{(\kappa')^{1/\mu} + 1} \quad (4.8)$$

with $\kappa' = \epsilon_{ss}/\epsilon_{ee}$

This gives a pair-interaction energy which is governed by both an anisotropic shape and an anisotropic energy function. The parameter ϵ_{ss} is the depth of the potential for a pair of parallel molecules arranged side-to-side and ϵ_{ee} is the equivalent depth for two parallel molecules arranged end-to-end. The exponents $\mu = 1$ and $\nu = 2$ were originally adjusted to obtain a good fit to a linear four-site Lennard-Jones potential representation of an anisotropic molecule. In this original parameterisation, the elongation of the molecule σ_e / σ_0 was set to 3 and the ratio $\epsilon_{ss} / \epsilon_{ee}$ to 5. The use of $\kappa = 1$ and $\kappa' = 1$ with any μ and ν leads back to the spherical LJ potential.

The Gay-Berne model was originally designed for studying thermotropic liquid crystals, and a substantial literature exists relating to this application [161–171]. The set of parameters $GB(\kappa, \kappa', \nu, \mu) = GB(3, 5, 2, 1)$ was shown to promote isotropic, nematic, smectic A and smectic B phases [162]. Later, an attempt to model a more realistic system was made. Estimates of the GB parameters were calculated for p-terphenyl, a non-polar and rigid typical mesogen, by fitting the parameters against a multi-site p-terphenyl potential. Two p-terphenyl molecules were constructed using 36 Lennard-Jones sites. Then, by comparing with several biaxially averaged contour sets obtained when rotating one molecule around the other, the set of parameters $GB(4.4, 39.6, 0.74, 0.8)$ was determined [168]. In this parameterisation, the GB particles are slightly more elongated than those with the original parameters and the well-depth anisotropy is significantly larger (κ' almost 8 times larger than the ‘standard’ value). Simulations performed using this potential showed that the isotropic and nematic phases, dominated by short range repulsion, remained unchanged, whereas the stability of the S_A was

critically dependant on the anisotropy in the attractive forces. A subsequent systematic study into the effects of molecular elongation on the Gay-Berne phase diagram [171] showed significant changes notably in the location of the isotropic-nematic transition. Also, an investigation of the generic effects of the attractive part of the potential [170] showed that smectic order is favoured as k' is increased, thus confirming the importance of attractive forces for the formation of smectic phases by rod-shaped particles.

Thus, due to many developments and an extended possibility of parameterisation, the Gay-Berne model is one of the most versatile and computationally efficient molecular models for liquid crystal simulation (see recent reviews in [172–174]). Depending on the chosen shape and energy parameterisation, it can be used to model many different liquid crystals, from linear mesogens to discotic LC [175,176] and even, recently, pear-shaped particles [177]. It can also be combined with other potentials leading to, e.g., GB+point dipole [178] and GB + point quadrupole [179,180].

4.2.2 The rod-sphere potential

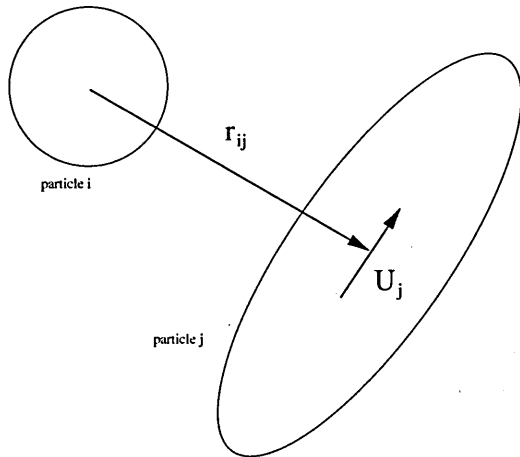


Fig. 4.3: schematic diagram of a rod and sphere

The Gay-Berne potential introduced in the previous section gives an interaction for

two identical but uniaxially anisotropic particles. Later developments by Cleaver *et al.* [181] generalised this potential to allow non identical particle to be dealt with. This lead to some simulation work on LC mixtures [182–187]. The GB potential can, alternatively, be simplified to make it appropriate for the interaction between a sphere and GB particle. In this case, the shape parameter is given by

$$\sigma(\hat{\mathbf{r}}_{ij} \cdot \hat{\mathbf{u}}_j) = \sigma_0 \left[1 - \frac{l_j^2 - d_j^2}{l_j^2 + d^2} \cdot (\hat{\mathbf{r}}_{ij} \cdot \hat{\mathbf{u}}_j)^2 \right]^{-1/2} \quad (4.9)$$

where l_j , d_i and d are, respectively, the rod length, rod diameter and sphere diameter. The corresponding well-depth term is:

$$\epsilon(\hat{\mathbf{r}}_{ij} \cdot \hat{\mathbf{u}}_j) = \epsilon_0 \left[1 - \left(1 - \frac{\epsilon_E}{\epsilon_S} \right)^{1/\mu} (\hat{\mathbf{r}}_{ij} \cdot \hat{\mathbf{u}}_j)^2 \right]^\mu \quad (4.10)$$

where $\frac{\epsilon_S}{\epsilon_E} = \kappa'$ controls the well-depth anisotropy of the interaction.

The form. 4.9 was first noted in an aside in Berne and Pechukas original paper [159]. It was only through the generalised form derived by Cleaver *et al.*, however, that it was made clear that there is a continuous route between the rod-rod and rod-sphere shape parameters, corresponding to a gradual shrinking of one of the rods to a sphere.

By changing the ratio κ' , it is possible to create systems in which the spheres either favour the ends of the rods ($\kappa' < 1$) or make no distinction between the rod's ends and sides ($\kappa' = 1$). Finally, if $\kappa' > 1$, the spheres can be made to favour the sides of the rods rather than their ends (see Fig. 4.4).

The behaviour of this class of system was investigated through a comprehensive simulation study by Antypov [185]. This showed the effects of adding small spherical particles to a fluid of rods which would otherwise represent a liquid crystalline substance [187].

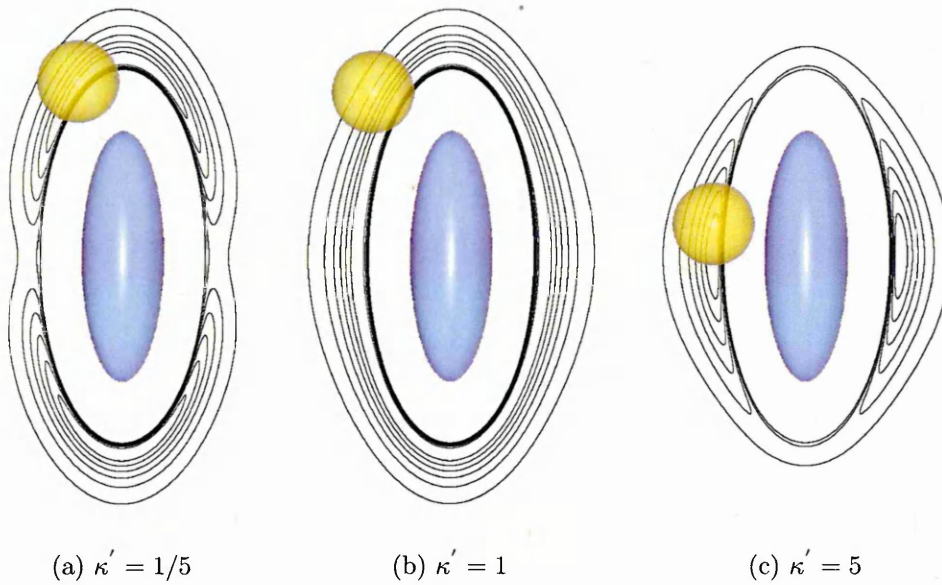


Fig. 4.4: Potential energy contour plot of the rod-sphere interaction for different value of $\kappa' = \frac{\epsilon_S}{\epsilon_E}$ [186]

4.2.3 Preliminary simulations results

Before dealing with the modifications made to this potential in order to retrieve amphiphilic behaviour, we first present a preliminary simulation study of this simple rod-sphere system. The aim here is to validate the simulation code by making comparison with Antypov's results.

A system of 1024 particles was simulated in the canonical or constant NVT ensemble using the MD algorithms described earlier. The parameterisation of the system studied was as follows. The sphere-sphere interactions, via the Lennard-Jones potential, set the unitary interaction strength of $\epsilon = \epsilon_0$ and the sphere diameter of $\sigma = \sigma_0$. The rod-rod interaction was set up with the original parameterisation with the elongation ratio $\kappa = \sigma_e/\sigma_0$ set to 3 (with the rod's diameter equal to the sphere's diameter) and the ratio $\epsilon_{ss}/\epsilon_{ee}$ set to 5. This parameterisation promotes normal liquid crystalline behaviour where the molecules tend to lie parallel with one another. Finally, the rod-sphere potential was set up with $\kappa' = 5$ by setting $\epsilon_E = 0.2\epsilon_0$ and $\epsilon_S = \epsilon_0$.

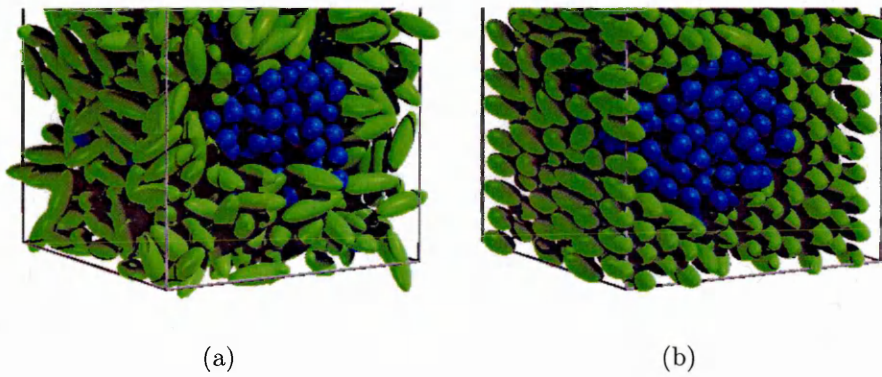


Fig. 4.6: (a) Isotropic ($\rho = 0.40$) and (b) LC phase ($\rho = 0.49$) for a rod-sphere mixture with $\kappa' = 5$ at $T = 0.7$

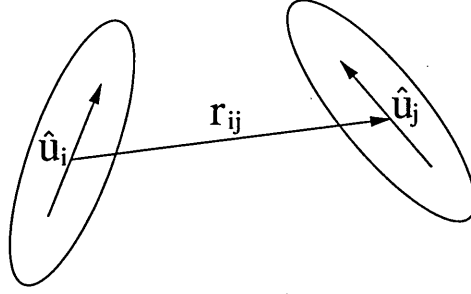


Fig. 4.2: Schematic diagram showing orientations and displacement of particle i and j

where $\hat{\mathbf{u}}_i$ and $\hat{\mathbf{u}}_j$ are unit vectors describing the orientations of the molecules and $\hat{\mathbf{r}}_{ij} = \mathbf{r}_{ij}/r_{ij}$ is the unit intermolecular vector (see Fig. 4.2.1). The energy parameter $\epsilon(\hat{\mathbf{u}}_i, \hat{\mathbf{u}}_j)$ and the shape parameter $\sigma(\hat{\mathbf{r}}_{ij}, \hat{\mathbf{u}}_i, \hat{\mathbf{u}}_j)$ (which are constant for the Lennard-Jones potential) are now given by

$$\epsilon(\hat{\mathbf{u}}_i, \hat{\mathbf{u}}_j) = \epsilon_0 [1 - \chi^2 (\hat{\mathbf{u}}_i \cdot \hat{\mathbf{u}}_j)^2]^{-\frac{1}{2}} \quad (4.2)$$

and

$$\sigma(\hat{\mathbf{r}}_{ij}, \hat{\mathbf{u}}_i, \hat{\mathbf{u}}_j) = \sigma_0 \left[1 - \frac{\chi}{2} \left[\frac{(\hat{\mathbf{r}}_{ij} \cdot \hat{\mathbf{u}}_i + \hat{\mathbf{r}}_{ij} \cdot \hat{\mathbf{u}}_j)^2}{1 + \chi(\hat{\mathbf{u}}_i \cdot \hat{\mathbf{u}}_j)} + \frac{(\hat{\mathbf{r}}_{ij} \cdot \hat{\mathbf{u}}_i - \hat{\mathbf{r}}_{ij} \cdot \hat{\mathbf{u}}_j)^2}{1 - \chi(\hat{\mathbf{u}}_i \cdot \hat{\mathbf{u}}_j)} \right] \right]^{-1/2} \quad (4.3)$$

where ϵ_0 and σ_0 define the units of energy and distance, respectively. The parameter χ controls the shape anisotropy of the rod such as:

$$\chi = \frac{\kappa^2 - 1}{\kappa^2 + 1} \quad (4.4)$$

where $\kappa = \sigma_e/\sigma_0$ is the length to breadth ratio with σ_e and σ_0 defined as the length and the width of the molecule, respectively.

When compared with the potential obtained for linear arrays of Lennard-Jones sites, this model was not entirely satisfactory; the energy parameter given in Eqn. 4.3 does not depend on the intermolecular vector \mathbf{r}_{ij} so that there is no difference between the side-side and the end-end interaction strengths. Also, the width of the attractive minimum scales with σ , whereas for linear Lennard-Jones arrays, it has little orientation dependence.

To address these unrealistic features of the Berne-Pechukas potential, Gay and Berne [160] proposed the alternative shifted form:

$$U_{GB}(\hat{\mathbf{r}}_{ij}, \hat{\mathbf{u}}_i, \hat{\mathbf{u}}_j) = 4\epsilon(\hat{\mathbf{r}}_{ij}, \hat{\mathbf{u}}_i, \hat{\mathbf{u}}_j) \left[\left(\frac{\sigma_0}{r_{ij} - \sigma(\hat{\mathbf{r}}_{ij}, \hat{\mathbf{u}}_i, \hat{\mathbf{u}}_j) + \sigma_0} \right)^{12} - \left(\frac{\sigma_0}{r_{ij} - \sigma(\hat{\mathbf{r}}_{ij}, \hat{\mathbf{u}}_i, \hat{\mathbf{u}}_j) + \sigma_0} \right)^6 \right] \quad (4.5)$$

Here, the shape parameter is the same as that in the Berne-Pechukas model, while the energy parameter is given by:

$$\epsilon(\hat{\mathbf{u}}_i, \hat{\mathbf{u}}_j) = \epsilon_0 [\epsilon_1(\hat{\mathbf{u}}_i, \hat{\mathbf{u}}_j)]^\nu [\epsilon_2(\hat{\mathbf{r}}_{ij}, \hat{\mathbf{u}}_i, \hat{\mathbf{u}}_j)]^\mu \quad (4.6)$$

where ϵ_0 is a constant and $\epsilon_1(\hat{\mathbf{u}}_i, \hat{\mathbf{u}}_j)$ is the energy parameter used in the Berne-Pechukas potential.

The second term of Eqn. 4.6 takes the same form as the Berne-Pechukas $\sigma(\hat{\mathbf{r}}_{ij}, \hat{\mathbf{u}}_i, \hat{\mathbf{u}}_j)$ (see Eqn. 4.3):

$$\epsilon_2(\hat{\mathbf{r}}_{ij}, \hat{\mathbf{u}}_i, \hat{\mathbf{u}}_j) = 1 - \frac{\chi'}{2} \left[\frac{(\hat{\mathbf{r}}_{ij} \cdot \hat{\mathbf{u}}_i + \hat{\mathbf{r}}_{ij} \cdot \hat{\mathbf{u}}_j)^2}{1 + \chi'(\hat{\mathbf{u}}_i \cdot \hat{\mathbf{u}}_j)} + \frac{(\hat{\mathbf{r}}_{ij} \cdot \hat{\mathbf{u}}_i - \hat{\mathbf{r}}_{ij} \cdot \hat{\mathbf{u}}_j)^2}{1 - \chi'(\hat{\mathbf{u}}_i \cdot \hat{\mathbf{u}}_j)} \right] \quad (4.7)$$

where χ' is the energy anisotropic parameter:

$$\chi' = \frac{(\kappa')^{1/\mu} - 1}{(\kappa')^{1/\mu} + 1} \quad (4.8)$$

with $\kappa' = \epsilon_{ss}/\epsilon_{ee}$

This gives a pair-interaction energy which is governed by both an anisotropic shape and an anisotropic energy function. The parameter ϵ_{ss} is the depth of the potential for a pair of parallel molecules arranged side-to-side and ϵ_{ee} is the equivalent depth for two parallel molecules arranged end-to-end. The exponents $\mu = 1$ and $\nu = 2$ were originally adjusted to obtain a good fit to a linear four-site Lennard-Jones potential representation of an anisotropic molecule. In this original parameterisation, the elongation of the molecule σ_e / σ_0 was set to 3 and the ratio $\epsilon_{ss} / \epsilon_{ee}$ to 5. The use of $\kappa = 1$ and $\kappa' = 1$ with any μ and ν leads back to the spherical LJ potential.

The Gay-Berne model was originally designed for studying thermotropic liquid crystals, and a substantial literature exists relating to this application [161–171]. The set of parameters $GB(\kappa, \kappa', \nu, \mu) = GB(3, 5, 2, 1)$ was shown to promote isotropic, nematic, smectic A and smectic B phases [162]. Later, an attempt to model a more realistic system was made. Estimates of the GB parameters were calculated for p-terphenyl, a non-polar and rigid typical mesogen, by fitting the parameters against a multi-site p-terphenyl potential. Two p-terphenyl molecules were constructed using 36 Lennard-Jones sites. Then, by comparing with several biaxially averaged contour sets obtained when rotating one molecule around the other, the set of parameters $GB(4.4, 39.6, 0.74, 0.8)$ was determined [168]. In this parameterisation, the GB particles are slightly more elongated than those with the original parameters and the well-depth anisotropy is significantly larger (κ' almost 8 times larger than the ‘standard’ value). Simulations performed using this potential showed that the isotropic and nematic phases, dominated by short range repulsion, remained unchanged, whereas the stability of the S_A was

critically dependant on the anisotropy in the attractive forces. A subsequent systematic study into the effects of molecular elongation on the Gay-Berne phase diagram [171] showed significant changes notably in the location of the isotropic-nematic transition. Also, an investigation of the generic effects of the attractive part of the potential [170] showed that smectic order is favoured as k' is increased, thus confirming the importance of attractive forces for the formation of smectic phases by rod-shaped particles.

Thus, due to many developments and an extended possibility of parameterisation, the Gay-Berne model is one of the most versatile and computationally efficient molecular models for liquid crystal simulation (see recent reviews in [172–174]). Depending on the chosen shape and energy parameterisation, it can be used to model many different liquid crystals, from linear mesogens to discotic LC [175,176] and even, recently, pear-shaped particles [177]. It can also be combined with other potentials leading to, e.g., GB+point dipole [178] and GB + point quadrupole [179,180].

4.2.2 The rod-sphere potential

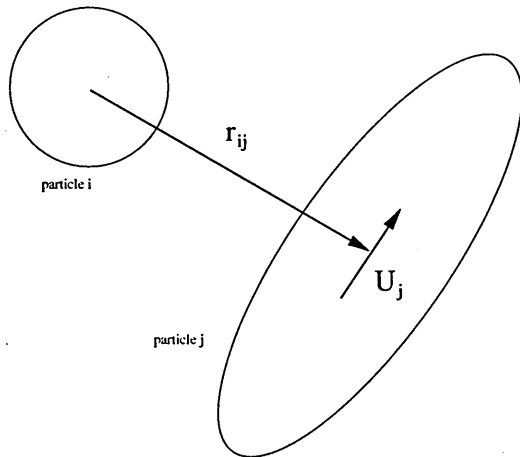


Fig. 4.3: schematic diagram of a rod and sphere

The Gay-Berne potential introduced in the previous section gives an interaction for

two identical but uniaxially anisotropic particles. Later developments by Cleaver *et al.* [181] generalised this potential to allow non identical particle to be dealt with. This lead to some simulation work on LC mixtures [182–187]. The GB potential can, alternatively, be simplified to make it appropriate for the interaction between a sphere and GB particle. In this case, the shape parameter is given by

$$\sigma(\hat{\mathbf{r}}_{ij} \cdot \hat{\mathbf{u}}_j) = \sigma_0 \left[1 - \frac{l_j^2 - d_j^2}{l_j^2 + d_j^2} \cdot (\hat{\mathbf{r}}_{ij} \cdot \hat{\mathbf{u}}_j)^2 \right]^{-1/2} \quad (4.9)$$

where l_j , d_i and d are, respectively, the rod length, rod diameter and sphere diameter. The corresponding well-depth term is:

$$\epsilon(\hat{\mathbf{r}}_{ij} \cdot \hat{\mathbf{u}}_j) = \epsilon_0 \left[1 - \left(1 - \frac{\epsilon_E}{\epsilon_S} \right)^{1/\mu} (\hat{\mathbf{r}}_{ij} \cdot \hat{\mathbf{u}}_j)^2 \right]^\mu \quad (4.10)$$

where $\frac{\epsilon_S}{\epsilon_E} = \kappa'$ controls the well-depth anisotropy of the interaction.

The form. 4.9 was first noted in an aside in Berne and Pechukas original paper [159]. It was only through the generalised form derived by Cleaver *et al.*, however, that it was made clear that there is a continuous route between the rod-rod and rod-sphere shape parameters, corresponding to a gradual shrinking of one of the rods to a sphere.

By changing the ratio κ' , it is possible to create systems in which the spheres either favour the ends of the rods ($\kappa' < 1$) or make no distinction between the rod's ends and sides ($\kappa' = 1$). Finally, if $\kappa' > 1$, the spheres can be made to favour the sides of the rods rather than their ends (see Fig. 4.4).

The behaviour of this class of system was investigated through a comprehensive simulation study by Antypov [185]. This showed the effects of adding small spherical particles to a fluid of rods which would otherwise represent a liquid crystalline substance [187].

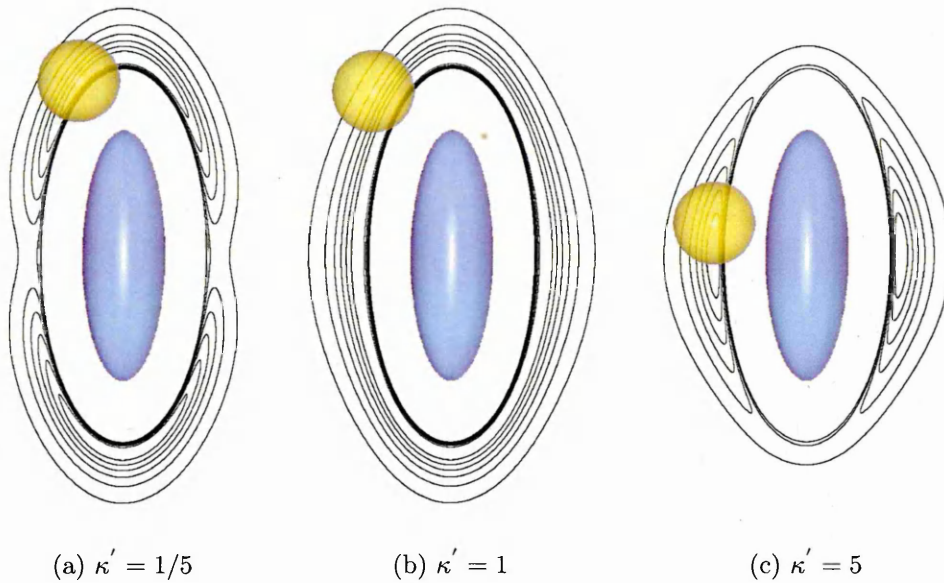


Fig. 4.4: Potential energy contour plot of the rod-sphere interaction for different value of $\kappa' = \frac{\epsilon_S}{\epsilon_E}$ [186]

4.2.3 Preliminary simulations results

Before dealing with the modifications made to this potential in order to retrieve amphiphilic behaviour, we first present a preliminary simulation study of this simple rod-sphere system. The aim here is to validate the simulation code by making comparison with Antypov's results.

A system of 1024 particles was simulated in the canonical or constant NVT ensemble using the MD algorithms described earlier. The parameterisation of the system studied was as follows. The sphere-sphere interactions, via the Lennard-Jones potential, set the unitary interaction strength of $\epsilon = \epsilon_0$ and the sphere diameter of $\sigma = \sigma_0$. The rod-rod interaction was set up with the original parameterisation with the elongation ratio $\kappa = \sigma_e/\sigma_0$ set to 3 (with the rod's diameter equal to the sphere's diameter) and the ratio $\epsilon_{ss}/\epsilon_{ee}$ set to 5. This parameterisation promotes normal liquid crystalline behaviour where the molecules tend to lie parallel with one another. Finally, the rod-sphere potential was set up with $\kappa' = 5$ by setting $\epsilon_E = 0.2\epsilon_0$ and $\epsilon_S = \epsilon_0$.

In a 50/50 system (512 rods and 512 spheres), a compression series was performed over the range of densities $0.22 \leq \rho \leq 0.50$ at a constant temperature of $T = 0.7$. At each density, the nematic order parameter, potential energy per particle and pressure were measured. As shown in Fig. 4.2.3, the order parameter results are in very good agreement with Antypov's. From these data, an ordering transition is apparent at around $\rho = 0.44$.

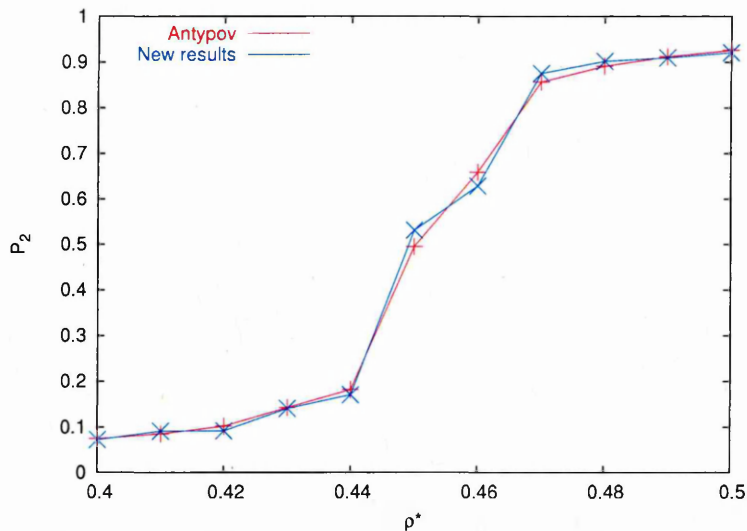


Fig. 4.5: Order parameter P_2 vs. ρ for a 50/50 rod-sphere mixture with $\kappa' = 5$ at $T = 0.7$

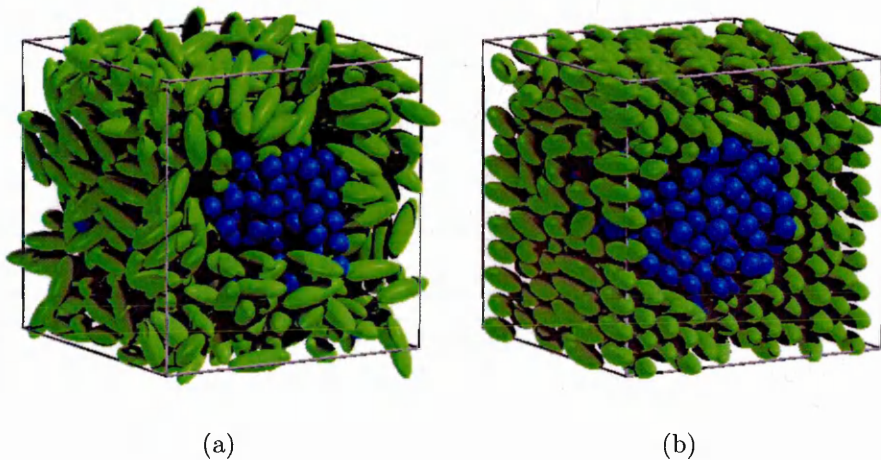


Fig. 4.6: (a) Isotropic ($\rho = 0.40$) and (b) LC phase ($\rho = 0.49$) for a rod-sphere mixture with $\kappa' = 5$ at $T = 0.7$

Two configuration snapshots taken below and above this transition density are shown in Fig. 4.6. These both indicate phase coexistence between rod-rich and sphere-rich phases, the sphere-rich droplet being cylindrical in shape due to the influence of the periodic boundary conditions. In agreement with Antypov’s analysis, the high density arrangement is found to be a smectic rod-rich phase, with director oriented parallel to the axis of the sphere-rich cylinder.

4.3 Modelling amphiphilic behaviour

The Gay-Berne model has been extensively used to simulate thermotropic LCs, but little work has been devoted to using it to model the properties of lyotropic systems. Here it is proposed to use the Gay-Berne model as the basis of a single-site potential with which to model amphiphilic behaviour with spheres acting as solvent particles. The rod-sphere interaction studied by Antypov can be modified for just this purpose.

In Antypov’s model, the parameter κ' controlled the well-depth anisotropy of the solvent spheres around the rod molecule (see Fig. 4.4). For instance, in the case $\kappa' = \frac{1}{5}$, the spheres favoured the rods’ ends only. In this study, it is proposed to develop Antypov’s rod-sphere potential further by giving it dipolar symmetry. By breaking the head-tail symmetry of the interaction, one can conceive of a potential in which the spheres favour only one end of each rod. This would then be analogous to the hydrophilic part of an amphiphilic molecule, the other, less attractive, end representing the hydrophobic part of the molecule. In order to achieve this, it is only necessary to modify the energy parameter part of the model. Thus, the energy parameter, ϵ , can be expressed as function of the dot product $\hat{\mathbf{u}}_j \cdot \hat{\mathbf{r}}_{ij}$ which effectively characterises the angle between the two vectors shown on Fig. 4.3.

4.3.1 The cubic model

To achieve this we consider, as an initial model, the functional form

$$\epsilon(\hat{\mathbf{r}}_{ij} \cdot \hat{\mathbf{u}}_j) = \epsilon_0 \left[1 + A(\hat{\mathbf{r}}_{ij} \cdot \hat{\mathbf{u}}_j) + B(\hat{\mathbf{r}}_{ij} \cdot \hat{\mathbf{u}}_j)^2 + C(\hat{\mathbf{r}}_{ij} \cdot \hat{\mathbf{u}}_j)^3 \right] \quad (4.11)$$

where A, B and C are real parameters.

A cubic form is an obvious initial choice here as polynomial functions are simply constructed using multiplication and addition only and, above all, are continuously differentiable. This polynomial of degree 3 is also an obvious extension of the polynomial of degree 2 used in Antypov's rod-sphere potential although it does, in principle, introduce two extra degree of freedom when tuning the model. The physical significance of the 3 parameters A, B and C is not readily seen from this basic expression. Instead, we seek to characterise the model using simple criteria directly related to the amphiphilic properties of the molecules.

To this end, we impose that:

- $\kappa' < 1$
- $\epsilon(\hat{\mathbf{r}}_{ij} \cdot \hat{\mathbf{u}}_j = -1) = \epsilon_0 \kappa'$ (hydrophobic tail, less attractive to water)
- $\epsilon(\hat{\mathbf{r}}_{ij} \cdot \hat{\mathbf{u}}_j = +1) = \epsilon_0 / \kappa'$ (hydrophilic head, more attractive to water)

On imposing these conditions on Eqn. 4.11, it is straightforward to show that

$$A = -C + \frac{1}{2\epsilon_0} \left(\kappa' - \frac{1}{\kappa'} \right) \quad (4.12)$$

$$B = -\epsilon_0 + \frac{\kappa'}{2} + \frac{1}{2\kappa'} \quad (4.13)$$

where κ' is a parameter controlling the anisotropy of the interaction. The parameter C is then a free parameter controlling the degree of inflection of the potential curve (see Fig. 4.7(b)).

However, it can be clearly seen from Fig. 4.7(b) that, as C is increased, the potential becomes non-monotonic which would result in un-physical effects such as the end of the hydrophobic tail being more attractive than the middle of the rod. In order to resolve this problem, a further constraint of zero gradient is imposed at $\hat{\mathbf{r}}_{ij} \cdot \hat{\mathbf{u}}_j = -1$, i.e. $\frac{d\epsilon}{d(\hat{\mathbf{r}}_{ij} \cdot \hat{\mathbf{u}}_j)} = 0$. For small to moderate κ' , this point then corresponds to a maximum which, together with the condition $\epsilon(\hat{\mathbf{r}}_{ij} \cdot \hat{\mathbf{u}}_j = +1) = \epsilon_0/\kappa'$, leads to a monotonic function. This then leads to the following relationships:

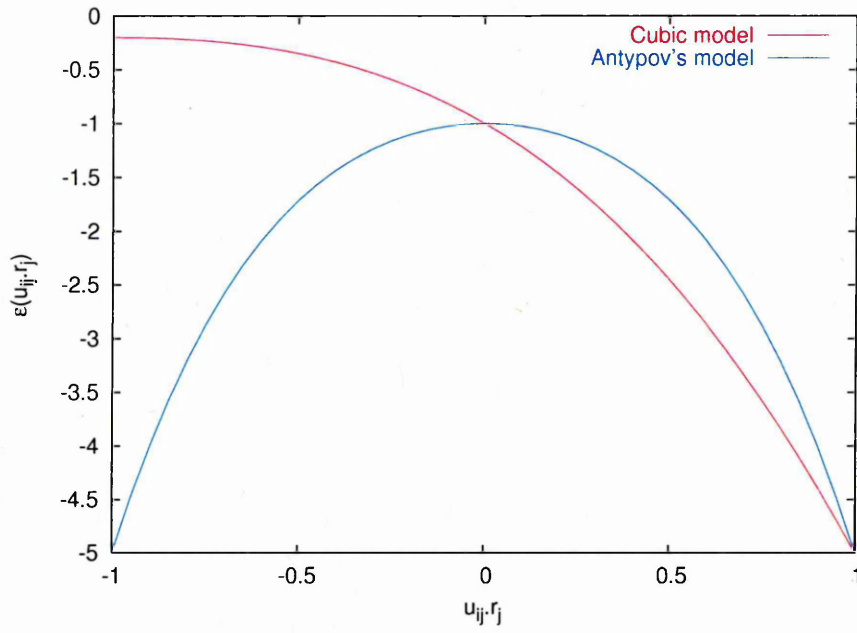
$$A = -\frac{3}{2} \left(\frac{2B}{3} + \frac{1}{2\epsilon_0} \left(\kappa' - \frac{1}{\kappa'} \right) \right) \quad (4.14)$$

$$B = -\epsilon_0 + \frac{\kappa'}{2} + \frac{1}{2\kappa'} \quad (4.15)$$

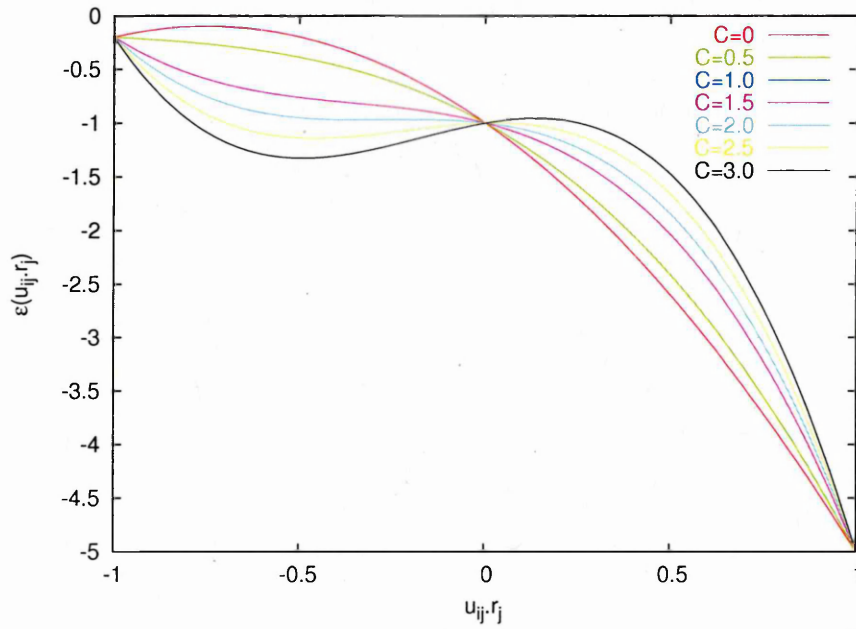
$$C = \frac{2B - A}{3} \quad (4.16)$$

Given this approach, the asymmetric rod-sphere potential becomes fully defined by the parameter κ' alone. Fig. 4.7(a) shows a comparison between Antypov's model and this 'cubic' model for $\kappa' = 1/5$ and $\epsilon_0 = 1$ ($A = 2$, $B = 1.6$, $C = 0.4$). In this figure, one can clearly see the breaking of the symmetry present in the original model developed by Antypov.

However, the zero gradient condition at $\hat{\mathbf{r}}_{ij} \cdot \hat{\mathbf{u}}_j = -1$ could also correspond to a minimum rather than a maximum and this would make the potential non-monotonic. The relevant second derivative $\frac{d^2\epsilon}{d(\hat{\mathbf{r}}_{ij} \cdot \hat{\mathbf{u}}_j)^2}$ shown in Fig. 4.8 indicates that, if $1/\kappa'$ is greater than 7, the second derivative becomes positive and the



(a)



(b)

Fig. 4.7: (a): Comparison between Antypov's model and the cubic model for $\kappa' = 5$ with a constraint on the gradient at $\hat{\mathbf{r}}_{ij} \cdot \hat{\mathbf{u}}_j = -1$ (b): plot of the cubic model for different values of C for $\kappa' = 5$ with no constraint on the gradient at $\hat{\mathbf{r}}_{ij} \cdot \hat{\mathbf{u}}_j = -1$

point $\hat{\mathbf{r}}_{ij} \cdot \hat{\mathbf{u}}_j = -1$ corresponds to a minimum.

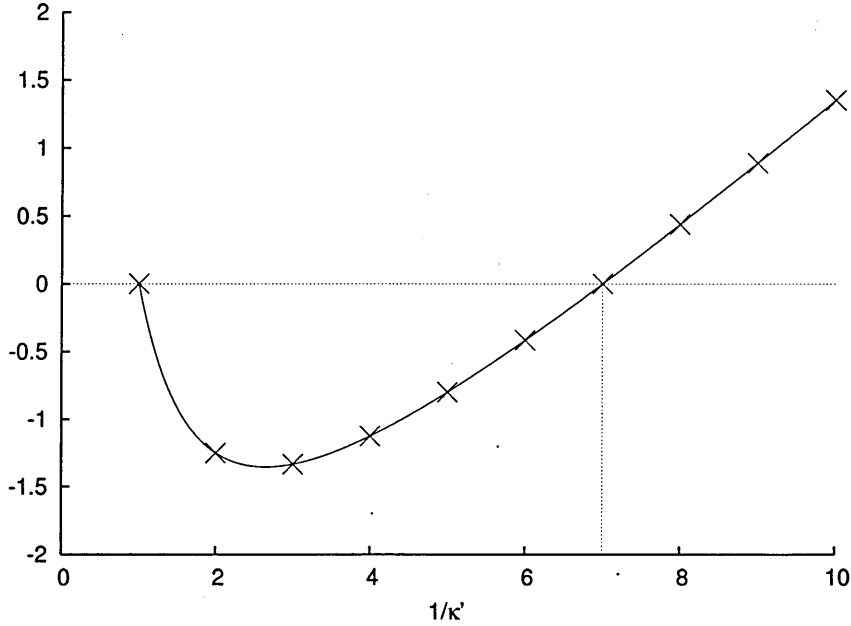


Fig. 4.8: Plot of the second derivative $\frac{d^2\epsilon}{d(\hat{\mathbf{r}}_{ij} \cdot \hat{\mathbf{u}}_j)^2}$ at $\hat{\mathbf{r}}_{ij} \cdot \hat{\mathbf{u}}_j = -1$ as a function of $1/\kappa'$ which becomes positive when $1/\kappa' > 7$

In this model, the sphere-sphere potential representing the solvent-solvent interaction via the Lennard-Jones potential has an interaction strength of $\epsilon_{LJ} = \epsilon_0$. One can then take the hydrophilic region to be the part of the rod where the strength of the rod-potential is greater than that of the sphere-sphere interaction. This allows one to define the HLB (see previous chapter) as the length ratio between the region where $\epsilon < \epsilon_0$ and the region where $\epsilon > \epsilon_0$. For this model, $\epsilon = \epsilon_0$ at $\hat{\mathbf{r}}_{ij} \cdot \hat{\mathbf{u}}_j = 0$ which corresponds to the middle region of the rod and, therefore, given an HLB ratio of 50%

Thus, this 'cubic' model satisfies the initial requirements of an amphiphilic potential between the rods and the spheres: one end of the rod is strongly attracted to spheres whereas the other end has a reduced well-depth (though it is still attractive). However, this initial mathematical form shows some limitations : the parameter $1/\kappa'$ has to be smaller than 7 in order to avoid non-monotonic behaviour and no free parameter is available with which to change the HLB value of

the model. However, in seeking a model capable of modelling generic amphiphilic behaviour, a functional form, where both the amphiphilic strength and the HLB ratio can vary, is preferable.

4.3.2 The exponential model

In order to achieve this, we now consider an exponential form for the mathematical expression of the energy parameter:

$$\epsilon(\hat{\mathbf{r}}_{ij} \cdot \hat{\mathbf{u}}_j) = \epsilon_0 [-A - B \cdot \exp(C \cdot (\hat{\mathbf{r}}_{ij} \cdot \hat{\mathbf{u}}_j))] \quad (4.17)$$

where the coefficients A,B and C are clearly different from those used in the cubic alternative.

Here again (and recalling that $\kappa' < 1$), the two basic initial constraints used earlier for the cubic model are applied:

- $\epsilon(\hat{\mathbf{r}}_{ij} \cdot \hat{\mathbf{u}}_j = -1) = \epsilon_0 \kappa'$ (hydrophobic tail, less attractive to water)
- $\epsilon(\hat{\mathbf{r}}_{ij} \cdot \hat{\mathbf{u}}_j = +1) = \epsilon_0 / \kappa'$ (hydrophilic head, more attractive to water)

Imposing these conditions on Eqn. 4.17, one can readily find that:

$$A = \kappa' + \left(\kappa' - \frac{1}{\kappa'} \right) \left(\frac{e^C}{e^C - e^{-C}} \right) \quad (4.18)$$

$$B = \frac{\left(\frac{1}{\kappa'} - \kappa' \right)}{e^C - e^{-C}} \quad (4.19)$$

The third parameter, C , then controls the sharpness of the decay between the two fixed end points. From this, it is then possible to define a HLB using C to set the

crossover point between the hydrophobic and the hydrophilic parts of the model, defined by the point where the potential curve $\epsilon(\hat{\mathbf{r}}_{ij} \cdot \hat{\mathbf{u}}_j) = \epsilon_0$. A value for the HLB can then be defined as x_0 with $\epsilon(\hat{\mathbf{r}}_{ij} \cdot \hat{\mathbf{u}}_j = x_0) = \epsilon_0$, where $-1 < x_0 < +1$. Rewriting this in terms of conventional HLB language, we then define the model parameter

$$H = 50(1 + x_0) = 50 \cdot \left(1 + \frac{1}{C} \cdot \ln \left(\frac{(1-A)}{B} \right) \right) \quad (4.20)$$

where H can vary from 0 to 100% and corresponds to the relative size of the hydrophobic region compared to the total length of the rod. Note that while Eqn. 4.20 cannot be analytically inverted to give C as a function of H , numerical inversion is always possible. Fig. 4.9 shows plots of C vs. H for different values of $1/\kappa'$.

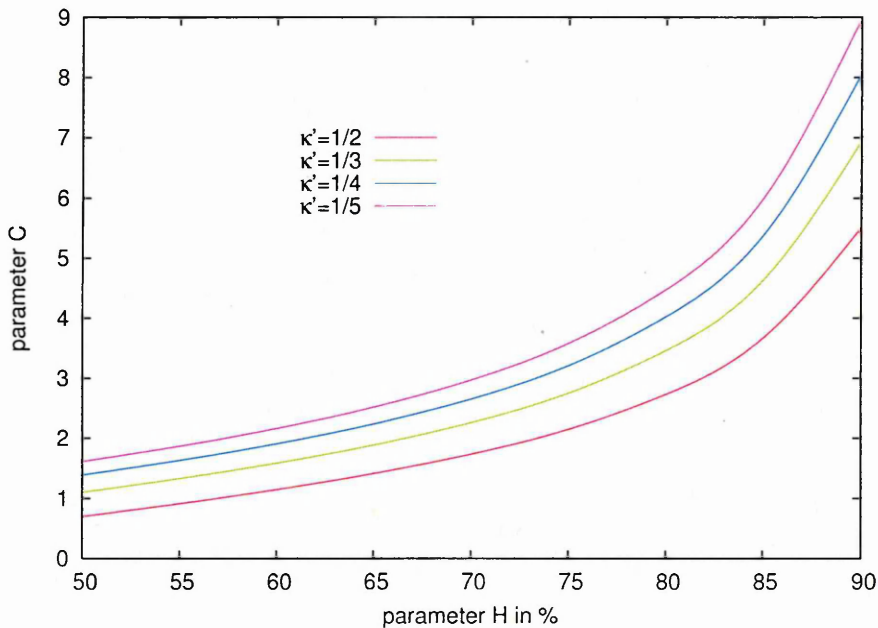


Fig. 4.9: Plot of the parameter C as a function of H for different values of $1/\kappa'$

In this new formulation, then, the well-depth function is controlled by just 2 parameters: the hydrophilic to hydrophobic ratio and the hydrophilic strength, respectively, H and κ' .

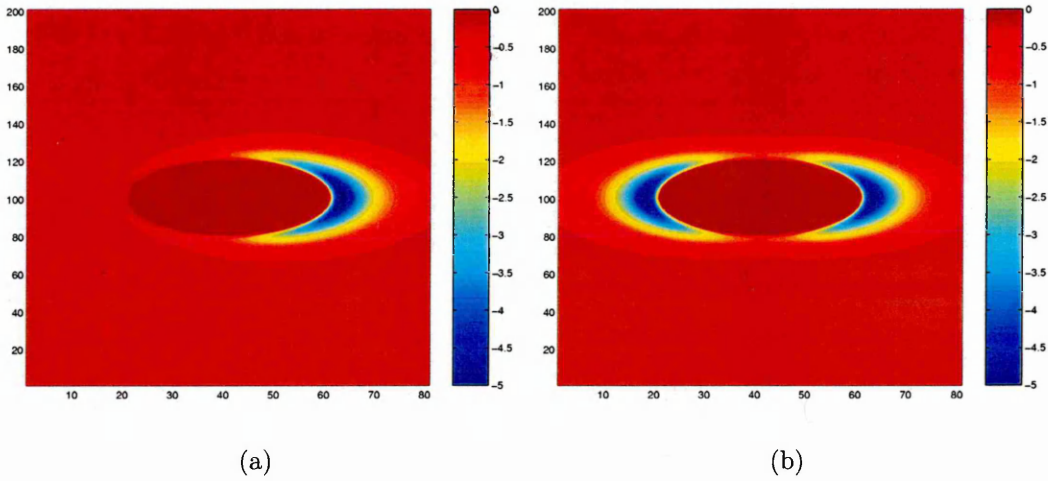


Fig. 4.10: Equipotential contour plot of the two models: (a) Exponential model for $\kappa' = 1/5$ and $H=50$ - (b) Antypov's model for $\kappa' = 1/5$

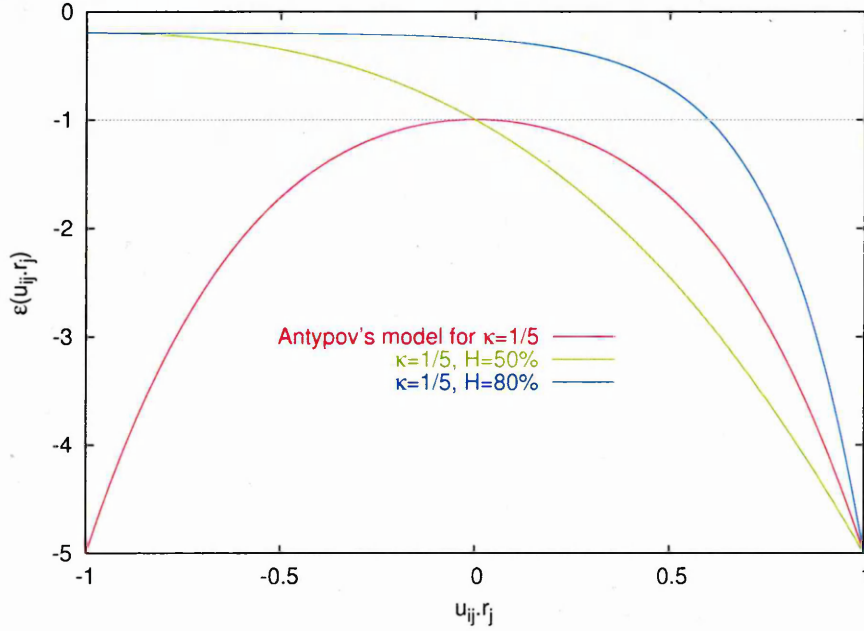


Fig. 4.11: Energy functions for Antypov's rod-sphere interaction and two different parameterisations of the exponential model. The black dotted line corresponds to the constant $\epsilon_0 = -1$

Thus, Fig. 4.10 and 4.11 show comparisons with Antypov's model in the case $\kappa' = 1/5$. In Antypov's model, both ends of the rod are attracted to the spheres (high negative well-depth values at $\epsilon(\hat{\mathbf{r}}_{ij} \cdot \hat{\mathbf{u}}_j = -1)$ and $\epsilon(\hat{\mathbf{r}}_{ij} \cdot \hat{\mathbf{u}}_j = 1)$). In comparison, for the new 'exponential' model only one end of the rod is strongly attractive.

Furthermore, by modifying the H value, it is possible to control the extent of the hydrophobic attractive region.

4.4 Results

In the previous section it was shown that the basic rod-sphere interaction can be modified to give a variable and controllable strength anisotropy and HLB ratio. However, the interaction between rod-like particles, that is, the amphiphile-amphiphile interaction, could also be considered a significant factor when modelling amphiphilic self-assembly. Clearly, this interaction must play a role in determining the ways in which the rods pack together and, therefore, the shapes of the resulting self-assembled aggregates.

In the Gay-Berne potential, it is straightforward to modify the rod-rod interaction so that the side-side arrangement is favoured over the end-end configuration or vice-versa. However, in this study, we have elected to focus on the amphiphile solvent interaction. Thus the parametrization $l/d = 3.0$, $\epsilon_{ss}/\epsilon_{ee} = 1.0$, $\mu = 1.0$ and $\nu = 1.0$ is adopted, so that there is no orientational dependance in the well-depth of the rod-rod interaction. This assumption is obviously not physical in the sense that, in real amphiphilic molecules, the head group does not interact in the same way with another head group as it does with an hydrophobic tail. However, the aim of this study is to find the minimum requirements, in terms of modelling, needed to achieve amphiphilic behaviour. To this end, we ignore the orientation dependance of the rod-rod interaction on the grounds that it may play only a secondary role in self-assembly processes. Indeed, investigation of the validity of this assumption is central to the work presented in this thesis.

The sphere-sphere Lennard-Jones potential used to represent the solvent-solvent interactions remains the same as that used in the previous section and will not be changed through the remainder of this thesis.

4.4.1 Effect of concentration on phase behaviour

In order to examine the amphiphilic properties of the ‘exponential’ model, a systematic series of exploratory simulations has been performed to investigate the concentration dependence of the $H = 80\%$ and $1/\kappa' = 5$ system (denoted ‘H80K5’). These simulations were all performed in the constant NVT ensemble using the standard MD algorithm described in the previous chapter. Except where stated otherwise, the total number of particles in the system was kept at $N = 1024$ while the numbers of rods and spheres were adjusted so as to provide each desired concentration. In order to judge the ability of this model to recover genuinely global amphiphilic behaviour, the different concentration systems were quenched from random isotropic configurations previously equilibrated at high temperature. In doing this, care was taken to compensate for the differing volumes of the different particle shapes. Specifically, this was achieved by running all systems at approximately the same volume fraction.

Considering the rod as a linear chain of spheres the volume of a rod can be approximated by

$$V_{rod} \approx \frac{\Pi}{6} \kappa \sigma_0^3 = \kappa \cdot V_{sph} \quad (4.21)$$

Therefore, taking $\kappa = 3$, the total volume of particles in the system is:

$$V_{occ} \approx N_{sph} \cdot V_{sph} + N_{rod} \cdot 3V_{sph} = V_{sph} \cdot (N_{sph} + 3N_{rod}) = V_{sph} \cdot (N_{total} + 2N_{rod}) \quad (4.22)$$

Thus, the volume fraction can be expressed as:

$$V_f = \frac{V_{occ}}{V_{total}} \approx \frac{V_{sph} \cdot (N_{total} + 2N_{rod})}{V_{total}} = V_{sph} \cdot (\rho + 2C_{rod}) \quad (4.23)$$

Therefore, for each concentration, the box density was adjusted so as to achieve a volume fraction of 0.44 which, at moderate temperatures, corresponds to a liquid phase for Lennard-Jones particles.

The initial configuration for each concentration was prepared by taking an isotropic configuration of 100% rods and substituting a proportion of these rods by spheres in order to obtain the required concentration ratio. Each of these configurations was then initially equilibrated to the required volume fraction at $T = 2.0$ in the constant NVT ensemble before quenching to lower temperatures in order to generate amphiphilic phases.

5% rod system

At 5% (by number), in this small system size, the rods aggregated into a single roughly spherical object (see Fig. 4.12). In the equilibrated structure, the green tails, representing the hydrophobic regions, are agglomerated together while the red heads, representing the hydrophilic head groups, are in contact with the spheres (solvent molecules). This structure, therefore, has the form expected for a micelle-like object.

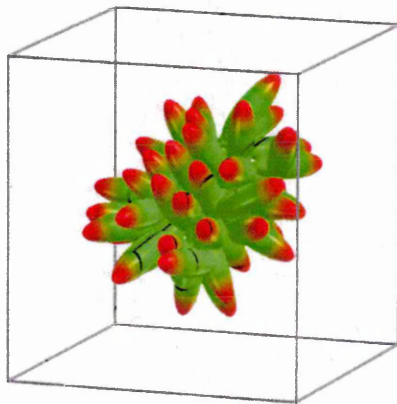


Fig. 4.12: spherical self-assembled agglomerate found at 5% rod at $T = 0.7$ - For clarity the solvent spheres are not represented

The sequence of configuration snapshots shown in Fig. 4.13 illustrates the dynamics of the self-assembly exhibited by this system. From this, one can see that a rapid initial clustering takes place during the opening $0.2 \cdot 10^6$ MD steps. Subsequently, these clusters persist and unite to give a pair of aggregates ($t = 0.4 \cdot 10^6$ MD steps). Eventually, these two objects fuse and form a single aggregate ($t = 1.0 \cdot 10^6$ MD steps). This roughly spherical aggregate then persists for the remaining $1.0 \cdot 10^6$ MD steps.

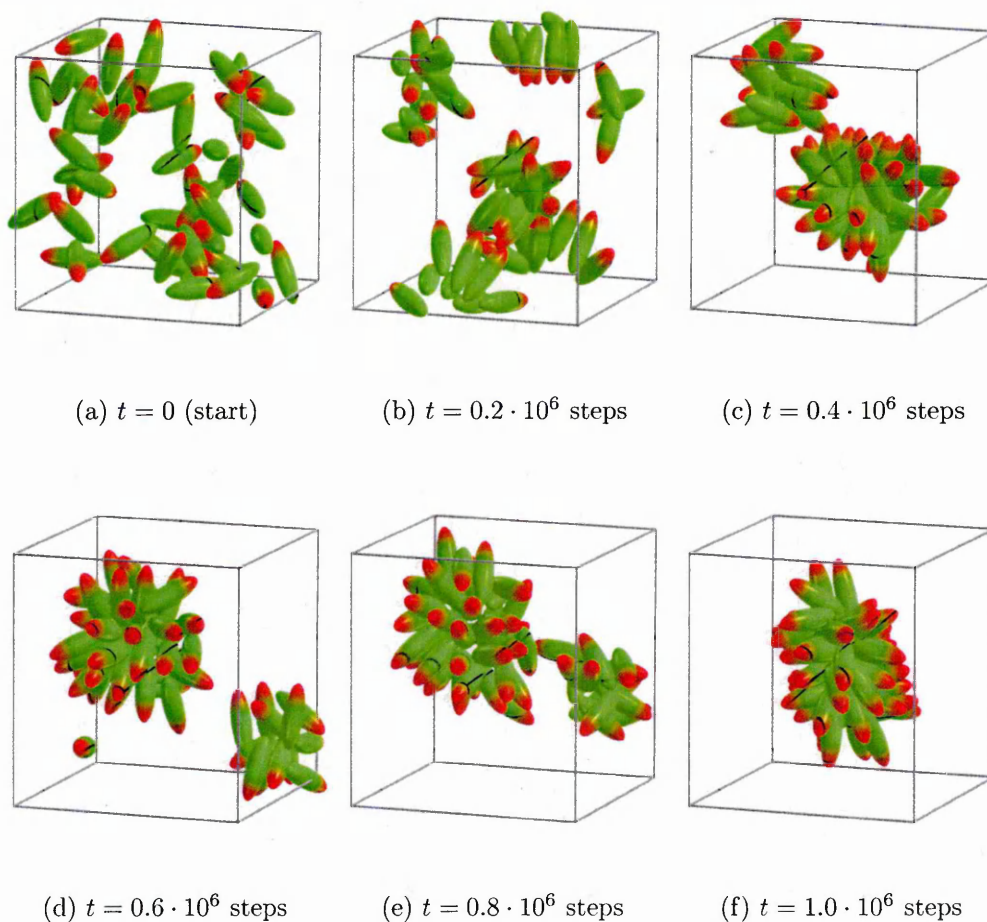


Fig. 4.13: Configuration snapshot sequence for 5% rod system at $T = 0.7$

The evolution of the number of particles involved in the aggregate, plotted on Fig. 4.14, clearly shows a two-stage process where the main aggregate rapidly forms after only $50 \cdot 10^3$ steps and remains unchanged for about $150 \cdot 10^3$ steps at

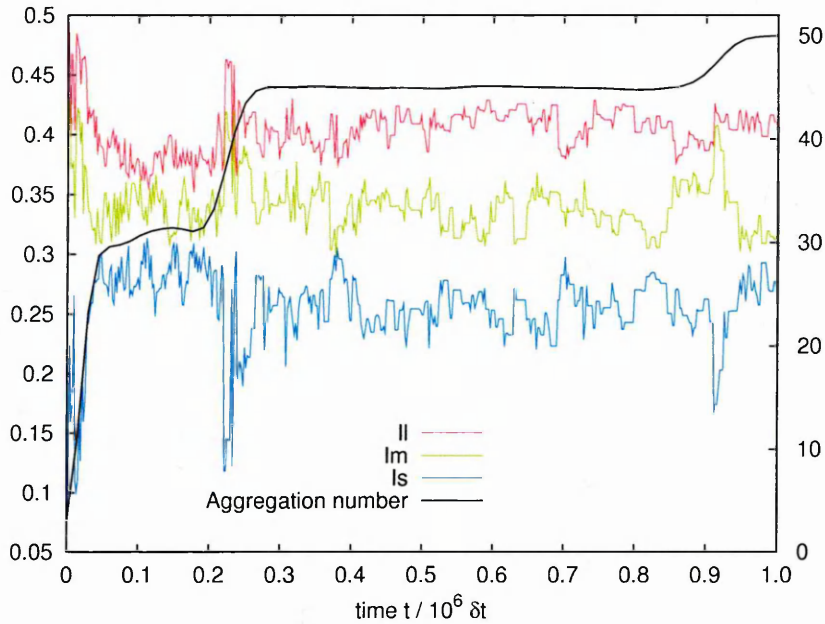


Fig. 4.14: Evolution of the principal moments of Inertia and size of the main aggregate in the 5% system at $T = 0.7$

which point it coalesces with the other smaller aggregates almost simultaneously over a short period (about $10 \cdot 10^3$ steps). It is interesting to compare this plot with that for the principal moments of inertia of the main aggregate. One can observe that the aggregate formed before $0.2 \cdot 10^6$ steps is nearly spherical as its moments of inertia are close to each other. Furthermore, when the other aggregates first join the main one, these data indicate a cylindrical shape ($I_L \approx I_M \gg I_S$) which rapidly adjusts into near-spherical again. Note that the time required for the aggregate to return to a spherical shape is about the same as that of the initial self-assembly from the isotropic configuration.

Fig.4.15 shows the radial distribution functions (RDF) for the sphere-sphere and the rod-rod species calculated over the second 10^6 time steps of this run. These plots suggest that both the spheres and the rods are in their liquid state as their RDFs are characteristic of a liquid. Furthermore, there is steady monotonic decrease in the rod-rod radial distribution function $g_{rr}(r)$ at large separations, which is indicative of macrophase separation between the two components. This is con-

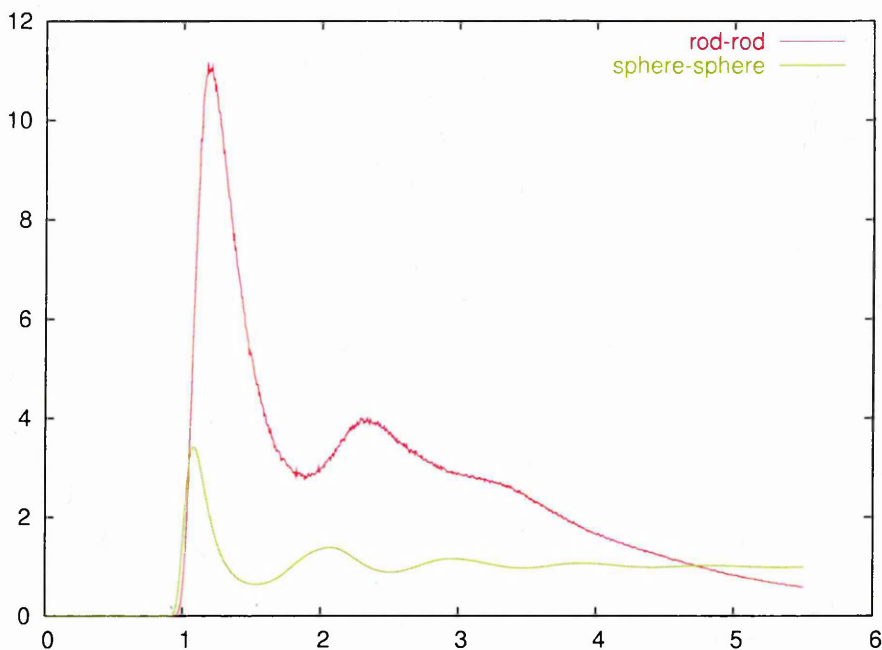


Fig. 4.15: Sphere-sphere and rod-rod radial distribution functions of the 5% rod system at $T = 0.7$ averaged over 10^6 steps after equilibration of 10^6 steps

sistent with the aggregation of the rods into a single cluster as observed from the configuration snapshots. This can be explained by the fact that only a single micelle formed here, and, emphasises that, this arrangement is indistinguishable from that of a completely phase separated system (recall, *e.g.* Fig. 4.6).

Due to the small system size used here, it is not possible to establish, from this simulation, whether this result corresponds to a genuine micellar phase or if the system has simply undergone bulk phase separation as seen with other mixtures of hard rods and spheres [185, 187]. Also, the structure of this aggregate and the associated self-assembly dynamics might have been affected by the influence of the periodic boundary conditions.

In order to address this question, a larger system was required to allow the longer length-scale properties of this system to be probed. To this end, a system of 8192 particles (containing 410 rods corresponding to a 5% system) was created by replicating eight images of the initial configuration of the 1024 particle system.

The 8192 particle system was then run for $1 \cdot 10^6$ MD steps, all of the simulation parameters such as the time step, cutoff radius, neighbour list radius, etc., being set to those used in the previous simulation. A configuration file was dumped every 1000 steps for post-simulation analysis. This run took approximately 15 days to run on a single node of a 2.8 GHz Opteron processor.

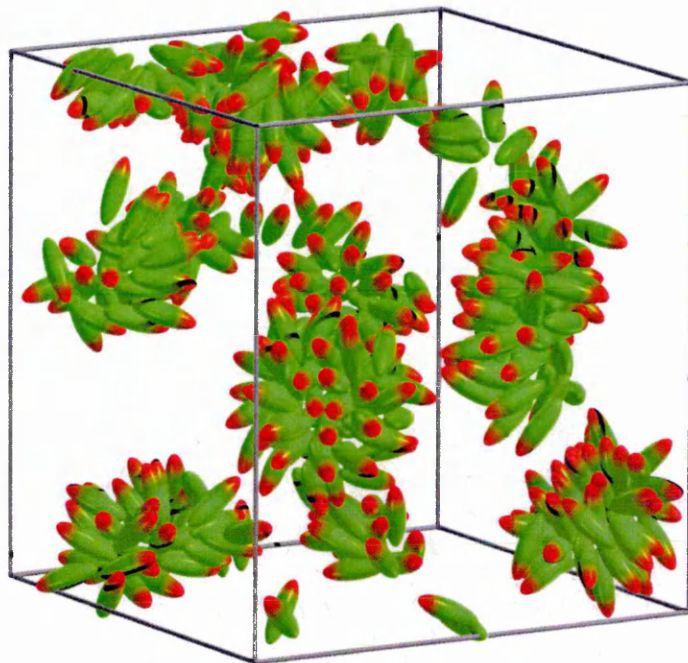


Fig. 4.16: Configuration snapshot after 10^6 MD steps with $N = 8192$ for 5% rod concentration at $T = 0.7$

Fig. 4.16 shows a configuration snapshot of the resultant structure suggesting a multi-micellar arrangement after $1 \cdot 10^6$ steps at $T = 0.7$. From this, one can see a number of aggregates, all of which, have roughly the same size and shape and a similar arrangement of the amphiphiles.

To enable a more rigorous analysis of this system, a cluster counting algorithm was developed. In such an algorithm, when distinguishing between a non-aggregated particle and a particle belonging to a cluster, it is common for a simple cutoff distance between particles to be used as the criterion. For the amphiphilic systems

considered here, however, the distance between the particle centres of mass proved poor at differentiating between monomers and aggregated particles. Rather, the distance between the ‘hydrophobic ends’ (green ends) of the rod particles was found to be a more robust indicator. These sites form a dense cloud of points in the core of each micelle, which can be identified using relatively small cutoff distances. Reducing the cutoff distance is useful since it helps avoid counting nearby monomers (or particles from another micelle) as being part of a given cluster.

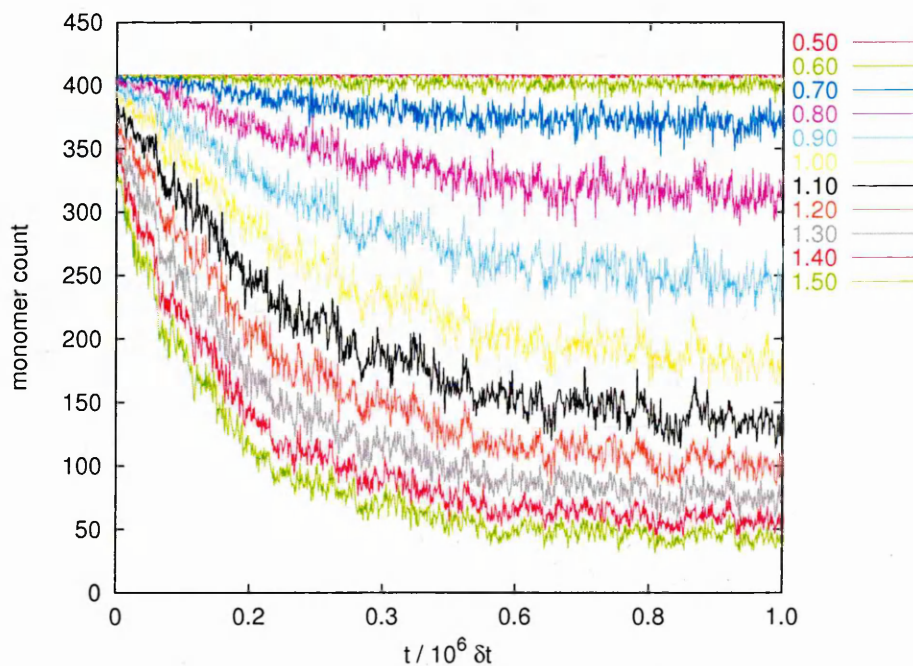


Fig. 4.17: Evolution of the number of monomers with time for a range of cluster cut-off distance r_c

To check the equilibration of the 8192 particle system, the number of monomers in the system was monitored in time with this cluster counting algorithm (see Fig. 4.17). From this analysis, one can observe that, for a range of cutoff values, the monomer number attained a non-zero steady state value, after about $0.6 \cdot 10^6$ time steps, the early stage of the run being characterised by a rapid initial clustering of the particles. Following the initial self-assembly process of $0.6 \cdot 10^6$ steps, a number of clusters had formed in equilibrium with these monomers. From the cluster-

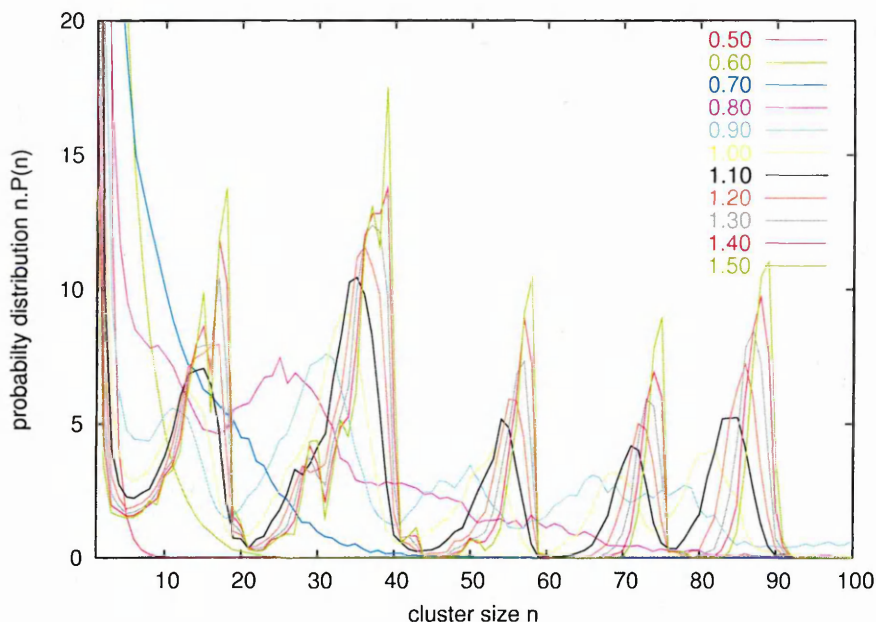


Fig. 4.18: Probability distribution $n \cdot P(n)$ vs. cluster size n for the 8912 particle system at 5% rod concentration and $T = 0.7$ averaged over $0.6 \cdot 10^6 \delta t < t < 1.0 \cdot 10^6 \delta t$ for a number of cutoff distances r_c

counting algorithm, a probability size distribution function $P(n)$, where n is the cluster size, can be calculated for different cutoff distances. These distributions functions $n \cdot P(n)$ shown in Fig. 4.18, averaged over all configurations for $0.6 \cdot 10^6 < t < 1.0 \cdot 10^6$, appear to be very sensitive to the cutoff distance r_c . Thus, as r_c becomes larger (i.e. $\geq 1.20\sigma_0$), the algorithm starts identifying two separate aggregates as a single cluster, resulting in a noisier distribution function with some sharp peaks at large n . On the other hand, if the cutoff distance is kept too small, no or very few clusters are identified, and the distribution function just shows a monotonic decay. At the intermediate cutoff values ($r_c = 0.90\sigma_0$), smoother distribution functions can be found where a high monomer peak is followed by a broad second peak centered on the aggregate preferred size or mean aggregation number (of ~ 25 in this system). The minimum appearing in between these favorable n values demonstrates that particles are less likely to reside in clusters of intermediate sizes (i.e. sub-micellar aggregates) than as monomers or in 25-member micelles (as confirmed by the configuration snapshot Fig. 4.16). The long

tail that we can observe in the $n \cdot P(n)$ data for $n > 40$ arises due to the occasional appearance of large assemblies. This is likely due to micelle fusion followed by fission, leading to large but short-lived aggregates.

Aggregate moment of inertia data, averaged over the same time window, give information about the shapes of the aggregates present in the system as a function of their size. From the cluster-counting algorithm, it was possible to calculate the inertia tensors for all clusters of size $n > 1$ (i.e. not counting monomers) and average them over time and cluster size.

Fig. 4.19 shows the 3 principal moments of inertia averaged over time as a function of the cluster size. By correlation of this plot with the micelle size distribution function (Fig. 4.18), it can be seen that at the mean aggregation number, the micelles are at their most spherical (I_L , I_M and I_S are at their closest to $\frac{1}{3}$). At larger n , these data become rather noisier, due to the worsening statistics, but they tend increasingly to those expected for cylindrical micelle shape, again consistent with these larger assemblies being related to fusion and fission events.

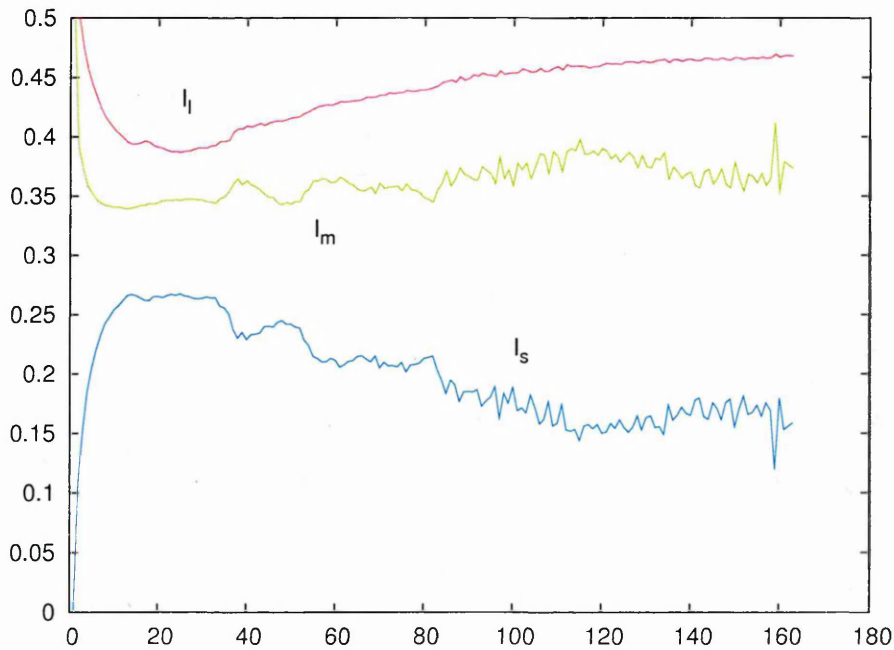


Fig. 4.19: Principal moments of inertia as a function of aggregate size for 8192 particle 5% system at $T = 0.7$, based on an r_c value of $0.9\sigma_0$

10% rod concentration system

At a rod concentration of 10%, the 1024 particle system developed to form a single aggregate which distorted and eventually fused with its periodic image (through the PBCs) to form a rod-shaped or tubular aggregate that stretched across the simulation box (see Fig. 4.20(a)).

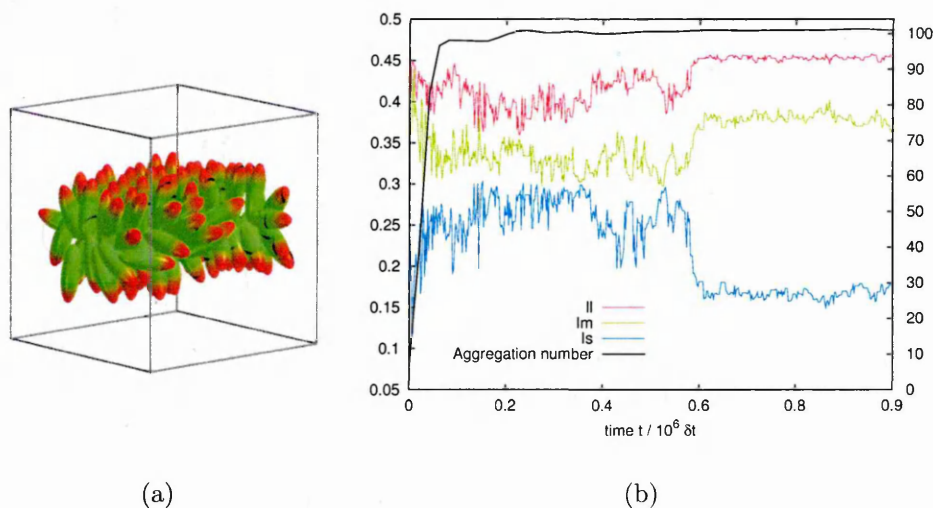


Fig. 4.20: (a): Final configuration snapshot of a 10% rod system at $T = 0.7$ showing a 'tubular' micelle (b): Evolution of the principal moments of inertia and size of the main aggregate in the 10% system at $T = 0.7$

The evolution of the size of the main aggregate (see Fig. 4.20(b)) shows again a rapid initial clustering that took place in about $50 \cdot 10^3 \delta t$ as for the 5% system. However, this self-assembly process took place in only one stage, presumably due to the higher concentration of rods. Also, the moment of inertia data indicate that the aggregate was only slightly cylindrical before it fused with its own image through the PBC at $0.6 \cdot 10^6 \delta t$. The aggregate then clearly changed its shape to this tubular 'micelle'.

Furthermore, the fact that the system remained stable for nearly $0.5 \cdot 10^6 \delta t$, before being 'trapped' by the PBC, indicates that the system size is probably an issue here. Thus, it is difficult to state categorically whether this particular concentration

corresponds to a cylindrical micelle or if a ‘worm’ can really be obtained with this model parameterisation. Clearly, more study should be performed on this system to answer this question.

The configuration snapshot in Fig. 4.20(a) shows that the aggregate was not quite circular about its long axes. Rather, the cross-section of this cylinder corresponds to a small bilayer patch with cap-ends, which suggests that a bilayer might form with increasing concentration.

20% to 40% rod system

Increasing the rod concentration to 20%, and again starting from a random initial configuration, the system freely self-assembled into a lamellar bilayer structure.

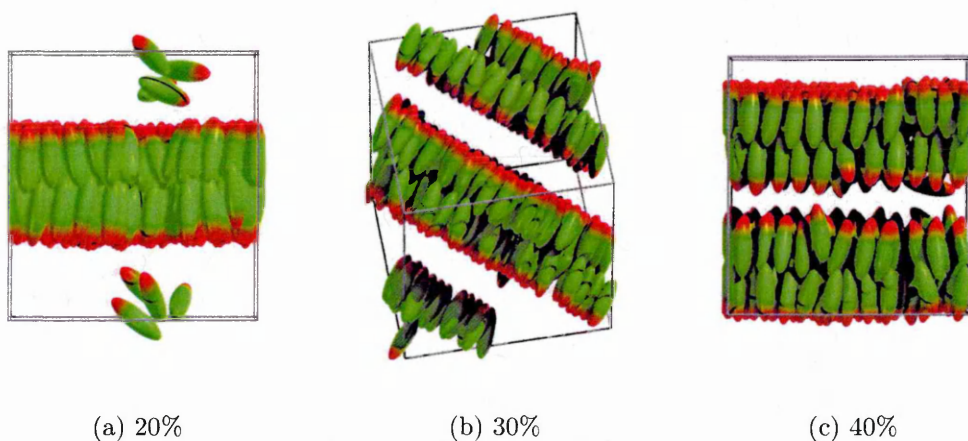


Fig. 4.21: Final configuration snapshots for different rod concentration at $T = 0.7$

As can be seen from Fig. 4.21(a), this increase in the rod concentration resulted in the formation of a bilayer-like structure from an initial random configuration. For this system size, this lamellar phase was found to persist up to 40% concentration. At 20%, a single bilayer was formed and stabilised by the periodic boundary conditions. In this system, a few amphiphiles remained out of the bilayer, aggregating together in the solvent (possibly trying to form a micelle). At 30% and 40%, two bilayers were formed. However, the inter-bilayer distance changed from

approximately 3 layers of spheres to only 2 layers of spheres with this increase in rod concentration.

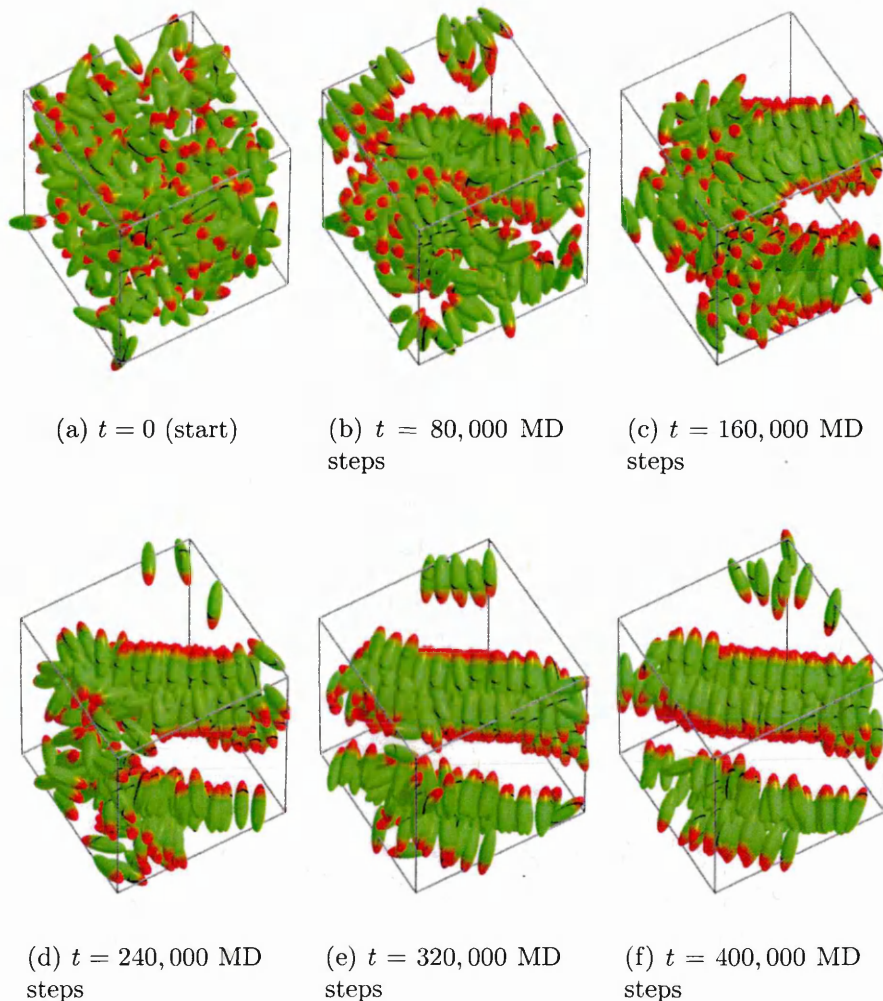


Fig. 4.22: Evolution of the 30% system in time

The self-assembly process of this lamellar phase was also found to be in qualitative agreement with the free energy pathway described by Marrink *et al.* (see Chapter 2). As can be seen from the series of configuration snapshots shown in Fig. 4.22, the formation of the bilayer by the initially homogeneous 30% system involved a rapid aggregation into micelle-like objects which then readily fused into a bilayer. Finally the development of this defect-free bilayer proved to be a much slower process, consistent with the slow free energy variation in time identified by Marrink

for this process (see chapter 2).

Fig. 4.23, which shows the evolution of the total potential energy of the 30% system, also illustrates the different stages of development involved in this lamellar phase formation. The initial stage corresponds to a rapid aggregation of the free amphiphiles (see configuration snapshot in Fig. 4.22(a)) into randomly shaped aggregates (see configuration snapshot in Fig. 4.22(b)). These aggregates, then, slowly arrange themselves before the bilayer forms through the PBC, leading to a steep section in the potential energy time line at around $0.2 \cdot 10^6$ steps. Finally, a slow re-arrangement process takes place in which the bilayer frees itself of various defects, but the system potential energy remains virtually unchanged. After $0.4 \cdot 10^6$ steps the lamellae are equilibrated and the potential energy remains constant at a steady state value of about $-8.7\epsilon_0$ per particle.

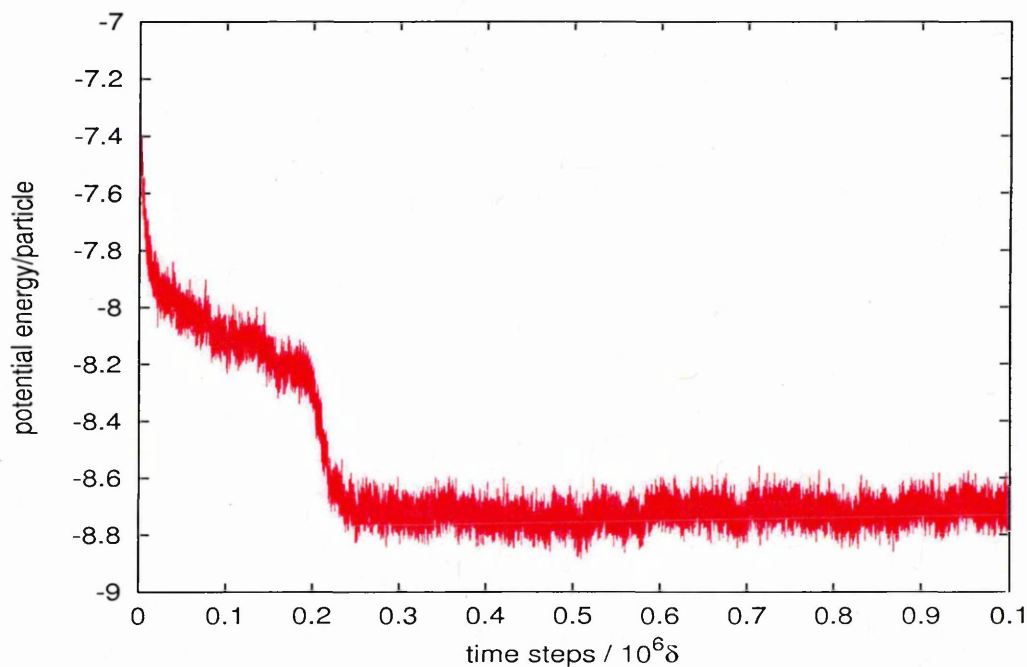


Fig. 4.23: Potential energy of the 30% system versus time steps

The evolution of the bilayer size, shown in Fig. 4.24, for the 30% system indicates a longer time of initial self-assembly of about $1.0 \cdot 10^5$ (twice as long as for the lower concentration systems). Also, the moment of inertia data indicate a 'flat' shape

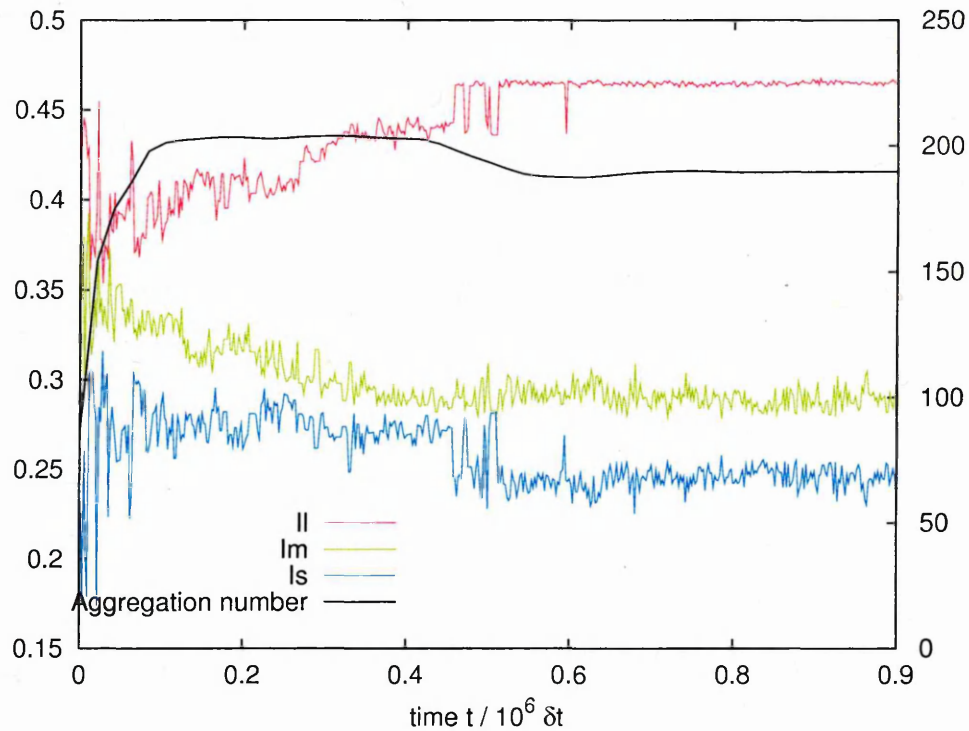


Fig. 4.24: Evolution of the principal moments of Inertia and size of the main aggregate in the 30% system at $T = 0.7$

indicative of a flat bilayer as confirmed by the configuration snapshots. Note the sharp change in the aggregate shape at about $0.5 \cdot 10^6$ step, probably indicative of the bilayer merging through the PBC with its own image as the configuration snapshots also suggest. The associated decrease in the number of particles is probably due to a rearrangement of the particles between the two bilayers present in the simulation box.

Fig 4.25 shows the rod-rod parallel distribution function $g_{//}(r)$ for different concentrations and temperatures. This illustrates the variation of $g_{//}(r)$ with temperature for the 30% rod concentration system. These plots clearly indicate a layered structure with a spacing of around $5\sigma_0$ which becomes increasingly diffuse with increasing temperature.

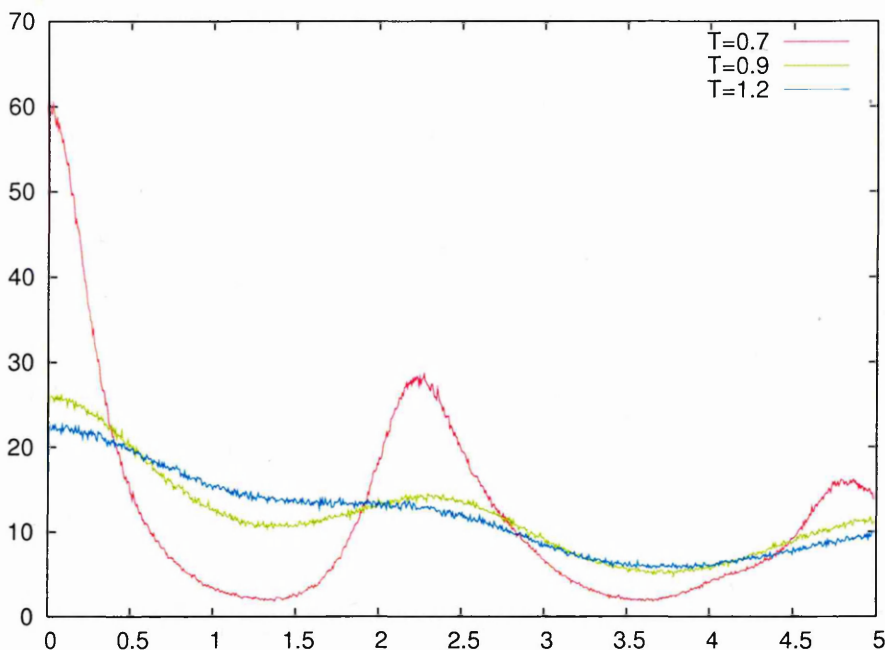
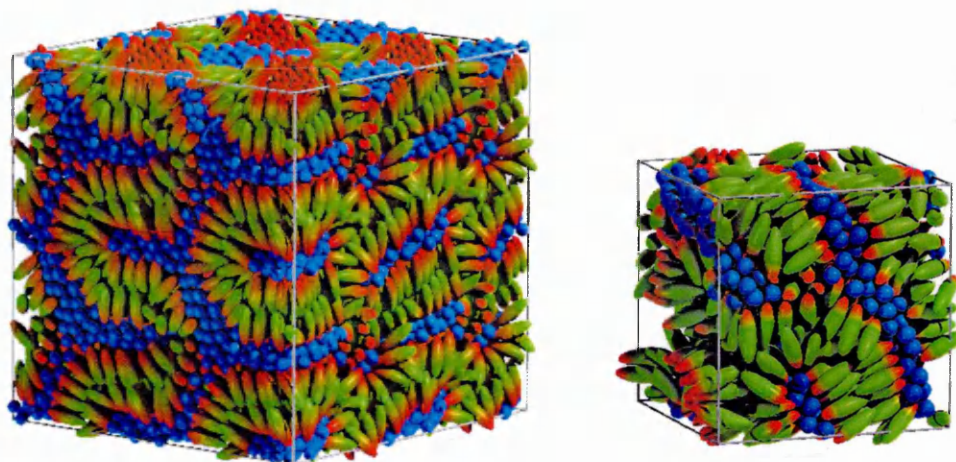


Fig. 4.25: Rod-rod parallel distribution function, $g_{//}(r)$ for different temperature at 30% rod concentration

50% and 60% rod system

At 50 – 60% rods, the bilayer structure still persists locally, but develops larger length-scale curvature. Furthermore, the structures formed are bi-continuous. However, on repeating runs with different initial configurations, no ‘global’ structure could be formed reproducibly at these concentrations for this system size and ensemble. Fig. 4.26(a) shows an example of one of the structures adopted by a 50% rod system. We show eight replicated periodic images of this configuration here to illustrate the range and complexity of the curved bilayer network formed by this system. Generally, at these concentrations, these systems appear to seek to maximise their bilayer interfacial area because the rod-sphere interaction is sufficiently strong to dominate at low temperature, leading to fingering of the water domain. The 60% rod system also consists of very curvy bilayers though the solvent-sphere phase continues to percolate.



(a) 50% - represented with boundary conditions

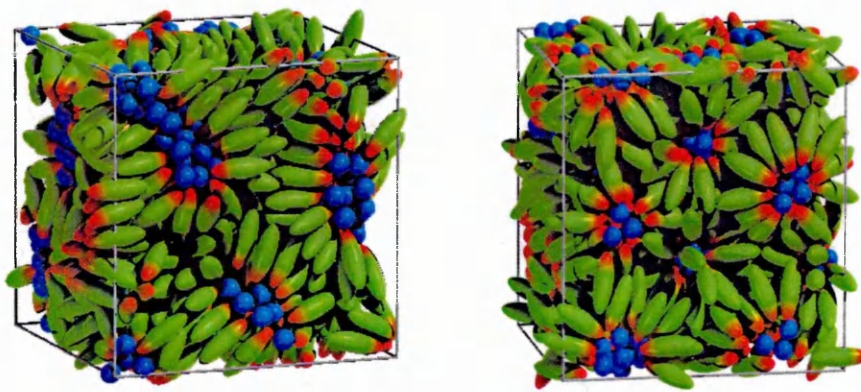
(b) 60%

Fig. 4.26: Configuration snapshots of two systems forming curved lamellar phases

70% to 90% rod concentration systems

At 70%, the solvent domains appeared, from configuration snapshots, to cease to be continuous, shrinking to form solvent droplets surrounded by amphiphilic rods. Fig. 4.27 shows the final configuration snapshots for the 70% and 80% systems at $T = 0.7$. To explore the structural changes associated with this concentration increase, a cluster analysis on the spheres was performed for 70, 80 and 90% as shown on Fig. 4.28. These plots clearly illustrate the formation of stable sphere clusters for all three systems. However, for 70%, the number of cluster in the system is close to unity suggesting that the spheres could, in fact just percolate at this concentration. This is confirmed by the associated probability distribution function, which indicates a single cluster of about 300 sphere, confirms the bi-continuous state of this system. The probability distributions for 80% and 90%, in contrast, indicate isolated droplets with average cluster sizes of 15 and 5, respectively.

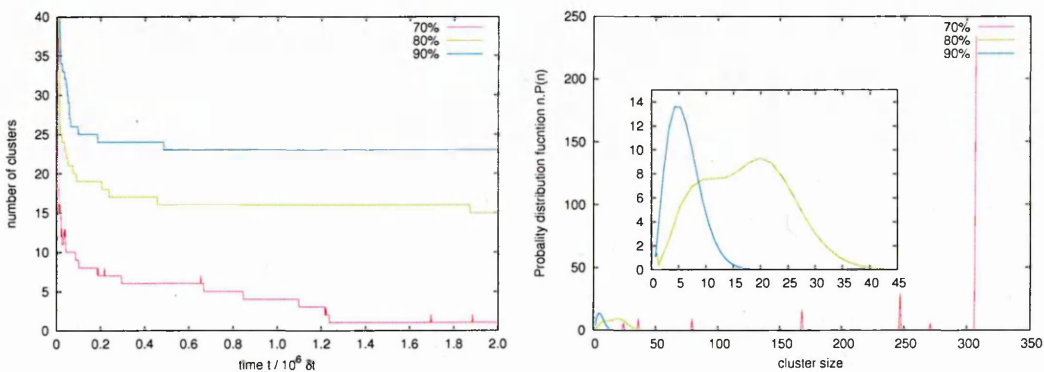
Thus, with increasing the concentration above 70%, the structures formed by these systems cease to be bi-continuous and inverse phases are formed. This behaviour



(a) 70% rod system, inverse cylindrical micelle

(b) 80% rod system, inverse spherical micelle

Fig. 4.27: configuration snapshots of amphiphilic inverse phases



(a) Evolution of the total number of clusters in the system

(b) Distribution probability $n.P(n)$ averaged over time from $1.0 \cdot 10^6 \delta t$ to $2.0 \cdot 10^6 \delta t$ at $T = 0.7$

Fig. 4.28: Cluster analysis on the spheres with $r_c = 1.3\sigma_0$ at $T = 0.7$

is, therefore, characterised by water droplets encapsulated within an amphiphile solution (the opposite of a normal micellar phase where surfactant droplets form in water). Thus the water fingers present in the 60% system have closed up to form inverse micelles.

Fig. 4.29 shows the sphere-sphere radial distribution function of the 80% rod system for 3 different temperatures $T = 0.7$, $T = 0.9$ and $T = 1.2$. These plots

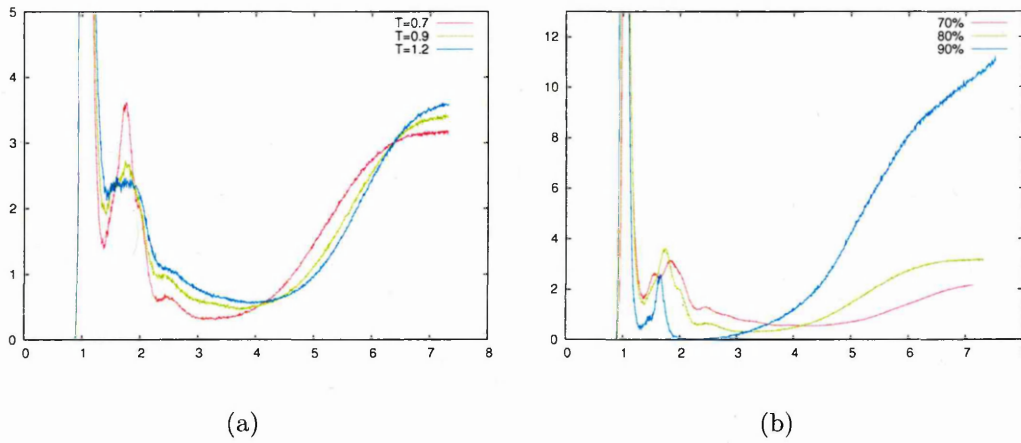


Fig. 4.29: (a): sphere-sphere radial distribution function, $g_{ss}(r)$, for 3 different temperatures for the 80% rod system - (b): $g_{ss}(r)$ for 70%, 80% and 90% rod concentration at $T = 0.7$

clearly indicate a peak at $7\sigma_0$. Also, the prohibited region at distances of around $3 - 4\sigma_0$ suggests both a clustering of the spheres and the possible formation of a regular array of these clusters. With increasing temperature, the mid-range peak is shifted to larger distances and becomes broader, suggesting relaxation of the structure. Also, at $T = 1.2$, an increased value of the sphere-sphere distribution function at around separation of $3 - 4\sigma$ indicates a higher incidence of spheres outside the main clusters, and, then, melting of the structure.

Evolution of amphiphilic structure with concentration

It is also interesting to observe the change in the RDFs with concentration in order to understand the structural changes that occur as the rod concentration is increased. Fig. 4.30 shows the variation of the sphere-sphere and rod-rod RDFs for the full range of concentrations studied at $T = 0.7$.

Although the $g_{ss}(r)$ does not show much structure, one can clearly see the gradual development of inverse phases as the peak at about $7\sigma_0$ grows continuously with increasing concentration. Note also the unliquid-like behaviour of the solvent

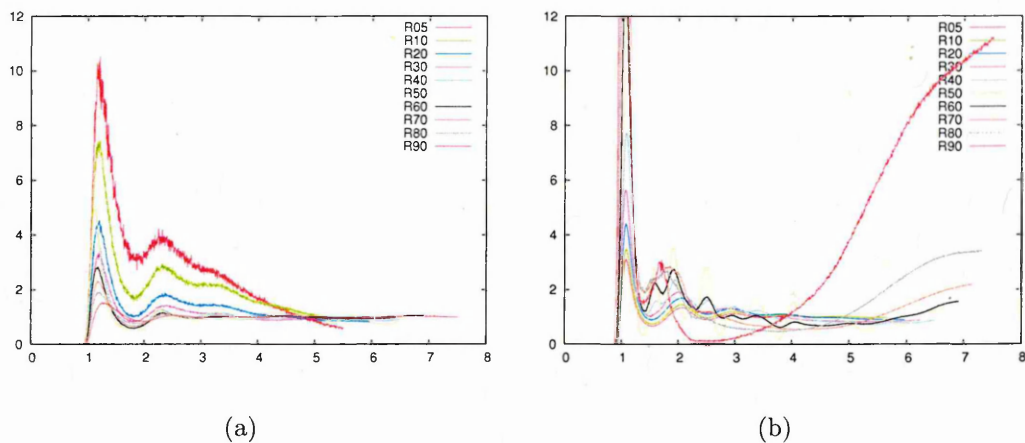


Fig. 4.30: (a) Rod-rod radial distribution function, $g_{rr}(r)$, and (b) sphere-sphere radial distribution function, $g_{ss}(r)$, as a function of the rod concentration at $T = 0.7$

spheres between 40 and 60%. This is probably due to a combination of a relatively low temperature and the fact that only 2 layers of spheres were present between the rod layers of these lamellar phases, leading to capillary-induced stratification or crystallisation.

In order to investigate the structural changes associated within the amphiphilic aggregates, the parallel component of the rod-rod RDF has been computed and is shown in Fig. 4.31.

At low concentrations (i.e. below 20%), $g_{//}(r)$ indicates a relatively flat distribution for all separation distances. Above 20%, a peak starts to appear at around $2.5\sigma_0$ indicative of a layering of the rods : a lamellar phase has formed. At 60%, the layering of the rods starts to disappear when the system starts to develop inverse phases. From 70%, the peaks become more diffuse and eventually disappear. Again a flat distribution is observed indicating that the layers formed at medium concentration have vanished being replaced by inverse phases.

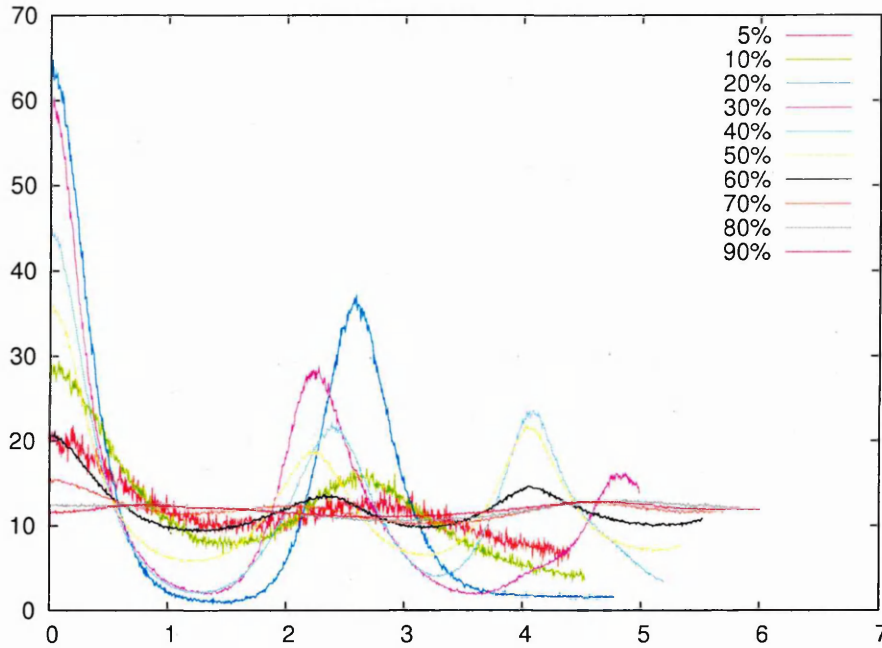


Fig. 4.31: Evolution of the parallel rod-rod distribution function, $g_{//}(r)$, with rod concentration

4.4.2 Effect of molecular parameters

In this section, we briefly survey the effect of the model parameters κ' and H on the system phase behaviour. The aim here is to determine the sensitivity of the model to changes in the interaction parameters.

Effect of κ' , the amphiphilic strength

The effect of the parameter κ' which controls the strength of the anisotropy of the rod-sphere interaction, i.e. the hydration strength, has been investigated with this model. To this end, a series of simulations has been performed on an $N = 1024$ 10% rod system at constant temperature ($T = 0.7$) with the HLB set to $H = 50\%$. Here, the value of the amphiphilic strength has been modified every $1.0 \cdot 10^6$ timesteps in the sequence $\kappa' = 1/5$, $\kappa' = 1/3$, $\kappa' = 1/2.5$ and finally $\kappa' = 1$ (where no amphiphilic behaviour should be expected).

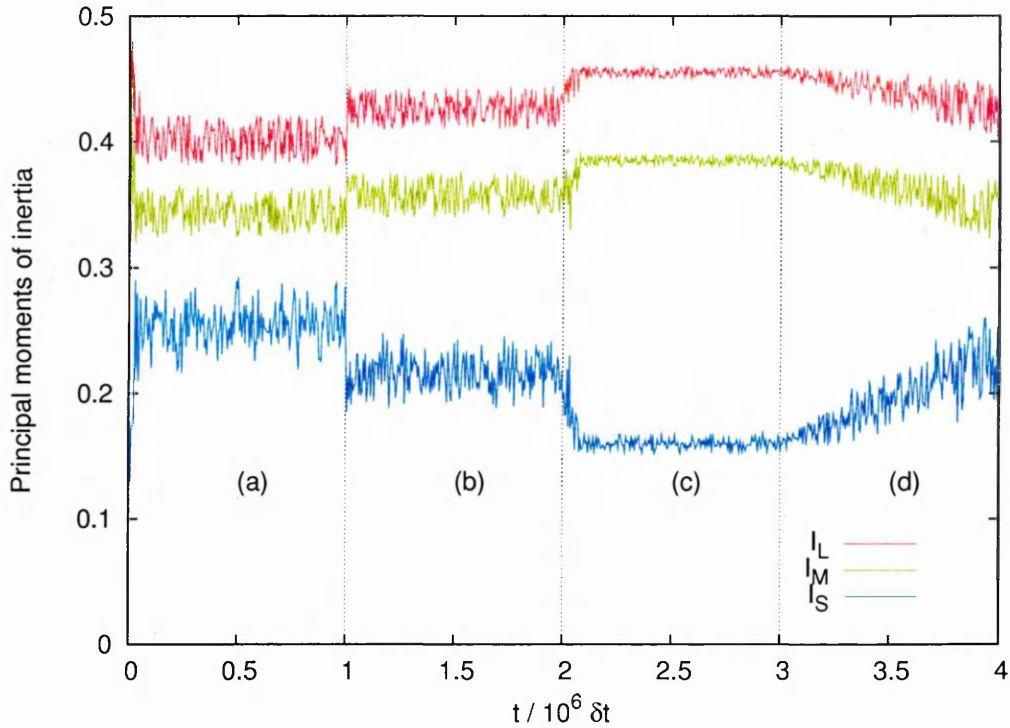


Fig. 4.32: Principal moments of inertia, I_L , I_M and I_S , of the largest cluster determined using $r_c = 0.9\sigma_0$. The regions (a), (b), (c) and (d) correspond to the κ' values and configurations snapshots shown on Fig. 4.33

The moments of inertia of the largest aggregate formed in this system has been monitored over the course of the simulation run and is shown on Fig. 4.32. From $t = 0\delta t$ to $t = 1.0 \cdot 10^6 \delta t$, ($\kappa' = 1/5$) one can observe the self-assembly of a near spherical aggregate from a random initial configuration. This is confirmed by the configuration snapshot on Fig. 4.33(a) that displays a multi-micellar arrangement of near-spherical micelles.

At $t = 1.0 \cdot 10^6 \delta t$, the amphiphilic strength was switched to $1/3$ and one can notice a repartitioning of the principal moments of inertia indicating a more cylindrical shape of the main aggregate in the system. As shown by the configuration snapshot of Fig. 4.33(b), here all the amphiphiles have aggregated into a single cluster with a cylindrical symmetry. This closed cylinder remained stable until the amphiphilic strength was reduced to $1/2.5$ at $t = 2.0 \cdot 10^6 \delta t$. Here, a similar change was found to that observed previously for the H80K5 system at 10% rod concen-

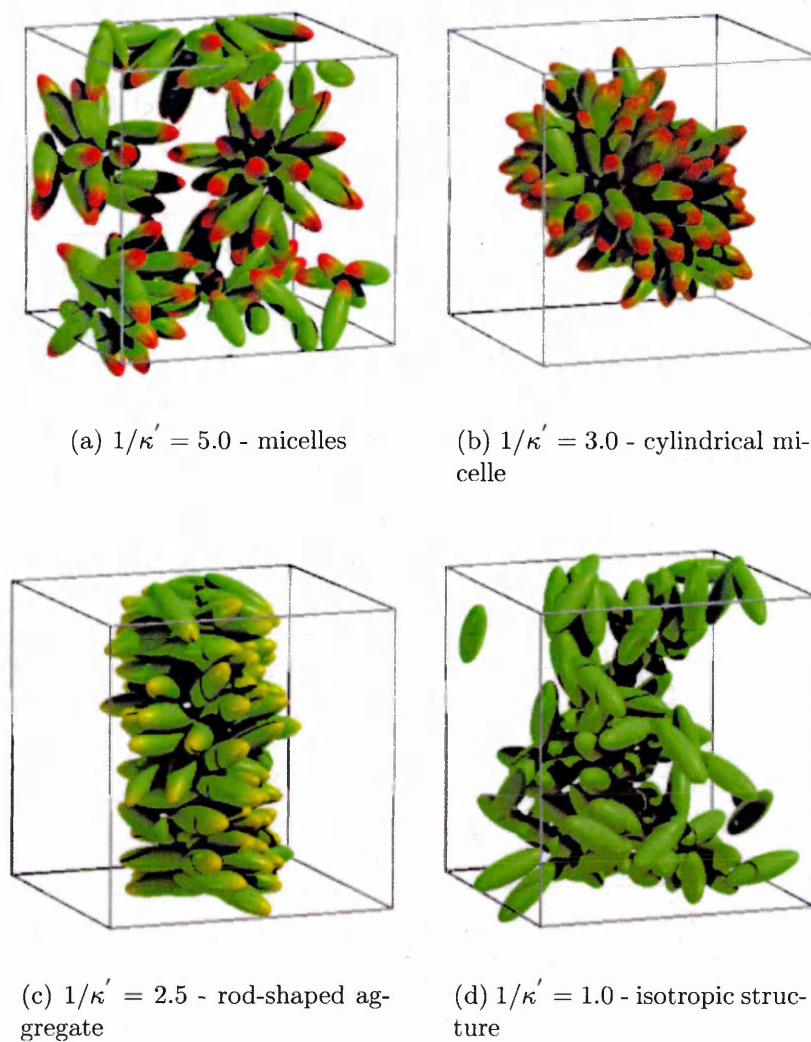


Fig. 4.33: Study of the effect of the rod-sphere interaction strength - 10% rod $H = 50\%$ system of 1024 particles at constant $T = 0.7$

tration (see Fig. 4.20(a) and Fig. 4.20(b)). Thus, the aggregate fused with itself through the PBC and formed a ‘tubular’ micelle (Fig. 4.33(c)). This transition is clearly stabilised by the PBC and much less noise can be observed on the moment of inertia data. At $t = 3.0 \cdot 10^6 \delta t$, the amphiphilic strength was switched to unity which, in principle, shall not promote and amphiphilic behaviour as no anisotropy is present in energy parameter of the rod-sphere potential. As expected, the previous structure then collapsed to give an isotropic mixture of rods and spheres (Fig. 4.33(d)).

This brief survey suggests that the amphiphilic behaviour (i.e. the structure shape) exhibited by these systems is sensitive to the hydrophilic interaction strength κ' : reducing the hydrophilic strength $1/\kappa'$ progressively reduces the curvature in the structure. The amphiphilic aggregates are surprisingly stable even at very low amphiphilic strength such as $\kappa' = 1/2.5$. It is, then, only when the amphiphilic strength is reduced to unity that the structure collapses. The sensitivity of phase properties to the model parameters κ' will be examined in more detail in the following chapter.

Effect of H , the hydrophilic to lipophilic balance(HLB)

Finally, in this initial survey, we have performed some simulations with another set of parameters specifically, we have examined the concentration dependence phase behaviour of an H50K5 system in order to analyse the effect of the hydrophilic to hydrophobic ratio, controlled by H , on the phase behaviour. The same procedures and simulation parameters used for the H80K5 system are applied here. The results are summarised via the configuration snapshots shown in Fig. 4.34.

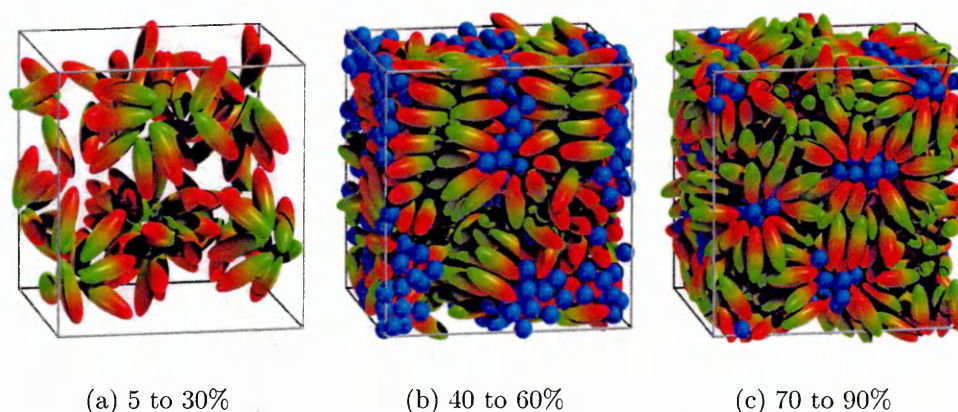


Fig. 4.34: Typical configuration snapshots of the H50K5 system for different rod concentration. Solvent spheres in (a) are omitted for clarity

With increased amphiphile concentration, the phase behaviour of this system has been found to be significantly different from that of the H80K5 system. At 5% rod

concentration, a micellar phase is found, which remains stable until 30%. These micelles appear, though, to be not as well defined as those obtained with the $H = 80\%$ systems. For rod concentration of 30% to 60%, a bilayer structure is formed when the micelles start to join through the periodic boundary conditions. However, no genuine lamellar phase has been formed. Rather, very curvy entangled bilayers have formed. From 70%, inverse phases, similar to those obtained with the H80 system, are found.

In conclusion, the H50K5 presents an expected sequence of amphiphilic behaviour with increasing concentration. However, the number of different phases observed seems to be significantly smaller than that seen for the H80K5 system, and the phase properties (*e.g.* micelle structure, bilayer flexibility) are clearly different.

4.5 Conclusion

In this chapter, a rod-sphere computer model has been developed based on a mixture of Gay-Berne and Lennard-Jones particles. This mixture involves the use of the Lennard-Jones potential for the spheres, the constant well-depth Gay-Berne potential for the rod particles and finally, a modified version of the Gay-Berne potential for the rod-sphere interaction. This rod-sphere potential has been adjusted in order to incorporate an amphiphilic behaviour into the system. In this, one end of the rod is strongly attracted to the solvent sphere, the other end being only weakly attracted.

Both ‘cubic’ and ‘exponential’ forms for of the energy parameter allow us to break the original symmetry imposed in Antypov’s formulation of the rod-sphere interaction. However, the ‘exponential’ model has proven to be preferable since only two parameters are needed to define it, and it does not suffer from mathematical limitations (unlike the ‘cubic’ model).

From the preliminary simulations presented in this chapter, it seems that this

model is suitable for studying the effects of molecular interaction parameters on self-assembly processes. Molecular characteristics such as the hydrophobic chain length and the hydrophobic strength can be readily changed within this generic model and their effects on phase properties assessed. The range of phases accessible to this model is surprisingly large, given its simplicity, and the simulation timescales accessible appear more than adequate for phase stability to be established. We are not aware of any other model capable of exhibiting this range of phase behaviour from a single molecular parameterisation. It is also noteworthy that the self-assembly processes observed here are driven purely by the amphiphilic effect (modelled here by the dipolar symmetry in the rod-sphere interaction). This contests starkly with the ‘solvent-free’ amphiphile models analysed in other recent studies of bilayers and vesicles [122–129]. Here, the effect of concentration has been studied for the set of parameters $H = 80\%$ and $\kappa' = 1/5$. Then, the effect of varying the hydrophobic strength κ' has been examined at constant $H = 50\%$. While concentration is the main determinant of phase stability, κ' also plays a key role. Little temperature dependence has been observed, other than to gain isotropy by imposing high temperature values.

There is also a clear dependence of the structure on the HLB ratio (parameter H). However, the $H = 50\%$ system did not produce a lamellar phase, possibly due to unrealistic features in its potential. This issue will be assessed in the next chapter, in which an alternative model will be developed and its phase behaviour assessed in detail, particularly in the low concentration, micellar region of phase space.

CHAPTER 5

Effect of amphiphilic properties on micellar behaviour

While the ‘exponential’ model investigated in the previous chapter successfully yields the conventional lyotropic self-assembling structures, it appears inappropriate for investigating the effect of the HLB ratio. Specifically, at moderate HLB values, the crossover between the hydrophobic and hydrophilic regions of the intermolecular potential appears too diffuse for this aspect of amphiphilic behaviour to be recoverable. In this chapter, therefore, we investigate an alternative ‘tanh’ form for the well-depth component of the intermolecular potential and what effect this has on the resultant phase behaviour. The structure of this chapter is as follows. First, a description of this alternative potential and some comparisons with the previous ‘exponential’ model are presented. Then, as an example, a detailed simulation study of a particular micellar system, performed using this alternative amphiphile-solvent potential, is presented. Finally, we study the effect of varying the model parameters H and κ' on the properties of the resulting micellar phases.

5.1 Refinement of the rod-sphere potential

5.1.1 Definition of the model

As summarised in Chapter 3, recent simulation studies have shown successful coarse-graining of all-atom lipid molecules [117–119]. The effective lipid-water potentials used in these studies showed a sharp transition between the hydrophobic and hydrophilic parts of the amphiphilic molecules. In designing a potential possessing this characteristic feature, adopting an S-shaped hyperbolic tangent (\tanh) dependence in the well-depth function appears a viable approach.

This S-shaped curve (Fig. 5.1) shows early exponential growth for negative x , which slows to linear growth near $x = 0$, then approaches $f(x) = 1$ with an exponentially decaying gap. The \tanh function describes a type of sigmoidal function (name due to the sigmoid shape of its graph) employed for many applications involving the S-curve of population growth, and is used in a wide range of fields, from biology to economics. This smooth switch from -1 to 1 would be useful for modelling the hydrophobic-hydrophilic transition described earlier.

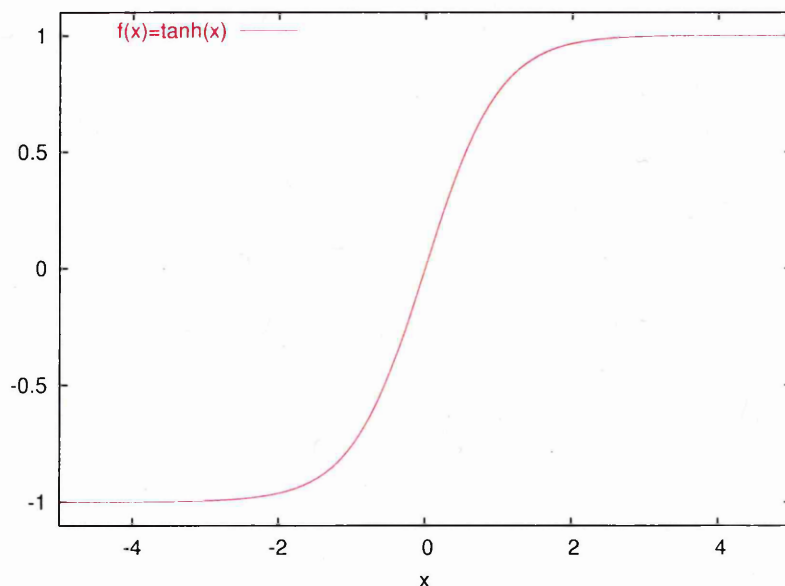


Fig. 5.1: Plot of the hyperbolic tangent function $f(x) = \tanh(x)$

By using a generic form such as $\epsilon(x) = a + b * \tanh((x - x_0)/c)$, one could tune the parameters a , b and c to control the shape of the energy parameter function: the parameter c can change the slope of the linear growth part. b controls the amplitude of the switch while a is just a shifting value along the ordinate axis. Finally, the x_0 value can be used to set the location of the transition position either to positive or negative values of x .

Relating this functional form to the amphiphilic potential of interest here, one can define the following mathematical expression:

$$\epsilon(\hat{\mathbf{r}}_{ij} \cdot \hat{\mathbf{u}}_j) = a + b \tanh\left(\frac{(\hat{\mathbf{r}}_{ij} \cdot \hat{\mathbf{u}}_j) - S}{l}\right) \quad (5.1)$$

where $S = 1 - \frac{2H}{100}$, $a = (\epsilon_{min} + \epsilon_{max})/2$ and $b = (\epsilon_{max} - \epsilon_{min})/2$

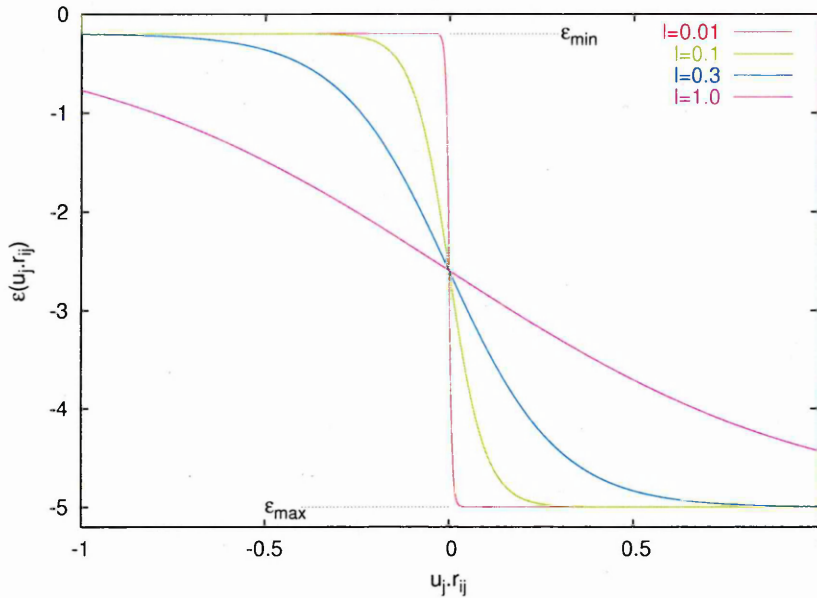


Fig. 5.2: Alternative ‘tanh’ energy functions of the rod-sphere interaction

ϵ_{max} and ϵ_{min} correspond to the depth of the potential at the rod’s ends, *i.e.* the head and the tail. Thus, in this model, ϵ_{max} controls the hydrophilic strength, *i.e.* the head’s hydration level, and ϵ_{min} controls the tail’s hydrophobicity. These two parameters could be set independently. However, in order to be consistent with

the previous model, these two parameters are set to $\epsilon_{min} = \kappa'$ and $\epsilon_{max} = 1/\kappa'$. The parameter H is defined, as previously, by the ratio of the length of the ‘hydrophobic’ region over the rod’s total length. A third parameter, l , controls the sharpness of the cross-over. As can be seen in Fig. 5.2, for $l = 0.01$, the potential corresponds nearly to a step-function, whereas, for $l = 1.0$, the potential is nearly linear in $\hat{\mathbf{u}}_j \cdot \hat{\mathbf{r}}_{ij}$. Obviously, this parameterisation does not fit our requirement for a sharp switch, whereas too sharp a transition could induce very high intermolecular forces. The intermediate parameter value $l = 0.1$, corresponding to an intermediate transition sharpness, has therefore been adopted for the rest of this study.

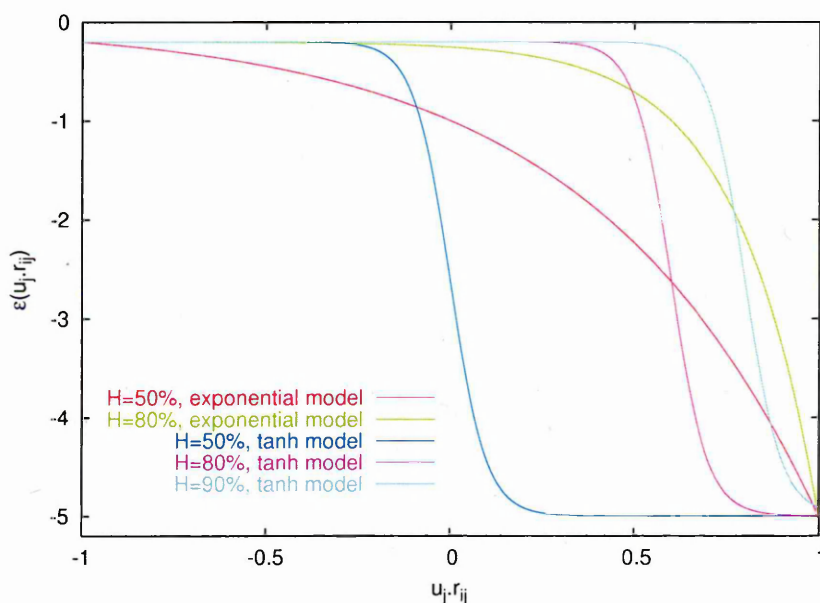


Fig. 5.3: Comparison of different energy functions for the rod-sphere interaction

Fig. 5.3 shows a comparison between this tanh model and the exponential model for different H values with $\kappa' = 1/5$. From this graph, one can see that the two $H = 50\%$ potential curves display very different switching behaviours between the ‘hydrophobic’ and ‘hydrophilic’ regions. Conversely, the ‘exponential form’ with $H = 80\%$ (used for the simulations in Chapter 4) is numerically quite similar to the ‘tanh form’ with $H = 90\%$. As such, one would expect the tanh form to be both able to access the range of phase behaviour observed in chapter 4 and, due

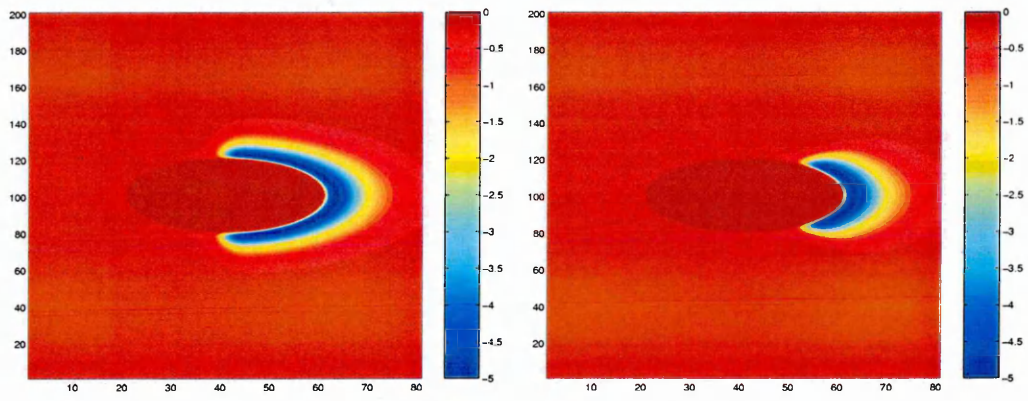
to its consistently sharp switching between the head and the tail regions, more appropriate for investigating the behaviour of lower H systems.

Contour plots of the rod-sphere potential energy, shown on Fig. 5.4 for different H and κ' values, illustrate these differences more clearly. Fig. 5.4(a) and Fig. 5.4(b) illustrate the form of the tanh model for $H = 50\%$ and $H = 80\%$, respectively, for $\kappa' = 1/5$. Fig. 5.4(c) and Fig. 5.4(d) show the equivalent contour plots obtained with the ‘exponential’ form of the potential. With the exponential model, as H is decreased to 50%, the crossover region of the potential becomes very diffuse and the strongly attractive region becomes very small, giving a poor representation of a genuine amphiphile having 50% of its length hydrophilic. The extreme cases, corresponding to $H = 50\%$, $\kappa' = 1/2$ and $H = 90\%$, $\kappa' = 1/5$ are shown on Fig. 5.4(e) and Fig. 5.4(f) with the tanh formulation of the potential energy. Note that Fig. 5.4(f) confirms that the $H = 90\%$, $\kappa' = 1/5$ potential with the tanh model is close to the $H = 80\%$, $\kappa' = 1/5$ potential with the exponential model, *i.e.* the exponential model becomes close to the tanh model for high H values.

5.1.2 Phase behaviour as a function of H and κ' with increasing concentration

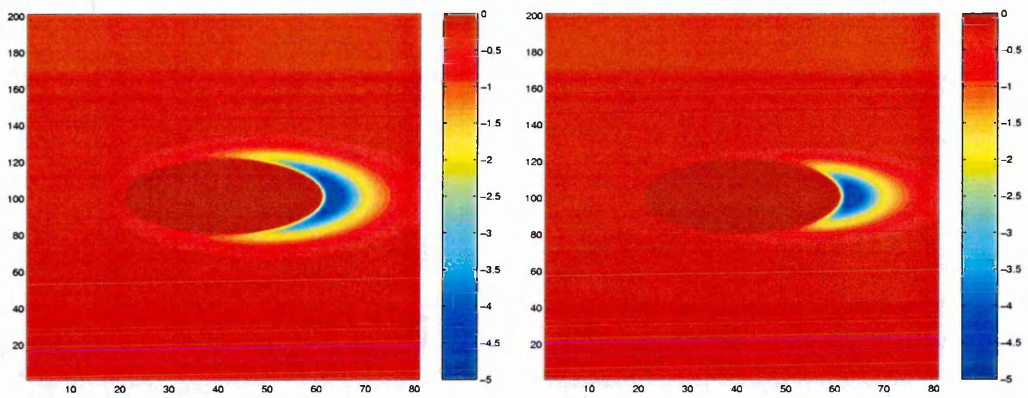
As for the exponential model, the approximate phase behaviour of the tanh systems has first been determined from a series of quenching runs performed in, constant NVT simulations, at a temperature of $T = 0.9$ for different rod concentrations. Starting from an isotropic configuration of 1024 particles, previously equilibrated at high temperature, each system was run for $2 \cdot 10^6$ steps.

Fig. 5.5 shows the resulting final configuration snapshots of the H80K5 system (defined as $H = 80\%$ and $\kappa' = 1/5$) for different rod concentrations. This system shows an extensive range of amphiphilic phase behaviours in agreement with experimental results: at low amphiphilic concentrations, spherical micelles are formed (Fig. 5.5(a)) which transform into cylindrical micelles with increasing



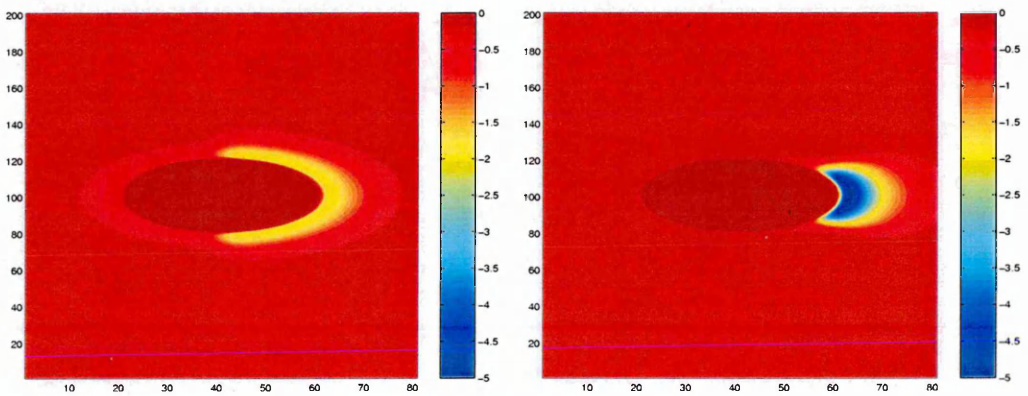
(a) $H = 50\%$, $\kappa' = 1/5$, 'tanh' form

(b) $H = 80\%$, $\kappa' = 1/5$, 'tanh' form



(c) $H = 50\%$, $\kappa' = 1/5$, 'exponential' form

(d) $H = 80\%$, $\kappa' = 1/5$, 'exponential' form



(e) $H = 50\%$, $\kappa' = 1/2$, 'tanh' form

(f) $H = 90\%$, $\kappa' = 1/5$, 'tanh' form

Fig. 5.4: Contour plots of a range of rod-sphere potentials

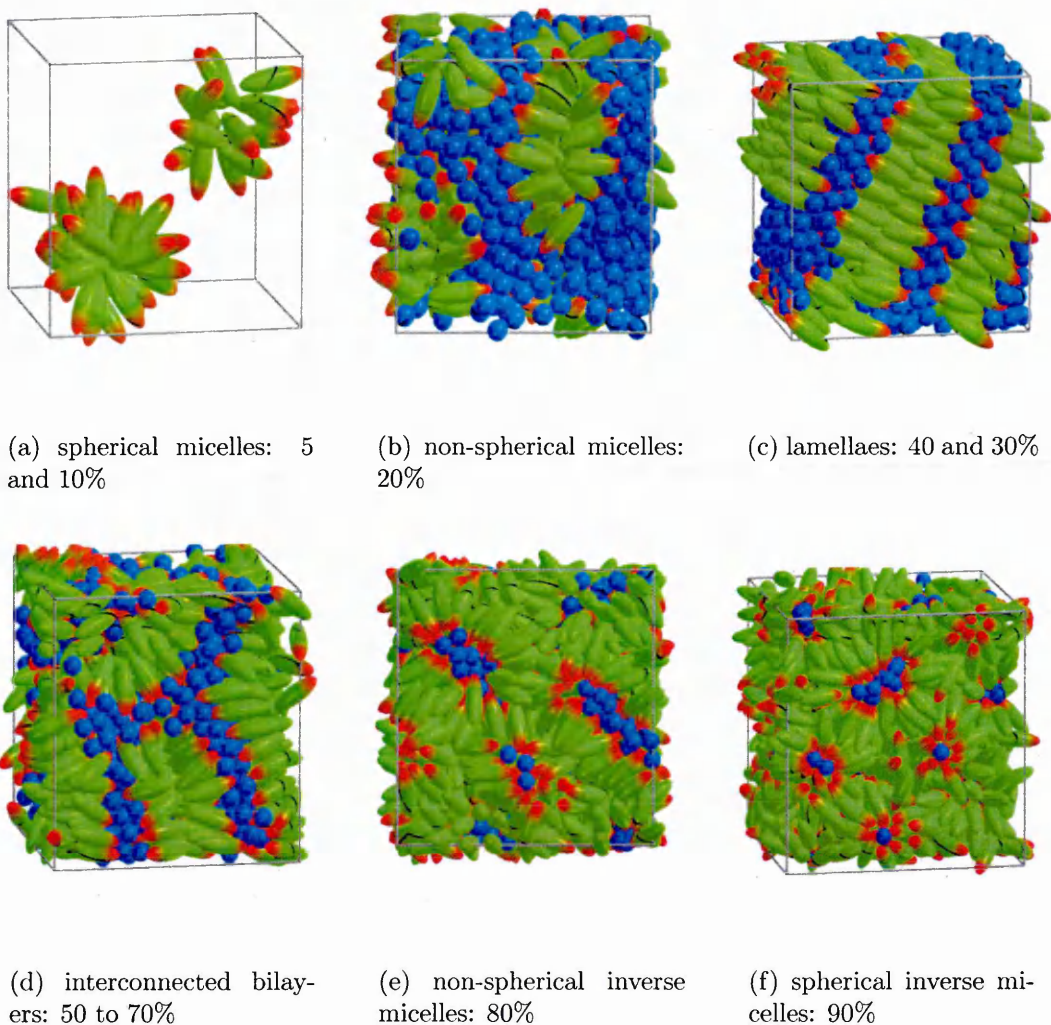


Fig. 5.5: Configuration snapshots of the H80K5 system at $T = 0.9$ for different rod concentrations

concentration (Fig. 5.5(b)). At 30%, a lamellar phase is formed which persists at 40% (Fig. 5.5(c)). Then, from 50% to 70%, curved bilayer formation occurs (Fig. 5.5(d)). Finally, at 80% and 90%, inverse micellar phases develop (Fig. 5.5(e) and Fig. 5.5(f)).

Similar quenches on systems with different H values and concentrations have been performed for a number of other $\kappa' = 1/5$ and $\kappa' = 1/2$ systems. The results of these simulations are summarised in Fig. 5.6 in the form of approximate phase diagrams constructed by analysing the final configuration snapshots.

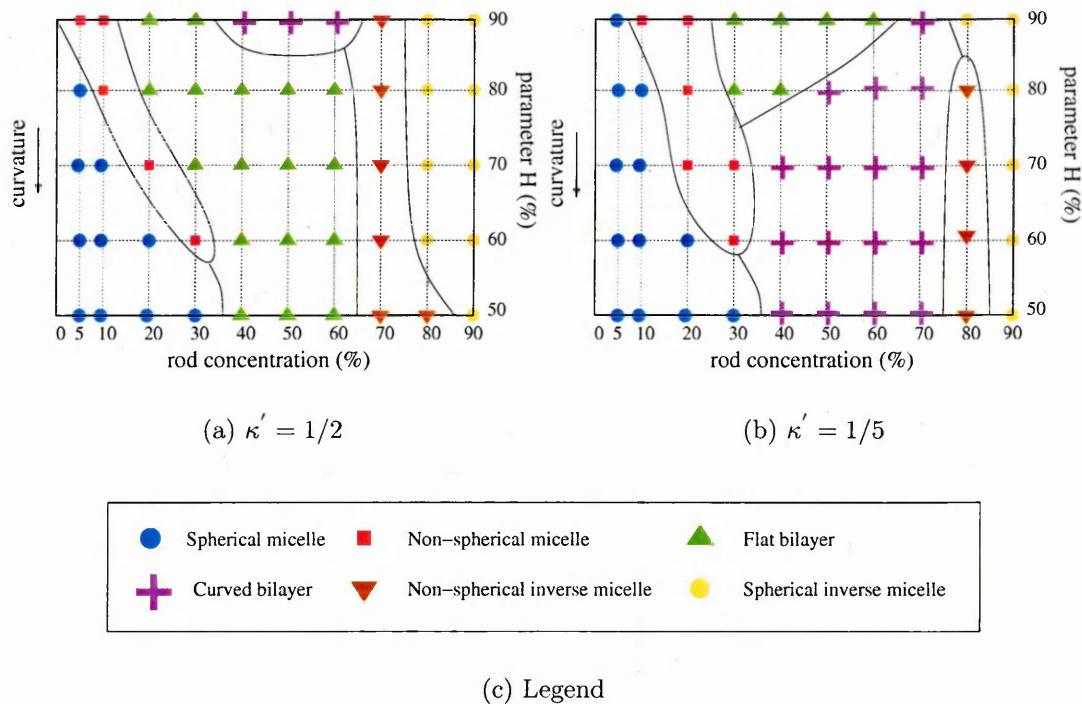


Fig. 5.6: Approximate H vs.rod concentration phase diagrams for tanh model system at $T = 0.9$. Black lines are guides to the eyes

From these phase diagrams, one can clearly see the effects of concentration and the HLB on the phase behaviour: As the concentration and H are increased, the shapes of the aggregates vary from positive curvature (micelles) to negative curvature (inverse micelles) via a broad region of near-zero curvature, bilayer-forming systems. Decreasing κ' to $1/5$ causes aggregates with more curvature to be formed. The flat bilayer region is, thus, reduced to a small area of the phase diagram with high H values, whereas the $\kappa' = 1/2$ system displays flat bilayers over the entire range of H values studied. In the same way, the inverse micelle regions are smaller for the strongly hydrophilic head group systems and cover only the high amphiphile concentrations.

In all cases, the lyotropic phase sequence follows the form expected for system with inherent positive curvature:

spherical micelle \rightarrow cylindrical micelle \rightarrow curved bilayers \rightarrow flat bilayers \rightarrow non-spherical inverse micelle \rightarrow spherical inverse micelle

This sequence is in generic agreement with experiment, theory (see Chapter 2) and simulation (see Chapter 3). However, some phases are absent from these phase diagrams. Phases such as the hexagonal phases (normal and inverse), cubic phases, sponge phases and the vesicle region are missing. This may be due to system size effects as these phases are, indeed, mesoscopic, requiring large length-scale structures, and, therefore, a much bigger system to be simulated. Furthermore, it has been shown that some phases are difficult to obtain unless, non-cubic simulation boxes are used [105,106]. Alternatively, the phases may simply not be formed for this model parameterisation or might require, *e.g.*, a multicomponent system to stabilise.

5.2 Preliminary simulations at 5% rod concentration

Having established that the tanh model yields a wide range of amphiphilic phases, we now use it to examine in greater detail, just one of these phases: the spherical micellar phase.

Preliminary to some bigger system runs, a series of simulations on small size systems were performed for a wider range of κ' and HLB values at a fixed concentration ratio of 5%. The motivation for studying these 5% system in more detail was to perform an initial exploration of parameter space in order to guide the choice of system for subsequent much larger and longer simulation runs.

Fig. 5.7 shows a table representing the final configuration snapshots obtained for systems ranging from $\kappa' = 1/2$ to $\kappa' = 1/5$ and $H = 50\%$ to 90% . From these snapshots, it is apparent that the shapes and structures of the aggregates formed

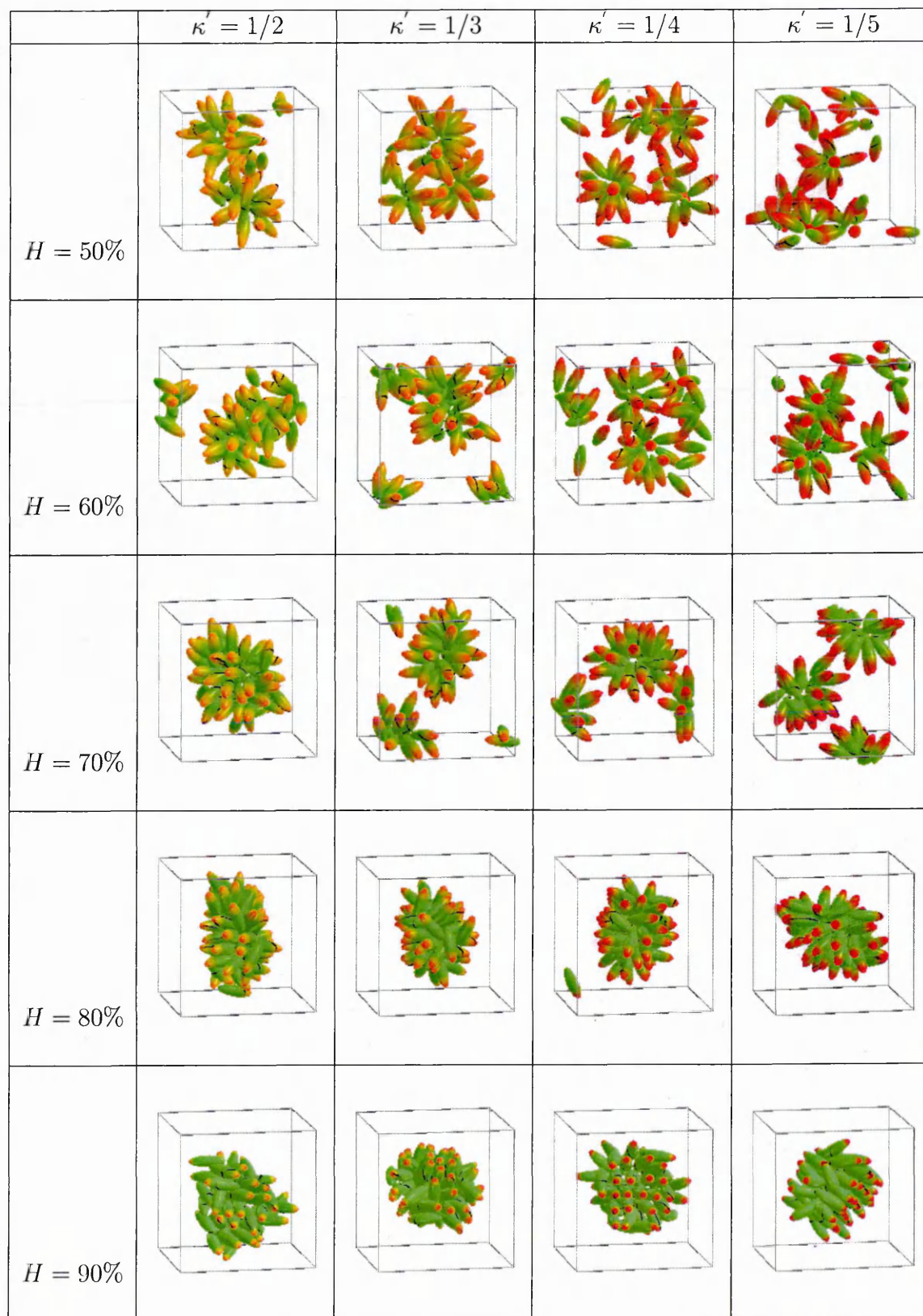


Fig. 5.7: Final configuration snapshots obtained from NVT simulation at $T = 0.9$ for systems ranging from $\kappa' = 1/2$ to $\kappa' = 1/5$ and $H = 50\%$ to 90%

are sensitive to changes in both κ' or H . Looking at extreme cases, the H90K2 system forms a single aggregate with, apparently, low radial ordering of the rods, while the H50K5 system has hardly formed a micelle. The latter observation may be due to too low a temperature (or a comparatively high well-depth energy) being used which limits the mobility within the system. Intermediate parameterisations show structures involving multiple micelle arrangements (*e.g.* H70K5), more radially ordered micelles (*e.g.* H70K3) and cylindrical aggregates (*e.g.* H80K2).

For all of these systems, however, the PBCs have a significant effect on the self-assembly, as the sizes of the micellar objects are of the same order as the box size. Clearly, therefore, much bigger system are required in order to draw any firm conclusions on the behaviour of these systems as a function of H and κ' . From this initial exploration, then, we have chosen to use the $\kappa' = 1/2$ and $\kappa' = 1/4$ systems over a range of different H values for larger scale runs. Comparison of the behaviour of these systems is made in section 5.4, following a description of the processes found accessible to these simulations.

5.3 Observed structures and processes of the micellar phase

Before exploring the effect of molecular interactions on micellar properties, a detailed study of the H70K2 system at 5% rod concentration is presented. In this, a system of 8192 particles (containing 410 rods, corresponding to a 5% system) was created by replicating (in a $2 \times 2 \times 2$ cube) eight images of the initial disordered configuration of the 1024 particle system previously equilibrated at high temperature ($T = 2.0$). This 8192 particle system was then run for $1 \cdot 10^6$ MD steps in *NVT* at $T = 0.9$, all of the simulation parameters such as the time step, cutoff radius, neighbour list radius, etc., being set to those used in the previous simulations. A configuration file was dumped every 1000 steps for post-simulation

analysis.

5.3.1 Self-assembly properties

Configuration snapshots taken at different times during this simulation run are presented in Fig. 5.8. The configuration at $t = 0\delta t$ (Fig. 5.8(a)) shows the initial random configuration. Then, a rapid aggregation of the rods can be noticed similar to the evolution observed with the exponential model in the previous chapter. At $t = 0.06 \cdot 10^6 \delta t$, one can observe the formation of several distinct aggregates. These assemblies increase their size as further monomers join the developing aggregates until a dynamic equilibrium is attained at $t \approx 0.4 \cdot 10^6 \delta t$ (Fig. 5.8(e)). Fig. 5.8(f) shows the final configuration snapshot from this run. Here, the rods are clearly aggregated into several distinct clusters, coexisting with free non-agglomerated amphiphiles or monomers.

The evolution of the number of monomers during the course of the simulation run, calculated with the cluster counting algorithm described in chapter 4, is shown in Fig. 5.9 for a range of values of the cluster counting cut-off distance r_c . These plots indicate an equilibration time of about $0.4 \cdot 10^6$ steps at which the monomer number attains a steady value for all values of r_c . As for the exponential model, the number of monomers decreases with increasing cut-off distance r_c . This is consistent with the clustering of the amphiphilic rods observed on the configuration snapshots (Fig. 5.8), but offers little information on which contact distance is most appropriate for this micellar system. The corresponding $n.P(n)$ curves, shown in Fig. 5.10, indicate how the cluster size distribution function of the system varies as the cluster counting cut-off distance is increased from 0.1 to $1.6\sigma_0$. These distribution functions (as well as other observables presented in what follows) were averaged over configuration snapshots taken from time-steps $4 \cdot 10^5 \delta t$ to $10^6 \delta t$. From these plots, one can observe a similar behaviour to that found for the exponential model. For small contact distances (i.e. $r_c < 0.7\sigma_0$),

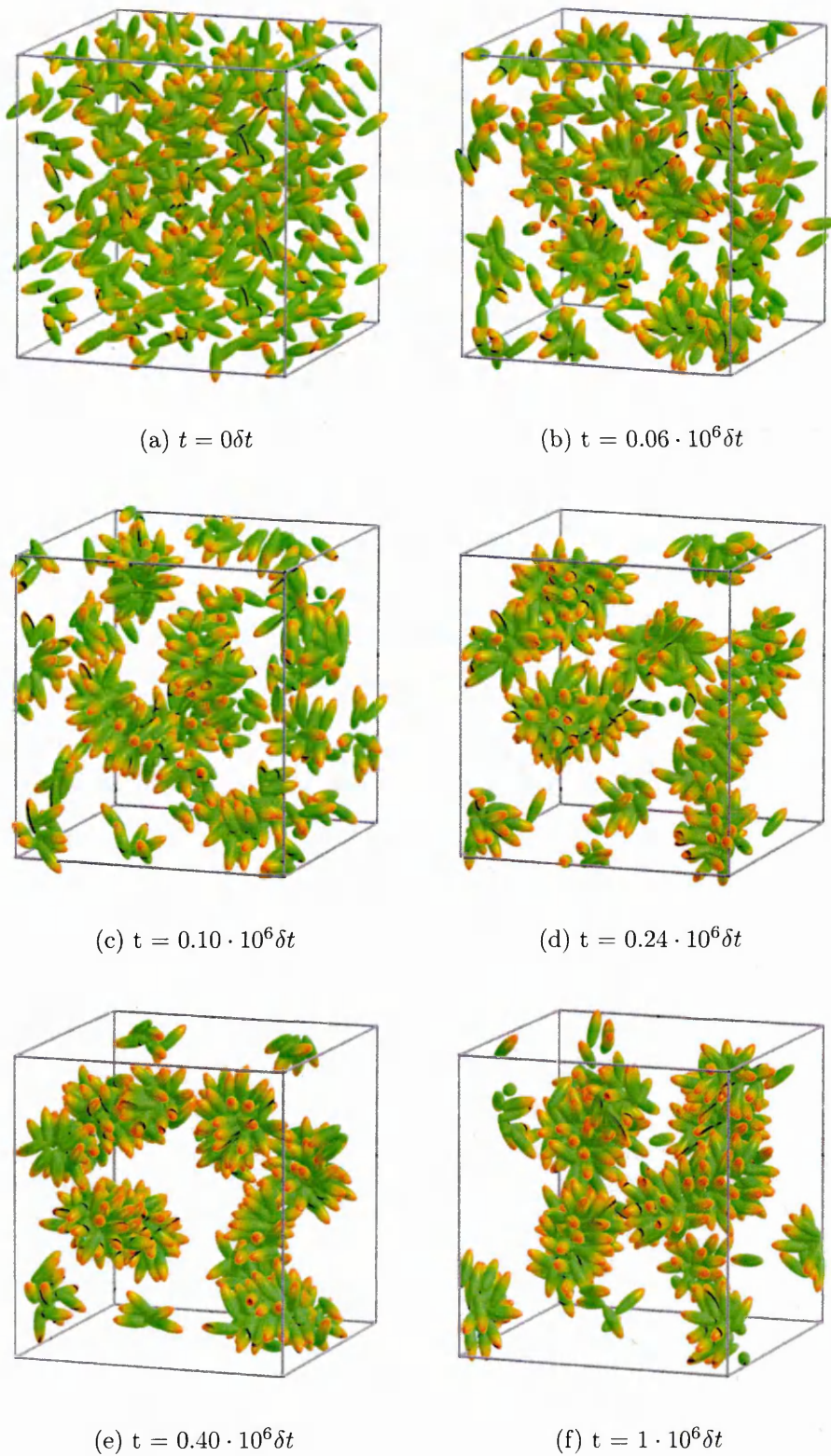


Fig. 5.8: Configuration snapshots of the H70K2 system taken at different time steps at $T = 0.9$

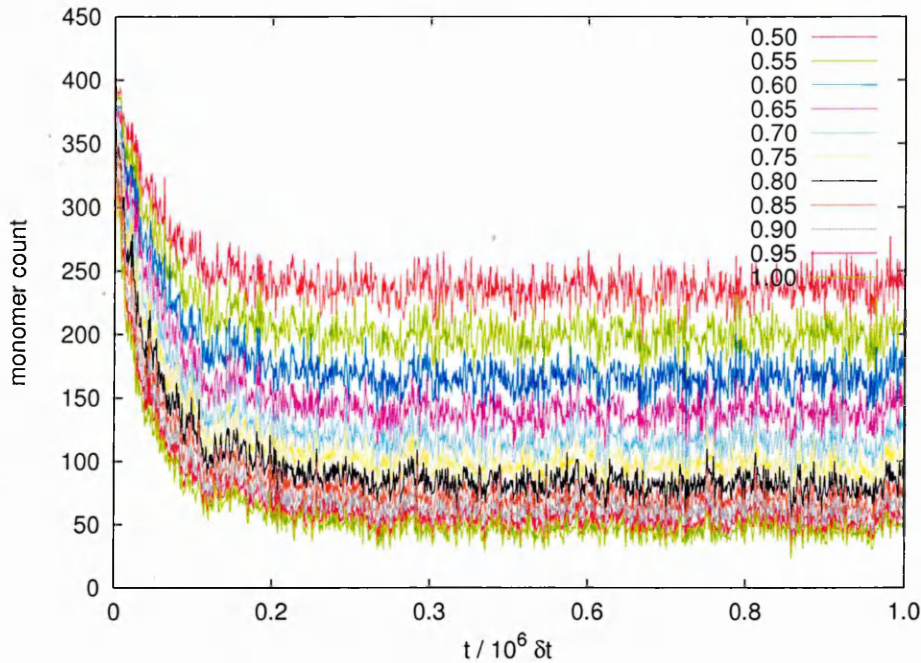
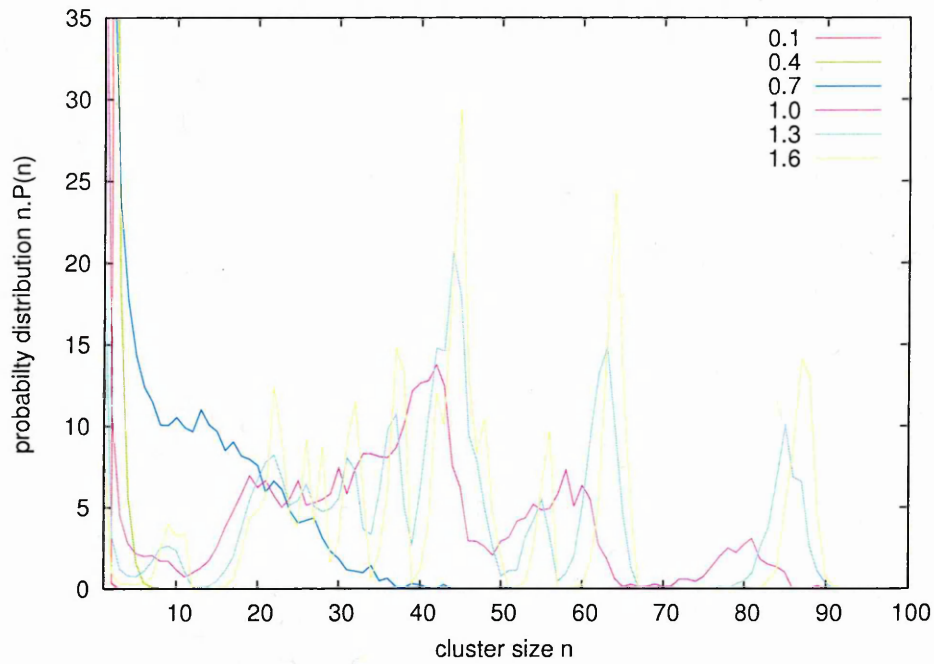


Fig. 5.9: Monomer count vs. time step for the H70K2 system at $T = 0.9$ and a range of r_c values

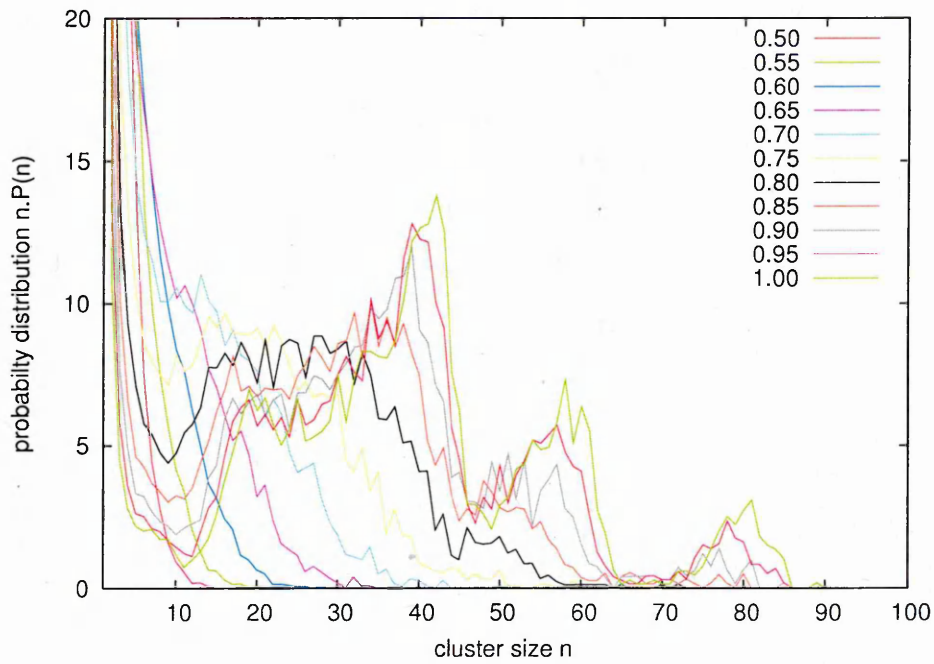
the probability distribution function is just a monotonic decay. For large contact distances ($r_c > 1.0\sigma_0$), peaks develop at large cluster sizes. Intermediate contact distances lead, however, to the classic form of a standard micelle size distribution function with a high monomer peak and a micelle peak at $n \approx 25$ (the aggregation number) for $r_c = 0.80\sigma_0$.

5.3.2 Micelle structure

The average principal moments of inertia, shown in Fig. 5.11, illustrate the behaviour of the corresponding aggregate shapes as a function of the aggregate occupancy or size n . When the micelle size is smaller than the aggregation number, the shapes of the aggregates tend to be cylindrical. Interestingly, the aggregation number, *i.e.* the most stable micelle size, corresponds to the n -value at which the cluster shape is closest to being spherical. From $n \approx 25$ to $n \approx 60$, the moments of inertia diverge slightly indicating a shape change from spherical to



(a) $r_c = 0.1$ to $1.6\sigma_0$ with $\Delta = 0.3\sigma_0$



(b) $r_c = 0.7$ to $1.0\sigma_0$ with $\Delta = 0.05\sigma_0$

Fig. 5.10: Probability distribution function $n.P(n)$ of the H70K2 system at $T = 0.9$ for different range of contact distances r_c

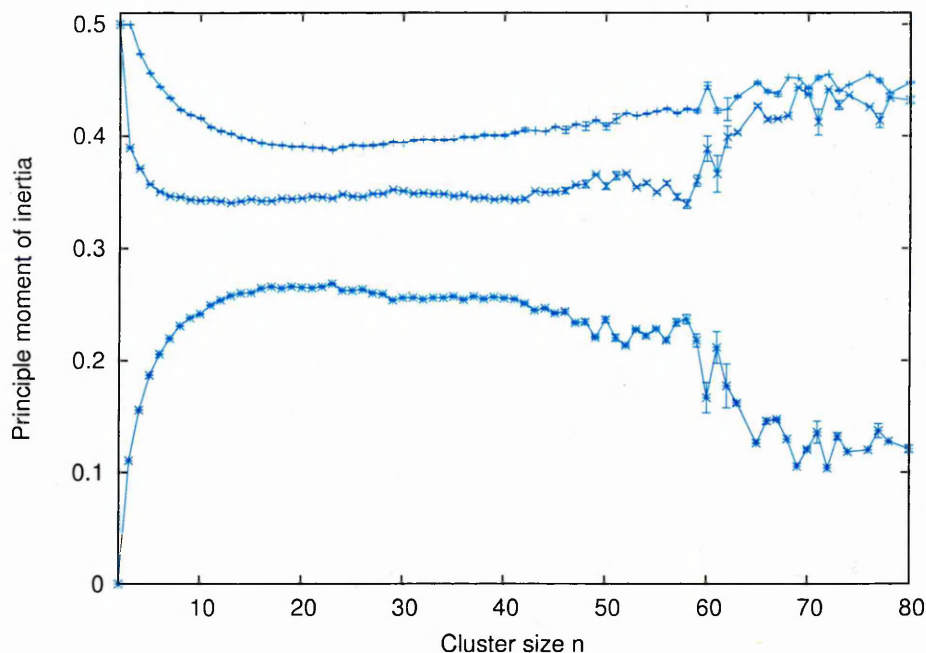


Fig. 5.11: Principal moments of inertia of the H70K2 system at $T = 0.9$ computed for $r_c = 0.80\sigma_0$

slightly cylindrical. When the micelle size reaches $n \approx 60$, more changes are seen in the distribution of the moments of inertia, indicating a possible discontinuous change in the aggregate shape, although the statistics here are poor. This apparent sphere-cylinder crossover is possibly related to occasional micelle-micelle fusion events.

Conformational information can also be readily calculated from the simulation configurations. Thus, the structural conformations adopted within the micelles can be extracted from the computation of appropriate molecular angular and positional correlation functions, namely $g_{ang}(\cos(\theta))$ and $g_{pos}(r)$. The approach used in the computation of $g_{pos}(r)$ is very similar to that used for $g(r)$, $g_{\parallel}(r_{\parallel})$ and $g_{\perp}(r_{\perp})$. For $g_{pos}(r)$, histograms of the distance between the centre of mass (COM) of each micelle and each of its component particles are considered. This distribution is therefore equivalent to an RDF between the micelle COM and its component particle and is, therefore, similar to a density distribution of the amphiphiles within a micelle. To calculate $g_{ang}(\cos\theta)$, where θ is the angle subtended

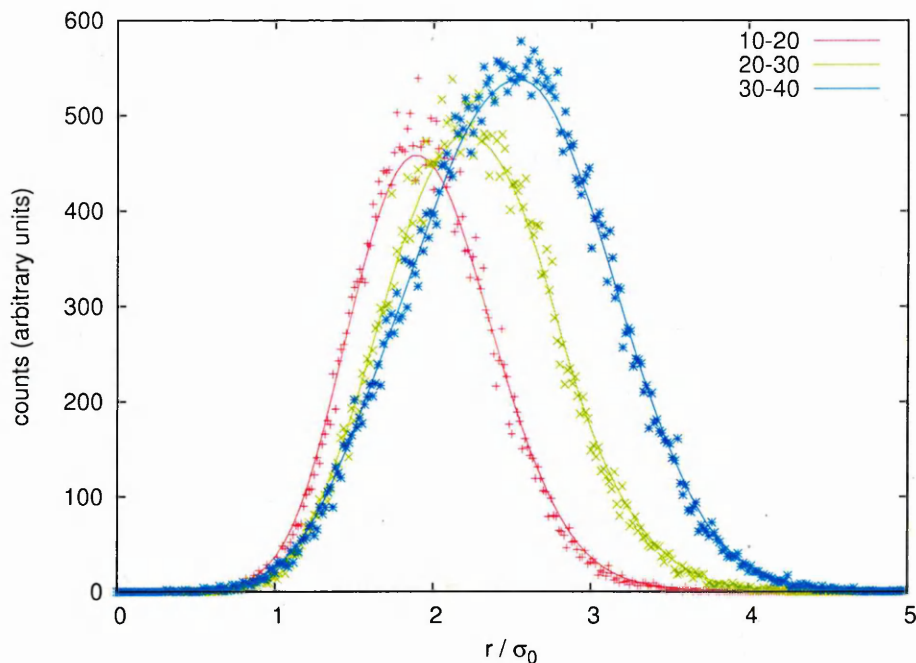


Fig. 5.12: Positional distribution functions $g_{pos}(r)$ for H70K2 particles in micelles of occupancy $n = 10 - 20$, $n = 20 - 30$, $n = 30 - 40$

by two molecular centres at a micelle COM, again only the particles belonging to each micelle are considered. These distributions are then averaged over the run and the number of micelles formed by each system. Note that a computation depending on micelle size is required for both of these distribution functions since the structural conformations show some size-dependence. Due to the relatively small system sizes available here, there are rather few micelles of each particular size. Therefore, the $g_{pos}(r)$ and $g_{ang}(\cos(\theta))$ data have been grouped (and averaged) over 3 categories of micelle size: 10-20, 20-30 and 30-40 particles.

Fig 5.12 illustrates the Gaussian-like distribution of the $g_{pos}(r)$ data obtained for this system for the three different micelle size categories. From these plots, the distribution mean value clearly increases with micelle size. This is an expected behaviour due to the packing properties of the particles. As the particles aggregate, their excluded volumes also lead to the formation of a forbidden region in the centre of the micelles. For micelle sizes of 10 to 20 particles, the distribution function displays a forbidden radius of $\approx 0.5\sigma_0$ from the micelle COM in which

the particles centres cannot reside. This indicates a sphere of about $1\sigma_0$ diameter containing no particle centres. As the micelle size increases, the size of the forbidden region does not change as all distributions start to accumulate at $r \approx 0.5\sigma_0$. However, the mean value of the distributions is shifted to larger values as n is increased. If a micelle remained spherical as its size increased, the forbidden region would become larger which is not the case here. This implies, therefore, that with increasing size, the micelle changes shape and adopts a more cylindrical shape, as shown by the moment of inertia data.

The angular distribution functions on Fig. 5.13 also offer useful insight into micellar structure. Here, for all micelle size ranges this function shows approximately the same structure, displaying one peak at around $\cos(\theta) \approx 0.8$. This suggests that each particle in a micelle has a ring of nearest neighbours at an angular displacement of $\sim \cos^{-1}(0.8) = 37^\circ$. However the position of the first peak does show some dependence on the micelle size as shown on Tab. 5.1

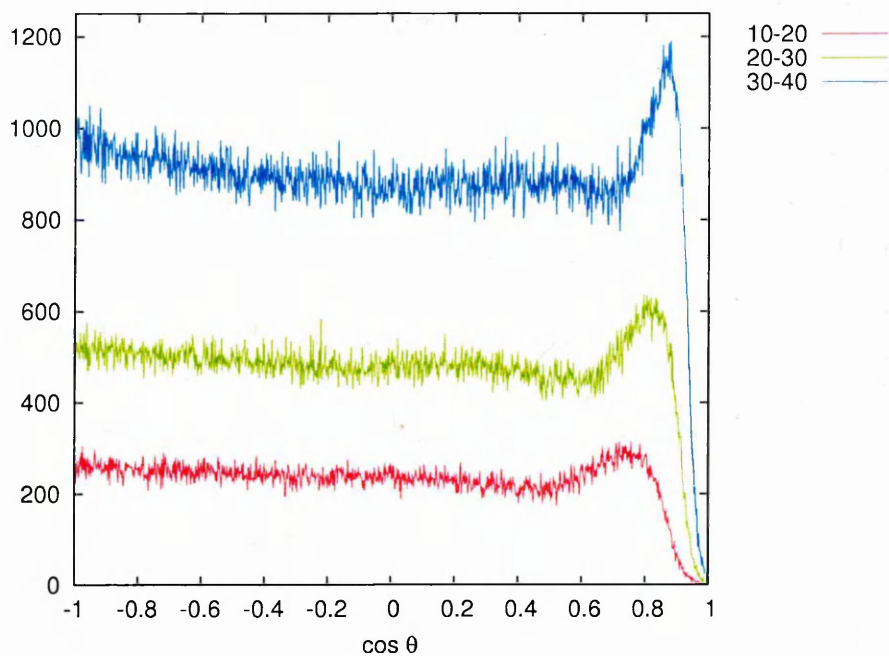
size	10-20	20-30	30-40
$\cos(\theta)$	0.75	0.80	0.85
θ	41°	37°	32°

Tab. 5.1: Highest peak position of $g_{ang}(\cos\theta)$ for different micelle sizes

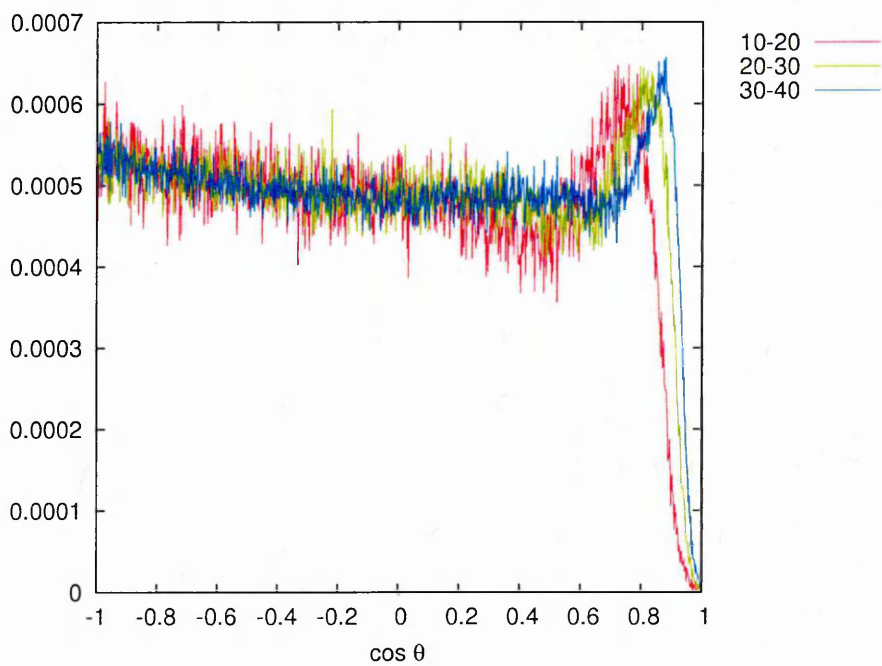
The normalised data shown on Fig. 5.13(b) clearly show the shifting of the peak position toward smaller angle values as the micelle size is increased. This peak can also be seen as a signature of the curvature of the aggregate, which decreases with increasing micelle size.

5.3.3 Micelle dynamics

In the previous section, the structure of micelles has been assessed by analysis of their sizes and shapes as well as the positional and orientational conformations of their constituent particles. We now consider larger length-scale structure, i.e. the micelle-micelle structure. Here, individual micelles can be regarded as single



(a) un-normalised



(b) normalised

Fig. 5.13: Angular distributions functions $g_{ang}(\cos\theta)$ for H70K2 particles in micelles of occupancy $n = 10 - 20$, $n = 20 - 30$, $n = 30 - 40$

entities and the individual amphiphiles can be ignored. At this supra-molecular scale, properties such as micelle diffusion and the micelle-micelle radial distribution function can be examined. Furthermore, micelle histories can be captured by tracking population change through time, with a view to gaining information on micelle life-times.

To achieve these analyses, it is necessary to be able to track each micelle through time, *i.e.* from stored configuration to stored configuration. In the analysis performed so far, micellar clusters were identified for each given configuration but no attempt was made to follow them in time through several configurations. However, as the list of particles within each micelle changes over time, this micelle tracking is not a trivial matter and a population comparator was required.

This has been achieved by calculating the intersection \cap and the union \cup between two populations P_i and P_j .

$$C_{i,j} = \frac{\cap(P_i, P_j)}{\cup(P_i, P_j)} \quad (5.2)$$

with P_i denoting the population of cluster i , with i and j being clusters identified from designated configurations.

The ratio $C_{i,j}$ can be seen as a self-similarity coefficient between micelles i and j as it is equal to unity if the two populations are the same and identical to zero if they are completely dissimilar. Alternatively, if one particle has left or joined the micelle, the intersection is reduced, leading to a slight decrease in $C_{i,j}$. In the same way, if two micelles coalesce, the union shows a large increase, leading to a big drop in the calculated self-similarity coefficient.

This population comparator was used to track micelles through time as follows: given a particular micelle i of population P_i at a time t , its self-similarity coefficients with all of the clusters j present at time $t + 1000\delta t$ were calculated. The cluster j showing the maximum similarity with cluster i was then considered to

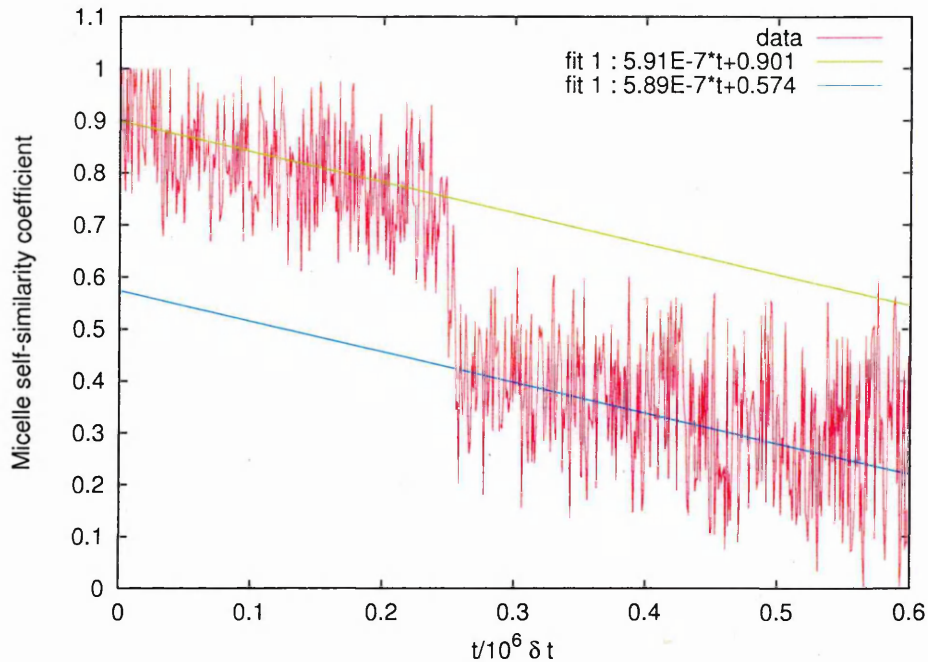


Fig. 5.14: Plot of the time evolution of the self-similarity coefficient for a single micelle from system H70K2

be the ‘same’ micelle subject to a slight time-evolution in its population. The occupancy list of this new micelle was then used as the reference population for the next comparison at $t + 2000\delta t$.

Micelle population change and renewal

In order to calculate the change of micelle’s population with time, the self-similarity coefficient has been calculated with respect to an original population for all subsequent populations identified by the procedure described above.

Fig. 5.14 shows a plot of the resulting self-similarity coefficient evolution calculated for a single micelle selected from the H70K2 system. Here, $t = 0\delta t$ corresponds to the time when the micelle being considered was first identified. Between $t = 0 \cdot 10^6\delta t$ and $t \approx 0.4 \cdot 10^6\delta t$, a slow linear decay can be observed, such that after approximately $0.3 \cdot 10^6\delta t$, the self-similarity coefficient has decreased from

unity to ≈ 0.80 . This suggests a slow turnover of the micelle's population due to monomers leaving and/or joining the main aggregate. The large amplitude noise component associated with this decay indicates that these leaving and rejoining events take place on a very short timescale. This noisy character with an underlying linear trend suggests, then, two distinct monomer behaviours operating on well-separated timescales.

At $t \approx 0.4 \cdot 10^{-6} \delta t$, the self-similarity coefficient shows a clear drop indicating a significant event: either a fusion with another micelle or breakdown of this micelle into two clusters. From detailed investigation of the configuration files, we have found that it does, in fact, correspond to a fusion with another micelle. This process is described in more detail in the next section.

After this fusion event, the 'new' population exhibits once more, a noisy, slow, linear decay, somewhat slower than that from before the fusion. This decrease in gradient may be due to a change of the monomer exchange rate due to a change in micelle size. It would be interesting to analyse the effect of micelle size on this exchange rate, however, the relatively small number of long-lived micelles identifiable here limits the statistical significance of such a measurement.

To summarise, these self-similarity evolution indicate that the micelle's population can be changed by 3 different processes acting on different timescales

- rapid rattling motion of monomers leaving and rejoining the micelle
- monomer exchange between micelles
- fusion/break-up process of micelles

The moment of inertia timelines confirm the rapid piston-like motion of monomers and leads to rapid shape changing of micelles, *i.e.* the cylindrical micelles identified earlier change their shape and orientation very rapidly due to a radial pistoning of the monomers.

It is also interesting to note that the self-similarity coefficient does not reduce to zero over the course of the simulation. This means that the micelle has not, actually, completely renewed its population, although the self-similarity is down to ≈ 0.25 . Furthermore, the fusion event had a particularly dramatic effect on the micelle population. If no fusion between micelles were possible, the self-similarity coefficient would have decreased to only ~ 0.544 after $1.0 \cdot 10^6 \delta t$ timesteps.

Fusion process between two micelles

The fusion event responsible for the sharp drop in the self-similarity coefficient of the micelle history described in the previous section (recall Fig. 5.14), is now described in detail. By identifying the final micelle and applying our tracking scheme backward through time, we have been able to trace the evolution of this process. This observation is confirmed by the configuration snapshots taken at different time during this fusion process shown on Fig. 5.15.

On these snapshots, two initial independent micelles have been coloured red and green. Note a initial single monomer coloured blue. That way, it is possible to follow the behaviour of the these two initial populations after the fusion event. The snapshots presented here illustrate the different stages involved in this fusion process.

The formation of the two initial micelles takes place in about $0.1 \cdot 10^6 \delta t$. First randomly aggregated (Fig. 5.15(a)), the red and green rods self-assemble together forming two distinct micellar clusters (Fig. 5.15(b)). These two micelles are very stable and remain relatively unchanged similar over $\approx 0.2 \cdot 10^6 \delta t$. As they come close enough to each other, a red rod bridges the gap between the two micelles briefly, leaving the 'red' micelle for the 'green' micelle. The two micelles then join, forming a cylindrically shaped assembly (Fig. 5.15(e) and Fig. 5.15(f)), which then relaxes to a spherically shaped micelles (Fig. 5.15(g) and Fig. 5.15(h))

Fig. 5.16 shows the evolution of the number of amphiphiles in the micelle during

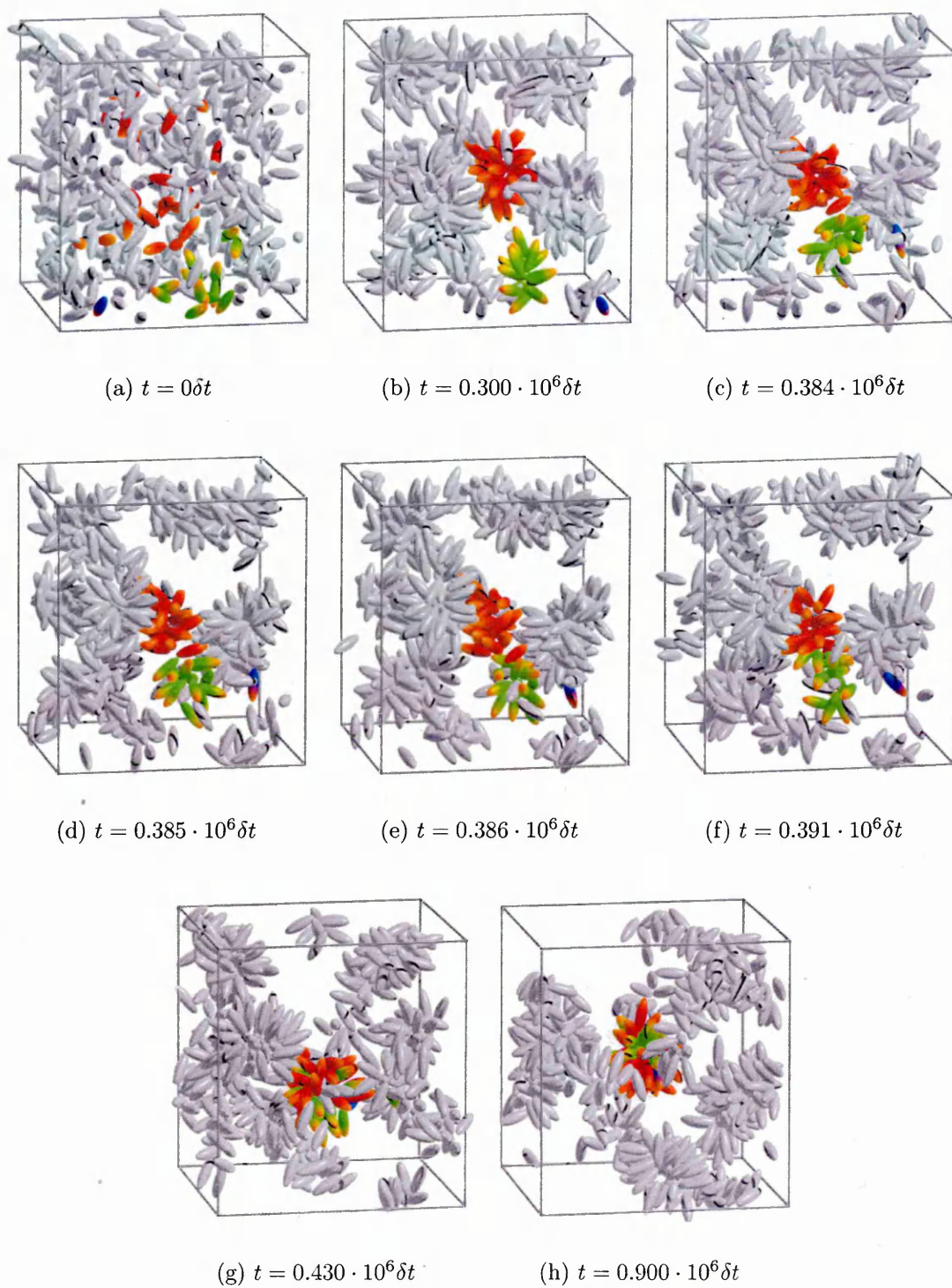


Fig. 5.15: Configuration snapshots of the fusion process taking place for the H70K2 system. The two initial micelles are coloured in red and green. The separate monomer is coloured blue

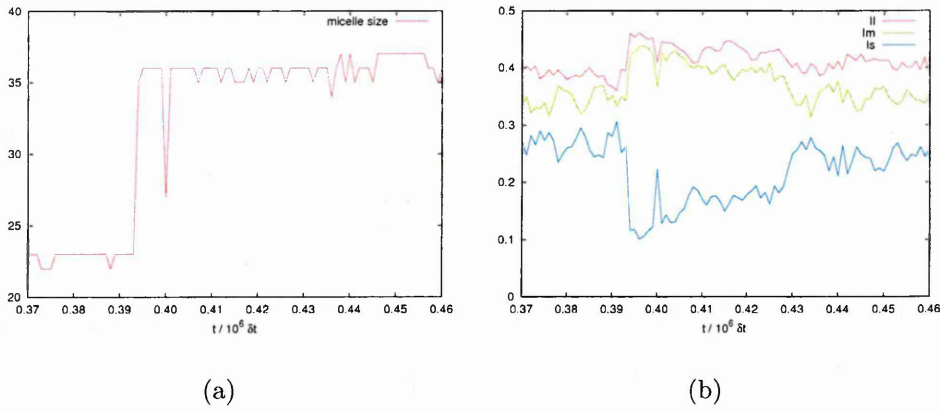


Fig. 5.16: (a): measure of the micelle size vs timesteps (b): history of the micelle principal moments of inertia

the fusion process (micelle size) and the associated principal moments of inertia. From these two graphs, and consistent with the drop in Fig. 5.14, it appears that this fusion event takes place between $0.39 \cdot 10^6 \delta t < t < 0.40 \cdot 10^6 \delta t$. The noise associated with the micelle size evolution is due to monomer exchange fluctuation, i.e. entering and exiting out of the main aggregate. It can also be seen that the fusion process is accompanied by an important change in the shape of the aggregate: as the two micelles come into contact, the aggregate retains a cylindrical shape that quickly relaxes to a near-spherical shape in about $0.04 \cdot 10^6 \delta t$, in agreement with the configuration snapshots observation. Later, at $t = 0.44 \cdot 10^6 \delta t$, one can observe the blue monomer joining the main aggregate, as can be seen by an increase of 1 in the micelle size evolution graph.

Fusion events such as this one likely to be more frequent during the self-assembly phase of a quench than in an equilibrated system since sub-micelle size assemblies are more likely during equilibration. These sub-micelles are likely to join in order to attain the preferred size and shape. Once equilibration is achieved, however, less fusion will be observed though break-up may be noticed more frequently than before equilibration. However, it is difficult to observe this effect in these simulations as the time and length scales are still too small and the number of fusion/break-up events is too low for a correct statistical analysis to be performed.

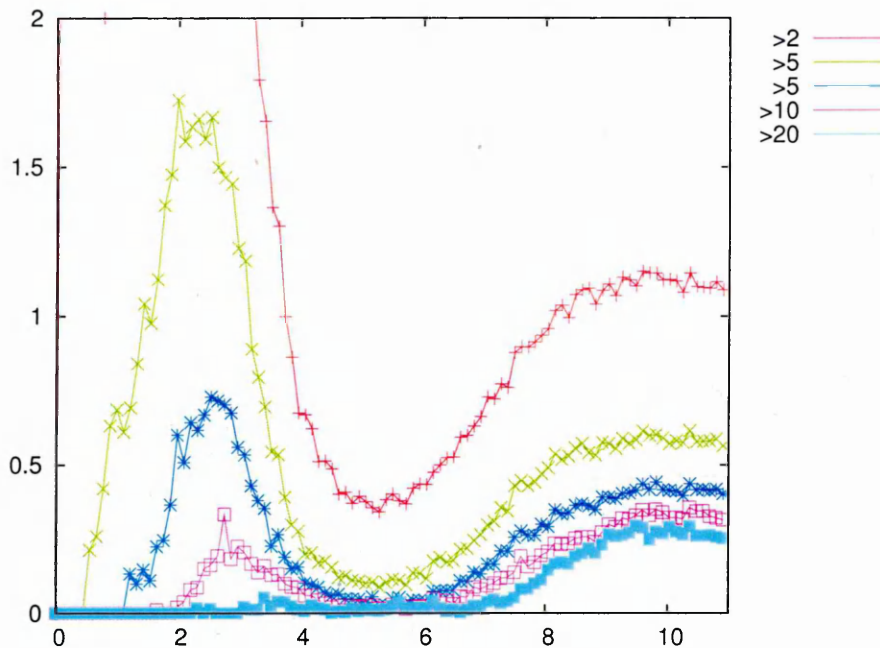


Fig. 5.17: Micelle-micelle $g(r)$ for different cluster size

Micelle-micelle interaction

The micelle-micelle interaction can also be investigated by calculating the micelle-micelle $g(r)$. This is achieved by calculating the center of mass of each micellar cluster at every time step, considering a certain category of cluster sizes. Fig. 5.17 illustrates the behaviour of the micelle-micelle $g(r)$ for different cluster sizes.

Note that for small cluster sizes ($n < 20$), a fictitious peak appears at small distances ($\sim 2 - 3\sigma_0$). This is probably due to the fact that very small identified clusters can be very close to each others. However, these are not to be taken into account as they represent sub-micellar aggregates. Thus, only the $g(r)$ for large cluster sizes ($n > 20$) has a significance when considering micelles of sizes close to the aggregation number. For this size category, the fictitious peak at small distances has disappeared and only the second peak remains at $\sim 10\sigma_0$.

In terms of interaction potential, the micelle-micelle radial distribution can be very useful when compared with other fluid models. Fig. 5.18 display the different

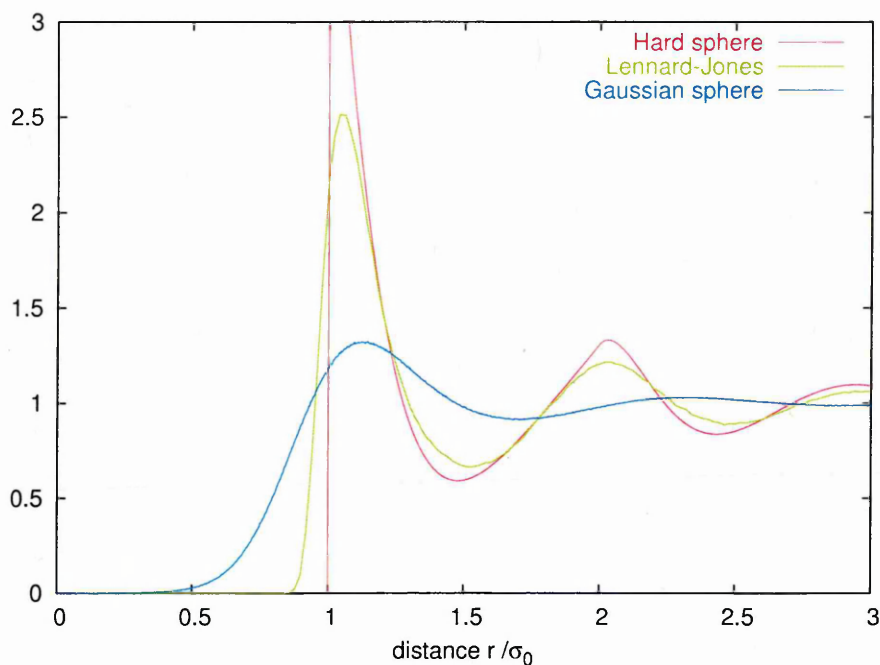


Fig. 5.18: Comparison of radial distribution functions from different fluid models

RDFs obtained from simulation of hard spheres, gaussian spheres and Lennard-Jones spheres of size $\sigma_0 = 1.0$. The hard sphere model, as its name indicates, doesn't allow particle to overlap. This can be easily seen on the RDF with a prohibited region at $r < \sigma_0$. On the contrary, the gaussian model, initially designed to represent coarse-grained star polymer [188], posses a slow decay down to $\approx 0.5\sigma_0$. The Lennard-Jones fluid, being 'softer' than the hard sphere model, allows some overlapping of the particles and, therefore, corresponds to an intermediate behaviour between the two previously cited models.

Compared with these models, the micelle-micelle radial distribution functions calculated here display a 'very soft' micelle-micelle effective potential which allow overlapping in order to permit fusion events. Thus, the micelle-micelle interaction could be modelled using an bounded pair-potential, that is with a finite potential value at full full particle overlap ($r = 0$) such as the Gaussian sphere model, with a sphere of size $\sim 6 - 7\sigma_0$.

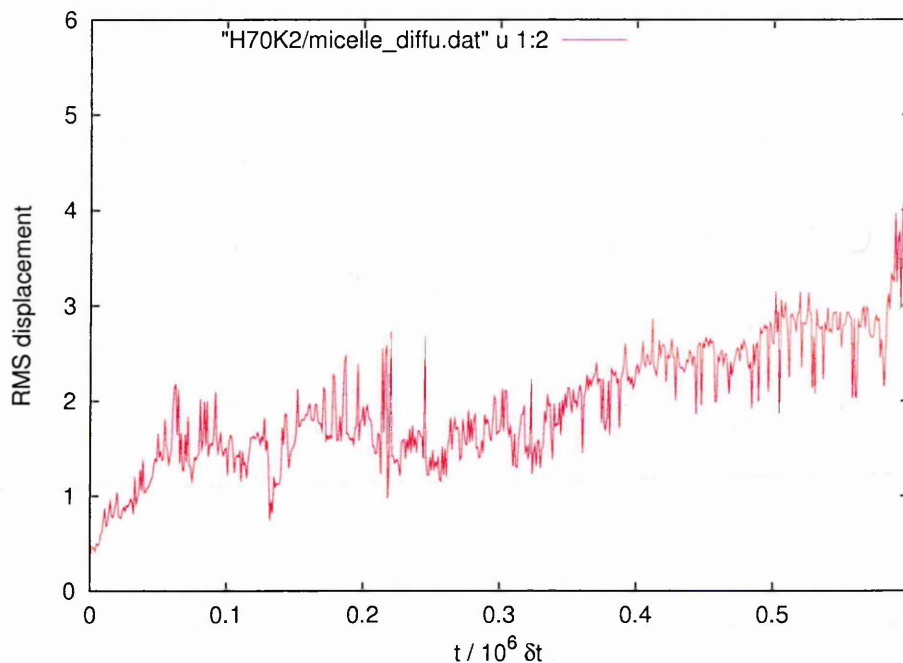


Fig. 5.19: Micelle RMS displacement of cluster of size $n > 2$ in the H70K2

Micelle diffusion

The micelle diffusion was difficult to measure due to the relatively small number of micelles in the system (< 10) and a very low displacement rate. The averaged micelle displacement after $0.6 \cdot 10^6$ steps was $\approx 3\sigma_0$ which corresponds to half the micelle's effective size determined earlier by the micelle-micelle RDF.

5.3.4 Monomer exchange and dynamics

The monomer behaviour noted from Fig. 5.14 suggests a rattling motion in which monomers rapidly enter and leave the micelle. Also, the slow underlying decay of the self-similarity coefficient indicates that monomers are lost and replaced by others ones as the micelle size remains roughly constant. Furthermore, the monomer number has been shown to be constant after equilibration (recall Fig. 5.9). All of this evidence suggests a degree of exchange of monomers between the micelles.

Further evidence for this can be found by measuring the monomer life-time distribution as shown on Fig. 5.20. This plot displays a very large number of short-lived monomers and has a discernible long tail of long-lived monomers with a life times of as much as $0.225 \cdot 10^6 \delta t$ for this system. This raises the prospect of being able to trace the paths of long-lived monomers to assess how they are exchanged between micelles.

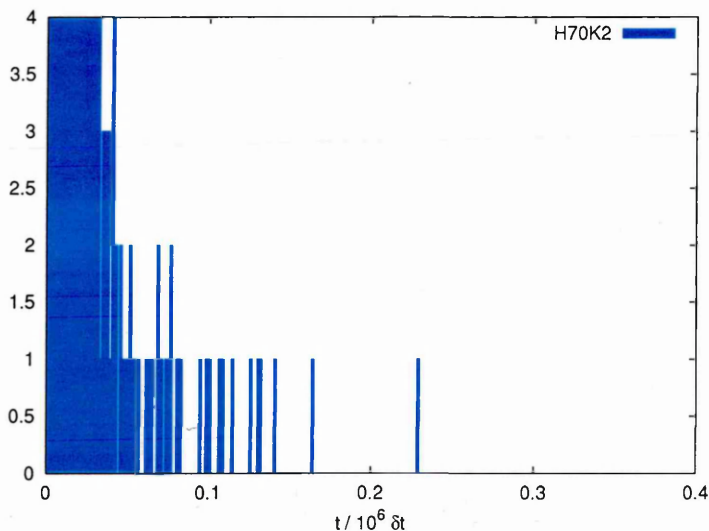


Fig. 5.20: Monomer life-time distribution

This entering and leaving processes of the monomers can be observed through an exchange process taking place in the H70K2 system. As shown on the configuration snapshots of Fig. 5.21, a monomer leaves the top micelle to later join a neighbouring micelle. During this process, the monomer has to turn round in order to be able to insert itself into its new micelle, the hydrophobic tail entering first. Another process that can take place is a monomer leaving a micelle for a significant time and, instead of joining another cluster, eventually coming back to its initial micelle (see configuration snapshots on Fig. 5.22).

The dynamics of the long-lived monomers identified above are, presumably, the diffusive behaviour observed for a single monomer in a sea of spheres subject to perturbations by some effective micelle-monomer interaction. To investigate the behaviour of a monomer in the proximity of a micelle, either to enter or

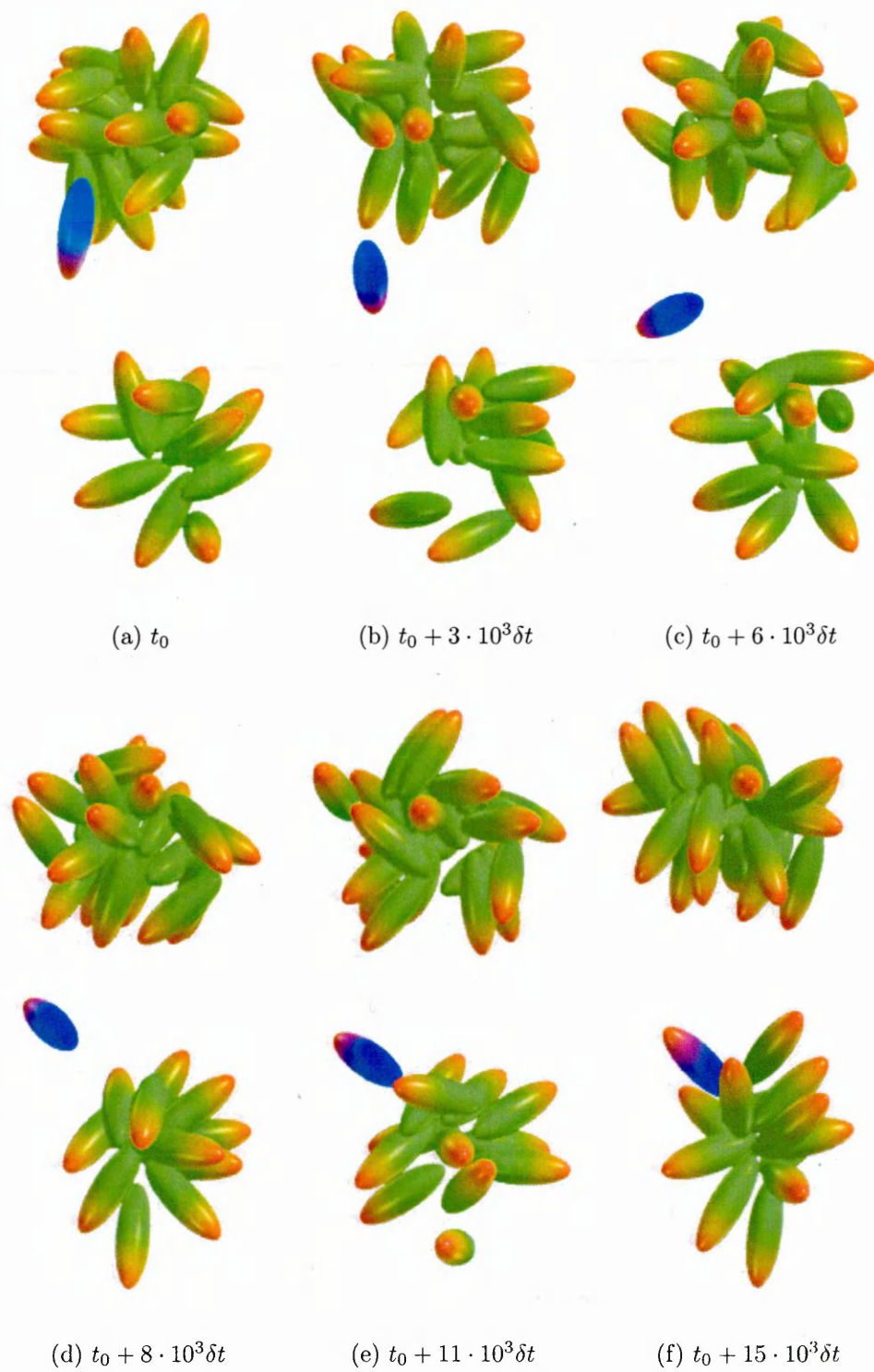


Fig. 5.21: Snapshots of a monomer exchange process between two distinct micelles

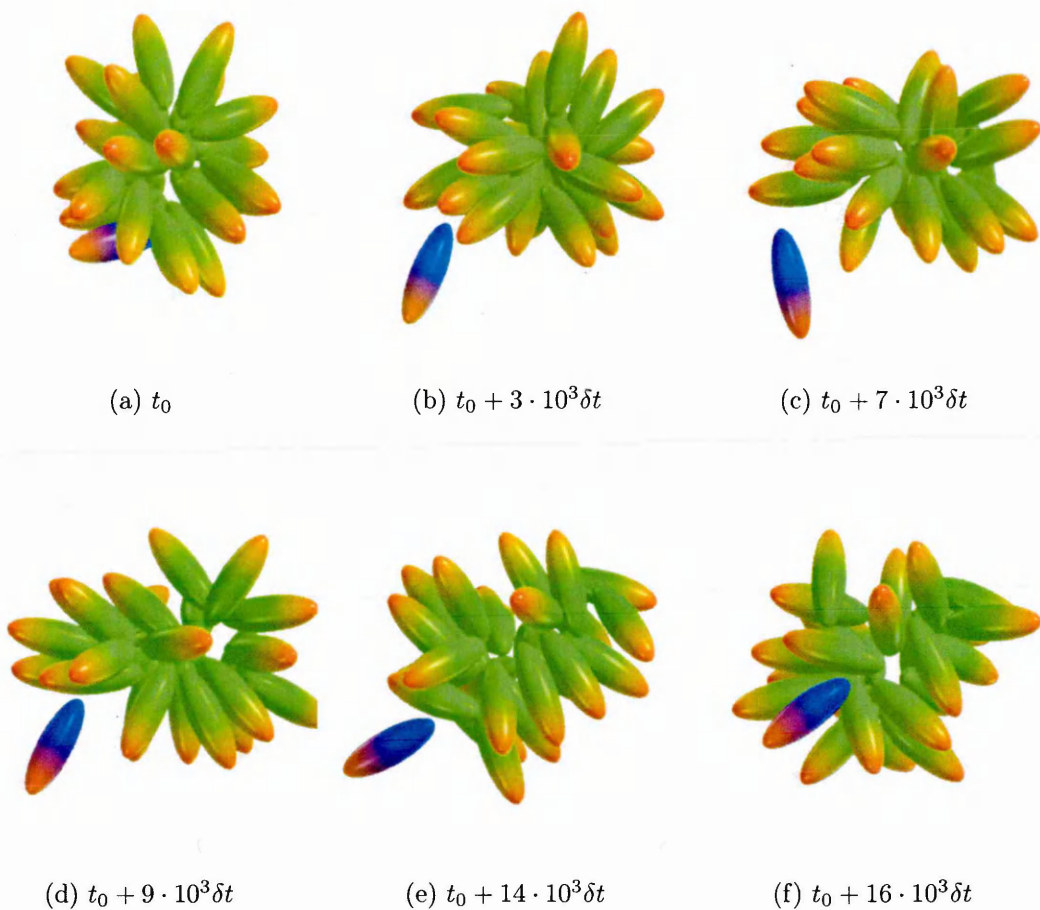


Fig. 5.22: Snapshots of a monomer coming in and out of the same micelle

leave it, a 3D distribution of the angle between the monomer ideal trajectory (*i.e.* the micelle COM to particle center vector) and its orientation vector θ as a function of the micelle-monomer distance has been computed. Only the entering/leaving monomers are considered and the micelle-monomer distance is shifted by the micelle radius so as to reduce the effect of micelle size on this measurement. In practice this is achieved by calculating $R(t) - d$ where $R(t)$ is the distance from the micelle COM to the monomer at a time t and d corresponds to the distance between the micelle COM and the rod's position once it has joined the micelle. (Fig. 5.23).

As it appears that H and κ' have little impact on this measurement, these distri-

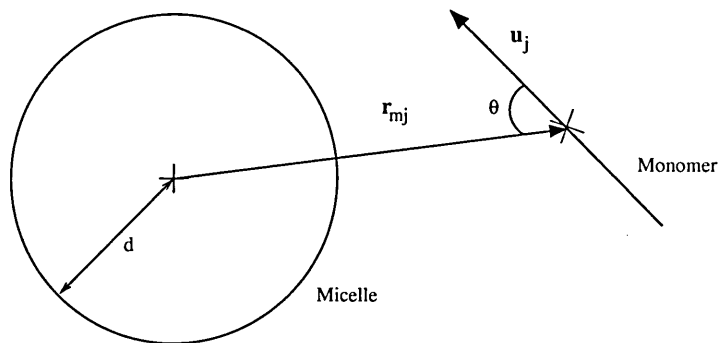


Fig. 5.23: Diagram representing a micelle and a free monomer

butions have been averaged over all the simulated systems to give the probability map shown on Fig. 5.24(a). This shows that when the monomer-micelle distance is small, the monomers preferably adopt $\cos(\theta)$ values of ≈ -1 corresponding to radial alignment with the hydrophilic end pointing outwards. At $R - d$ values of $\sim 2 - 3\sigma_0$, the preferred $\cos(\theta)$ value is $\approx +1$. This suggests that the orientation flipping mechanism illustrated in Fig. 5.21 is a relatively common event. These data also points the possibility of determining an effective monomer-micelle interaction for this class of systems.

However, it is not clear whether this observation indicates a genuine phenomena as the calculation has been restricted to entering and leaving monomers only. One could argue, alternatively, that there is no particular angular dependence in this effective micelle-monomer interaction and that Fig. 5.24 only shows that monomers have got to 'turn in' in the right way for a successful insertion. This could particularly be the case here, due to the lack of flexibility of the particle used. This alternative view is supported by a second calculation of the micelle-monomer radial distribution function as a function of $\cos(\theta)$, this time averaged over all of the monomers in the system (Fig. 5.24(b)). This plot clearly indicates the independence of this distribution function on $\cos(\theta)$, suggesting that monomers of all orientations get close to the micelle, but that they do not join it unless their orientations are appropriate.

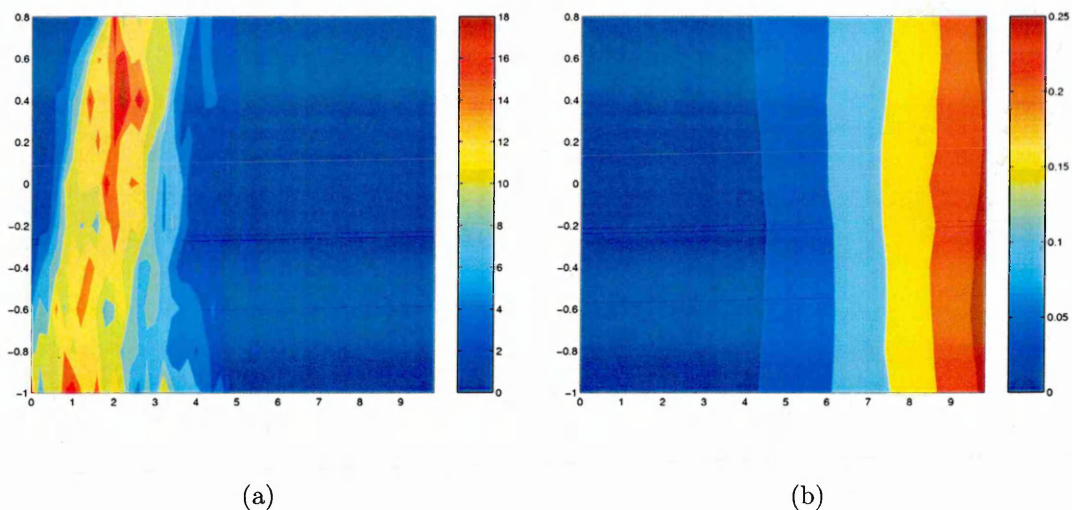
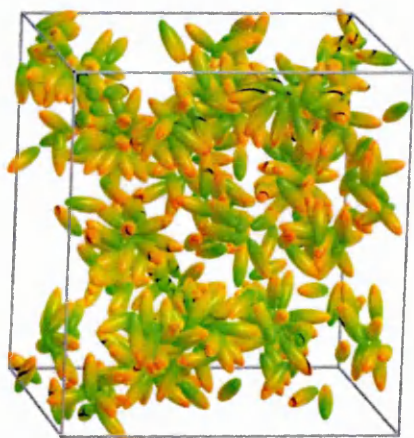


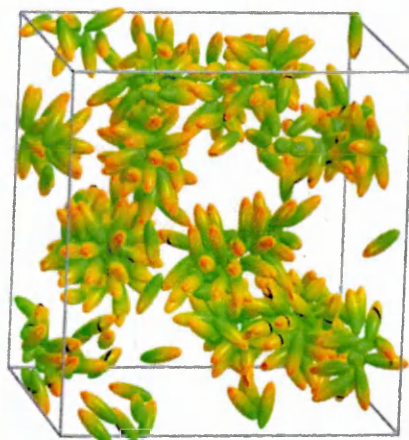
Fig. 5.24: (a): Averaged distribution of $\cos(\theta)$ as a function of r of entering and leaving monomers only from a micelle (b): Averaged distribution function $g(r, \cos(\theta))$ of all monomers

5.4 Effect of model parameterisation on system properties

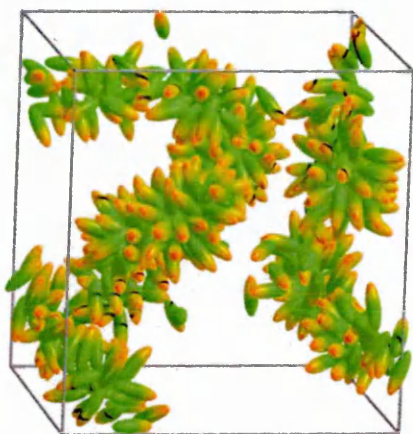
The aim of this section is to investigate the sensitivity of the model system properties to the molecular parameters H and κ' . For this purpose, a range of H values ($H = 50, 60, 70, 80$ and 90%) and 2 values of κ' ($\kappa' = 1/2$ and $\kappa' = 1/4$) have been used. Thus, the whole range of amphiphilic behaviour is covered here, from large to small hydrophilic head group and from low to high amphiphilic strength. All of the simulations presented in this section have been performed with the same parameters, system size and run lengths as were used in the previous section.



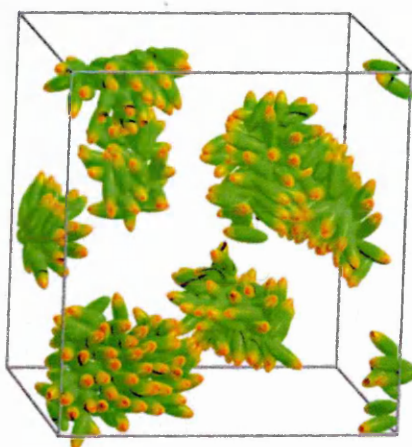
(a) $H = 50\%$



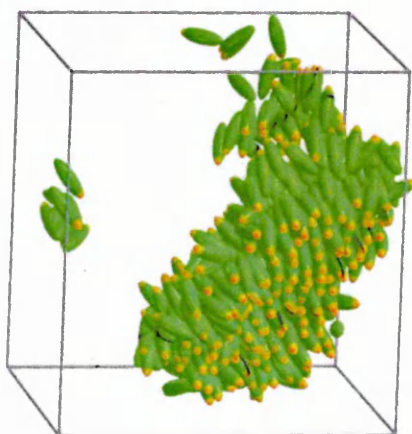
(b) $H = 60\%$



(c) $H = 70\%$

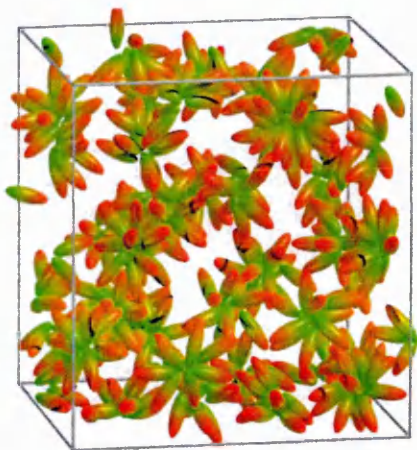


(d) $H = 80\%$

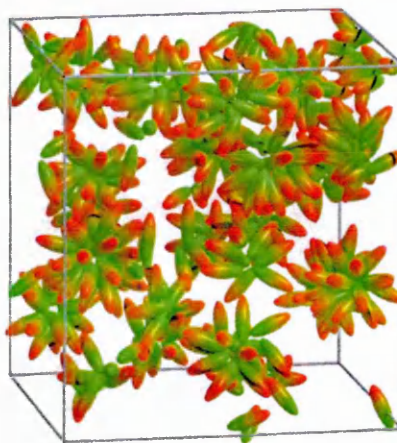


(e) $H = 90\%$

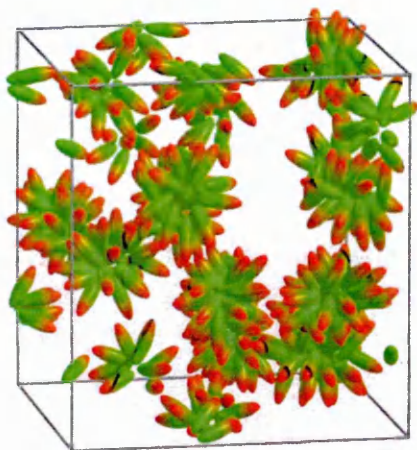
Fig. 5.25: Final configuration snapshots for different values of H at $T = 0.9$ and $\kappa' = 1/2$



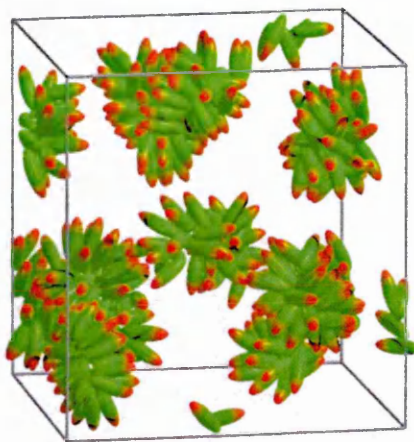
(a) $H = 50\%$



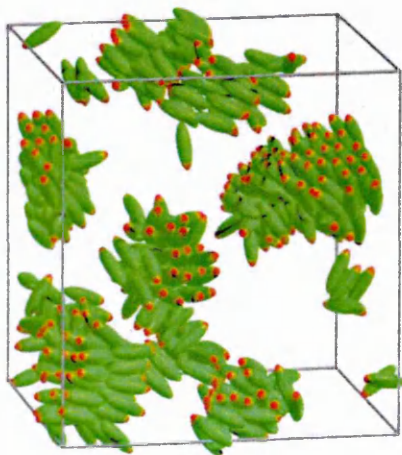
(b) $H = 60\%$



(c) $H = 70\%$

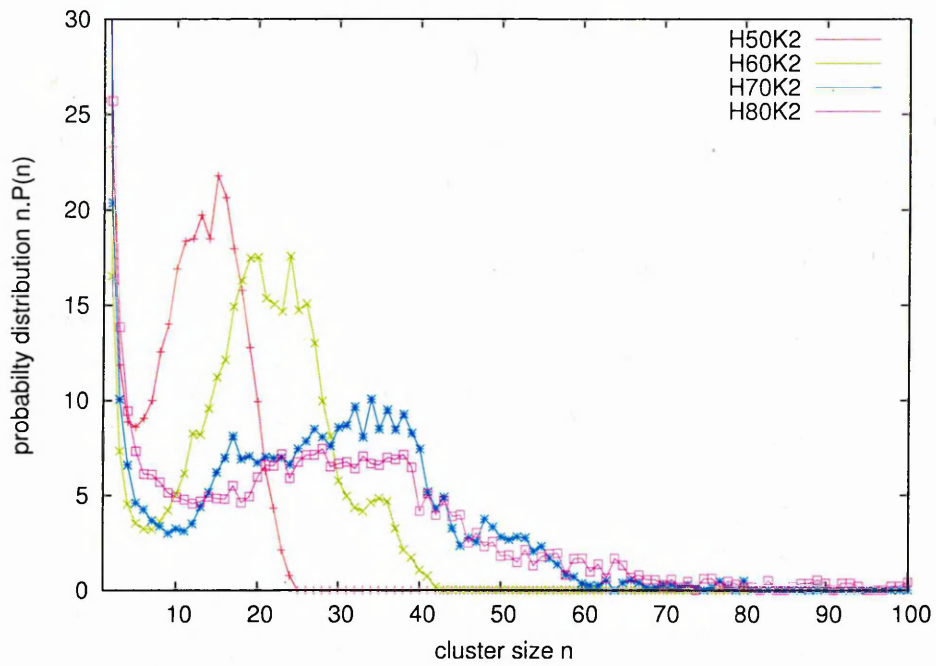


(d) $H = 80\%$

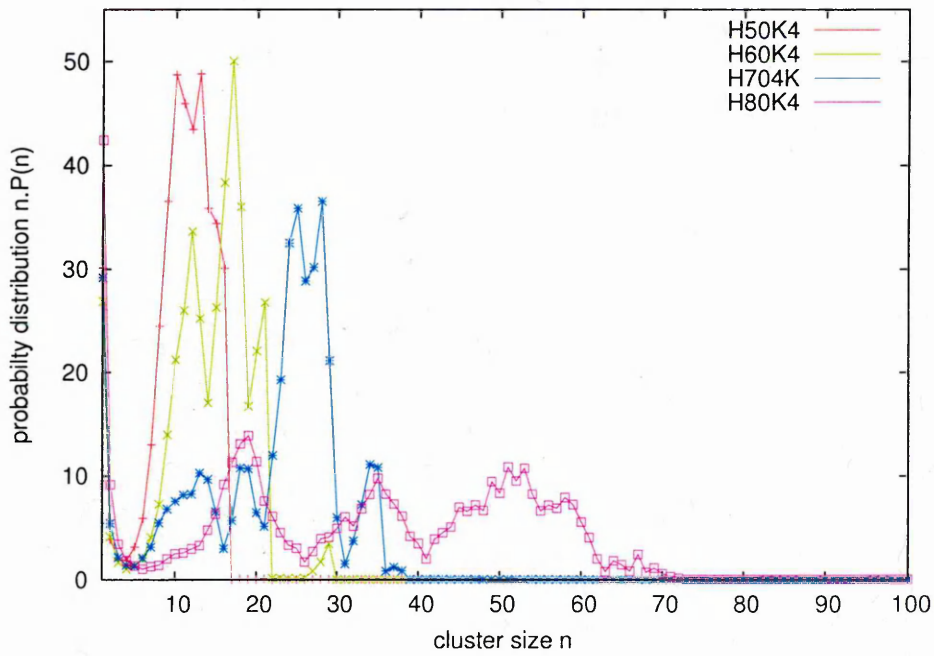


(e) $H = 90\%$

Fig. 5.26: Final configuration snapshots for different values of H at $T = 0.9$ and $\kappa' = 1/4$



(a) $\kappa' = 1/2$



(b) $\kappa' = 1/4$

Fig. 5.27: Cluster size distribution functions $n \cdot P(n)$ for $H = 50, 60, 70$ and 80% at both $\kappa' = 1/4$ and $\kappa' = 1/2$ computed with $r_c = 0.80\sigma_0$

5.4.1 Micelle structures

Micelle size and shape

The final configuration snapshots obtained from these runs are shown on Fig. 5.4 for $\kappa' = 1/2$ and Fig. 5.4 for $\kappa' = 1/4$. From these, the effect of H seems to be significant with respect to micelle size and shape. For both κ' values, bigger clusters appear as H is increased. This is due to the fact that smaller headgroups lead to less curvature and, therefore, the formation of larger aggregates. This view is confirmed by the $n \cdot P(n)$ plots shown in Fig. 5.27. In both cases, small head group (large H value) is associated with large micelles and broad distribution functions. Compared with $\kappa' = 1/2$, the distributions shown for $\kappa' = 1/4$ display higher peaks, slightly shifted to smaller aggregation numbers. Thus, an increase in the amphiphilic strength (equivalent to decreasing κ') results in smaller micelles, these being available in larger quantities for a given monomer concentration. For $H=80\%$ and $\kappa' = 1/4$, micellar behaviour breaks down as the distribution starts showing multiple peaks. Ultimately, decreasing head group size combined with an increasing head-solvent attraction seems to, instead, develop bilayer-like patches of different size (see Fig. 5.25(e) and Fig. 5.26(e)).

The effects of H and κ' on micelle shape are shown on Fig. 5.28 with the principal moments of inertia plotted as a function of the cluster size n . For both κ' values, the variation of the shape with H generally follows the same trend as was observed for the exponential model (see Chapter 4) and is consistent with other studies [189].

Tab. 5.2 shows the moment of inertia values at the aggregation number for each system. From these data, the micelle shape appears largely independent of H and κ' . Fig. 5.28(b) and Fig. 5.28(d) show a close-up of the MOI data over the cluster size range $2 < n < 15$. This reveals an interesting behaviour of the micelle shape for different H values at low n . Thus, for any $n < 15$, $I_S(H = 80\%) < I_S(H = 70\%) < I_S(H = 60\%) < I_S(H = 50\%)$ and $I_L(H = 80\%) > I_L(H = 70\%) >$

	I_L	I_M	I_S	\sim Agg. Numb.
H50K2	0.398	0.341	0.25	14
H60K2	0.389	0.345	0.265	22
H70K2	0.393	0.350	0.255	30
H80K2	0.396	0.346	0.256	35
H50K4	0.404	0.341	0.253	12
H60K4	0.396	0.343	0.260	15
H70K4	0.391	0.345	0.262	25
H80K4	-	-	-	-

Tab. 5.2: Principal moments of inertia taken at the aggregation number for all systems. Note the H80K4 system with no values as no true peak can be observed in the cluster size distribution function $n \cdot P(n)$

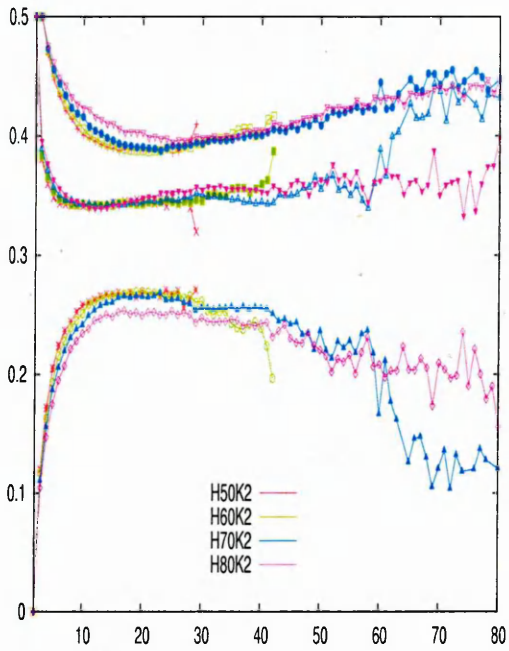
$I_L(H = 60\%) > I_L(H = 50\%)$ although, I_M remains constant with H . This corresponds to a slight flattening combined with an elongation of the micelles as H is increased.

The effect of the model parameters on the aggregate shape can, then, be summarised as such:

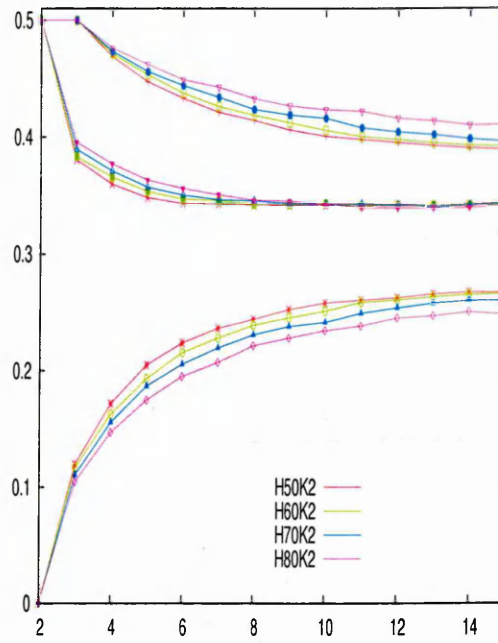
- As n is increased, the micelle shape becomes increasingly cylindrical for a given set of parameters H and κ' .
- A slight flattening and elongation of the micelles is seen with increasing H .
- κ' has virtually no effect on the shape of a given micelle size although their $n \cdot P(n)$ distribution functions are significantly different.

Micelle structural conformation

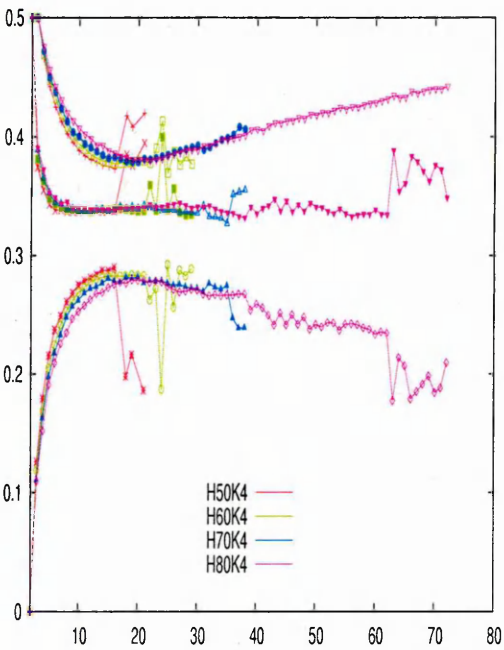
The positional distribution functions, $g_{pos}(r)$, computed for all of the systems studied are shown on Fig. 5.29. From these plots, the effect of n , H and κ' on the internal positional organisation of the micelle components is apparent. The variation of the peak heights here reflects to the variation of the numbers of micelles observed for each size category of sizes. Certain categories are not



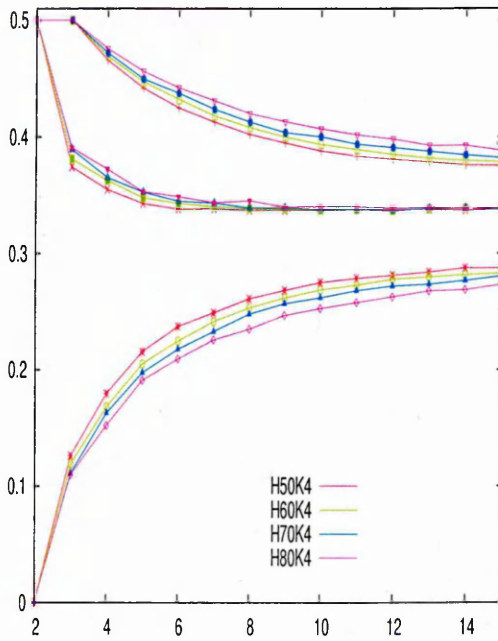
(a)



(b)



(c)



(d)

Fig. 5.28: Principal moments of inertia vs. cluster size n . (a) and (c) illustrate data for the systems with $\kappa' = 1/2$ and $\kappa' = 1/4$, respectively. (b) and (d) show the same plots zoomed into the region $2 < n < 15$

represented in all cases, since some systems simply do not exhibit these cluster sizes.

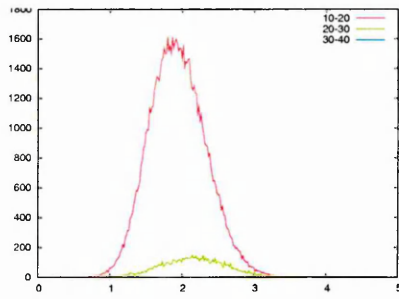
A good way of comparing these distributions is to characterise them by their different moments. Fig. 5.30 shows the first moment or *mean* with increasing H as a function of κ' and micelle size.

From these data, it is clear that the average radial position of the amphiphiles remains largely independent of H for a given micelle size and value of the amphiphilic strength κ' . Also, it can be observed that this average position increases with micelle size and is smaller for all $\kappa' = 1/4$ systems than for the equivalent $\kappa' = 1/2$ systems. The $\kappa' = 1/4$ distributions for small and moderate cluster sizes are generally sharper than those for $\kappa' = 1/2$.

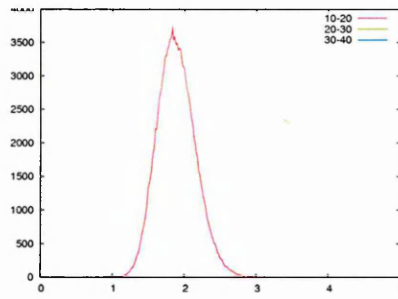
One can also observe that some of the distributions are slightly skewed towards larger r values. This is consistent with the breathing of the micelles and piston-like motion of the amphiphiles observed in animation of these systems. However, it is difficult to quantify this skewness due to poor statistics: too few micelles are present to allow statistically significant measurements to be achievable.

Fig. 5.31 illustrates the behaviour of the orientational structure of the amphiphilic rods within a micelle for different size categories. These $g_{ang}(\cos(\theta))$ curves indicate a qualitative change related to the amphiphilic strength parameter κ' . For $\kappa' = 1/4$, two or more relatively narrow peaks can be found whereas for $\kappa' = 1/2$, less structure and only one peak can be found at large $\cos(\theta)$.

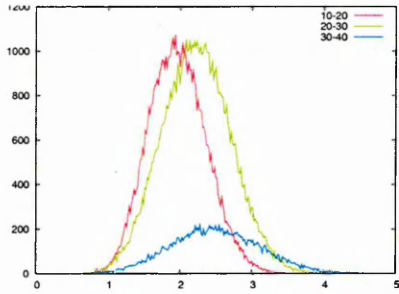
This fact is confirmed by the radial ordering of the molecular orientation \mathbf{u}_i with respect to their position to COM vector r_i . The radial order parameter $P_R(\mathbf{u}_i \cdot r_i)$ has been calculated and averaged over micelles of the three size category considered here, and is plotted in Fig. 5.32 as a function of H and κ' . From this graph, it becomes apparent that the radial ordering of the micelles is larger for the $\kappa' = 1/4$ systems than for the $\kappa' = 1/2$ systems which, as we have seen above, display a more diffuse internal structure. Also, it can be noted that this radial order pa-



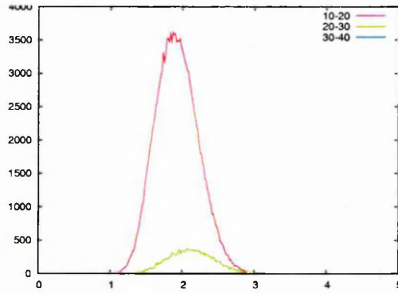
(a) $H = 50\%$, $\kappa' = 1/2$



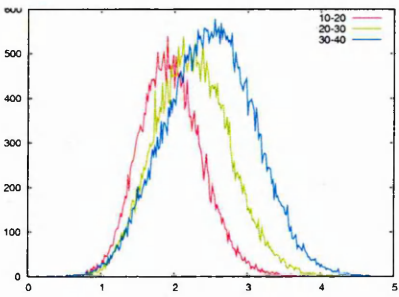
(b) $H = 50\%$, $\kappa' = 1/4$



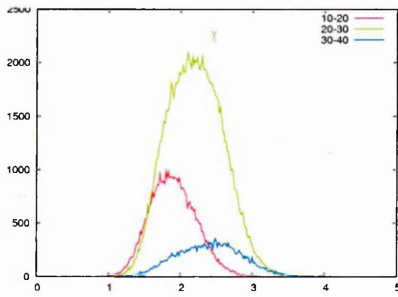
(c) $H = 60\%$, $\kappa' = 1/2$



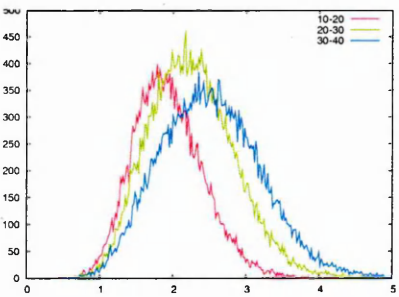
(d) $H = 60\%$, $\kappa' = 1/4$



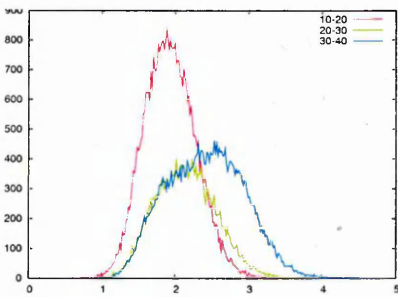
(e) $H = 70\%$, $\kappa' = 1/2$



(f) $H = 70\%$, $\kappa' = 1/4$



(g) $H = 80\%$, $\kappa' = 1/2$



(h) $H = 80\%$, $\kappa' = 1/4$

Fig. 5.29: The positional distribution functions, $g_{pos}(r)$ for eight of the systems studied, broken down into 3 different micelle size categories

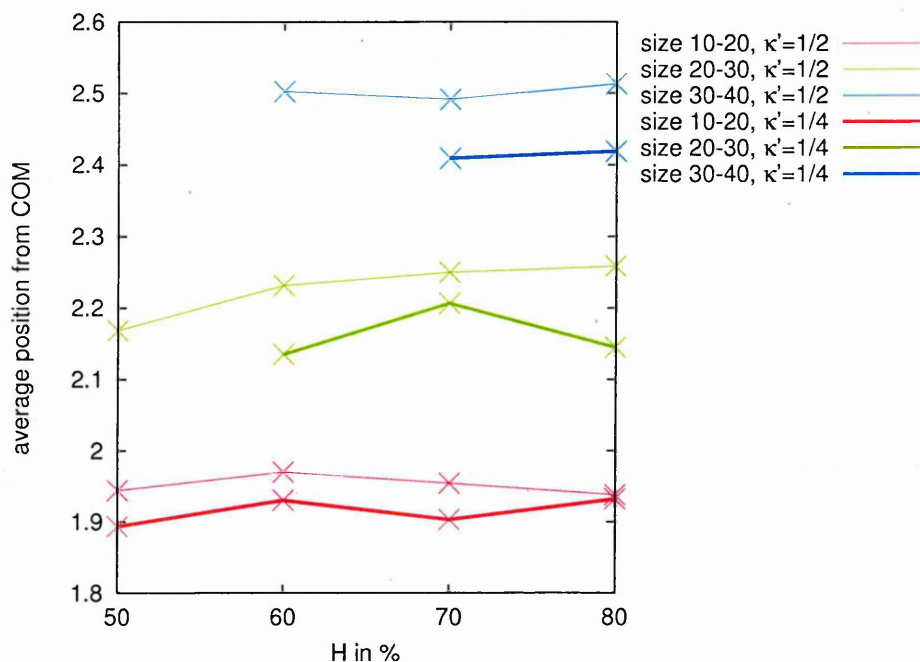
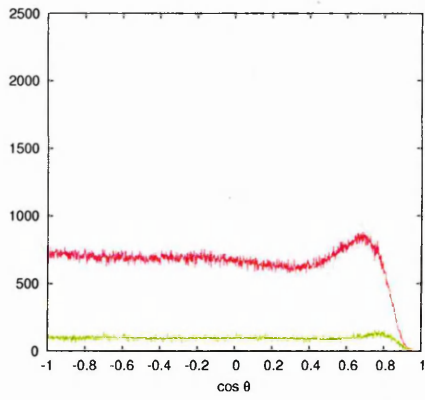


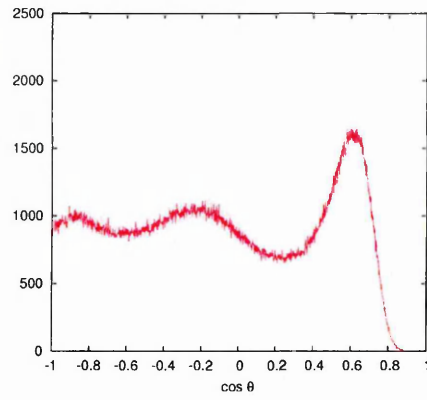
Fig. 5.30: mean or first moment of the positional distribution function $g_{pos}(r)$

parameter increases with decreasing H . Confirmed by the configuration snapshots, the H50K4 micelles are well defined (P_R of $\sim 0.8-0.9$) whereas the H80K2 micelles display low P_R values of ~ 0.5 , consistent with their bilayer patch structure.

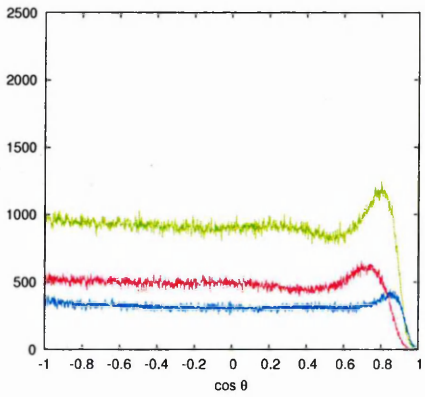
The positions of the primary peaks in $g_{ang}(\cos(\theta))$ are summarised in Fig. 5.33. The variation of these distributions as the parameter H is increased is quite marked and agrees with previous analysis performed in this chapter. In both cases ($\kappa' = 1/2$ and $\kappa' = 1/4$), the reduction of headgroup size causes the highest peak position to be shifted to smaller angles.



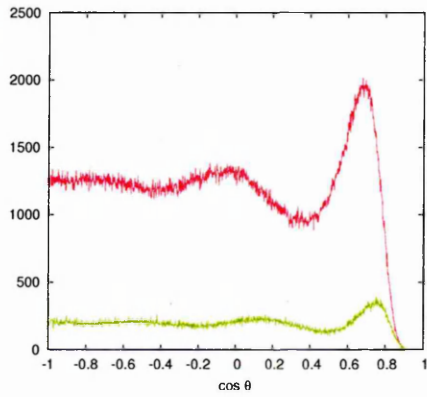
(a) $H = 50\%$, $\kappa' = 1/2$



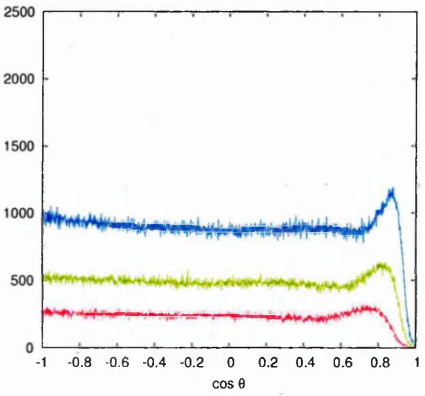
(b) $H = 50\%$, $\kappa' = 1/4$



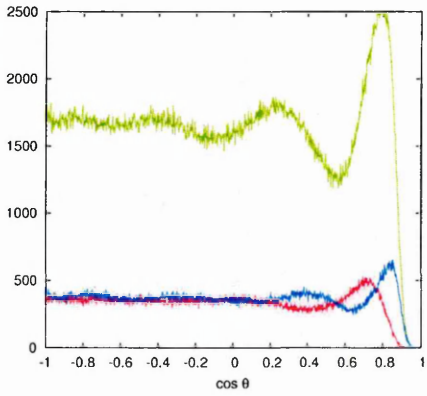
(c) $H = 60\%$, $\kappa' = 1/2$



(d) $H = 60\%$, $\kappa' = 1/4$

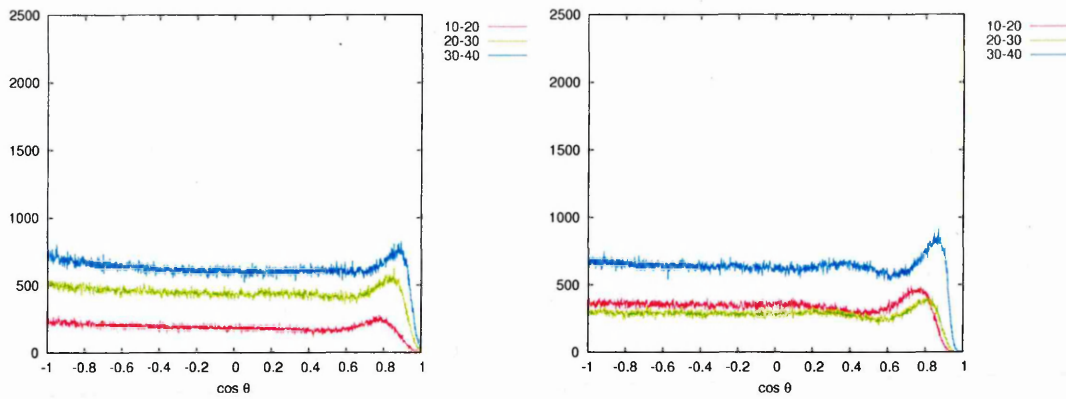


(e) $H = 70\%$, $\kappa' = 1/2$



(f) $H = 70\%$, $\kappa' = 1/4$

Fig. 5.31: Angular distribution function, $g_{ang}(\cos(\theta))$, for eight of the systems studied, broken down into 3 different micelle size categories



(g) $H = 80\%$, $\kappa' = 1/2$

(h) $H = 80\%$, $\kappa' = 1/4$

Fig. 5.31: (Continued)

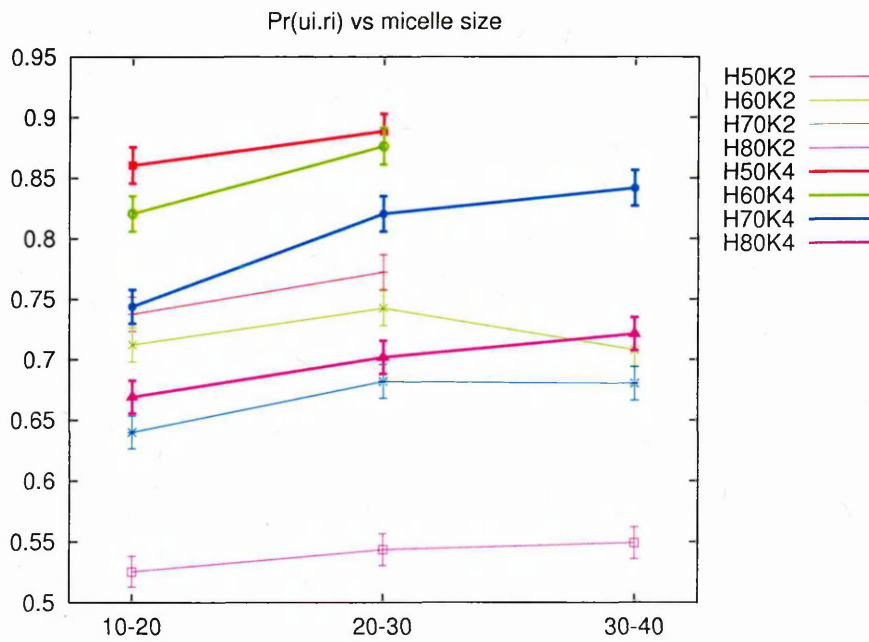


Fig. 5.32: Radial order parameter $P_R(\mathbf{u}_i \cdot \mathbf{r}_i)$

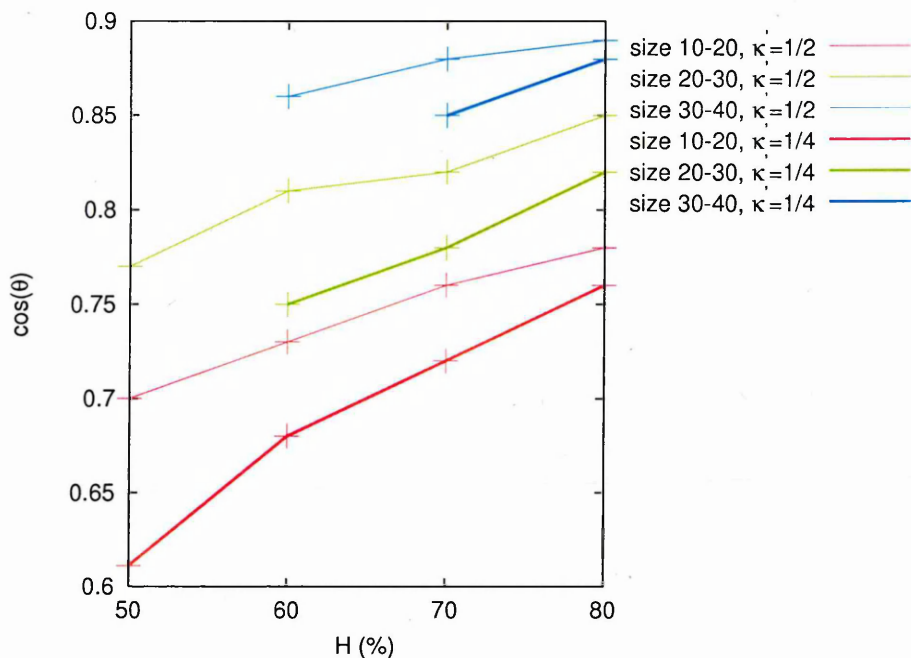


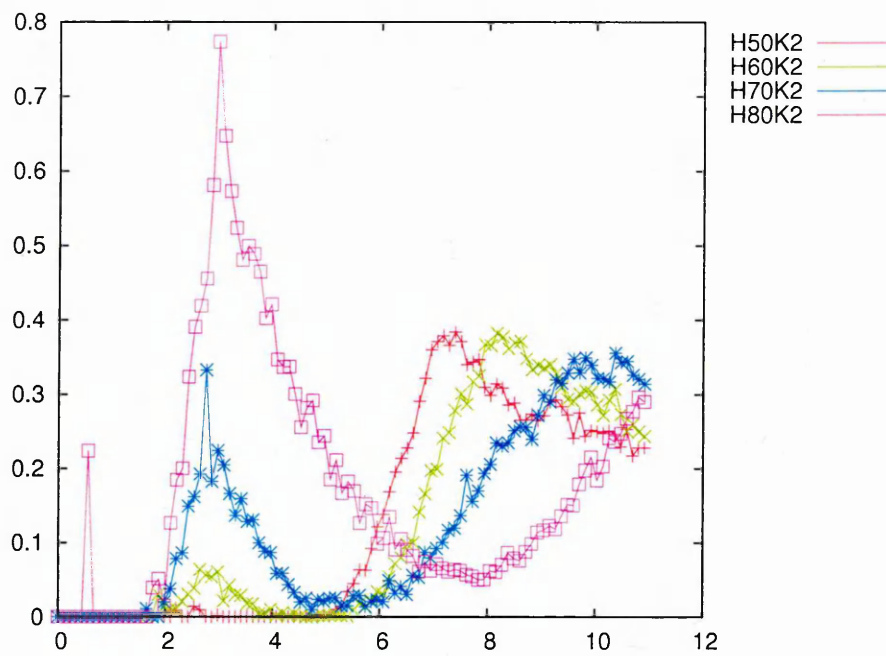
Fig. 5.33: Position of the highest peak in the $g_{ang}(\cos(\theta))$

5.4.2 Structure and dynamic aspects of the micellar behaviour

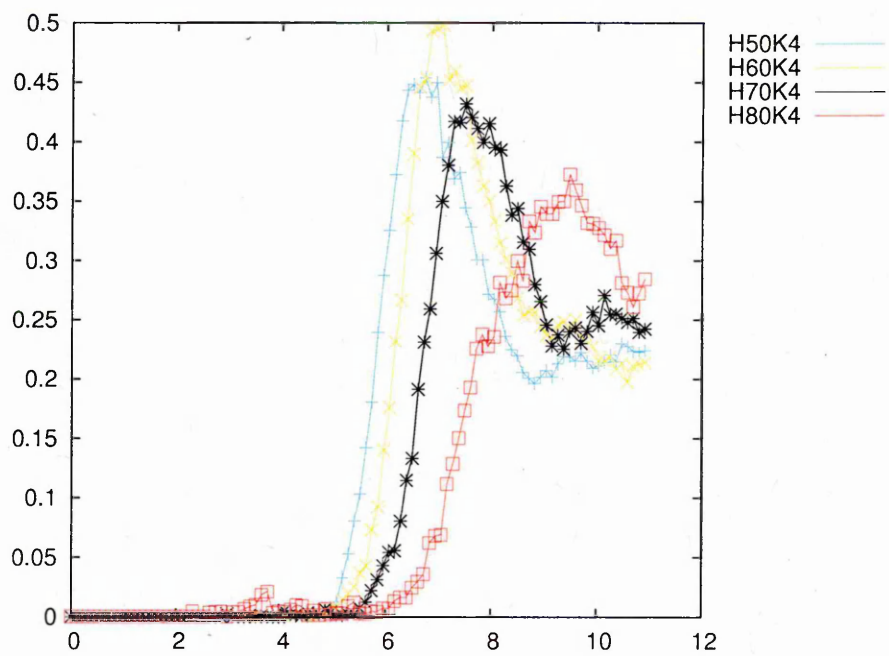
micelle-micelle interaction

As it has been shown earlier, the observed change in micellar population is due to monomer exchange and, even more dramatically, to micelle-micelle events such as fusion or break-up. The fusion/breakup events can be viewed as being influenced by an effective micelle-micelle-interaction which can itself be characterised by the micelle-micelle radial distribution function. This RDF has, therefore, been computed for all of the systems studied by considering the centres of mass of all micelles of a given size category. Fig. 5.34 shows the resulting curves for micelle sizes $n \geq 10$ for the $\kappa' = 1/2$ and $\kappa' = 1/4$

In all cases, as H is increased, the peaks of the RDF functions are shifted to higher values. This is consistent with the previous analysis which linked increasing H to enlargement of micelles. Note that for the $\kappa' = 1/2$ systems, an anomalous



(a) $\kappa' = 1/2$



(b) $\kappa' = 1/4$

Fig. 5.34: Micelle-micelle radial distribution functions

H	50	60	70	80
$\kappa' = 1/2$	7.28	8.43	10.15	-
$\kappa' = 1/4$	6.73	7.46	7.90	9.51

Fig. 5.35: Averaged distance between micelles estimated from radial distribution functions

peak appears at short distances ($\approx 3\sigma_0$) which becomes more pronounced as H is increased. This is probably a consequence of the micelle size lower limit chosen for this calculation being too small for these systems (micelles are generally bigger for these $\kappa' = 1/2$ systems) so that the algorithm picks up small sub-aggregates in addition to the main micelles. For $\kappa' = 1/4$, this effect is not apparent as the micelles are smaller and better defined for these systems.

Tab. 5.35 indicates the position of the first true micelle-micelle peak in the radial distribution functions of Fig. 5.34. From these data, it can clearly be seen that the average distance between micelles increases with H and decreases with κ' .

An interesting comparison can be then made between the $H70K4$ and $H60K2$ systems. By looking at the configuration snapshots of Fig. 5.26(c) and Fig. 5.25(b), these two systems seem to be similar in terms of number of micelles present. The associated cluster size distribution functions indicate that the $H60K2$ system has a broad peak positioned at an aggregation number of ~ 20 whereas the $H70K4$ system has a narrower peak centered around ~ 25 . The $H70K4$ micelles are, therefore, slightly bigger in terms of the number of amphiphiles they contain. However, if one looks at the associated radial distribution functions, the average distance between micelles is bigger for the $H60K2$ system than for $H70K4$ by about $0.5\sigma_0$. This apparent contradiction is explained, however, by the micelle structural conformation analysis presented earlier. While the inertia analysis indicates that the two systems contain both near-spherical micelles with no significant differences (Fig. 5.28 and Fig. 5.2) in their shape, the positional distribution functions (Fig. 5.29) indicate that the $H60K2$ micelles are more diffuse and that their average radii are bigger than those of the $H70K4$ micelles. The

strong amphiphilicity of the *H70K4* system, then, seems to induce the amphiphile to pack more efficiently within the micellar aggregate. This is confirmed by the orientational distribution function showing more structure for *H70K4* than for *H60K2* (Fig. 5.31). For the low amphiphilicity system, in contrast, the effective micelle radius is larger allowing more monomer exchange with the solvent. This is also confirmed by the broad peak observed of the $\kappa' = 1/2$ systems on the size distribution functions compared with the narrower peak observed with $\kappa' = 1/4$ (Fig. 5.27).

Micelle diffusion

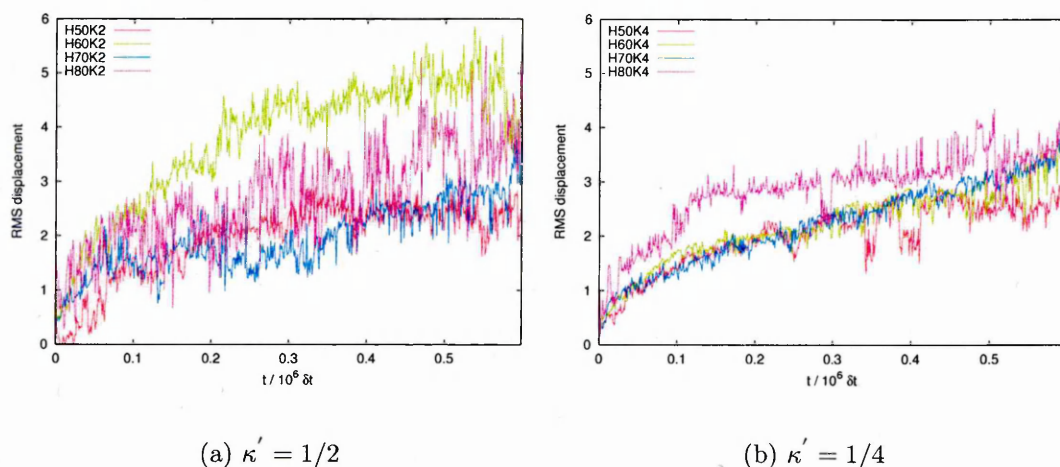


Fig. 5.36: RMS displacement of micelles (micelle size > 10) for different systems.

Micelle mobility has also been measured for all systems, yielding the results shown on Fig. 5.36. By examining these plots for $\kappa' = 1/2$ and $\kappa' = 1/4$, all of the systems display a similar diffusion pattern migrating from $\sim 2\sigma_0$ to $\sim 5\sigma_0$ after $0.6 \cdot 10^6 \delta t$. However, these data are very noisy due to the small number of long-lived micelles present in each system. While these data indicate that micelle migration does take place on the timescales accessible to our simulations, the average displacement over $0.6 \cdot 10^6 \delta t$ is less than the micells radius values. This indicates that our simulations are not able to access the diffusive behaviour of the micelles. Given

the considerable level of overlaps in these data, it appears inappropriate to use them to infer any H or κ' dependence of micelle mobility.

5.4.3 Monomer Dynamics

It has been shown so far that this model is able to access the length and time scales required to observe micelle-micelle events like fusion and break-up. Also, it has been established that all $\kappa' = 1/2$ and $\kappa' = 1/4$ systems with $H \leq 80\%$ spontaneously form micelles with coexistence in free monomers. In this section, the dynamics of these free monomers is considered.

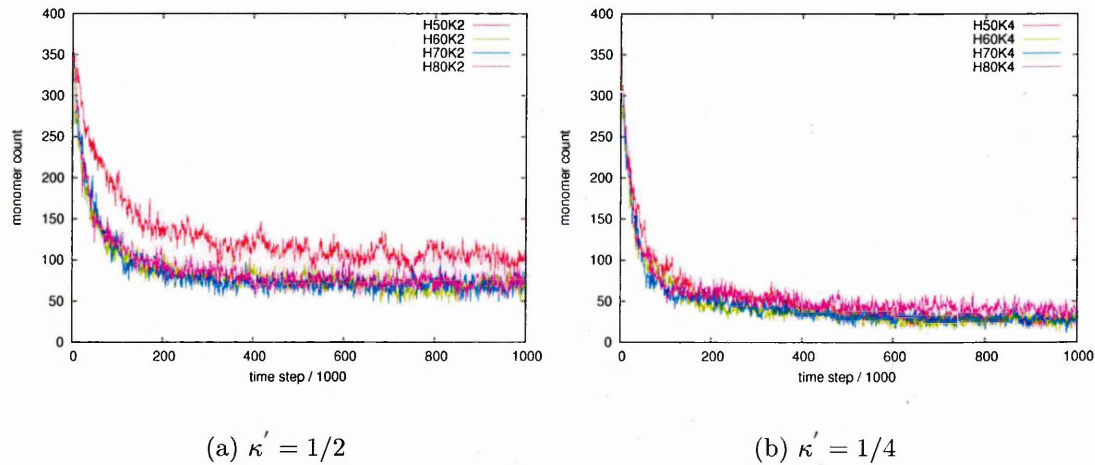


Fig. 5.37: Evolution of the monomer number, $r_c = 0.85\sigma_0$

Fig. 5.37 represents the evolution of the monomer number in each system for $\kappa' = 1/2$ (Fig. 5.37(a)) and $\kappa' = 1/4$ (Fig. 5.37(b)). From these data, it appears that all systems share the same dynamic pathway to cluster formation. As has been seen earlier, the monomer numbers attain non-zero steady state values after a rapid initial clustering. It can be also observed that the steady state monomer number is approximately equal for all H values for a given κ' and that this value is higher for $\kappa' = 1/2$ than for $\kappa' = 1/4$. The one exception to this is the H50K2 system which possesses the highest number of monomers of all the system

simulated.

It is also interesting to analyse the life-times of the monomers for each system: a distribution of the monomer life-times is plotted for each system on Fig. 5.38.

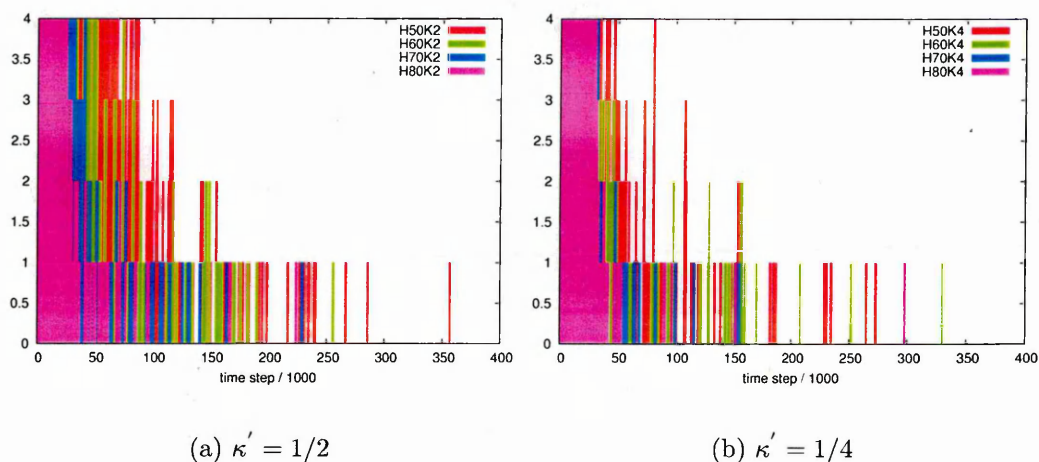


Fig. 5.38: Monomer life-time distribution

These distributions of monomer life time show for all systems:

- High number of short-lived monomers
- A long-tail for the long-lived monomers

The large number of short-lived monomers corresponds to particles which are, in fact, bouncing in and out of their micelle. Thus, in line with the high frequency fluctuations in the micelle shapes and occupancies, these are amphiphiles which are considered monomers by the cluster counting algorithm but remain associated with a particular micelle.

The behaviour of the long-lived micelles appears to show some H dependence, the distributions progressively widening with decrease in H . For all systems, though, some monomer lifetimes in excess of $5 \cdot 10^4 \delta t$ were observed, confirming that monomers are able to reside in the solvent for extended periods before eventually joining one of the micelles.

5.5 Conclusion

In this chapter, an alternative amphiphilic potential with a sharper ‘switch’ between the hydrophilic region and lipophilic region has been developed. This tanh model has proved to be successful at reproducing amphiphilic phases and capable of showing changes in system behaviour due to variation of the model’s two main parameter H and κ' , the HLB and the amphiphilic strength.

The micellar phase region has then been investigated in greater detail in a large simulation of the H70K2 system ($H = 70\%$ and $\kappa' = 1/2$). This has yielded genuine micellar behaviour with a multiple micelle arrangement forming in equilibrium with monomers. Specifically, this CG model has exhibited to the self-assembly of several micelles of ~ 30 amphiphiles. Different micellar shapes have been identified by analysis of the moments of inertia, cylindrical micelles seeming to be favoured as the micelle size n increases. A tracking algorithm has been developed to identify and follow the history and components of the micelles in the system. Using this, the micelle population change has been measured through calculation of self-similarity coefficient. This self-similarity coefficient has shown that micelle occupancies change via several processes:

- The rattling motion of amphiphiles joining and leaving the main aggregate on a very fast timescales. This is closely related to the breathing mode or shape fluctuations of the micelle.
- Some monomers leave the micelle on a longer timescale either rejoining their initial micelle or joining another micelle. During this joining process, monomers which flip their orientations appear to ‘dock’ more readily with the receiving micelle.
- Fusion between two micelles. This process leads to dramatic changes in micelle population.

The micelle-micelle radial distribution function is similar to that of a Gaussian

sphere potential. This is consistent with the above observation: the ability of the micelles to overlap, permits fusion events.

The effect of the molecular interaction parameters H and κ' on the properties of the micellar phase have also been investigated through further large system simulations. These have shown that the micelle size distribution function $n \cdot P(n)$ is very sensitive to the model's parameters. Thus, bigger micellar aggregates can be generated by either increasing H or decreasing κ' . This enlargement is accompanied by an elongation and flattening of the micelles. Structural analysis indicates the dominating effect of H on the micelle curvature. In comparison, κ' has a minor effect on the curvature but it does affect the intra-micellar structural organisation.

The effective micelle-micelle interaction is also affected by H and κ' . As H (κ') is increased (decreased), the micelle size increases, leading to a significant change in the micelle-micelle $g(r)$. However, micelle diffusion has proved difficult to assess due to low mobility on the timescales accessible to our model. The monomer dynamics showed broadly similar behaviour for all the systems studied, despite the differences in the characteristics of the micelles coexisting with those monomers.

CHAPTER 6

Behaviour of mixed micelles

In the previous chapter, a detailed study of one-component micellar systems was presented. Experimentally, however, isometrically pure systems are expensive to produce and generally have limited performance compared to less expensive mixture systems. It is therefore both interesting and relevant to investigate amphiphilic mixture systems by computer simulation. In this chapter, binary mixtures of amphiphiles are considered and their micellar behaviours analysed. Specifically, we investigate how micellar systems are affected by the mutual interaction strength between the two types of amphiphiles and the composition of the amphiphile mixtures.

6.1 Simulation methods

In the binary mixture systems investigated here, all of the amphiphilic rods employed have the same geometry as has been used in the previous chapters ($\sigma_{ee} = 3$ and $\sigma_{ss} = 1$). The key difference between the two types of amphiphiles, lies, then, in their rod-sphere interaction potentials, defined via the parameters H and κ' . Specifically, we have chosen to investigate mixtures of particles with

parameterisation H70K2 and H50K4. These molecules have been selected as they both form well-defined, near spherical micelles when present as the only amphiphile but yield very different cluster size distribution functions (recall Chapter 5).

In our model, the amphiphilic character of the rods is set via the rod-sphere (*i.e.* the amphiphile-solvent) interaction only. Therefore, in studying the effect of the mutual interaction between the two types of amphiphiles, only the Gay-Berne potential dealing with the interaction between unlike rods is considered.

It is known from some recent coarse-grained models [118, 119] that the accurate modelling of an amphiphile-amphiphile interaction is non-trivial due to the complexity of the molecules involved. For instance, studies of lipid mixtures in all-atom simulations of bilayer systems have revealed complex structures and arrangements of the different lipid molecules [190]. In our model, the rod-rod potential is modelled by the Gay-Berne potential using the parameterisation GB($\kappa = 3$, $\kappa' = 1$, $\nu = 2$, $\mu = 1$) corresponding to a symmetric amphiphile-amphiphile interaction. This means that the well-depth is independent of the relative orientations of the two rods, *i.e.* the tail-tail, head-head and head-tail interaction strengths are equal. As shown in the preceding chapter, this parameterisation, although unrealistic, proved successful in forming one-component micellar phases. Therefore, we now extend the use of this assumption to mixtures in order to determine its limits and analyse its effects on mixture behaviour.

Using our model, the mutual interaction strength between unlike amphiphiles can be modified while keeping the orientational dependence symmetric. As described in Chapter 2, theoretical treatments show that reducing or increasing the interaction strength can significantly modify the CMC and the distribution of the two types of amphiphiles between the monomer phase and micelle phase. Here, therefore, we focus on the effects of varying this interaction strength. In doing this, more complex micellar structures than those found in one-component systems are

expected.

To achieve this, a coefficient β is introduced as weight factor on the attractive part of the Gay-Berne potential (see Chapter 4).

$$U_{GB}(\hat{\mathbf{r}}_{ij}, \hat{\mathbf{u}}_i, \hat{\mathbf{u}}_j) = 4\epsilon(\hat{\mathbf{r}}_{ij}, \hat{\mathbf{u}}_i, \hat{\mathbf{u}}_j) \left[\left(\frac{\sigma_0}{r_{ij} - \sigma(\hat{\mathbf{r}}_{ij}, \hat{\mathbf{u}}_i, \hat{\mathbf{u}}_j) + \sigma_0} \right)^{12} - \beta \left(\frac{\sigma_0}{r_{ij} - \sigma(\hat{\mathbf{r}}_{ij}, \hat{\mathbf{u}}_i, \hat{\mathbf{u}}_j) + \sigma_0} \right)^6 \right] \quad (6.1)$$

When β is equal to 1.0, no change is made to the original potential. As β is reduced, the ‘amount of attraction’ is reduced relatively to the ‘amount of repulsion’. When β is set to zero, Eqn. 6.1 corresponds to a purely repulsive potential. Reducing the strength of the attractive component in this way has been used in other simulation work [191, 192] investigating phase separation of mixtures of symmetric Lennard-Jones particles.

The same simulation setup as that for the one-component systems has been used: total number of particle $N = 8192$, cutoff distance $r_{cut} = 4\sigma_0$, neighbour list shell $r_{nl} = 4.5\sigma_0$. The simulations were run for $1 \cdot 10^6 \delta t$ at a constant temperature of $T = 0.9$. All measurements were averaged from $0.4 \cdot 10^6 \delta t$ to $1 \cdot 10^6 \delta t$ every $1 \cdot 10^3 \delta t$.

6.2 Results

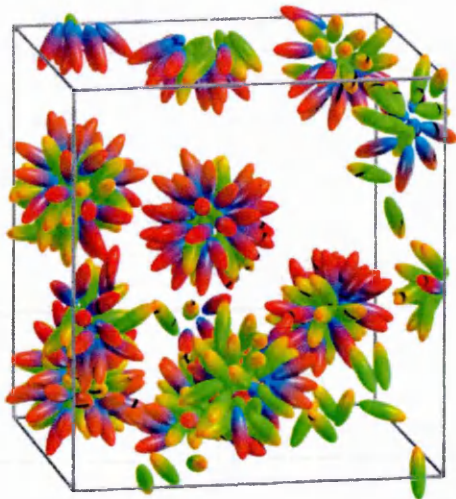
In this section, the effects of reducing the mutual attraction and varying the composition ratio of the two types of amphiphile are presented. Comparisons of micelle structures and compositions is then made with pure-component systems.

6.2.1 Effect of mutual attraction between unlike amphiphiles

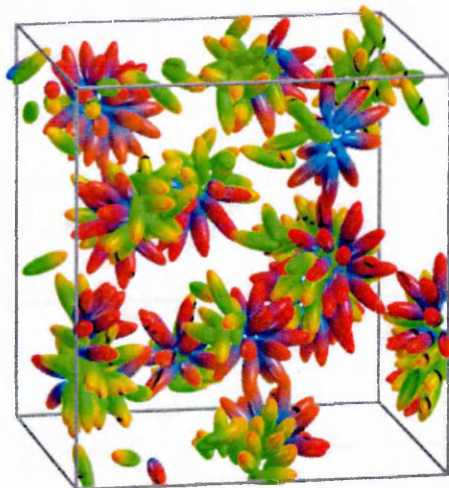
In these simulations, the β parameter has been varied from 1.0 to 0.25 at a constant 50/50 composition ratio. For an ideal mixture, at this composition ratio, an isotropic mixture of the two amphiphiles should be observed in both the micellar phase and the monomer phase, *i.e.* micelles and monomers both composed of 50% type A and 50% type B. Neglecting the effects of the different amphiphilic-solvent interactions present, an ideal mixing behaviour should then be expected for $\beta = 1.0$, whereas in the system with $\beta = 0.25$ unlike amphiphiles would tend to phase separate. Final configuration snapshots are shown on Fig. 6.1 for $\beta = 1.00$, $\beta = 0.75$, $\beta = 0.50$ and $\beta = 0.25$. From these, one can clearly observe the effect of decreasing β on the micellar structure. For $\beta = 1.0$, the micelles seem to be well mixed (bi-disperse) while the system with $\beta = 0.25$ suggests both phase separation of the two amphiphiles types within individual micelles and a few pure micelles.

Micelle size distribution function

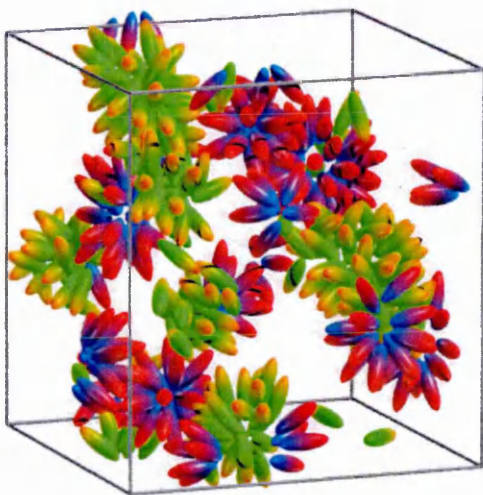
The size distribution functions calculated for the last $6 \cdot 10^6$ timesteps of these runs are shown on Fig. 6.2 along with the corresponding size distributions (recall Fig.5.27) obtained previously for each of the pure components. From these, Fig. 6.2(a) illustrates that even the $\beta = 1.0$ system departs significantly from the ideal mixing behaviour for these two systems. Whereas the H50K4 amphiphile exhibits a large number of small micelles and H70K2 a rather broad distribution of larger micelles, the $\beta = 1.0$ mixture distribution function displays a prevalence of even larger clusters. Contrary to the pure H70K2 amphiphiles, the mixture exhibits a reasonably sharper peak at aggregation number $A_n \approx 32$. This aggregation number is much higher than that of the small micelles formed by H50K4 and also exceeds that of the micelles formed by H70K2. This is a surprising result as one might have expected a linear mixing of the aggregation number for $\beta = 1.0$. Thus, an aggregation number of approxi-



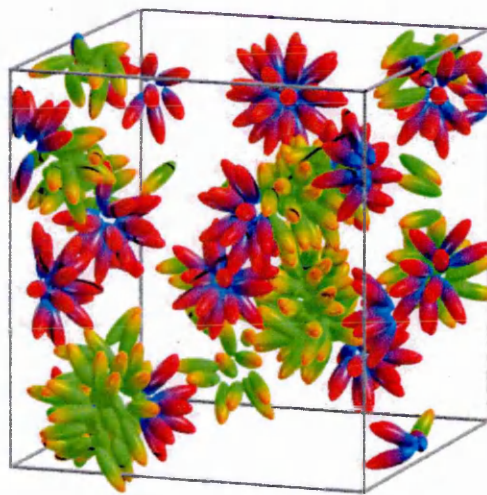
(a) $\beta = 1.0$



(b) $\beta = 0.75$

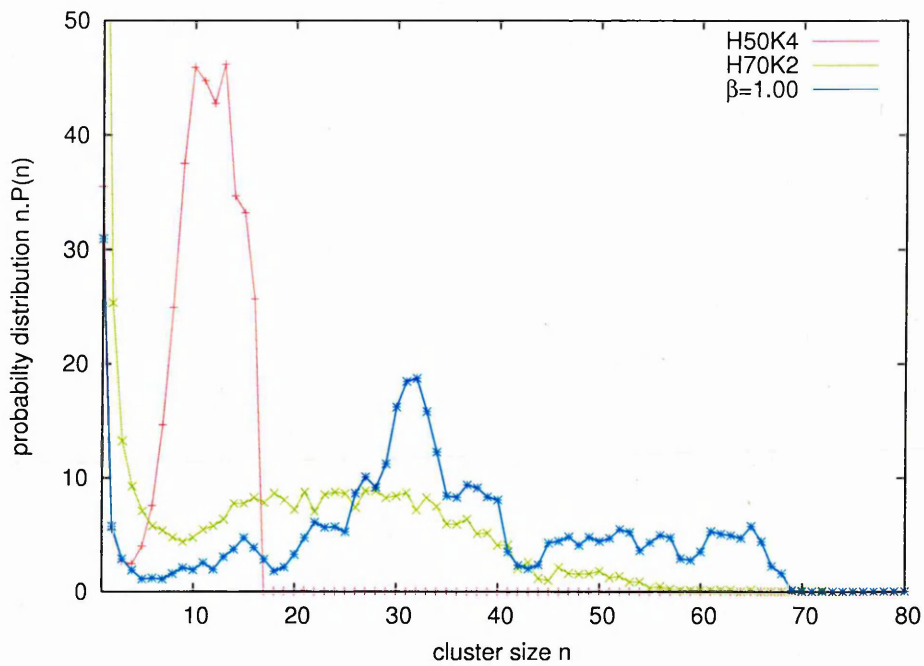


(c) $\beta = 0.50$

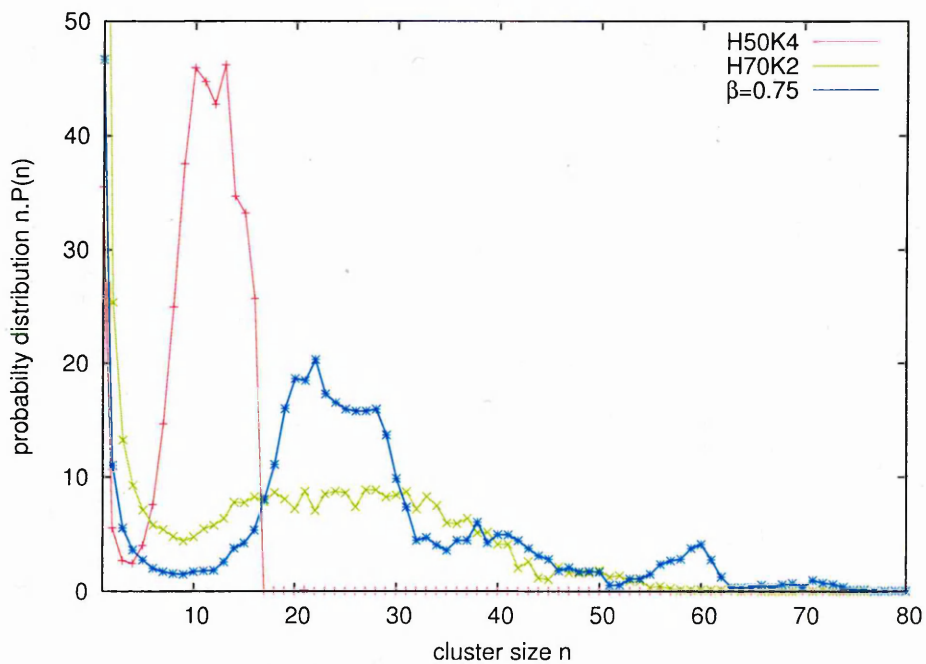


(d) $\beta = 0.25$

Fig. 6.1: Configuration snapshots of 50/50 mixtures of H70K2 (green+orange rods) and H50K4(blue+red rods) systems for a range of β values

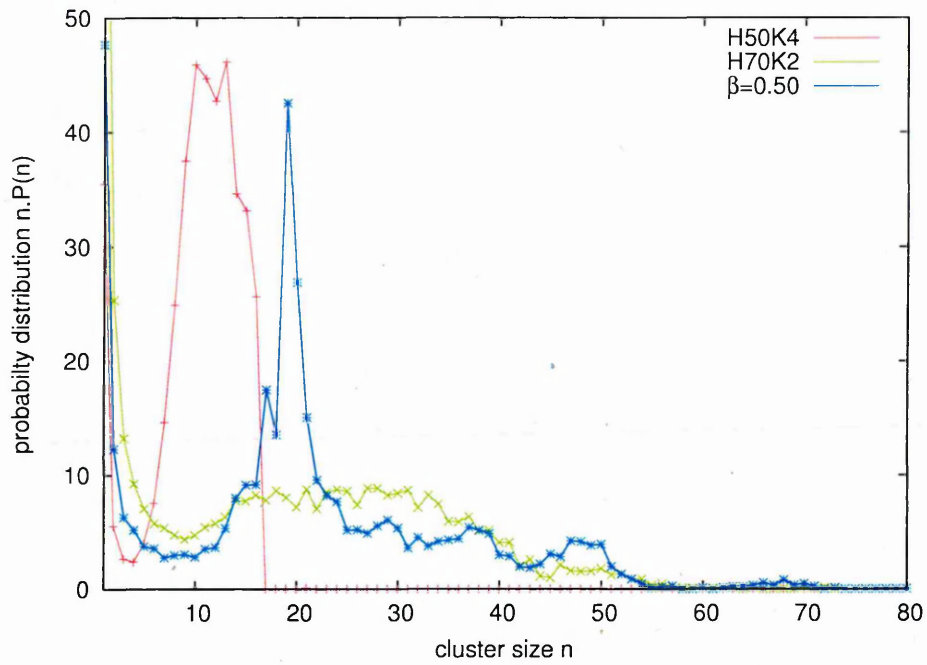


(a) $\beta = 1.00$

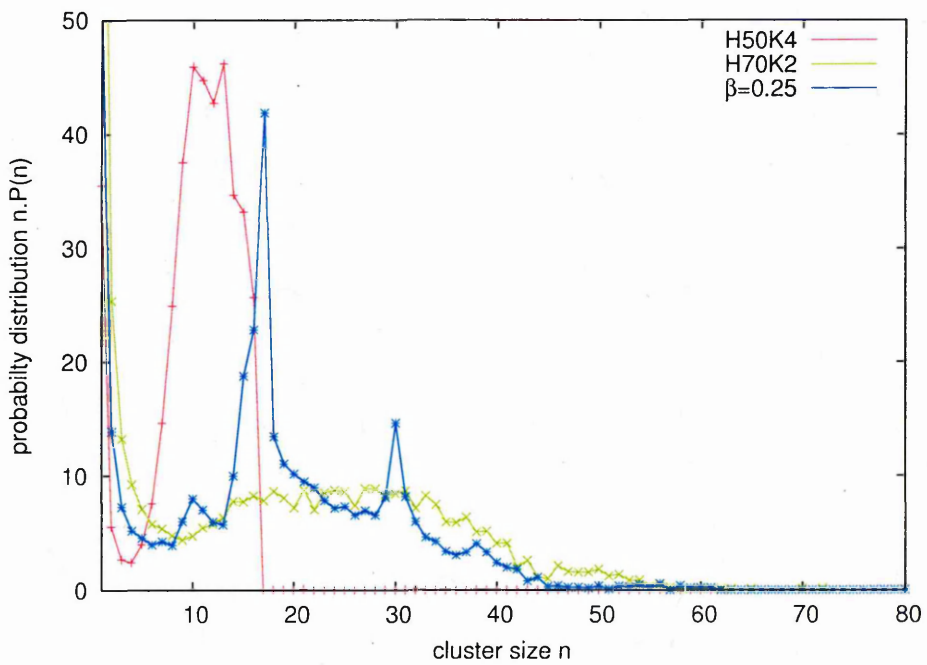


(b) $\beta = 0.75$

Fig. 6.2: Cluster size distribution functions $n.P(n)$ for the 50/50 mixtures of H70K2 and H50K4 amphiphiles for a range of β values compared with the pure systems



(c) $\beta = 0.50$



(d) $\beta = 0.25$

Fig. 6.2: (Continued)

mately $A_n^{mix} = (A_n^{H50K4} + A_n^{H70K2})/2 \approx (12 + 30)/2 = 26$ was expected. As the mutual interaction strength is reduced to $\beta = 0.75$ (Fig. 6.2(b)) and $\beta = 0.5$ (Fig. 6.2(c)), the peak corresponding to the micelle aggregation number is shifted towards smaller values and a long tail is developed at large cluster sizes. This behaviour reaches a limit where, at $\beta = 0.25$ (Fig. 6.2(d)), a second peak appears at a relatively high aggregation number ($A_n \approx 30$). Here, the long tail observed for intermediate β seems to have transformed into a distinctive peak. This behaviour is a signature of a second micellar phase formation and of phase separation of the two amphiphile types. The first peak (at $A_n \approx 18$) seems to correspond to the H50K4 peak, whereas the second peak seems to relate to the formation of H70K2-dominated micelles. However, further analysis is required in order to quantify the degree of phase separation found as β is decreased and its effect on micellar structures.

Shape analysis

Micell shape analysis has been carried out on these mixture systems by measuring the principle moments of inertia using the methodology presented in the previous chapter. The resulting plots (Fig. 6.3) show a general trend which is very similar to those exhibited by the one-component systems. For small cluster sizes, a cylindrical shape is noted which converges to a more spherical shape as cluster size is increased. The range $15 < n < 25$ corresponds to the region where the mixed micelles are the most spherical. However, from $n > 25$, a dissimilar behaviour can be observed from that seen for pure systems. In the pure systems, as n reaches large cluster sizes, I_L becomes larger and I_S becomes smaller while I_M remains constant for virtually all H and κ' . This behaviour of the inertia tensor indicates a change in the aggregate shape going from near-spherical to a 'flattened' ellipsoid. Here, though, the behaviour is qualitatively different as β is decreased: I_L and I_S still go, respectively, larger and smaller but I_M now increases. This is a signature of cylindrical micelle shapes developing for $n \gtrsim 25$ as β is decreased.

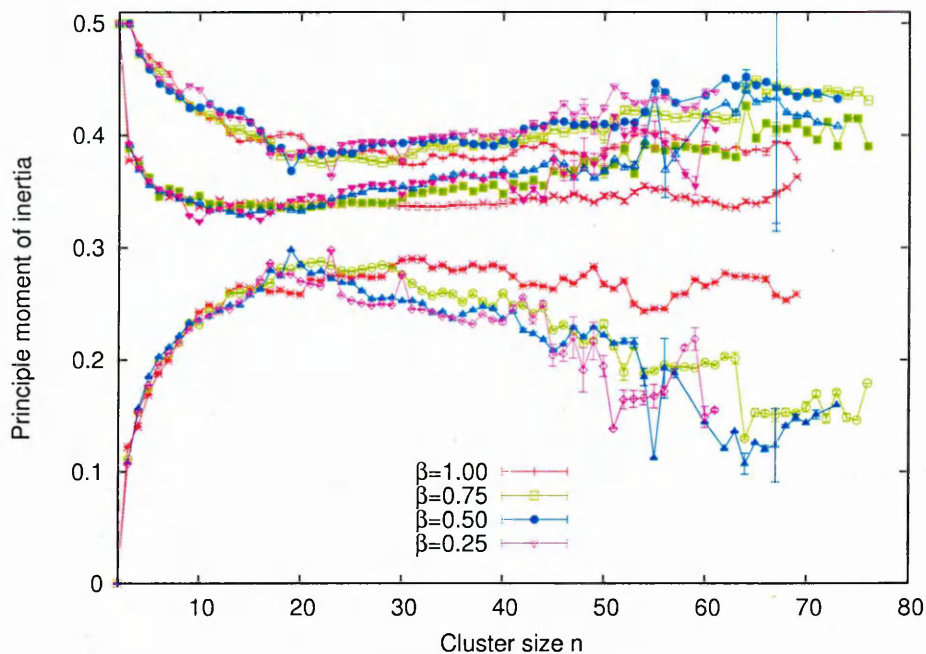


Fig. 6.3: Principal moments of inertia vs. cluster size for the 50/50 composition mixtures at different values of β

	$\beta = 1.00$	$\beta = 0.75$	$\beta = 0.50$	$\beta = 0.25$	H50K4	H70K2
A_n	32	24	19	18/30	12	30
I_L	0.364	0.381	0.368	0.386/0.377	0.404	0.393
I_M	0.336	0.339	0.334	0.337/0.347	0.342	0.351
I_S	0.289	0.281	0.250	0.285/0.245	0.253	0.256

Tab. 6.1: Principal moments of inertia for all mixture systems at their aggregation number(s) compared with the one-component systems taken at their aggregation number

For one-component systems, we have concluded that the interaction parameters (H and κ') had little effect on aggregate shape for a given micelle size. The micelle shape was, then, mainly determined by the micelle size, *i.e.* the number of amphiphiles in a cluster. Differences in the overall micellar phase were, therefore, mainly seen as changes in the cluster size distribution function. Here, however, clusters of a given size are seen to have significantly different shapes due to variation of the mutual interaction strength β . This suggests that the intramicellar packing of the two types of amphiphiles may have a larger impact on the micelle

shape than does anything observed for single component systems.

Tab. 6.1 lists the principal moments of inertia taken at the cluster size corresponding to the aggregation number for each of the mixture systems. For comparison the corresponding data for both pure amphiphiles are also given. For $\beta = 1.0$, it is interesting to note the fact that the mixed micelles seem to be surprisingly ‘spherical’ for this relatively large aggregation number. For all pure systems studied in the previous chapter, the moment of inertia corresponding to a cluster size of ≈ 32 would be more divergent. Furthermore, Fig. 6.3 indicates that these micelles remain close to being spherical up to very large cluster sizes ($n = 70$). In what follows, we present further structural analysis aimed at characterising the behaviour that underlies this observation. As β is decreased, the principal moments of inertia correspond to cylindrical micelle shapes. At $\beta = 0.25$, the small micelles seems to have a relatively spherical shape whereas the bigger ones display a cylindrical shape.

Radial density distribution

The radial density distributions for particles in micelles have been calculated using the methodology described in the previous chapter. The results shown in Fig. 6.4, are broken down to show the contributions from each amphiphile type as well as the total contributions regardless of the particle type. From this, one can assess the effect of β and micelle size on the radial distributions of both amphiphile types within the micelles.

Fig. 6.4(a), 6.4(b) and 6.4(c) show these distributions for $\beta = 1.0$. For small micelles (cluster size $10 < n < 20$), the two types of amphiphile exhibit very similar distributions with maxima at virtually the same radii. As the micelle size is increased to 20-30 and 30-40, however, a distinction can be seen between the distributions of the two types amphiphiles. The peaks are shifted from each other by $\approx 0.5 - 0.6\sigma_0$ for the clusters of size 30-40. As the aggregation

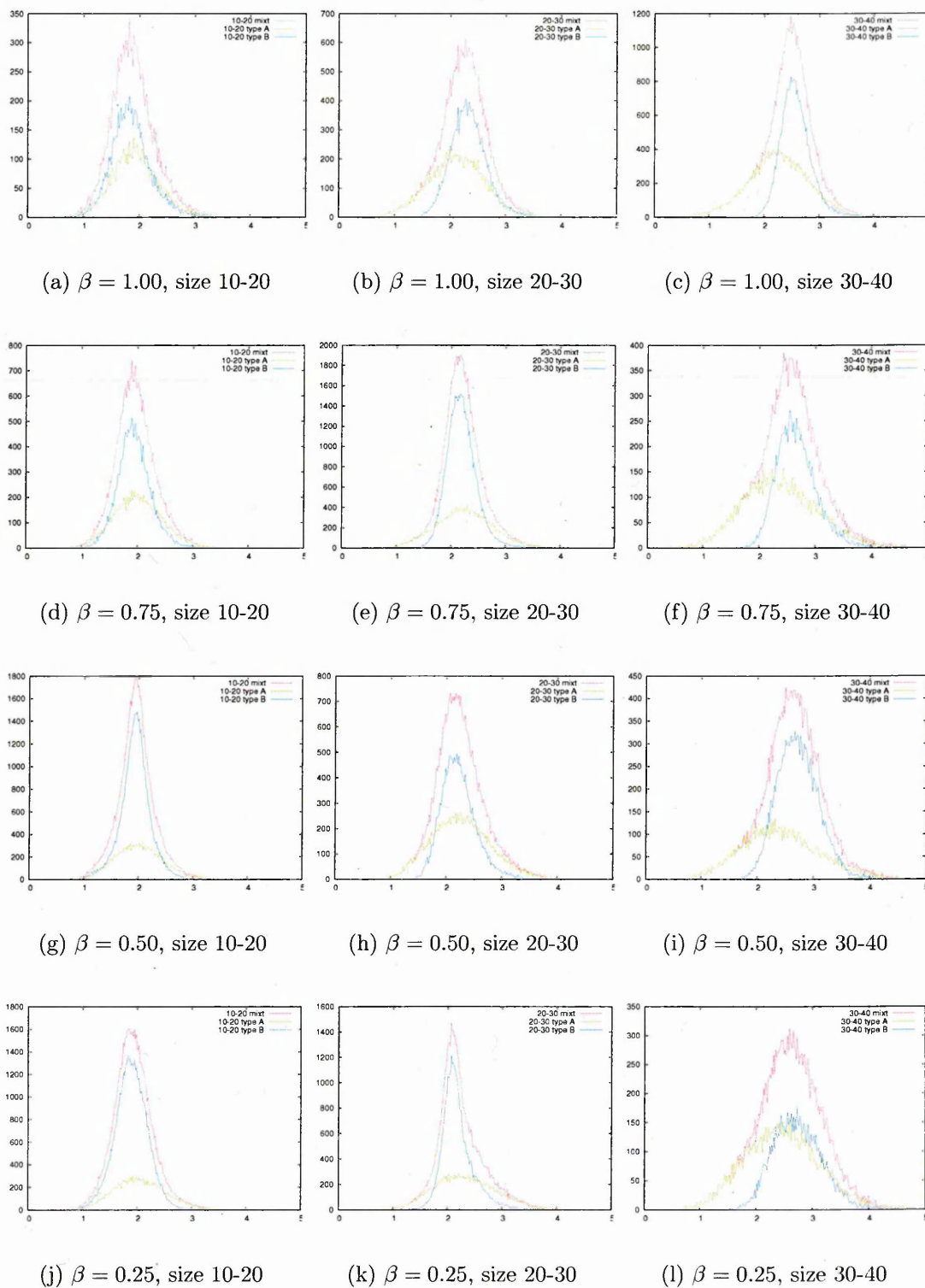


Fig. 6.4: Positional distribution functions, $g_{pos}(r)$, for different values of β and 3 micelle size categories

number of this system is $A_n \approx 32$, and therefore belongs to this size category, this shift corresponds to the dominant radial structure found for this system. When $\beta = 1.0$, there is no difference in the interaction potentials between like and unlike amphiphiles. However, it seems that the H50K4 amphiphiles are more likely to be positioned further away from the micelle center of mass than the H70K2 amphiphiles. This suggests that the H50K4 amphiphiles, which have longer hydrophilic heads, form a slightly displaced outer shell overlapping with an inner core of H70K2 molecules. This is confirmed by the configuration snapshot on Fig. 6.1(a) the H50K4 being seen to act as wedges between the H70K2 particles so as to satisfy the hydration requirement of the long H50K4 head group and the ‘hydrophobicity’ of the H70K2 tail. This packing arrangement probably arises so as to a maximise of the cohesive interaction between the solvent spheres and the hydrophilic head groups, while creating a minimal disruption of the interfacial region between the solvent and the micelle hydrophobic core. The diagram on Fig. 6.5 illustrates schematically this packing of the two amphiphiles with different HLB ratios. This behaviour could, in principle, be induced by any incompatibility in the chain length and/or the head group size, resulting in this particular packing geometry.

As β is decreased, the observed differences in the radial peak position diminishes and at $\beta = 0.25$, no significant difference can be noticed. This probably due to the fact that as β is decreased, the mutual interaction between the two types of amphiphile is greatly reduced, so that amphiphiles of the same type start to cluster. Thus, the structure shown in Fig. 6.5 is no longer representative. However, from these radial distribution data, it is difficult to determine the actual structures adopted by the amphiphiles in these low β micelles.

With a strong miscibility, the two amphiphiles seems to adopt a preferred position from the micelle centre of mass according to their HLB ratio in order to satisfy the solvation requirement of the head group. However, the widths of the two distributions are also very different. As can be seen on Fig.6.4(c), the distribution

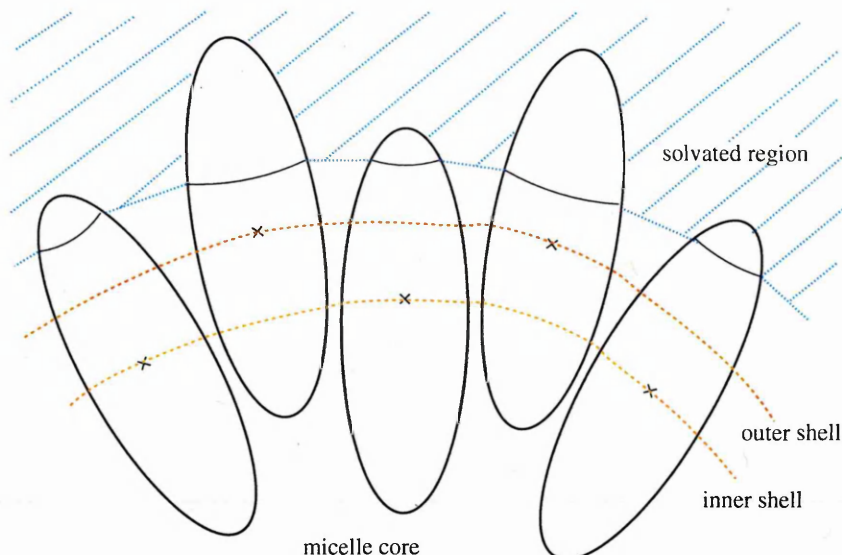


Fig. 6.5: Schematic diagram representing the packing geometry of two amphiphiles with incompatible HLB for $\beta = 1.00$

corresponding to the H50K4 molecules has a width at half maximum of $\sim 1\sigma_o$ whereas that for the H70K2 is $\sim 1.65\sigma_o$. Thus, whereas the H50K4 amphiphiles appear pinned to the outer shell with little radial diffusion, the H70K2 amphiphiles seem to be able to reside at radial distances spanning from $\sim 0.7\sigma_o$ up to $\sim 4.5\sigma_o$. This suggests that most of the piston motion comes from the inner core of H70K2 particles, occasionally ‘poking’ their head into the solvent spheres (but not so far that their tails get too ‘exposed’ to the solvent).

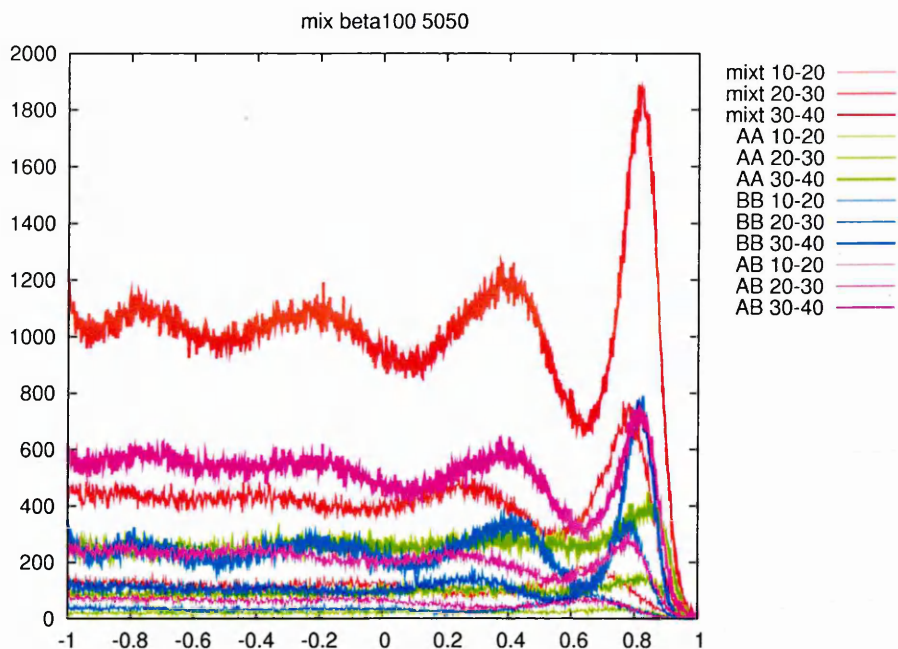
The structural conformations of the mixed micelles have been further analysed by calculating $g_{cos}(\theta)$ for all systems. For each system, the size categories ‘small’ ($10 < n < 20$), ‘medium’ ($20 < n < 30$) and ‘large’ ($30 < n < 40$) have been analysed separately. The total contribution (noted ‘mixt’), the like contributions from each type of amphiphiles (noted ‘AA’ for H70K2 and ‘BB’ for H50K4) and the unlike contribution (noted ‘AB’) are presented in Fig. 6.6.

For $\beta = 1.00$ (Fig. 6.6(a)), the size category 30-40 is most dominating since the aggregation number of this system is ≈ 32 . From these plots, it can be seen that the structure of the AB contribution and the BB contribution are in phase with

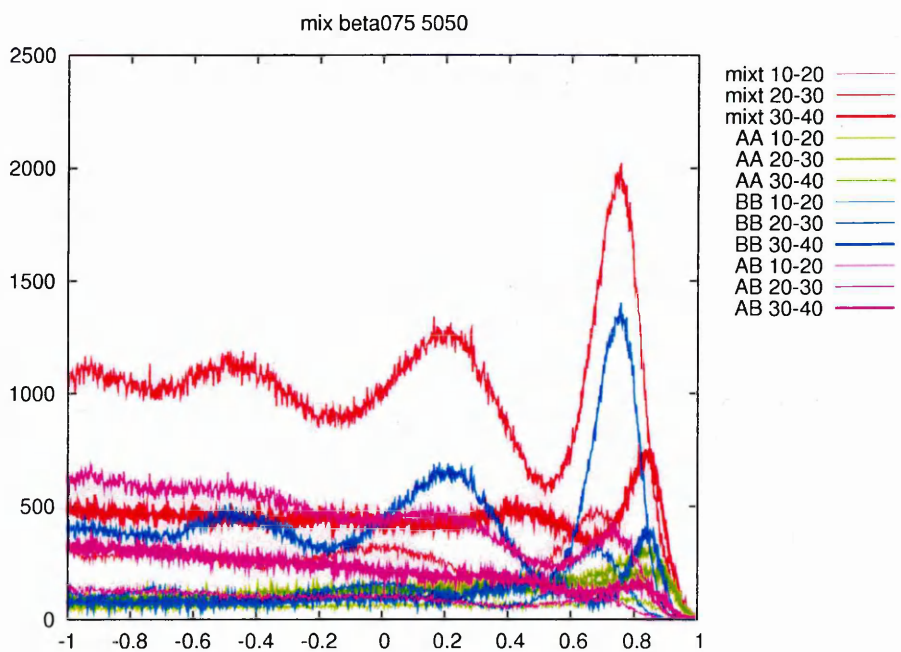
the total contribution. While, the contribution from the H70K2 amphiphiles is rather small and does not show much structure, the H50K4 amphiphiles appear to set the structure observed in the mixed micelles. Furthermore, it is important to note that all contributions show significant structure for all sizes, such that the total distributions comprise approximately 50% from the AB contribution and 50% from equal contributions from the two like terms. This indicates that these micelles have a composition of roughly 50% of both amphiphiles. Moreover, no evidence of phase separation can be observed in these plots, indicating that the micelles are well-mixed for all size categories. This is consistent with the isotropic character of the structure described by Fig. 6.5.

For $\beta = 0.75$ (Fig. 6.6(b)), the overall distributions present a similar pattern to that of $\beta = 1$, the main contributions coming from the H50K4 amphiphiles. However, a significant slope is now apparent in the AB contributions for the medium and large size categories (20-30 + 30-40). This indicates a degree of local phase separation due to the reduction in the mutual interaction strength.

On decreasing this mutual interaction strength even further to $\beta = 0.50$ (Fig. 6.6(c)), the slope observed in the AB contribution is stronger and present for all size categories. Also, it is clear that the mixed micelles have lost some of the structure seen for higher β values. Thus, only micelles with the smallest size retain the structural pattern observed above for $\beta = 1.0$ and single component $\kappa' = 1/4$ systems. Furthermore, the very modest AB contribution observed for this size category indicates a more marked phase separation between the two amphiphile types, leading to the formation of pure H50K4 micelles. At larger micelle size, the AB contribution increases but has a slope characteristic of phase separation. However, the lack of structure found in the total distribution for these systems indicates that the micelles are not pure. Also, it is known from previous analysis that the two amphiphiles present very different curvatures when forming pure aggregates. This analyse explains the sphero-cylindrical structures observed on the configuration snapshots in Fig. 6.1(c). As shown schematically on Fig. 6.7, the

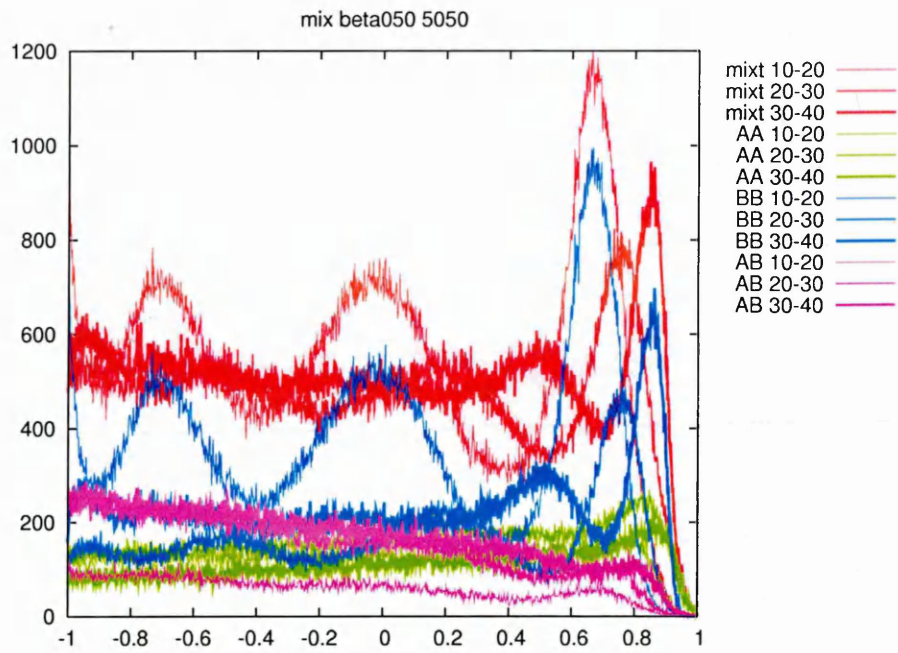


(a) $\beta = 1.00$

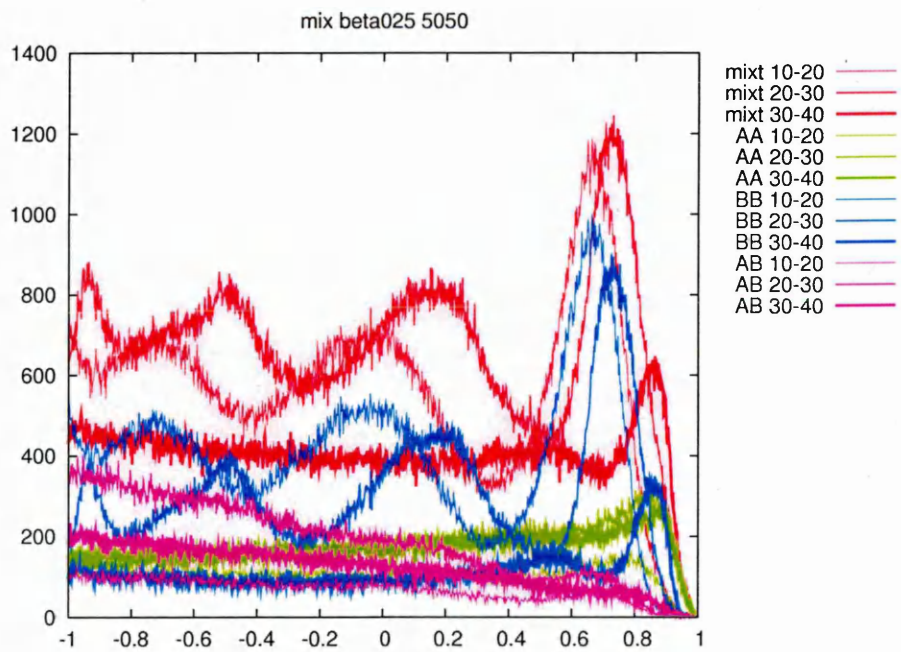


(b) $\beta = 0.75$

Fig. 6.6: Angular distribution functions, $g_{ang}(r)$ for different β values, different micelle size categories. The mixture is noted "mixt", the H70K2 particles "A" and the H50K4 particles "B".



(c) $\beta = 0.50$



(d) $\beta = 0.25$

Fig. 6.6: (Continued)

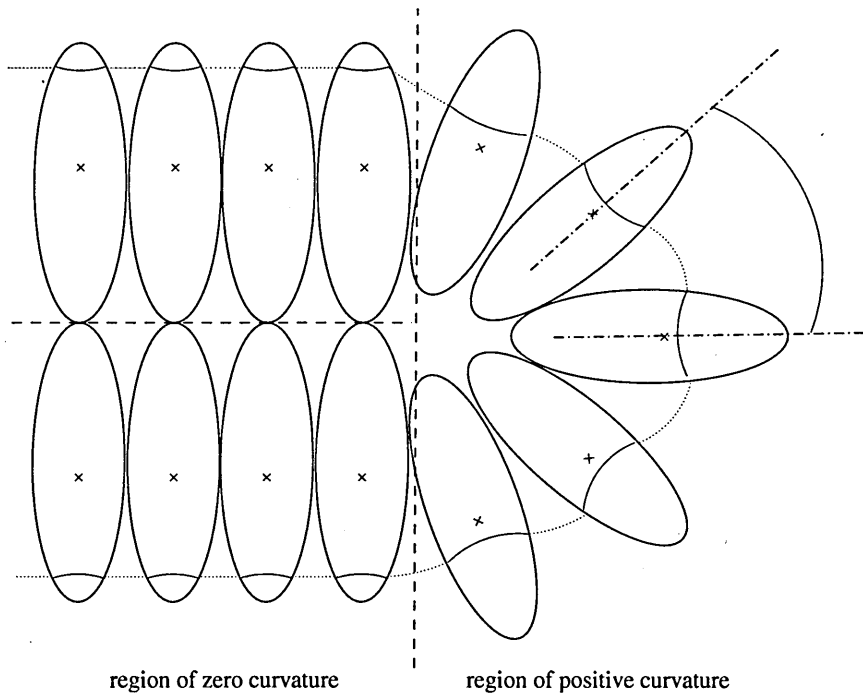


Fig. 6.7: Schematic diagram representing the sphero-cylindrical micelle. The two amphiphiles are phase separated within the micelle and the high curvature forming amphiphile is acting as cap-ends closing a cylindrical core formed by low curvature amphiphiles

amphiphiles with low curvature (*e.g.* H70K2) tend to make up cylindrical core whose ends are closed up by semi-spherical end caps made of amphiphiles with high curvature (*e.g.* H50K4).

As β is decreased even further to 0.25 (Fig. 6.6(d)), the phase separation is stronger. Pure H50K4 and H70K2 micelles are then seen in co-existence for the small and medium size categories. For large aggregates, the sphero-cylinder form is still preferred.

Composition vs. cluster size

Finally, in this section, an analysis of the composition of the micellar aggregates has been performed for all systems. From this, the proportion of H70K2 particles observed in the micelles is plotted in Fig. 6.8 as a function of cluster size n .

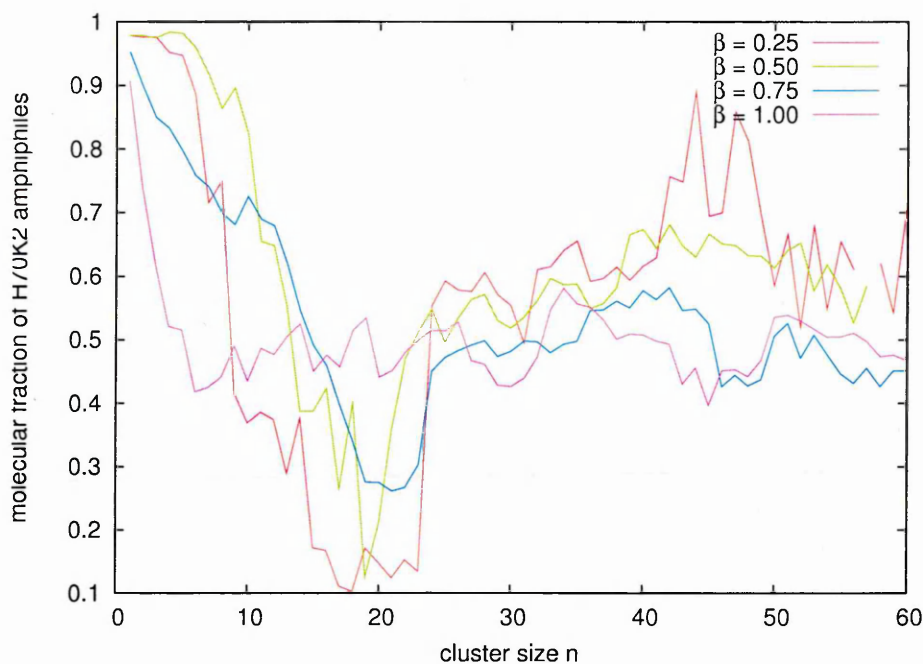


Fig. 6.8: Proportion of H70K2 molecules in clusters of size n for different values of β

For an ideal mixture, one would expect the composition to be independent of the cluster size, indicating a constant composition of 50% for all aggregates: *i.e.* a 50/50 ratio for the free monomers and a 50/50 composition within each micelles. However, this behaviour is not even observed for $\beta = 1.00$. For cluster sizes above ≈ 10 , the average composition seems to be constant at approximately 48%. However, when $n < 10$, a net preference for H70K2 can be noticed reaching 90% composition for monomers ($n = 1$).

As β is decreased, the composition starts to show stronger dependance on micelle size. The proportion of H70K2 in micelles exhibits a large drop between ~ 15 and ~ 25 . This is consistent with the cluster size distribution functions shown previously as this size region corresponds to the aggregation number of pure H50K4. As β is decreased, then, more micelles with a high fraction of H50K4 amphiphiles are formed at n values close to the aggregation number for pure H50K4. for equivalent reasons, micelles with a high fraction of H70K2 amphiphiles appear at

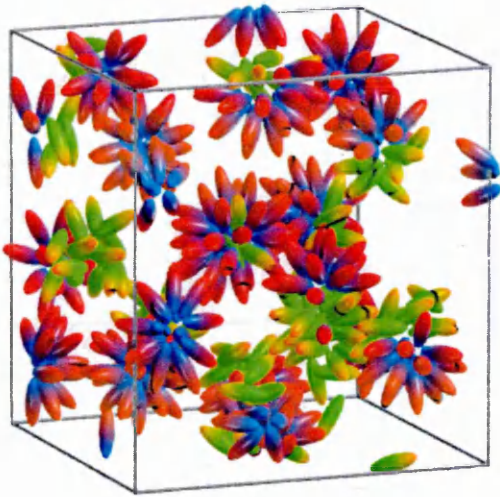
a cluster size of $\gtrsim 30$ (corresponding to the aggregation number of pure H70K4).

Interestingly, the monomer composition seems to be relatively independent of the parameter β and is always dominated by H70K2 amphiphiles. Even though the micelles show diverse structural and compositional changes as a function the mutual interaction between the two amphiphiles, the monomer composition is virtually unchanged at over 90% of the amphiphile with the longer tail (or shorter head group), *i.e.* a large HLB ratio.

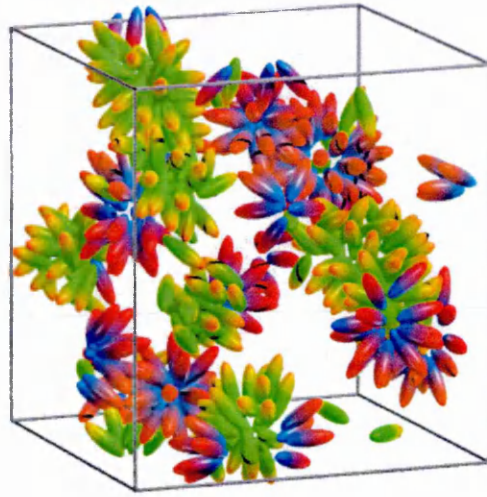
6.2.2 Effect of changing mixing ratios

In the preceding section, the effect of reducing the mutual interaction strength between the two types of amphiphiles was studied. It was found from this that very different micellar structures form at a constant 50/50 composition ratio. In this section, the effect of the composition ratio is studied for $\beta = 0.50$ and $\beta = 0.75$. For each case, 3 concentration ratios has been used: 25/75, 50/50 and 75/25, all at the same fixed total amphiphile concentration of 5%.

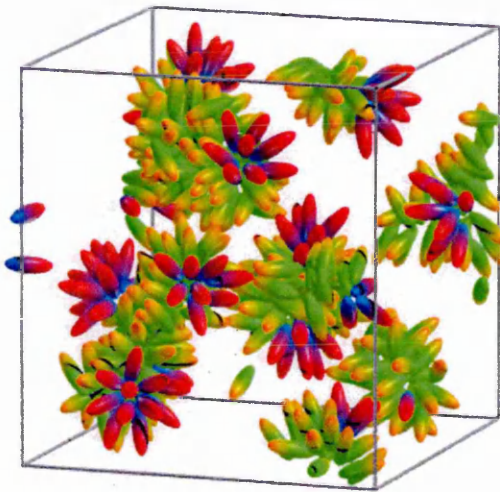
Simulations were run in the same conditions as were used in the previous section and the final configuration snapshots are shown on Fig. 6.2.2 for $\beta = 0.50$ and on Fig. 6.2.2 for $\beta = 0.75$. The cluster size distribution functions $n \cdot P(n)$ have been computed and are shown on Fig. 6.11 for $\beta = 0.50$ and $\beta = 0.75$. In both cases, one can observe a smooth transition in the shape of the distributions as the proportion in H70K2 is increased. At 25/75 composition, only a few H70K2 amphiphiles are present and the cluster size distribution function is very close to that seen for pure H50K4. The 50/50 composition ratio corresponds to the equi-concentration systems studied in the previous section. At 75/25 composition, relatively few H50K4 are present in the solution and the size distribution function is close to that for a pure H70K2 system.



(a) 25% H70K2 , 75% H50K4, $\beta = 0.50$

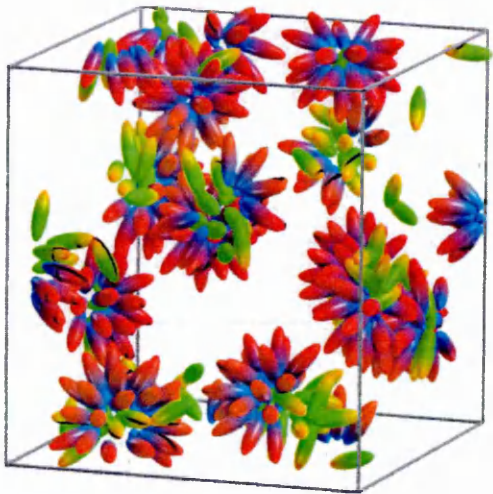


(b) 50% H70K2, 50% H50K4, $\beta = 0.50$

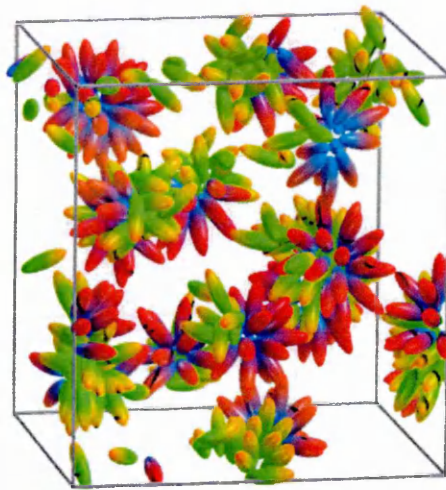


(c) 75% H70K2, 25% H50K4, $\beta = 0.50$

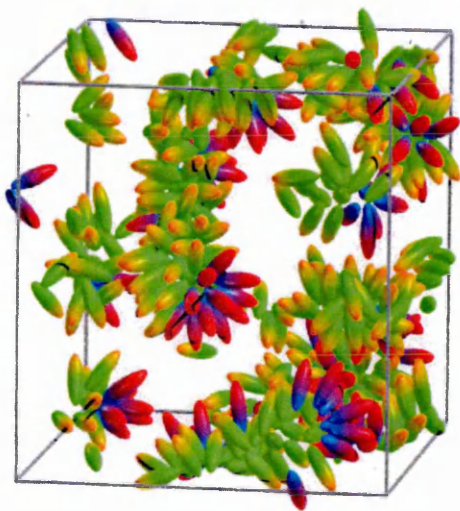
Fig. 6.9: Configuration snapshots for $\beta = 0.50$ for 3 different composition ratios



(a) 25% H70K2, 75% H50K4, $\beta = 0.75$

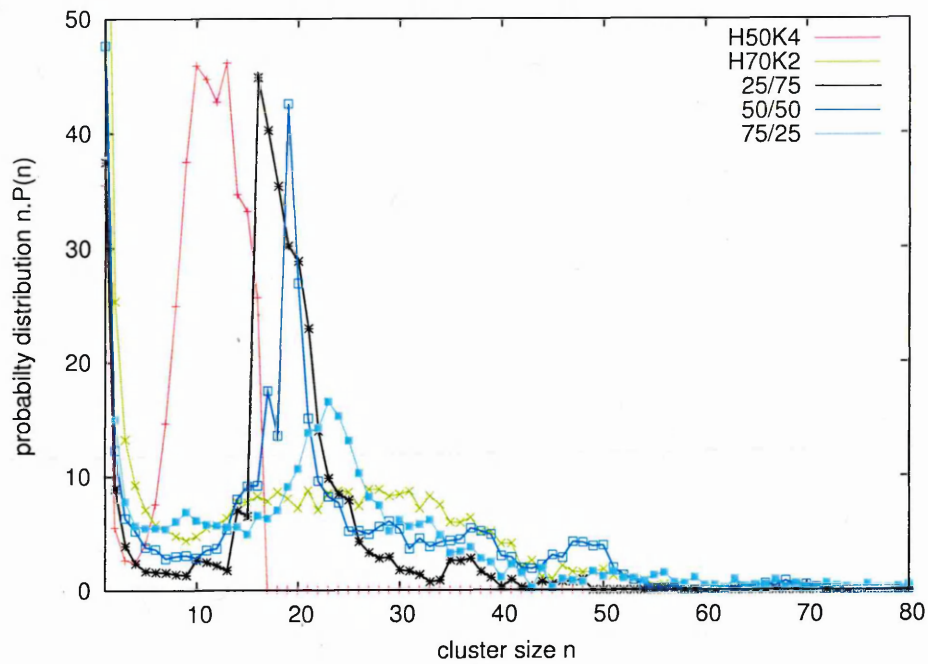


(b) 50% H70K2, 50% H50K4, $\beta = 0.75$

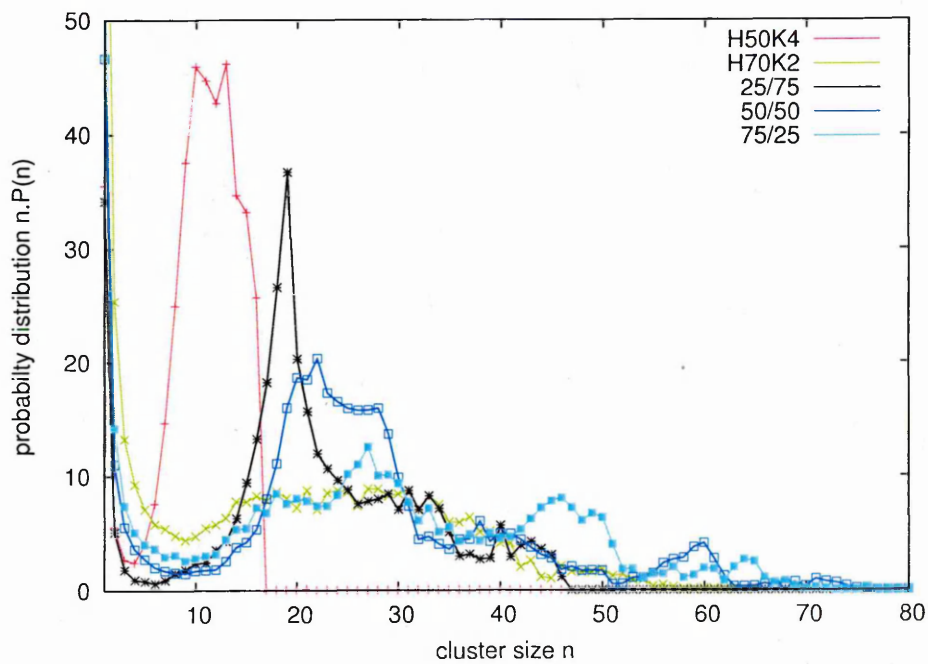


(c) 75% H70K2, 25% H50K4, $\beta = 0.75$

Fig. 6.10: Configuration snapshots for $\beta = 0.75$ for 3 different composition ratios



(a) $\beta = 0.50$



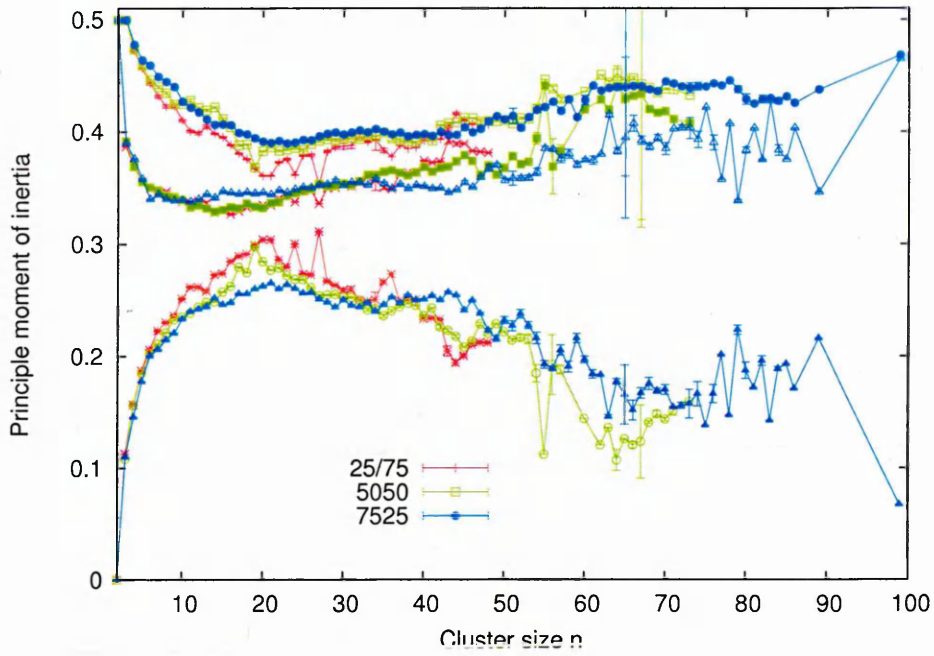
(b) $\beta = 0.75$

Fig. 6.11: Cluster size distribution functions $n.P(n)$ for $\beta = 0.5$ (a) and $\beta = 0.75$ (b) and for three different composition ratios, compared with the pure systems

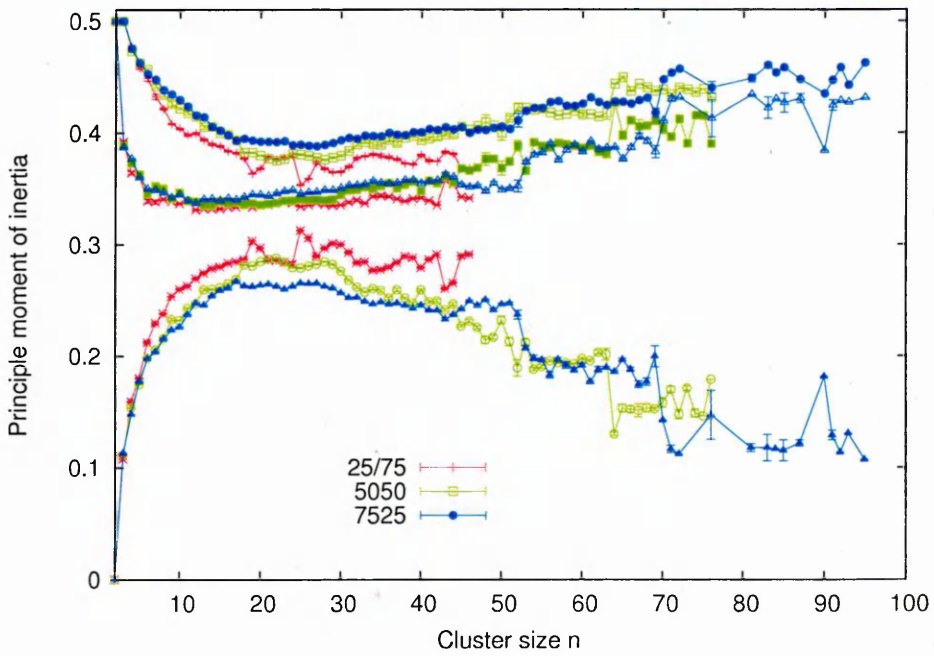
The principal moments of inertia for these systems are shown on Fig. 6.12 for both $\beta = 0.50$ and $\beta = 0.75$. These exhibit behaviour consistent with previous analysis. However, it is difficult to draw any novel conclusions regarding the effect of the composition ratio on micelle shape.

Even though the shape analysis does not suggest much by way of original behaviour, the effect of the composition ratio does have a dramatic effect on intramicellar structure. As can be seen on Fig. 6.13(a), the structure of the 25/75 composition system for $\beta = 0.75$ is dominated by the H50K4 amphiphiles and displays 5 characteristic peaks. The absence of a slope in the long range AB contribution indicates that no phase separation occurred here and that bi-disperse micelles developed for all sizes. As the concentration of H70K2 is increased, there is a gradual loss of structure in the resulting mixed micelles. At a composition ratio of 75/25, the H70K2 amphiphiles dominate the structure and a high degree of phase separation can be observed in the AB contribution. This indicates the presence of spherocylindrical micelles, particularly at large n . The effect of the composition on the $\beta = 0.50$ systems follows this same pattern with a gradual loss of structure as the concentration of H70K2 is increased.

The variation of composition with cluster size has also been analysed and is shown in Fig. 6.14. For both $\beta = 0.50$ and $\beta = 0.75$, the mole fraction of H70K2 displays a similar behaviour with increasing cluster size as the composition ratio is changed. It can be seen that the molar fraction within micelles tends to the total molar fraction in the solution at large micelle size. Thus, the plot corresponding to the total composition 25/75 tend towards ~ 0.25 at large n , the 50/50 towards ~ 0.5 and the 75/25 toward ~ 0.75 . Interestingly, the monomer composition does not vary much with the composition ratio and continues to show a very high mole fraction of H70K2 amphiphiles. Even when only 25% of the total amphiphile concentration is made of H70K2 amphiphiles, more than 90% of the monomer phase is made up of H70K2 amphiphiles. For $\beta = 0.50$, one can observe a drop in the fraction of H70K2 molecules for micelles of size $10 < n < 25$. As seen in

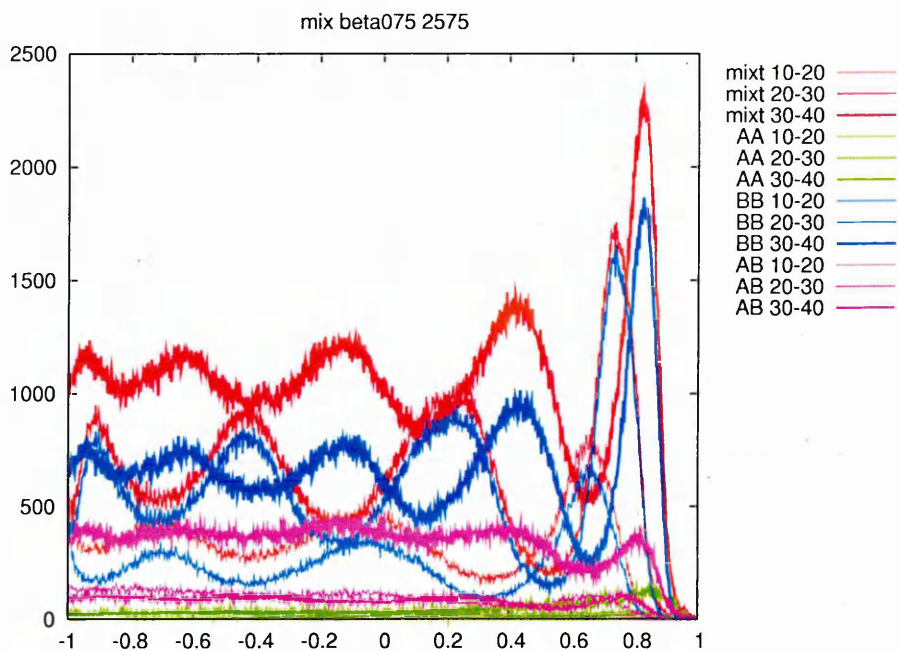


(a) $\beta = 0.50$

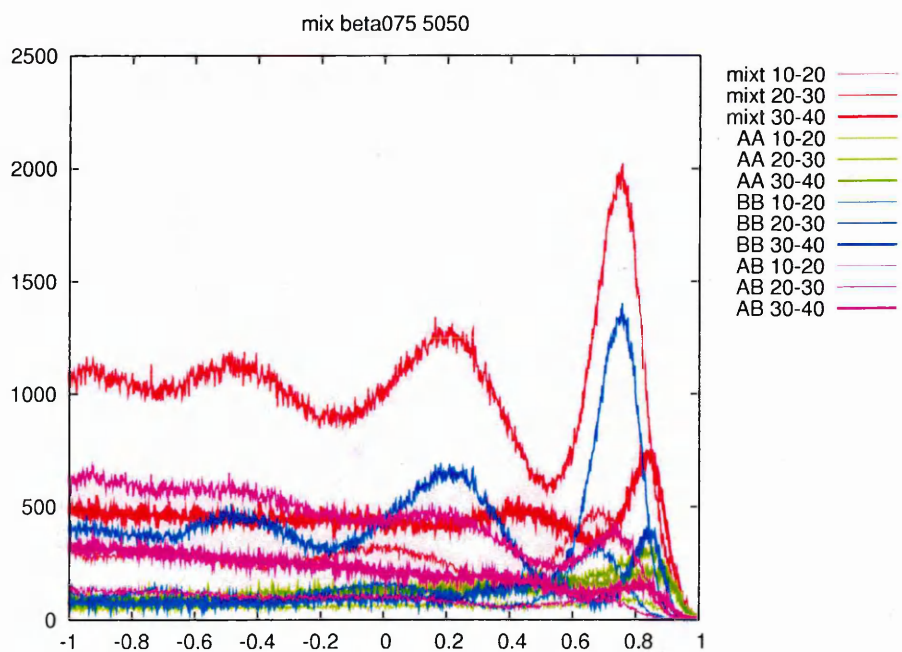


(b) $\beta = 0.75$

Fig. 6.12: Principal moments of inertia vs. cluster size for $\beta = 0.5$ (a) and $\beta = 0.75$ (b) and for three different composition ratios.

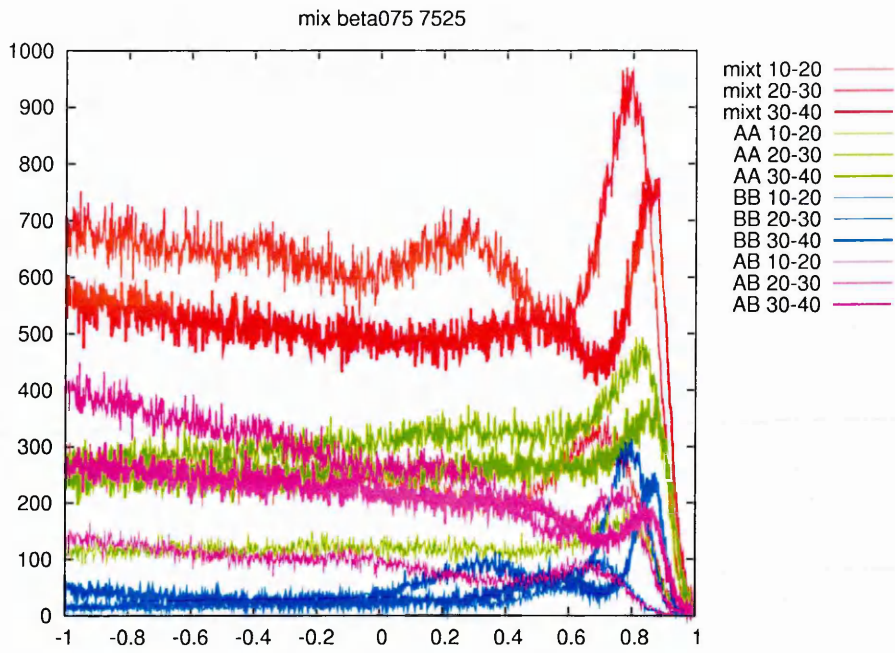


(a) $\beta = 0.75$, composition 25/75

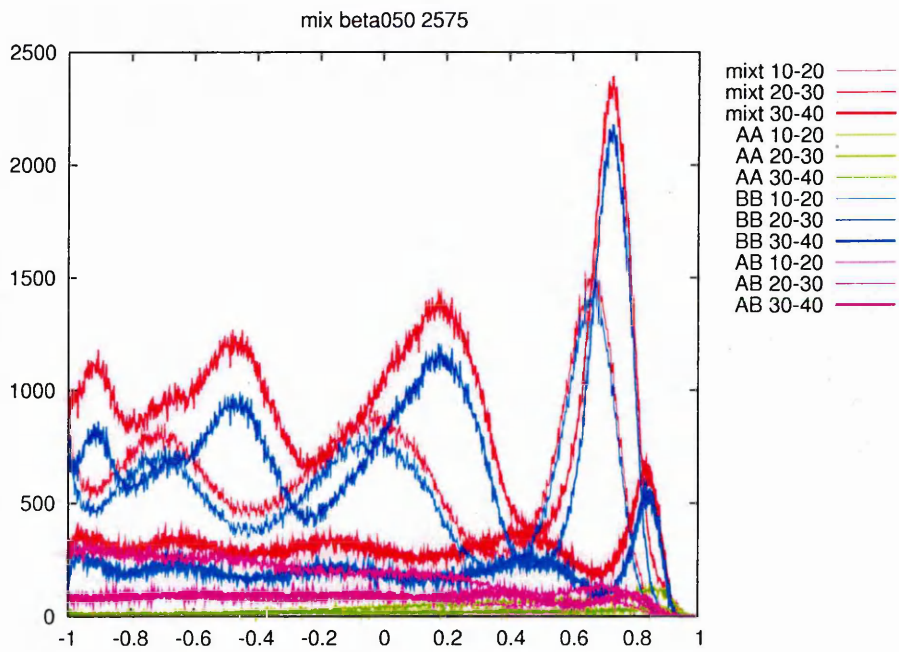


(b) $\beta = 0.75$, composition 50/50

Fig. 6.13: Angular distribution functions, $g_{ang}(r)$ for different β values, different composition and different micelle size categories. The mixture is noted "mixt", the H70K2 particles "A" and the H50K4 particles "B". different

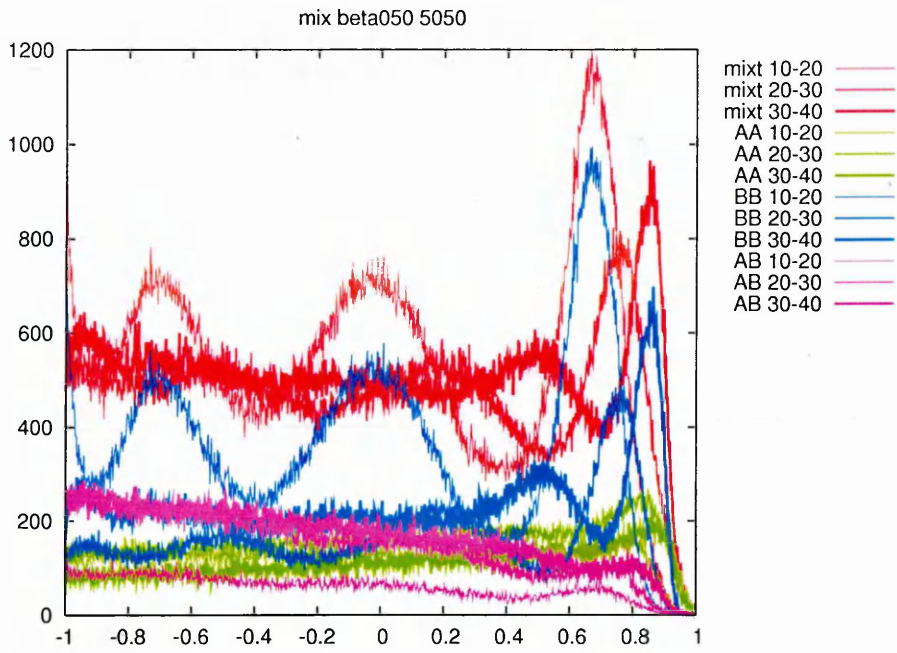


(c) $\beta = 0.75$, composition 75/25

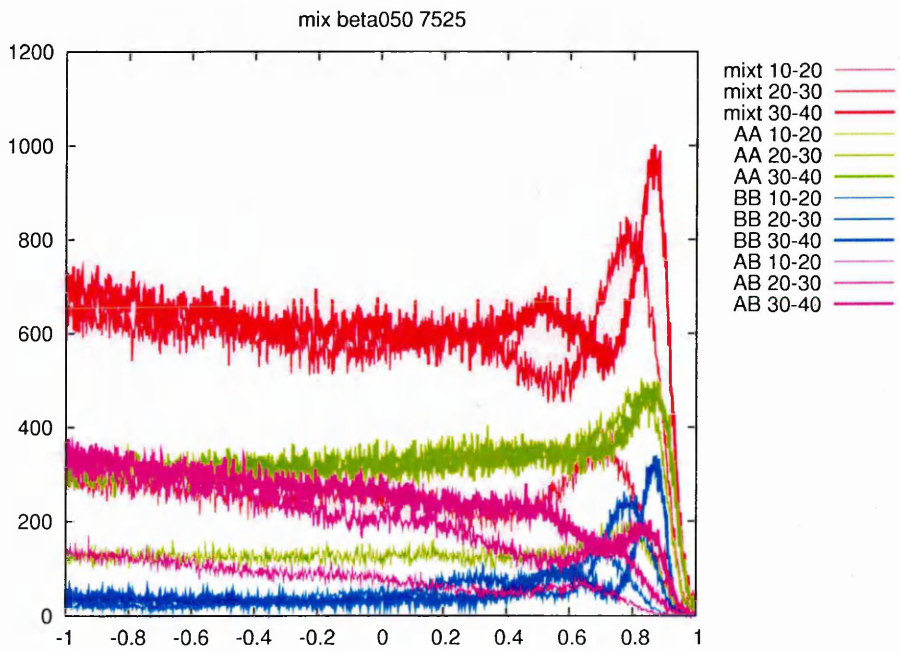


(d) $\beta = 0.50$, composition 25/75

Fig. 6.13: (Continued)

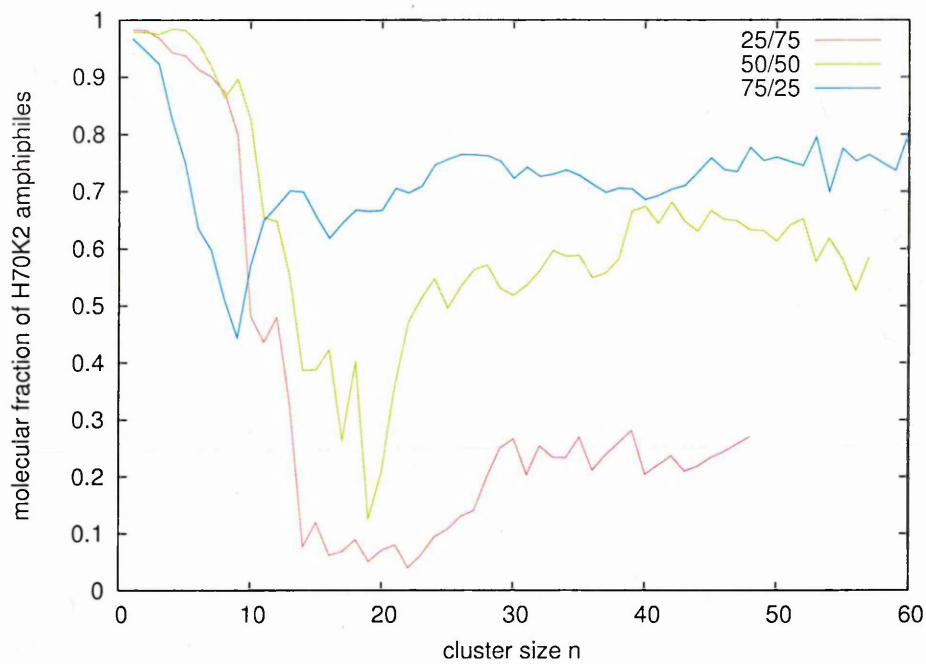


(e) $\beta = 0.50$, composition 50/50

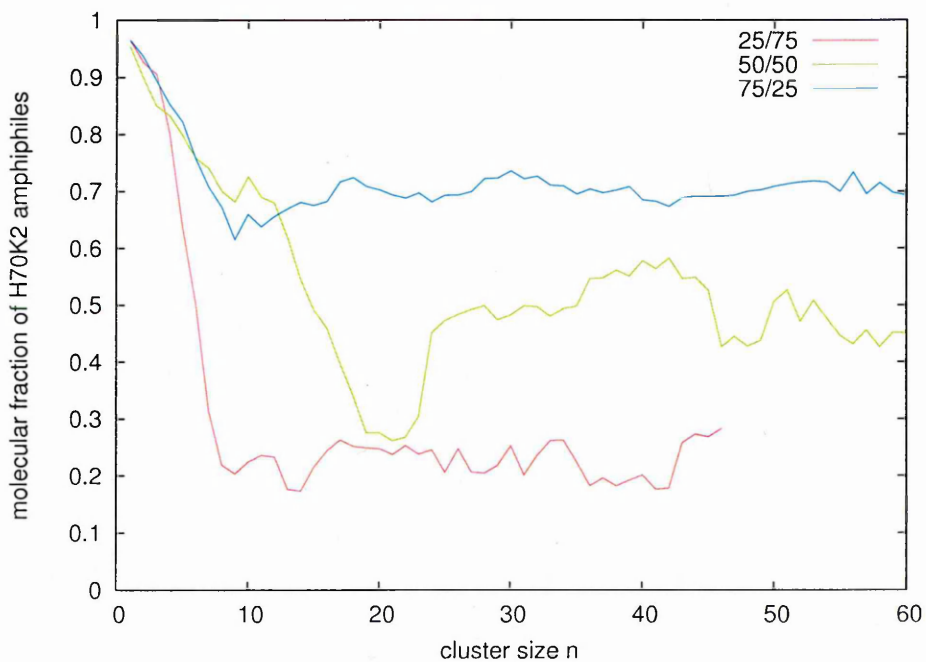


(f) $\beta = 0.50$, composition 75/25

Fig. 6.13: (Continued)



(a) $\beta = 0.50$



(b) $\beta = 0.75$

Fig. 6.14: Proportion of H70K2 in clusters of size n for different concentration ratios

the previous section, this reduction is due to a phase separation process. At this range of n values, the formation of pure H50K4 micelle is favoured. As the mole fraction of H50K4 is increased, this feature becomes more marked. For $\beta = 0.75$, in contrast, this effect is slightly weaker due to the reduced tendency to phase separate. Note that for the 75/25 composition, only few H50K4 amphiphiles are present and this reduction is no longer apparent.

6.2.3 Summary

In this Chapter, binary mixtures of amphiphiles with different HLB ratio have been studied. The effects of the mutual interaction strength β between the two different types of amphiphiles and the amphiphile composition ratio have been studied. From the simulation results, it is clear that the systems do not display a linear mixing behaviour even for a neutral mutual interaction strength ($\beta = 1.00$). The deviation from linearity increases as either the total composition ratio is changed or β is reduced. In all of the mixture systems, the composition is dominated by H70K2 particles (amphiphile with the longest chain).

	$\beta = 1.00$	$\beta = 0.75$	$\beta = 0.50$	$\beta = 0.25$
25/75	-	(i)BD (ii)BD (iii)SC	(i)PS (ii)PS (iii)SC	-
50/50	(i)BD (ii)BD (iii)BD	(i)BD (ii)SC (iii)SC	(i)PS (ii)SC (iii)SC	(i)PS (ii)PS (iii)SC
75/25	-	(i)BD (ii)SC (iii)SC	(i)SC (i)SC (iii)SC	-

Tab. 6.2: BD = bi-disperse, SC = sphero-cylinder, PS = phase-separated. For each case, the structures corresponding to the three size categories, (i)10-20, (ii)20-30 and (iii)30-40 is indicated

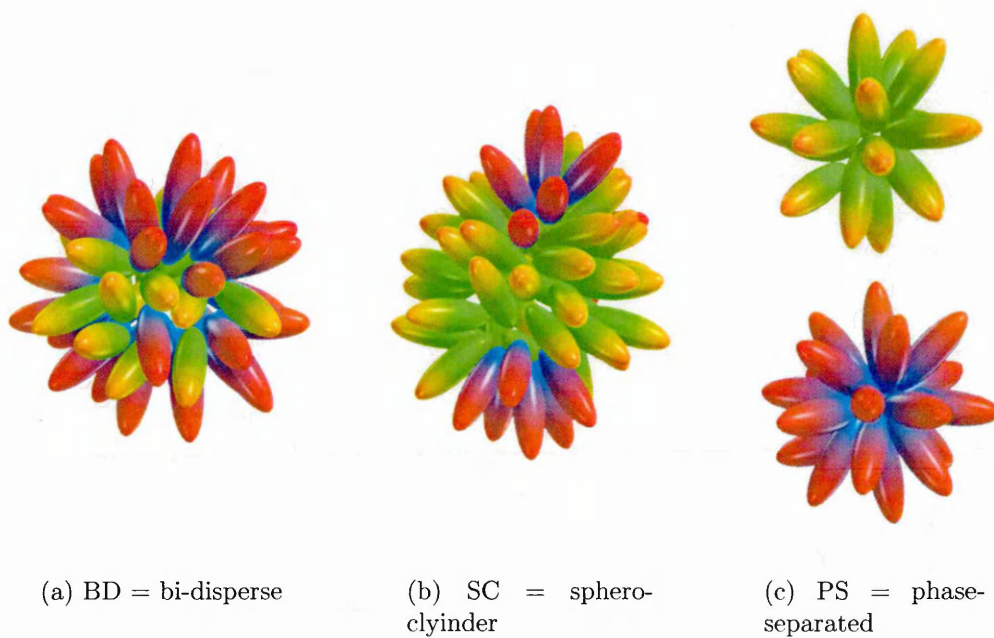


Fig. 6.15: The three different structures of mixed micelles

The phase behaviour of these mixed micelles is summarised in Tab. 6.2 as a function of β , composition ratio and micelle size categories. Whatever interaction is set between the two amphiphiles, the micelle structure is strongly dependant on the degree of attraction between the two amphiphile types and three different structures have been found. The first of these is large bi-disperse micelle where no intramicellar micro-phase separation can be noticed (see Fig. 6.15(a)). This mixed micelle presents, however, a degree of ‘radial’ phase separation since each type of amphiphile prefers to reside at a different distance from the micelle centre of mass. Thus, amphiphiles with long head groups tend to reside on an outer shell of the micelle whereas the amphiphiles with shorter heads tend to occupy the micelle core. This radially ordered mixed micelle structure is consistent with the findings of other simulations [193] and experimental work [194–196] which promotes the existence of a radial-shell model for certain micelle mixtures such as bile salt. We have argued that this structure arises due to the specific energetic scales of the different interaction strengths in the system. The strong water-head group

interaction strength is required for the solvation of the head group and a strong amphiphile-amphiphile interaction is also required compared to the solvent-tail in order to maintain this radial order.

When micro-phase separation is favoured, spherocylindrical mixed micelles tend to be the dominant structure (see Fig. 6.15(b)). In this, the amphiphiles with long head groups, capable of forming high curvature aggregates, form endcaps to a cylindrical core made of amphiphile with shorter head. When the tendency to phase separate is made even stronger, two different types of spherical micelles are formed in coexistence, each with a distinctive micelle size and shape (see Fig. 6.15(c)). This behaviour is characterised by the development of an extra peak in the micelle size distribution function $n \cdot P(n)$.

CHAPTER 7

Conclusion

In this chapter, the principal results of this thesis are summarised and discussed, and suggestions for future work are made.

7.1 Conclusions

The trend in simulation of biological systems has been towards more and more complex all-atom models with increasing structural detail, more complex all-atom force fields and greater computational expense. In contrast, the model presented in this thesis is moving in the opposite direction, moving towards simpler physical models focusing on global properties and generic phenomena. Here, to gain computational efficiency, we chose to represent each amphiphile using a single-site particle. Avoiding chemical specificity, the general elongated shape of amphiphilic molecules was modelled by the well-known Gay-Berne potential, commonly used for rod-shaped thermotropic liquid crystal particles. Using a simple 12-6 Lennard-Jones potential for the solvent spheres, the rod-sphere potential, governing the amphiphile-solvent interaction, was then modified such that the solvent spheres

were strongly attracted to only one end of the rod particle. The rod-rod potential well-depth, governing the amphiphile-amphiphile interaction strengths, was set to have no orientational dependence such that the tail-tail, head-head and head-tail interaction were equal in strength.

Throughout this thesis, we have shown that this simple molecular model is able to simulate the essential features of the phase behaviour of real lyotropic systems. Given the unrealistic symmetry of the amphiphile-amphiphile interaction, the self-assembly processes observed here, are driven purely by the anisotropy of the rod-sphere potential. The use of the Molecular Dynamics simulation technique has permitted us to study of the self-assembling behaviour of various amphiphilic aggregates: from roughly spherical micelles, to cylindrical micelles, lamellae and inverse micellar structures (see Chapter 4).

In Chapter 5, we showed that the use of an alternative amphiphile-solvent potential, with a sharp switch between the solvophobic and solvophilic regions has allowed us to study the effect of simple molecular parameters on the micellar phase. In particular, the effects of the hydrophilic-lipophilic balance (HLB) and the amphiphilic strength have been studied. The results suggest that all the phase behaviour changes observed arise due to a change in the curvature adopted by each aggregate. As the HLB increases, the hydrophilic head group reduces and the curvature is decreased. Conversely, an increase in the amphiphilic strength results in an increase in the curvature as more solvent spheres are packed around each headgroup. As a consequence of this curvature change, different micelle sizes and shapes have been observed. The HLB was found to be the dominant factor in setting these micellar behaviour, a secondary role being played by the amphiphilic strength. Nevertheless, the amphiphilic strength had an important impact on the radial order and angular distribution of the amphiphiles within the micelles. As the amphiphilic strength was decreased, less structure could be found, the micelles being less well defined and more diffuse.

Other interesting phenomena were also observed in these simulations. The micellar

aggregates were found to be very soft and active with an important ‘rattling motion’ characterising the amphiphiles leaving and re-entering the micelles at a high frequency. Changes in the micelle’s molecular occupancy were also observed involving both fusion of two micelles and long-lived monomer exchange through the solvent. During this process, monomers were observed to flip their orientations as they left the initial micelle in order to readily ‘dock’ with their new host micelle. Complex breathing and oscillation modes of the micelles, although not studied here, were found for all of the systems studied here.

In Chapter 6, mixtures of two amphiphiles, with different HLB and amphiphilic strength parameterisations, were studied as a function of the mixture composition and the mutual amphiphile attraction. For mutually attractive amphiphiles, isotropically mixed micelles were found with a two-layer radial shell structure. By reducing the mutual attraction, however, structurally segregated spherocylindrical micelles were stabilised, the large head group amphiphiles forming high curvature end caps of a low curvature cylinder made of amphiphiles with short head groups. Further reduction in the mixed amphiphile-amphiphile interaction strength then led to two coexisting micelle structures, each one dominated by just one of the amphiphile types.

7.2 Discussion and critique

Many of the coarse-grained models (CG) developed over the past years have given improved understanding of self-assembling molecular systems in ways that complement more complex all-atom model approaches. Bead-chain models are usually tuned to fit properties from all-atom models and/or experimental results. This model, in contrast, is based on a single-site particle and, thus, pushes the limit of the coarse-graining approach rather further. The resulting lack of flexibility of the model certainly has an important impact on certain observed phenomena, but approaches for incorporating flexibility into Gay-Berne models have recently been

investigated [197].

The head group - solvent interactions used in this study are probably unrealistically high. In fact, we have seen that even for low amphiphilic strength set to $\kappa' = 1/2$ (*i.e.* solvent-head group set to $2\epsilon_0$ and solvent-tail set to $0.5\epsilon_0$), micelle like self-assembly is occurring. This suggests that a high solvent-head group interaction may not be required provided that the solvent-tail interaction is the weakest in the system.

Another issue arising from these results is the weak dependence of the monomer dynamics on the HLB and amphiphilic strength. As we have seen in Chapter 5, the concentration of monomers is equivalent in all the studied systems. Although their lifetimes seems to be different, the behaviour of the monomers in the binary mixtures presented in Chapter 6 is also somewhat different from what could be expected as the solubility of these amphiphiles should be different.

As discussed in the thesis, the entropy-driven ordering of water molecules near a hydrophobic (non hydrogen-bonding) solute is not explicitly represented in this model. One could incorporate this effect by introducing, in the sphere-sphere potential an orientation dependant ‘hydrogen bonding’ interaction. This way, the local ordering of the solvent particle near an hydrophobic surface would be mimicked, and hopefully the entropy-driven hydrophobic effect modelled explicitly [198–204].

7.3 Suggestions for future work and improvements

Due to the large number of independent model parameters, the work described in this thesis is largely preliminary. Despite its relative simplicity, the model has produced encouraging results and has opened up several possible directions for further research listed below:

- Study the effect of the hydration strength (head group - water interaction) and the lipophilic strength (tail-tail interaction) independently.
- Map a 'real' amphiphile-amphiphile potential from an all-atom model and/or use an inverse Monte-Carlo like-scheme to generate an effective amphiphile-amphiphile interaction. It would then be interesting to see if this generic model can retrieve the phase behaviour of a specific amphiphile without recourse to more a complex solvent representation
- Study the bilayer region in greater detail. A series of slow quenching of this system should give more insight into the behaviour of this phase.
- Study vesicle self-assembly.
- Study the possible cubic region found with the exponential model.
- Study ternary systems. The introduction of an oil-like particle can easily be achieved by introducing a second type of sphere with an 'opposite' tanh potential. The effect of molecular interactions on oil absorption by micelles could then be investigated.
- Study the insertion of colloidal particles (*i.e.* a coarse-grained protein-like molecule) through a bilayer.
- Use pear-shaped particles recently developed by [177] in order to induce more curvature effects into the bilayers and study mixtures of amphiphilic rods and pears. The incorporation of amphiphilic character to pear-shaped particles should be relatively easy as the necessary modifications concern only the energy parameters of the Gay-Berne potential which are already used in the design of pear-shaped particles. One could then design amphiphiles with either positive or negative induced curvature by associating the hydrophilic interaction with either the thick or thin end of the pear.

APPENDIX A

Derivation of Forces and Torques

In this appendix, the derivations of the forces and torques involved in the Molecular Dynamics programme used in this thesis, are presented. Following the simple case of the Lennard-Jones fluid, the forces and torques are derived for the rod-rod interaction and the rod-sphere interaction. For the latter, the original definition [185–187] and the 3 developments investigated in this thesis, namely the cubic model, the exponential mode and the tanh model are presented.

A.1 Calculation of forces for Lennard-Jones particles

Provided that the analytical expression of the potential is continuous, it is possible to calculate the force as such:

$$\mathbf{f}(\mathbf{r}) = -\nabla_r U(r) \tag{A.1}$$

In the case of two spherical particles i and j interacting via the Lennard-Jones

potential (see chapter 3, section 3.1.1), Eqn. A.1 can be written as

$$\mathbf{f}_{ij} = -\frac{dU_{LJ}(r_{ij})}{dr_{ij}} \frac{\mathbf{r}_{ij}}{r_{ij}} = \frac{24\epsilon}{r_{ij}} \left[2 \left(\frac{\sigma}{r_{ij}} \right)^{12} - \left(\frac{\sigma}{r_{ij}} \right)^6 \right] \hat{\mathbf{r}}_{ij} \quad (\text{A.2})$$

Here, the potential depends only on the separation r_{ij} between the two particles i and j . Due to the spherical shape of the particle, no rotational forces or torques have to be determined.

If a cutoff scheme at a distance r_c is applied to the system, the potential becomes

$$U_{SS}(r_{ij}) = \begin{cases} U_{LJ}(r_{ij}) - U_{LJ}(r_c) & (r_{ij} \leq r_c) \\ 0 & (r_{ij} > r_c) \end{cases} \quad (\text{A.3})$$

Since $U_{LJ}(r_c)$ is a constant, the expression of the forces is not affected by the application of a cutoff scheme. The net force \mathbf{F}_i on particle i is then given by a simple vectorial sum over pairwise forces between i and its neighbouring particles specified by the cutoff spherical range.

$$\mathbf{F}_i = \sum_j \mathbf{f}_{ij} = - \sum_j \nabla_{\mathbf{r}_{ij}} U_{SS}(\mathbf{r}_{ij}) \quad (\text{A.4})$$

A.2 Calculation of forces and torques for Gay-Berne particles

A.2.1 Derivation of the forces and torques

In the case of single-site anisotropic particles, the molecular motion can be divided into translational motion of the centre of mass and rotational motion about it.

Consider two Gay-Berne particles i and j with centre of mass position vectors \mathbf{r}_i and \mathbf{r}_j , respectively. As in a Lennard-Jones fluid, the distance between the two particles is defined by the intermolecular vector $\mathbf{r}_{ij} = \mathbf{r}_j - \mathbf{r}_i$. The orientation of the particles is described by two unit vectors $\hat{\mathbf{u}}_i$ and $\hat{\mathbf{u}}_j$, parallel to the symmetry axes of the molecules.

As the potential depends not only on the particle separation \mathbf{r}_{ij} but also on the relative orientations of the two particles $\hat{\mathbf{u}}_i$ and $\hat{\mathbf{u}}_j$, the Gay-Berne potential cannot be tabulated and has to be calculated from its analytical expressions. Likewise, the forces and torques need to be also evaluated analytically from the potential.

As for the case of the Lennard-Jones fluid, a truncated and shifted form of U_{ij} , U_{RR} is considered when applying a cutoff scheme. In the conventional approach to the calculation of forces and torques, the orientation dependance of $U_{RR}(\hat{\mathbf{r}}_{ij}, \hat{\mathbf{u}}_i, \hat{\mathbf{u}}_j)$ can be written in terms of scalar products of unit vectors $\hat{\mathbf{r}}_{ij}$, $\hat{\mathbf{u}}_i$ and $\hat{\mathbf{u}}_j$:

$$U_{RR}(r, a, b, c) = 4\epsilon(r, a, b, c) \left[\left(\frac{\sigma_0}{r - \sigma(r, a, b, c) + \sigma_0} \right)^{12} - \left(\frac{\sigma_0}{r - \sigma(r, a, b, c) + \sigma_0} \right)^6 \right] - 4\epsilon(r, a, b, c) \left[\left(\frac{\sigma_0}{r_c - \sigma(r, a, b, c) + \sigma_0} \right)^{12} - \left(\frac{\sigma_0}{r_c - \sigma(r, a, b, c) + \sigma_0} \right)^6 \right].$$

with $r = \hat{\mathbf{r}}_{ij} \cdot \mathbf{r}_{ij}$, $a = \hat{\mathbf{u}}_i \cdot \mathbf{r}_{ij}$, $b = \hat{\mathbf{u}}_j \cdot \mathbf{r}_{ij}$ and $c = \hat{\mathbf{u}}_i \cdot \hat{\mathbf{u}}_j$.

Note that the energy and shape parameters ϵ and σ remain functions of r and not r_c being dependant upon scalar products of the form $\mathbf{r}_{ij} \cdot \hat{\mathbf{u}}_i$.

Considering this formulation of the potential, the force calculation is straightforward and, according to Newton's third law on the action-reaction principle, can be written as:

$$\mathbf{f}_i = -\mathbf{f}_j = \mathbf{f}_{ij} = -\nabla_{\mathbf{r}_{ij}} U_{RR} = - \left(\frac{\partial U_{RR}}{\partial \mathbf{r}_{ij}^x}, \frac{\partial U_{RR}}{\partial \mathbf{r}_{ij}^y}, \frac{\partial U_{RR}}{\partial \mathbf{r}_{ij}^z} \right) \quad (\text{A.5})$$

In order to express \mathbf{f}_{ij} as a function of unit vectors $\hat{\mathbf{r}}_{ij}$, $\hat{\mathbf{u}}_i$ and $\hat{\mathbf{u}}_j$, the chain rule can be applied such that

$$\mathbf{f}_{ij} = - \sum_s \frac{\partial U_{RR}}{\partial (\mathbf{s} \cdot \mathbf{r}_{ij})} \nabla_{\mathbf{r}_{ij}} (\mathbf{s} \cdot \mathbf{r}_{ij}) \quad (\text{A.6})$$

where the sum over \mathbf{s} represents the sum over all the scalar products of unit vectors involving \mathbf{r}_{ij} , namely a , b and r .

Furthermore, it can be found that,

$$\nabla_{\mathbf{r}_{ij}} (\mathbf{s} \cdot \mathbf{r}_{ij}) = \left(\frac{\partial r_{ij}^x s^x}{\partial r_{ij}^x}, \frac{\partial r_{ij}^y s^y}{\partial r_{ij}^y}, \frac{\partial r_{ij}^z s^z}{\partial r_{ij}^z} \right) = (s^x, s^y, s^z) = \mathbf{s} \quad (\text{A.7})$$

Therefore, Eqn. A.6 becomes:

$$\mathbf{f}_{ij} = - \frac{\partial U_{RR}}{\partial r} \hat{\mathbf{r}}_{ij} - \frac{\partial U_{RR}}{\partial a} \hat{\mathbf{u}}_i - \frac{\partial U_{RR}}{\partial b} \hat{\mathbf{u}}_j \quad (\text{A.8})$$

For the rotational motion, in the case of the Gay-Berne potential, the particle is axially symmetric and the torque acting on particle i can be expressed as:

$$\boldsymbol{\tau}_i = \sum_j \boldsymbol{\tau}_{ij} = \hat{\mathbf{u}}_i \times \mathbf{g}_i = \hat{\mathbf{u}}_i \times \sum_j \mathbf{g}_{ij} \quad (\text{A.9})$$

$$\mathbf{g}_{ij} = - \nabla_{\hat{\mathbf{u}}_i} U_{RR} \quad (\text{A.10})$$

Here, \mathbf{g}_i is defined as the torque and is the derivatives of the potential U_{RR} with respect to the orientational vector $\hat{\mathbf{u}}_i$. This is the rotational equivalent to the translational force \mathbf{F}_i defined as the derivative of U_{RR} with respect to \mathbf{r}_i .

Note that the velocity Verlet algorithm used for the integration scheme of the Molecular Dynamics programme uses the perpendicular component of the torque,

\mathbf{g}_i^\perp , rather than the torque when updating particle orientations and velocities (see chapter 3, section 3.1.1).

$$\mathbf{g}_i^\perp = \mathbf{g}_i - (\mathbf{g}_i \cdot \hat{\mathbf{u}}_i) \hat{\mathbf{u}}_i \quad (\text{A.11})$$

As for the translational motion, the chain rule can be used to expand the expressions for the torques such as:

$$\mathbf{g}_{ij} = -\nabla_{\hat{\mathbf{u}}_i} U_{RR} = -\sum_{\mathbf{s}} \frac{\partial U_{RR}}{\partial (\mathbf{s} \cdot \hat{\mathbf{u}}_i)} (\mathbf{s} \cdot \hat{\mathbf{u}}_i) \quad (\text{A.12})$$

$$\mathbf{g}_{ij} = -\frac{\partial U_{RR}}{\partial a} \mathbf{r}_{ij} - \frac{\partial U_{RR}}{\partial c} \hat{\mathbf{u}}_j \quad (\text{A.13})$$

A.2.2 Explicit analytical forms of all necessary derivatives

Using the standard definition of the Gay-Berne potential, the partial derivatives $\frac{\partial U_{RR}}{\partial r}$, $\frac{\partial U_{RR}}{\partial a}$, $\frac{\partial U_{RR}}{\partial b}$ and $\frac{\partial U_{RR}}{\partial c}$ are given below.

$$\begin{aligned} \frac{\partial U_{RR}}{\partial r} = & 4\epsilon \left[\frac{\mu\chi'}{\epsilon_2 r^3} \left(\frac{(a+b)^2}{1+\chi'c} + \frac{(a-b)^2}{1-\chi'c} \right) (A - A_c) - \frac{B}{\sigma_0} \right. \\ & \left. - \frac{\sigma^3 \chi}{2\sigma_0^3 r^3} \left(\frac{(a+b)^2}{1+\chi c} + \frac{(a-b)^2}{1-\chi c} \right) (B - B_c) \right] \quad (\text{A.14}) \end{aligned}$$

$$\begin{aligned} \frac{\partial U_{RR}}{\partial a} = & 4\epsilon \left[-\frac{\mu\chi'}{\epsilon_2 r^2} \left(\frac{a+b}{1+\chi'c} + \frac{a-b}{1-\chi'c} \right) (A - A_c) \right. \\ & \left. + \frac{\sigma^3 \chi}{2\sigma_0^3 r^2} \left(\frac{a+b}{1+\chi c} + \frac{a-b}{1-\chi c} \right) (B - B_c) \right] \quad (\text{A.15}) \end{aligned}$$

$$\begin{aligned} \frac{\partial U_{RR}}{\partial b} = & 4\epsilon \left[-\frac{\mu\chi'}{\epsilon_2 r^2} \left(\frac{a+b}{1+\chi'c} - \frac{a-b}{1-\chi'c} \right) (A - A_c) \right. \\ & \left. + \frac{\sigma^3\chi}{2\sigma_0^3 r^2} \left(\frac{a+b}{1+\chi c} - \frac{a-b}{1-\chi c} \right) (B - B_c) \right] \end{aligned} \quad (\text{A.16})$$

$$\begin{aligned} \frac{\partial U_{RR}}{\partial c} = & 4\epsilon \left[(A - A_c) \left(\nu\epsilon_1^2\chi^2 c + \frac{\mu\chi'^2}{2\epsilon_2 r^2} \left(\left(\frac{a+b}{1+\chi'c} \right)^2 - \left(\frac{a-b}{1-\chi'c} \right)^2 \right) \right) \right. \\ & \left. - (B - B_c) \frac{\sigma^3\chi^2}{4\sigma_0^3 r^2} \left(\left(\frac{a+b}{1+\chi c} \right)^2 - \left(\frac{a-b}{1-\chi c} \right)^2 \right) \right] \end{aligned} \quad (\text{A.17})$$

where A_c, A, B, B_c are defined as:

$$\begin{aligned} A &= \left(\frac{\sigma_0}{r - \sigma(r, a, b, c) + \sigma_0} \right)^{12} - \left(\frac{\sigma_0}{r - \sigma(r, a, b, c) + \sigma_0} \right)^6 \\ A_c &= \left(\frac{\sigma_0}{r_c - \sigma(r, a, b, c) + \sigma_0} \right)^{12} - \left(\frac{\sigma_0}{r_c - \sigma(r, a, b, c) + \sigma_0} \right)^6 \\ B &= 12 \left(\frac{\sigma_0}{r - \sigma(r, a, b, c) + \sigma_0} \right)^{13} - 6 \left(\frac{\sigma_0}{r - \sigma(r, a, b, c) + \sigma_0} \right)^7 \\ B_c &= 12 \left(\frac{\sigma_0}{r_c - \sigma(r, a, b, c) + \sigma_0} \right)^{13} - 6 \left(\frac{\sigma_0}{r_c - \sigma(r, a, b, c) + \sigma_0} \right)^7 \end{aligned}$$

A.3 Calculation of forces and torques for the rod-sphere interaction

As shown previously, the forces acting between two Lennard-Jones spheres can easily be calculated. The forces acting between two Gay-Berne rods involve more complex calculations due to the anisotropic shape of the particles. Thus, not only forces but torques have to be taken in account. In this section, the forces

and torques involved in the rod-sphere interaction are derived for the 3 different potentials defined in this thesis, namely the cubic model, exponential model and tanh model.

The explicit forms of the force and torque exerted on a Gay-Berne particle i by a Lennard-Jones particle j are evaluated by applying Eqn. A.6 to the following rod-sphere potential

$$U_{RS}(r, a) = 4\epsilon(r, a) \left[\left(\frac{\sigma_0}{r - \sigma(r, a) + \sigma_0} \right)^{12} - \left(\frac{\sigma_0}{r - \sigma(r, a) + \sigma_0} \right)^6 \right] - 4\epsilon(r, a) \left[\left(\frac{\sigma_0}{r_c - \sigma(r, a) + \sigma_0} \right)^{12} - \left(\frac{\sigma_0}{r_c - \sigma(r, a) + \sigma_0} \right)^6 \right]. \quad (\text{A.18})$$

For this interaction, we have

$$\mathbf{f}_{ij} = -\frac{\partial U_{RS}}{\partial r} \hat{\mathbf{r}}_{ij} - \frac{\partial U_{RS}}{\partial a} \hat{\mathbf{u}}_i. \quad (\text{A.19})$$

While the torque acting upon the rod is given by

$$\tau_{ij} = -\hat{\mathbf{u}}_i \cdot \frac{\partial U_{RS}}{\partial a} \mathbf{r}_{ij} \quad (\text{A.20})$$

A.3.1 Original model

Using the same methodology as previously, one can find:

$$\frac{\partial U_{RS}}{\partial r} = 4\epsilon \left[\frac{2\mu\chi''a^2}{(1 - \chi''\frac{a^2}{r^2})r^3} (A - A_c) - \frac{\sigma^3\chi a^2}{\sigma_0^3 r^3} (B - B_c) - \frac{B}{\sigma_0} \right] \quad (\text{A.21})$$

$$\frac{\partial U_{RS}}{\partial a} = 4\epsilon \left[\frac{2\mu\chi''a}{(1 - \chi''\frac{a^2}{r^2})r^2}(A_c - A) + \frac{\sigma^3\chi a}{\sigma_0^3 r^2}(B - B_c) \right] \quad (\text{A.22})$$

A.3.2 Cubic model

Here are presented the explicit forms of $\frac{\partial U_{RS}}{\partial r}$ and $\frac{\partial U_{RS}}{\partial a}$. The same notation are used as previously. The model parameters are denoted A_k , B_k and C_k .

$$\frac{\partial U_{RS}}{\partial r} = 4\epsilon \left[C'_r(A - A_c) - 2(1 + C)\chi'' \left(\frac{a}{r}\right) (B - B_c) - (1 + C)\frac{B}{\sigma_0} \right] (\text{A.23})$$

$$\frac{\partial U_{RS}}{\partial a} = 4\epsilon \left[C'_a(A - A_c) + 2(1 + C)\chi''(B - B_c) \right] \quad (\text{A.24})$$

where

$$\chi'' = \frac{a\chi}{\mu r^2} \left(1 - \chi \left(\frac{a}{r}\right)^2 \right)^{-\frac{3}{2}} \quad (\text{A.25})$$

$$C = 1 + A_k \left(\frac{a}{r}\right) + B_k \left(\frac{a}{r}\right)^2 + C_k \left(\frac{a}{r}\right)^3 \quad (\text{A.26})$$

$$C'_r = A_k \left(\frac{a}{r^2}\right) + 2B_k \left(\frac{a^2}{r^3}\right)^2 + 3C_k \left(\frac{a^3}{r^4}\right)^3 \quad (\text{A.27})$$

$$C'_a = A_k \left(\frac{1}{r}\right) + 2B_k \left(\frac{a}{r^2}\right)^2 + 3C_k \left(\frac{a^2}{r^3}\right)^3 \quad (\text{A.28})$$

A.3.3 Exponential potential

For the exponential model, the same general forms of $\frac{\partial U_{RS}}{\partial r}$ and $\frac{\partial U_{RS}}{\partial a}$ found in Eqn. A.23 and Eqn. A.24 are used. Only the expression of C , C'_r and C'_a are modified such that

$$C = -A_k - B_k \exp\left(C_k \left(\frac{a}{r}\right)\right) \quad (\text{A.29})$$

$$C'_r = \frac{aB_k C_k}{r^2} \exp\left(C_k \left(\frac{a}{r}\right)\right) \quad (\text{A.30})$$

$$C'_a = -\frac{B_k C_k}{r} \exp\left(C_k \left(\frac{a}{r}\right)\right) \quad (\text{A.31})$$

A.3.4 Tanh potential

Similarly, the derivatives for the tanh model are defined by:

$$C = \left(\frac{1}{\kappa'} - \kappa'\right)^2 \left[1 - \tanh\left(\frac{1 + \left(\frac{a}{r}\right) + 2H}{l}\right)^2\right] \quad (\text{A.32})$$

$$C'_r = \left(\frac{1}{\kappa'} - \kappa'\right)^2 \left[1 - \tanh\left(\frac{1 + \left(\frac{a}{r}\right) + 2H}{l}\right)^2\right] \frac{a}{lr^2} \quad (\text{A.33})$$

$$C'_a = \left(\frac{1}{\kappa'} - \kappa'\right)^2 \left[1 - \tanh\left(\frac{1 + \left(\frac{a}{r}\right) + 2H}{l}\right)^2\right] \frac{1}{lr} \quad (\text{A.34})$$

Bibliography

- [1] M. Ash and I. Ash. *Handbook of industrial surfactants*. Gower, Aldershot, UK, 1993.
- [2] J.Y. Ying, C.P. Mehnert, and M.S. Wong. Synthesis and applications of supramolecular-templated mesoporous materials. *Angew. Chem. Int. Ed.*, 38:56–77, 1999.
- [3] P.B. Canham. The minimum energy of bending as possible explanation of the biconcave shape of the human red blood cell. *J. Theor. Biol.*, pages 61–81, 1970.
- [4] E.A. Evans. Bending resistance and chemically induced moments in membrane bilayers. *Biophys. J.*, 14:923–931, 1974.
- [5] W. Helfrich. Elastic properties of lipid bilayers: theory and possible experiments. *Z. Naturforsch. C*, 28(11):693–703, 1973.
- [6] M. Antonietti and S. Förster. Vesicles and liposomes: A self-assembly principle beyond lipids. *Adv. Mat. Prog. Rep.*, 15(16):1323–1333, 2003.
- [7] S. Rasmussen, L. Chen, M. Nilsson, and S. Abe. Bridging nonliving and living matter. *Artificial Life*, 9:269–316, 2003.
- [8] K. Saito, N. Kitamura, and M. Sorai. Thermodynamic study of phase transitions in lyotropic systems: Adiabatic calorimetry on nonionic surfactant $c_{16}e_8$ -water system. *J. Phys. Chem. B*, 107:7854–7860, 2003.
- [9] R. Strey, R. Schomcker, D. Roux, F. Nallet, and U. Olsson. Dilute lamellar and l3 phases in the binary water- $c_{12}e_5$ system. *J. Chem. Soc. Faraday Trans.*, 86(12):2253–2261, 1990.
- [10] D.J. Mitchell, G.J.T. Tiddy, L. Waring, T. Bostock, and M.P. MacDonald. Phase behaviour of polyoxyethylene surfactants with water. mesophase structures and partial miscibility (cloud points). *J. Chem. Soc. Faraday Trans.*, 79:975–1000, 1983.
- [11] G.S. Hartley. *Aqueous solutions of paraffin chain salts*. Hermann, Paris, 1936.

- [12] J. Israelachvili. *Intermolecular and Surface forces with applications to colloidal and biological systems*. Academic Press, 1991.
- [13] J. Forsman and B. Jönsson. Monte carlo simulations of hydrophobic interactions: a test particle approach. *J. Chem. Phys.*, 101(6):5116, 1994.
- [14] J. Forsman, B. Jönsson, and C.E. Woodward. Computer simulations of water between hydrophobic surfaces: The hydrophobic force. *J. Phys. Chem.*, 100(36):15005, 1996.
- [15] S. Sawamura, K. Nagaoka, and T. Machikawa. Effects of pressure and temperature on the solubility of alkylbenzenes in water: volumetric property of hydrophobic hydration. *J. Phys. Chem. B*, 105:2429–2436, 2001.
- [16] I. Sanemasa, M. Araki, T. Deguchi, and H. Nagai. Solubility measurements of benzene and the alkylbenzenes in water by making use of solute vapor. *Bull. Chem. Soc. Jpn.*, 55:1054–1062, 1982.
- [17] R.L. Bohon and W.F. Claussen. The solubility of aromatic hydrocarbons in water. *J. Am. Chem. Soc.*, 73:1571, 1951.
- [18] J.W. Owens, S.P. Wasik, and H. Devoe. Aqueous solubilities and enthalpies of solution of n-alkylbenzenes. *J. Chem. Eng. Data*, 31:47, 1986.
- [19] A. Ben-Naim. *Solvation Thermodynamics*. Kluwer Academic / Plenum Publishers, 1987.
- [20] D.D. Eley. *Trans. Faraday Soc.*, 35:1281–1293, 1939.
- [21] C.J.v. Oss, D.R. Absolom, and A.W. Neumann. The 'hydrophobic effect': essentially a van der waals interaction. *Coll. Polym. Sci.*, 258:424–427, 1980.
- [22] E.A. Vogler. Structure and reactivity of water at biomaterial surfaces. *Adv. Colloid Interface Sci.*, 74:69–117, 1998.
- [23] H.S. Frank and M.W. Evans. Free volume and entropy in condensed systems. ii. entropy in binary liquid mixtures; partial molar entropy in dilute solutions; structure and thermodynamics of aqueous electrolytes. *J. Chem. Phys.*, 13:507–532, 1945.
- [24] K. Minuzo, Y. Miyashita, Y. Shindo, and H. Ogawa. Nmr and ft-ir studies of hydrogen bonds in ethanol-water mixture. *J. Phys. Chem.*, 99:3225–3228, 1995.
- [25] J.H. Hildebrand. A criticism of the term hydrophobic bond. *J. Phys. Chem.*, 72:1841–1842, 1968.
- [26] K. Lum, D. Chandler, and J.D. Weeks. Hydrophobicity at small and large length scales. *J. Phys. Chem. B*, 103(22):4570–4577, 1999.

- [27] P. R. Ten Wolde, S.X. Sun, and D. Chandler. Model of a fluid at small and large length scales and the hydrophobic effect. *Phys. Rev. E Stat. Nonlin. Soft. Matt. phys.*, 65(1):011201, 2002.
- [28] D. Chandler. Interfaces and the driving force of hydrophobic assembly. *Nature*, 437(7059):640–647, 2005.
- [29] T. Raschke and M. Levitt. Detailed hydration maps of benzene and cyclohexane reveal distinct water. *J. phys. Chem. B*, 108:13492–13500, 2004.
- [30] M. Ramadan, D.F. Evans, and R. Lumry. Why micelles form in water and hydrazine. a reexamination of the origins of hydrophobicity. *J. Phys. Chem.*, 87:4538–4543, 1983.
- [31] M. Ramadan, D.F. Evans, R. Lumry, and S. Phillion. Micelle formation in hydrazine-water mixtures. *J. Phys. Chem.*, 89:3405–3408, 1985.
- [32] D.F. Evans, A. Yamauchi, R. Roman, and E.Z. Casassa. Micelle formation in ethylammonium nitrate, a low-melting fused salt. *J. Colloid. Int. Sci.*, 88(1):89–96, 1982.
- [33] C. McDonald. The effect of change of solvent on the critical micelle concentration of a non-ionic surfactant. *J. Pharm. Pharmacol.*, 22:148, 1970.
- [34] A. Ray. Solvophobic interactions and micelle formation in structure forming nonaqueous solvents. *Nature*, 231:313–315, 1971.
- [35] A.H. Beesley and D.F. Evans. Evidence for the essential role of hydrogen bonding in promoting amphiphilic self-assembly: Measurements in 3-mehtylsydnone. *J. Phys. Chem.*, 92:791–793, 1988.
- [36] B. Madan and B. Lee. Role of hydrogen bonding in hydrophobicity: the free energy of cavity formation in water models with and without the hydrogen bonds. *Biophys. Chem.*, 51:271–278, 1994.
- [37] B. Lee. Enthalpy-entropy compensation in the thermodynamics and hydrophobicity. *Biophys. Chem.*, 51:271–278, 1994.
- [38] A. Pohorille and L.R. Pratt. Cavities in molecular liquids and the theories of hydrophobic solubilities. *J. Am. Chem. Soc.*, 112:5066–5074, 1990.
- [39] T. Lazaridis. Solvent size vs. cohesive energy as the origin of hydrophobicity. *Acc. Chem. Res.*, 34(12):931–937, 2001.
- [40] L. Maibaum, A.R. Dinner, and D. Chandler. Micelle formation and the hydrophobic effect. *J. Phys. Chem. B*, 108(21):6778–6781, 2004.
- [41] K. Shinoda and E. Hutchinson. Pseudo-phase separation model for thermodynamic calculations on micellar solutions. *J. Phys. Chem.*, 66(4):557–582, 1962.

- [42] J. E. Desnoyers and G. Perron. *Thermodynamic methods*, pages 1–55. Surfactant solutions: New methods of investigations. Marcel Dekker, Inc, 1900.
- [43] J.E. Desnoyers, G. Garon, R. DeLisi, R. Roberts, R. Roux, and G. Perron. Thermodynamic properties of alkyldimethylamine oxides in water. application of a mass-action model for micellisation. *J. Phys. Chem.*, 87(8):1397–1406, 1983.
- [44] E.M. Wooley and T.E. Burchfield. Thermodynamics of ionic surfactant solutions containing added strong electrolyte. *Fluid Phase Equilib.*, 20:225–232, 1985.
- [45] J-C. Desplat. *Monte Carlo simulations of amphiphilic systems*. Ph.d. thesis, Sheffield Hallam University, 1996.
- [46] H. Wenneström and B. Lindman. Micelles. physical chemistry of surfactant association. *Phys. Rep.*, 52(1):1–86, 1979.
- [47] A. Ben-Shaul, I. Szleifer, and W. M. Gelbart. *Amphiphile chain organization in micelles of different geometries*, pages 303–335. Proceedings of the international school of physics ‘Enrico Fermi’ - Physics of Amphiphiles: Micelles, Vesicles and microemulsions. Italian Physical Society, 1985.
- [48] T.L. Hill. *Thermodynamics of small systems*, volume 1 and 2. Benjamin, New York, 1964.
- [49] D.G. Hall and B.A. Pethica. *Non-ionic surfactants*, chapter 16. Marcel Dekker, New York, 1967.
- [50] J. F. Scamehorn. *An overview of phenomena involving surfactant mixtures*, volume 311 of *Phenomena in mixed surfactant systems*, pages 1–27. American Chemical Society, Washington, DC, ACS symposium series edition, 1986.
- [51] M. Abe, H. Uchiyama, T. Yamagushi, T. Suzuki, K. Ogino, J.F. Scamehorn, and S.D. Christian. Micelle formation by pure nonionic surfactants and their mixtures. *Langmuir*, 8:2147–2151, 1992.
- [52] S. Puvvada and D. Blankschtein. Thermodynamic description of micellization, phase behaviour, and phase separation of aqueous solutions of surfactant mixtures. *J. Phys. Chem.*, 96:5567–5579, 1992.
- [53] S. Puvvada and D. Blankschtein. Theoretical and experimental investigations of micellar properties of aqueous solutions containing binary mixtures of nonionic surfactants. *J. Phys. Chem.*, 96:5579–5592, 1992.
- [54] M.R. Wenk. The emerging field of lipidomics. *Nature Rev. Drug discovery*, 4(7):594–610, 2005.
- [55] P.M. Holland and D.N. Rubingh. *Mixed surfactant systems*, volume 501. ACS Symposium Series, 1992.

- [56] R. Nagarajan. volume 501 of *Mixed surfactant systems*, page 54. American Chemical Society, Washington, DC, acs symposium series edition, 1992.
- [57] M.P. Allen and D.J. Tildesley. *Computer simulation of liquids*. Oxford University Press, 1987.
- [58] W.C. Swope, H.C. Andersen, P.H. Berens, and K.R. Wilson. A computer simulation method for the calculation of equilibrium constants for the formation of physical clusters of molecules: Application to small water clusters. *J. Chem. Phys.*, 76(1):637–649, 1982.
- [59] H. Goldstein, C. Poole, and J. Safko. pages 191–198. *Classical Mechanics*. Addison Wesley, 2001.
- [60] A.R. Leach. *Molecular modelling. Principles and applications*. Pearson Education limited, 2001.
- [61] S.W. Haan and L.R. Pratt. Monte carlo study of a simple model for micelle structure. *Chem. Phys. Lett.*, 79(3):436–440, 1981.
- [62] B. Owenson and L.R. Pratt. Molecular statistical thermodynamics of model micellar aggregates. *J. Phys. Chem.*, 88:2905–2915, 1984.
- [63] K.A. Dill and P.J. Flory. Molecular organization of micelles and vesicles. *Proc. Nat. Acad. Sci.*, 78:676, 1981.
- [64] F.M. Menger. On the structure of micelles. *J. Am. Chem. Soc.*, 106:1109–1113, 1984.
- [65] J.M. Haile and J.P. O’Connell. Internal structure of a model micelle via computer simulation. *J. Phys. Chem.*, 88:6363–6366, 1984.
- [66] M.C. Woods, J.M. Haile, and J.P. O’Connell. Internal structure of a model micelle via computer simulation. 2. spherically confined aggregates with mobile head groups. *J. Phys. Chem.*, 90:1875–1885, 1986.
- [67] R.G. Larson, L.E. Scriven, and H.T. Davis. Monte carlo simulation of model amphiphile-oil-water systems. *J. Chem. Phys.*, 83(5):2411–2420, 1985.
- [68] R.G. Larson. Monte carlo lattice simulation of amphiphilic systems in two and three dimensions. *J. Chem. Phys.*, 89(3):1642–1650, 1988.
- [69] R.G. Larson. Self-assembly of surfactant liquid crystalline phases by monte carlo simulation. *J. Chem. Phys.*, 91(4):2479–2488, 1989.
- [70] R.G. Larson. Monte carlo simulation of microstructural transitions in surfactant systems. *J. Chem. Phys.*, 96(11):7904–7918, 1992.
- [71] R.G. Larson. Molecular simulation of ordered amphiphilic phases. *Chem. Eng. Sci.*, 49(17):2833–2850, 1994.

- [72] R.G. Larson. Monte carlo simulations of the phase behaviour of surfactant solutions. *J. Phys. II France*, 6:1441–1463, 1996.
- [73] D. Brindle and C.M. Care. Self-assembly of bilayers in a lattice model of amphiphile and solvent systems. *Mol. Sim.*, 5:345–351, 1990.
- [74] D. Brindle and C.M. Care. Phase diagram for the lattice model of amphiphile and solvent mixtures by monte carlo simulation. *J. Chem. Soc. Faraday Trans.*, 88:2163–2166, 1992.
- [75] C.M. Care. Cluster size distribution in a monte carlo simulation of the micellar phase of an amphiphile and solvent mixture. *J. Chem. Soc. Faraday Trans.*, 83(9):2905–2912, 1987.
- [76] C.M. Care. Cluster partition function for the micellar phase of an amphiphile-solvent mixture in a lattice model. *J. Phys. Cond. Matt.*, 1:8583–8594, 1989.
- [77] C.M. Care, J-C. Desplat, and D. Brindle. Lattice models of surfactant systems. *Tenside Surf. Det.*, 30(4):281–286, 1993.
- [78] C.M. Care, T. Dalby, and J-C. Desplat. Micelle formation in a lattice model of an amphiphile and solvent mixture. *Progr. Coll. Polym. Sci.*, 103:130–137, 1997.
- [79] C.M. Care and T. Dalby. Packing entropy in micelle self-assembly. *Euro. Phys.*, 45(1):38–44, 1999.
- [80] S.K. Talsania, Y. Wang, R. Rajagopalan, and K.K. Mohanty. Monte carlo simulations for micellar encapsulation. *J. Coll. Int. Sc.*, 190(92):103, 1997.
- [81] P.H. Nelson, T. Alan Hatton, and G.C. Rutledge. Asymmetric growth in micelles containing oil. *J. Chem. Phys.*, 110(19):9673–9680, 1999.
- [82] J. Ding, T.J. Carver, and A.H. Windle. Self-assembled structures of block copolymers in selective solvents reproduced by lattice monte carlo simulation. *Comput. Theor. Polym. Sci.*, 11:483–490, 2001.
- [83] A. Bhattacharya, S.D. Mahanti, and A. Chakrabarti. Self-assembly of neutral and ionic surfactants: an off-lattice monte carlo approach. *J. Chem. Phys.*, 108(24):10281, 1998.
- [84] A. Bhattacharya and S.D. Mahanti. Energy and size fluctuations of amphiphilic aggregates in a lattice model. *Journal of Physics: Condensed Matter*, 12(28):6141–6160, 2000.
- [85] A. Bhattacharya and S.D. Mahanti. Critical micelle concentration in three-dimensional lattice models of amphiphiles. *J. Phys. Cond. Matt.*, 13:L861–L869, 2001.

- [86] A. Bhattacharya and S.D. Mahanti. Self-assembly of ionic surfactants and formation of mesostructures. *J. Phys. Cond. Matt.*, 13(7):1413–1428, 2001.
- [87] P.H. Nelson, G.C. Rutledge, and T. Alan Hatton. On the size and shape of self-assembled micelles. *J. Chem. Phys.*, 107(24):10777–10781, 1997.
- [88] B. Jönsson, O. Edholm, and O. Teleman. Molecular dynamics simulations of a sodium octanoate micelle in aqueous solution. *J. Chem. Phys.*, 85(4):2259–2271, 1986.
- [89] K. Watanabe, M. Ferrario, and M.L. Klein. Molecular dynamics study of sodium octanoate micelle in aqueous solution. *J. Phys. Chem.*, 92:819–821, 1988.
- [90] K. Watanabe and M.L. Klein. Shape fluctuations in ionic micelles. *J. Phys. Chem.*, 93:6897–6901, 1989.
- [91] J-P. Mailet, V. Lachet, and P.V. Coveney. Large scale molecular dynamics simulations of self-assembly processes in short and long chain cationic surfactants. *PCCP*, 1:5277–5290, 1999.
- [92] E. Egberts and H.J.C. Berendsen. Molecular dynamics simulation of a smectic liquid crystal with atomic detail. *J. Chem. Phys.*, 89:3718–3732, 1988.
- [93] S.E. Feller, Y. Zhang, and R.W. Pastor. Computer simulation of liquid/liquid interface. ii. surface tension-area dependence of a bilayer and monolayer. *J. Chem. Phys.*, 103(23):10267–10276, 1995.
- [94] H. Heller, M. Schaefer, and K. Schulten. Molecular dynamics simulation of a bilayer of 200 lipids in the gel and in the liquid-crystal phases. *J. Phys. Chem.*, 97:8343–8360, 1993.
- [95] E. Lindahl and O. Edholm. Mesoscopic undulations and thickness fluctuations in lipid bilayers from molecular dynamics simulations. *Biophys. J.*, 79:426–433, 2000.
- [96] E. Egberts, S.J. Marrink, and H.J.C. Berendsen. Molecular dynamics simulation of a phospholipid membrane. *Euro. Biophys. J.*, 22:423–436, 1994.
- [97] P. Huang, J.J. Perez, and G.H. Loew. Molecular dynamics simulations of phospholipid bilayers. *J. Biomol. Struct. Dyn.*, 11:927–956, 1994.
- [98] W. Shinoda, T. Fukada, S. Okasaki, and I. Okada. Molecular dynamics simulations of the dipalmitoylphosphatidylcholine (dppc) lipid bilayer in the fluid phase using the nose-parrileno-rahman npt ensemble. *Chem. Phys. Lett.*, 232:308–322, 1995.
- [99] K. Tu, D.J. Tobias, and M.L. Klein. Constant pressure and temperature molecular dynamics simulation of a fully hydrated liquid crystal phase dipalmitoylphosphatidylcholine bilayer. *Biophys. J.*, 69:2558–2562, 1995.

- [100] S.W. Chiu, M. Clark, V. Balaji, S. Subramaniam, and H.L. Scott. Incorporation of surface tension into the molecular dynamics simulation of an interface: a fluid phase lipid bilayer membrane. *Biophys. J.*, 69:1230–1245, 1995.
- [101] D.P. Tieleman and H.J.C. Berendsen. Molecular dynamics simulations of a fully hydrated dipalmitoylphosphatidylcholine bilayer with different macroscopic boundary conditions and parameters. *J. Chem. Phys.*, pages 4871–4880, 1996.
- [102] S.J. Marrink, E. Lindhal, O. Edholm, and A.E. Mark. Simulation of the spontaneous aggregation of phospholipids into bilayers. *J. Am. Chem. Soc.*, 123:8638–8639, 2001.
- [103] S.J. Marrink and A.E. Mark. Effect of undulations on surface tension in simulated bilayers. *J. Phys. Chem. B*, 105:6122–6127, 2001.
- [104] D.P. Tieleman, H. Leontiadou, A.E. Mark, and S.J. Marrink. Simulation of pore formation in lipid bilayer by mechanical stress and electric field. *J. Am. Chem. Soc.*, 125:6382–6383, 2001.
- [105] S.J. Marrink and D.P. Tieleman. Molecular dynamics simulation of a lipid diamond cubic phase. *J. Am. Chem. Soc.*, 123(49):12383–12391, 2001.
- [106] S.J. Marrink and D.P. Tieleman. Molecular dynamics simulation of spontaneous membrane fusion during a cubic-hexagonal phase transition. *Biophysical Journal*, 83:2386–2392, 2002.
- [107] A.H. De Vries, A.E. Mark, and S.J. Marrink. Molecular dynamics simulation of the spontaneous formation of a small dppc vesicle in atomistic detail. *J. Am. Chem. Soc.*, 126:4488–4489, 2004.
- [108] B. Smit. Molecular-dynamics simulations of amphiphilic molecules at a liquid-liquid interface. *Phys. Rev. A.*, 37(9):3431–3433, 1988.
- [109] B. Smit, P.A.J. Hilbers, and K. Esselink. Computer simulations of a water/oil interface in the presence of micelles. *Nature*, 348:624–625, 1990.
- [110] B. Smit, P.A.J. Hilbers, K. Esselink, L.A.M. Rupert, N.M.v. Os, and A.G. Schlijper. Structure of a water/oil interface in the presence of micelles: A computer simulation study. *J. Phys. Chem.*, 95:6361–6368, 1991.
- [111] B. Smit, K. Esselink, P.A.J. Hilbers, N.M.v. Os, L.A.M. Rupert, and I. Szleifer. Computer simulations of surfactant self-assembly. *Langmuir*, 9:9–11, 1993.
- [112] B. Smit, P.A.J. Hilbers, and K. Esselink. Computer simulations of simple oil/water/surfactants systems. *Tenside Surf. Det.*, 30(4):287–293, 1993.

- [113] R. Goetz and R. Lipowsky. Computer simulations of bilayer membranes: self-assembly and interfacial tension. *J. Chem. Phys.*, 108(17):7397–7409, 1998.
- [114] R. Goetz, G. Gompper, and R. Lipowsky. Mobility and elasticity of self-assembled membranes. *Phys. Rev. Lett.*, 82:221–224, 1999.
- [115] S.J. Marrink and A.E. Mark. the mechanism of vesicle fusion as revealed by molecular dynamics simulations. *J. Am. Chem. Soc.*, 125:11144–11145, 2003.
- [116] S.J. Marrink and A.E. Mark. Molecular dynamics simulation of the formation, structure, and dynamics of small phospholipid vesicles. *J. Am. Chem. Soc.*, 125:15233–15242, 2003.
- [117] S.J. Marrink, A.H. De Vries, and A.E. Mark. Coarse grained model for semi-quantitative lipid simulations. *J. Phys. Chem. B*, 108:750–760, 2004.
- [118] J.C. Shelley, M.Y. Shelley, R.C. Reeder, S. Bandyopadhyay, and M.L. Klein. A coarse grain model for phospholipid simulations. *J. Phys. Chem. B*, 105:4464–4470, 2001.
- [119] J.C. Shelley, M.Y. Shelley, R.C. Reeder, S. Bandyopadhyay, P.B. Moore, and M.L. Klein. Simulations of phospholipids using a coarse grain model. *J. Phys. Chem. B*, 105:9785–9792, 2001.
- [120] C.F. Lopez, P.B. Moore, J.C. Shelley, M.Y. Shelley, and M.L. Klein. computer simulation studies of biomembranes using a coarse grain model. *Comput. Phys. Comm.*, 147:1–6, 2002.
- [121] M.J. Stevens. Insights into the molecular mechanism of membrane fusion from simulation: Evidence for the association of splayed tails. *Phys. Rev. Lett.*, 91(18):188102, 2003.
- [122] O. Farago. Water-free computer model for fluid bilayer membranes. *J. Chem. Phys.*, 119:596, 2003.
- [123] I.R. Cooke, K. Kremer, and M. Deserno. Tunable generic model for fluid bilayer membranes. *Phys. Rev. E*, 72:011506, 2005.
- [124] I.R. Cooke and M. Deserno. Solvent-free model for self-assembling fluid bilayer membranes: Stabilization of the fluid phase based on broad attractive tail potentials. *J. Chem. Phys.*, 123:224710, 2005.
- [125] G. Brannigan, A.C. Tamboli, and F.L.H. Brown. The role of molecular shape in bilayer elasticity and phase behaviour. *J. Chem. Phys.*, 121(7):3259–3271, 2004.
- [126] G. Brannigan and F.L.H. Brown. Solvent-free simulations of fluid membrane bilayers. *J. Chem. Phys.*, 120(2):1059–1071, 2004.

- [127] G. Brannigan, P.F. Philips, and F.L.H. Brown. Flexible lipid bilayers in implicit solvent. *Phys. Rev. E*, 72:011915, 2005.
- [128] G. Brannigan and F.L.H. Brown. Composition dependence of bilayer elasticity. *J. Chem. Phys.*, 122:074905, 2005.
- [129] G. Brannigan, L.C.-L. Lin, and F.L.H. Brown. Implicit solvent simulation models for biomembranes. *Euro. Biophys. J.*, 35:104, 2006.
- [130] J.R. Gunn and K.A. Dawson. Microscopic model of amphiphilic assembly. *J. Chem. Phys.*, 91(10):6393–6403, 1989.
- [131] S. Jury, P. Bladon, M. Cates, S. Krishna, M. Hagen, N. Ruddock, and P. Warren. Simulation of amphiphilic mesophases using dissipative particle dynamics. *Phys. Chem. Chem. Phys.*, 1:2051–2056, 1999.
- [132] P. Prinsen, P.B. Warren, and M.A.J. Michels. Mesoscale simulations of surfactant dissolution and mesophase formation. *Phys. Rev. Letters.*, 89(14):148302, 2002.
- [133] P.B. Warren, P. Prinsen, and M.A.J. Michels. The physics of surfactant dissolution. *Phil. Trans. R. Soc. Lond. A*, 361:665–676, 2003.
- [134] D.R. Groot and P.B. Warren. Dissipative particle dynamics: Bridging the gap between atomistic and mesoscopic simulation. *J. Chem. Phys.*, 107(11):4423–4435, 1997.
- [135] M. Venturoli and B. Smit. Simulating the self-assembly of model membranes. *PhysChemComm*, 10, 1999.
- [136] M. Kranenburg, C. Laforge, and B. Smit. Mesoscopic simulations of phase transitions in lipid bilayers. *Phys. Chem. Chem. Phys.*, 6(19):4531–4534, 2004.
- [137] M. Kranenburg, J-P. Nicolas, and B. Smit. Comparison of mesoscopic phospholipid-water models. *Phys. Chem. Chem. Phys.*, 6(16):4142–4151, 2004.
- [138] M. Kranenburg and B. Smit. Phase behaviour of model lipid bilayers. *J. Phys. Chem. B*, 109(14):6553–6563, 2005.
- [139] M. Kranenburg and B. Smit. Simulating the effect of alcohol on the structure of a membrane. *FEBS Letters*, 568(1-3):15–18, 2004.
- [140] M. Kranenburg, M. Venturoli, and B. Smit. Molecular simulations of mesoscopic bilayer phases. *Phys. Rev. E*, 67:060901(R), 2004.
- [141] M. Kranenburg, M. Venturoli, and B. Smit. Phase behaviour and induced interdigitation in bilayers studied with dissipative particle dynamics. *J. Phys. Chem. B*, 107(41):11491–11501, 2003.

- [142] M. Kranenburg, M. Vlaar, and B. Smit. Simulating induced interdigitation in membranes. *Biophys. J.*, 87:1596–1605, 2004.
- [143] J.C. Shillcock and R. Lipowsky. Tension-induced fusion of bilayer membranes and vesicles. *Nature Materials*, 4:225–228, 2005.
- [144] H. Nogushi. Fusion and toroidal formation of vesicles by mechanical forces: a brownian dynamics simulation. *J. Chem. Phys.*, 117(17):8130–8137, 2002.
- [145] J.C. Shillcock and R. Lipowsky. Equilibrium structure and lateral stress distribution of amphiphilic bilayers from dissipative particle dynamics simulations. *J. Chem. Phys.*, 117:5048–5061, 2002.
- [146] G. Illya, R. Lipowsky, and J.C. Shillcock. Effect of chain length and asymmetry on material properties of bilayer membranes. *J. Chem. Phys.*, 122:244901, 2005.
- [147] V. Ortiz, S.O. Nielsen, D.E. Discher, M.L. Klein, R. Lipowsky, and J.C. Shillcock. Dissipative particle dynamics simulations of polymersomes. *J. Phys. Chem. B*, 109:17708–17714, 2005.
- [148] H. Nogushi and M. Takasu. Self-assembly of amphiphiles into vesicles. *Phys. Rev. E*, 64:041913, 2001.
- [149] H. Nogushi. Fusion pathways of vesicles: A brownian dynamics simulation. *J. Chem. Phys.*, 115(20):9547–9551, 2001.
- [150] H. Nogushi and M. Takasu. Adhesion of nanoparticles to vesicles: a brownian dynamics simulation. *Biophys. J.*, 83(1):299–308, 2002.
- [151] H. Nogushi. Polyhedral vesicles: A brownian dynamics simulation. *Phys. Rev. E*, 67:041901, 2003.
- [152] B.M. Boghosian, P.V. Coveney, and P.J. Love. A three-dimensional lattice-gas model for amphiphilic fluid dynamics. *Proc. Roy. Soc. A: Maths, Phys and Eng. Sci.*, 456(1998):1431–1454, 2000.
- [153] M. Nekovee, P.V. Coveney, H. Chen, and B.M. Boghosian. A lattice-boltzmann model for interacting amphiphilic fluids. *Phys Rev E Stat Phys Plasmas Fluids Relat Interdiscip Topics.*, 62:8282–8294, 2000.
- [154] P.J. Love, M. Nekovee, J. Chin, N. Gonzalez-Segredo, and P.V. Coveney. Simulations of amphiphilic fluids using mesoscale lattice-boltzmann and lattice-gas methods. *Comp. Phys. Comm.*, 153(3):340–358, 2003.
- [155] J. Höpken, C. Pugh, W. Richtering, and M. Möller. *Makromol. Chem.*, 189:911–925, 1988.
- [156] Y. Hayami and G.H. Findenegg. Surface crystallization and phase transitions of the adsorbed film of $f(cf_2)_{12}(ch_2)_{16}h$ at the surface of liquid. 1997.

- [157] M.P. Turberg and J.E. Brady. Semifluorinated hydrocarbons: primitive surfactant molecules. *J. Am. Chem. Soc.*, 110:7797, 1988.
- [158] P. Lo Nostro and S.H. Chen. Aggregation of a semifluorinated n-alkane in perfluorooctane. *J. Phys. Chem.*, 97:6535–6540, 1993.
- [159] B.J. Berne and P. Pechukas. Gaussian model potentials for molecular interactions. *J. Chem. Phys.*, 56(8):4213–4216, 1972.
- [160] J.G. Gay and B.J. Berne. Modification of the overlap potential to mimic a linear site-site potential. *J. Chem. Phys.*, 74(6):3316–3319, 1981.
- [161] D.J. Adam, G.R. Luckhurst, and R.W. Phippen. Computer simulation studies of anisotropic systems. xvii the gay-berne model nematogen. *Mol. Phys.*, 61:1575, 1987.
- [162] G.R. Luckhurst, R.A. Stephens, and R.W. Phippen. Computer simulation studies of anisotropic systems. xix mesophases formed by the gay-berne model mesogen. *Liqu. Crys.*, 8:451, 1990.
- [163] M.J. Chalam, K.E. Gubbins, E. de Miguel, and L.F. Rull. A molecular simulation of a liquid crystal model: bulk and confined fluid. *Mol. Sim.*, 7:357, 1991.
- [164] E. de Miguel, L.F. Rull, M.J. Chalam, and K.E. Gubbins. Location of the isotropic-nematic transition in the gay-berne model. *Mol. Phys.*, 72:593, 1991.
- [165] E. de Miguel, L.F. Rull, M.J. Chalam, and K.E. Gubbins. Liquid crystal phase diagram of the gay-berne fluid. *Mol. Phys.*, 74:405, 1991.
- [166] R. Berardi, A.P.J. Emerson, and C. Zannoni. Monte carlo investigations of a gay-berne liquid crystal. *J. Chem. Soc. Faraday Trans.*, 89:4069, 1993.
- [167] M.P. Allen, M.A. Warren, M.R. Wilson, A. Sauron, and W. Smith. Molecular dynamics calculation of elastic constants in gay-berne nematic liquid crystals. *J. Chem. Phys.*, 105:2850, 1996.
- [168] G.R. Luckhurst and P.S.J. Simmonds. Computer simulation studies of anisotropic systems. xxi. parametrization of the gay-berne mesogen. *Mol. Phys.*, 80:233, 1993.
- [169] M.A. Bates and G.R. Luckhurst. Computer simulation studies of anisotropic systems. xxx. the phase behaviour and structure of a gay-berne mesogen. *J. Chem. Phys.*, 110:7087, 1999.
- [170] E. de Miguel, E. Martin del Rio, J.T. Brown, and M.P. Allen. Effects of the attractive interactions on the phase behaviour of the gay-berne liquid crystal model. *J. Chem. Phys.*, 105:1, 1996.

- [171] J.T. Brown, M.P. Allen, E. Martin del Rio, and E. de Miguel. Effects of elongation on the phase behaviour of the gay-berne fluid. *Phys. Rev. E*, 57:6685, 1998.
- [172] C. Zannoni. Molecular design and computer simulations of novel mesophases. *J. Matter. Chem.*, 11:2637–2646, 2001.
- [173] M.R. Wilson. Progress in computer simulations of liquid crystals. *Int. Rev. Phys. Chem*, 24:421–455, 2005.
- [174] C.M. Care and D.J. Cleaver. Computer simulation of liquid crystals. *Rep. Prog. Phys.*, 68:2665–2700, 2005.
- [175] H. Zwedie. Computer simulation studies of liquid crystals: a new corner potential for a cylindrically symmetric particles. *J. Chem. Phys.*, 108:2117, 1998.
- [176] H. Zwedie. Computer simulations of diskotic liquid crystals. *Phys. Rev. E*, 57:1793, 1998.
- [177] F. Barmes, M. Ricci, C. Zannoni, and D.J. Cleaver. Computer simulation of pear shaped particles. *Phys. Rev. E*, 68:021708, 2003.
- [178] R. Berardi, S. Orlandi, and C. Zannoni. Antiphase structures in polar smectic liquid crystals and their molecular origin. *Chem. Phys. Lett.*, 261:357–362, 1996.
- [179] M.P. Neal and A.J. Parker. Computer simulations using a longitudinal quadrupolar gayberne model: effect of the quadrupole magnitude on the formation of the smectic phase. *Chem. Phys. Lett.*, 294(4-5):277–284, 1998.
- [180] M.P. Neal and A.J. Parker. Molecular dynamics study of mesophase formation using a transverse quadrupol gay-berne model. *Phys. Rev. E*, 63:011706, 2001.
- [181] D.J. Cleaver, C.M. Care, M.P. Allen, and M.P. Neal. Extension and generalisation of the gay-berne potential. *Phys. Rev. E*, 54:559–567, 1996.
- [182] R.A. Bemrose, C.M. Care, D.J. Cleaver, and M.P. Neal. Computer simulation of bi-disperse liquid crystals: the effect of concentration on phase behaviour and structural properties. *Mol. Cryst. Liq. Cryst.*, 299:27, 1997.
- [183] R.A. Bemrose, C.M. Care, D.J. Cleaver, and M.P. Neal. A molecular dynamics study of a bi-disperse liquid crystal mixture using a generalised gay-berne potential. *Mol. Phys.*, 90:625, 1997.
- [184] S.J. Mills and D.J. Cleaver. Gibbs ensemble simulation of nematic-isotropic coexistence in a liquid crystal mixture. *Mol. Phys.*, 98:1379, 2000.

- [185] D. Antypov. *Computer simulation of rod-sphere mixtures*. Ph.d. thesis, Sheffield Hallam University, 2003.
- [186] D. Antypov and D.J. Cleaver. The role of attractive potentials in rod-sphere mixtures. *J. Chem. Phys.*, 120:10307, 2004.
- [187] D. Antypov and D.J. Cleaver. The effect of spherical additives on a liquid crystal colloid. *J. Phys. Cond. Matt.*, 16:S1887, 2004.
- [188] A. Lang, C.N. Likos, M. Watzlawek, and H. Löwen. Fluid and solid phases of the gaussian core model. *J. Phys.: Condens. Matter*, 12:5087–5108, 2000.
- [189] T. Dalby. *Computer simulation of micelle self-assembly*. Ph.d. thesis, Sheffield Hallam University, 2000.
- [190] A.H. De Vries, A.E. Mark, and S.J. Marrink. The binary mixing behaviour of phospholipids in a bilayer: A molecular dynamics study. *J. Phys. Chem. B*, 108:2454–2463, 2004.
- [191] E. Diaz-Herrera, J. Alejandre, G. Ramirez-Santiago, and F. Forstmann. Interfacial tension behaviour of binary and ternary mixtures of partially miscible lennard-jones fluids: A molecular dynamics simulation. *J. Chem. Phys.*, 110(16):8084–8089, 1999.
- [192] W. Scott, F. Muller-Plathe, and W. F. Van Gunsteren. Molecular dynamics study of the mixing and demixing of a binary lennard-jones fluid. *Mol. Phys.*, 82(5):1049–1062, 1994.
- [193] S.J. Marrink and A.E. Mark. Molecular dynamics simulations of mixed micelles modelling human bile. *Biochem.*, 41:5375–5382, 2002.
- [194] J. Ulmius, G. Lindblom, H. Wennerström, L.B.-Å. Johansson, K. Fontell, O. Söderman, and G. Arvidson. Molecular organization in the liquid-crystalline phases of lecithin-sodium cholate-water systems studied by nuclear magnetic resonance. *Biochem.*, 21:1553–1560, 1982.
- [195] J.W. Nichols and J. Ozarowski. Sizing of lecithin-bile salt mixed micelles by size-exclusion high performance liquid chromatography. *Biochem.*, 29:4600–4606, 1990.
- [196] N.A. Mazer, G. Benedeck, and M.C. Carey. Quasielastic light-scattering studies of aqueous biliary lipid systems. mixed micelle formation in bile salt-lecithin solutions. *Biochem.*, 19(4):601–615, 1980.
- [197] L. Muccioli and C. Zannoni. A deformable gay-berne model for the simulation of liquid crystals and soft materials. *Chem. Phys. Lett.*, 423:1–6, 2006.
- [198] A. Ben-Naim. Statistical mechanics of ‘waterlike’ particles in two dimensions. i. physical model and application of the perkus-yevick equation. *J. Chem. Phys.*, 54(9):3682–3695, 1970.

- [199] A. Ben-Naim. Statistical mechanics of ‘waterlike’ particles in two dimensions. ii. one component system. *Mol. Phys.*, 24(4):705–721, 1972.
- [200] K.A.T. Silverstein, A.D.J. Haymet, and K.A. Dill. A simple model of water and the hydrophobic effect. *J. Am. Chem. Soc.*, 120:3166–3175, 1998.
- [201] K.A.T. Silverstein and K.A. Dill. Hydrophobicity in a simple model of water: Entropy penalty as a sum of competing terms via full, angular expression. *J. Chem. Phys.*, 114(14):6303–6314, 2001.
- [202] D. Bratko, L. Blum, and A. Luzar. A simple model for the intermolecular potential of water. *J. Chem. Phys.*, 83(12):6367–6370, 1985.
- [203] Y. Liu and T. Ichiye. Soft sticky dipole potential for liquid water: a new model. *J. Phys. Chem.*, 100:2723–2730, 1996.
- [204] C.J. Fennel and J.D. Gezelter. On the structural and transport properties of the soft sticky dipole and related single-point water models. *J. Chem. Phys.*, 120(19):9175–9184, 2004.